

University of Alberta

**THE USE OF MICROFLUIDICS FOR ANALYSIS OF
PROTEIN SAMPLES:
IMMUNOASSAY AND PROTEOMIC APPLICATIONS**

by



Justine Taylor

A thesis submitted to the Faculty of Graduate Studies in partial fulfilment of the requirements for the degree of Doctor of Philosophy

Department of Chemistry
Edmonton, Alberta

Spring 2004



Library and
Archives Canada

Bibliothèque et
Archives Canada

Published Heritage
Branch

Direction du
Patrimoine de l'édition

395 Wellington Street
Ottawa ON K1A 0N4
Canada

395, rue Wellington
Ottawa ON K1A 0N4
Canada

Your file *Votre référence*

ISBN: 0-612-96325-X

Our file *Notre référence*

ISBN: 0-612-96325-X

The author has granted a non-exclusive license allowing the Library and Archives Canada to reproduce, loan, distribute or sell copies of this thesis in microform, paper or electronic formats.

L'auteur a accordé une licence non exclusive permettant à la Bibliothèque et Archives Canada de reproduire, prêter, distribuer ou vendre des copies de cette thèse sous la forme de microfiche/film, de reproduction sur papier ou sur format électronique.

The author retains ownership of the copyright in this thesis. Neither the thesis nor substantial extracts from it may be printed or otherwise reproduced without the author's permission.

L'auteur conserve la propriété du droit d'auteur qui protège cette thèse. Ni la thèse ni des extraits substantiels de celle-ci ne doivent être imprimés ou autrement reproduits sans son autorisation.

In compliance with the Canadian Privacy Act some supporting forms may have been removed from this thesis.

Conformément à la loi canadienne sur la protection de la vie privée, quelques formulaires secondaires ont été enlevés de cette thèse.

While these forms may be included in the document page count, their removal does not represent any loss of content from the thesis.

Bien que ces formulaires aient inclus dans la pagination, il n'y aura aucun contenu manquant.

Canada

ABSTRACT

The research presented in this work explores the application of microfluidics to medical research with specific focus on protein analysis. A study of solution-phase immunoassays investigated the possible limits of detection for competitive assays. This was accomplished through experimental analysis utilizing a microfluidic platform and theoretical calculations. The experimental system was a competitive, solution-phase, capillary electrophoretic immunoassay (CEIA) for estradiol utilizing laser induced fluorescence detection. The proposed theoretical model was simple and could be applied to any competitive CEIA for estimation of possible detection limit. The lowest experimental detection limit was 310 pM which corresponded to 2100 molecules passing through the detection volume. Using the same conditions as were used experimentally a theoretical prediction of detection limit resulted in 590 pM. This was also compared to the theoretical minimum detection limit under optimized conditions of 125 pM. It was concluded that for assays requiring low limits of detection, such as hormone assays, the use of solid-phase assays is necessary in order to be able to first concentrate the analyte before detection.

The application of microfluidic devices to the field of proteomics was also explored through the design and testing of a multichannel microfluidic platform. This platform was designed to be coupled to an external protein separation technique followed by on-chip, automated, protein digestion, peptide

preconcentration and mass spectrometric identification of twenty samples sequentially. A platform prototype was designed, built and tested. A series of experiments lead to valuable insights as to the issues that must be addressed when designing such systems. Topics included: buffer/solvent compatibilities, sample cross-contamination, dead volume analysis, system flow rate with relation to throughput and analyte sensitivity, just to name a few. Thorough analysis of these topics allowed for system re-design, which will lead to enhanced platform performance.

ACKNOWLEDGEMENTS

There are many people I'd like to thank for their help during my time in Edmonton. First and foremost, my supervisor, Prof. D.J. Harrison, who provided me with the intellectual and financial support to explore the world of microfluidics. Who through his generosity gave me the opportunity to travel far and wide in order to experience fully the academic experience.

Many thanks go to the DJH group members both past and present. Thanks to my mentors, Gregor Ocvirk and Cameron Skinner, who guided my initial foray into microfluidics. As well as to my peers who aided me with thoughtful ideas and discussions. To Arlene Figley who helped with so many last minute emergencies that I can't even begin to express my gratitude. Special thanks go to Dolores Martinez who has become a dear friend and made my time in Edmonton somewhat more bearable. Without her company in these last years I surely would have been the worse off.

Many thanks go to the Department of Chemistry support staff, without their help the work in this thesis would never have been accomplished. Thanks to Ed Feschuk, Al Chilton and Kim Do who guided me through all things electronic. All the machine shop staff, who put up with my urgent demands for various pieces that needed to be made. Thanks to the folks in the glass shop who let me use the glass saw, and took over when uncertainty got the best of me.

I also have to extend my gratitude to the many friends I have throughout the chemistry department who lent me their guidance when I ventured outside of my expertise. Thanks to Bernd Keller, Russ Handy and Chris McDonald for their instrumental advice and friendship. To all my organic friends, David Rabuka, Michel Gravel, Mark Nitz and many more, for their help and for daring to cross the organic-analytical boundary. Thanks to Rob Polakowski for insightful discussions on anything relevant and to Rob Bujalski for being my Windsor

connection and staying that way. Thanks to all my friends who kept me entertained and sane throughout these years.

Finally thanks to my family, without their support and guidance I never would have made it this far.

TABLE OF CONTENTS

CHAPTER 1:	LITERATURE REVIEW AND TOPIC INTRODUCTION	1
1.1	INTRODUCTION	2
1.2	IMMUNOASSAYS	4
1.2.1	PHASE	5
1.2.2	CONFIGURATION	6
1.2.3	LABELS, SEPARATION AND DETECTION	7
1.2.4	IMMUNOASSAY TECHNIQUES UTILIZED IN THIS STUDY	8
1.2.5	CE BACKGROUND	9
1.2.6	IMMUNOASSAYS ON-CHIP	11
1.3	PROTEOMICS	12
1.3.1	CONVENTIONAL TECHNIQUES	13
1.3.2	ALTERNATIVE SEPARATION TECHNIQUES	16
1.3.2.1	CIEF	17
1.3.3	DEVELOPMENT OF MICROCHIP MS	20
1.3.4	MICROCHIPS FOR PROTEOMICS	27
1.3.4.1	PROTEIN SEPARATIONS ON-CHIP	27
1.3.4.2	PROTEIN DIGESTION AND PEPTIDE SEPARATION	27
1.4	OBJECTIVES OF THIS THESIS	28
1.5	REFERENCES	30
CHAPTER 2:	AN EVALUATION OF THE DETECTION LIMITS POSSIBLE FOR COMPETITIVE CAPILLARY ELECTROPHORETIC IMMUNOASSAYS	38
2.1	INTRODUCTION	39
2.2	IMMUNOASSAY THEORY	41
2.3	MATERIALS AND METHODS	46
2.3.1	SOLUTIONS AND REAGENTS	46
2.3.2	INSTRUMENTATION	46
2.3.3	DEVICE FABRICATION	48
2.3.4	COMPETITIVE ESTRADIOL IMMUNOASSAY	49

2.4	RESULTS	50
2.4.1	ESTRADIOL ASSAY RESULTS	50
2.4.2	DETERMINATION OF REAGENT QUALITY	53
2.4.3	THEORETICAL PREDICTIONS FROM THE JACKSON AND EKINS MODEL	60
2.4.4	EFFECT OF CONCENTRATION AND AFFINITY ON DETECTION LIMITS	62
2.4.5	MINIMUM DETECTION LIMIT FROM THE DOSE-RESPONSE FUNCTION	65
2.4.6	EXPERIMENTAL VS. THEORETICAL	69
2.5	CONCLUDING REMARKS	70
2.6	REFERENCES	72

CHAPTER 3:	DESIGN OF A MUTIPLICED PLATFORM FOR PROTEOMICS	76
3.1	INTRODUCTION	77
3.2	PROJECT GOALS	78
3.3	CHIP DESIGN	78
3.3.1	SAMPLE INTRODUCTION – ELECTRICAL FRACTIONATION AREA	79
3.3.2	BED REGION	81
3.3.2.1	BOTTOM WAFER.....	81
3.3.2.2	TOP WAFER	81
3.3.3	VARIABLE REGION	84
3.3.4	COLLECTION REGION	86
3.3.5	SINGLE CHANNELS	86
3.3.5.1	BOTTOM WAFER.....	86
3.3.5.2	TOP WAFER	86
3.3.6	CHANNEL WIDTH	88
3.3.7	MATERIALS AND METHODS - FABRICATION DETAILS.....	95
3.4	HOLDER AND FLUIDIC INTERFACES	98
3.5	ELECTRICAL FRACTIONATION SYSTEM	102
3.6	ESI INTERFACE	104
3.7	FINAL PLATFORM	111
3.8	REFERENCES	114

CHAPTER 4:	PLATFORM PERFORMANCE	117
4.1	INTRODUCTION	118
4.2	CIEF	119
4.2.1	MATERIALS AND METHODS	119
4.2.2	RESULTS AND DISCUSSION.....	120
4.3	PRESSURE DRIVEN FLOW THROUGHOUT THE SYSTEM.....	127
4.3.1	MATERIALS AND METHODS	127
4.3.2	PRESSURE DRIVEN FLOW – BEDS NOT PACKED	129
4.3.3	PRESSURE DRIVEN FLOW – TRYPSIN BEDS PACKED	131
4.3.4	PRESSURE DRIVEN FLOW – BEDS PACKED.....	134
4.3.5	ELUENT EFFECTS	138
4.3.6	ADDITION OF AMPHOLYTES.....	140
4.3.7	EFFECT OF CONCENTRATION.....	144
4.3.8	METHOD VALIDATION – STANDARD PROTEINS.....	147
4.3.8.1	BSA.....	147
4.3.8.2	LYSOZYME	150
4.4	ELECTRICAL FRACTIONATION	152
4.4.1	METHODS	152
4.4.2	RESULTS AND DISCUSSION.....	153
4.5	REFERENCES	156
4.6	APPENDIX.....	157
CHAPTER 5:	EXPLORING THE INDIVIDUAL COMPONENTS OF THE MULTICHANNEL DEVICE	164
5.1	INTRODUCTION	165
5.2	ELECTRICAL FRACTIONATION	165
5.2.1	EXPERIMENTAL.....	166
5.2.2	RESULTS AND DISCUSSION.....	167
5.3	SINGLE CHANNEL WORK	173
5.3.1	EXPERIMENTAL.....	173
5.3.2	COMPARISON TO THE MULTICHANNEL SYSTEM.....	174
5.3.3	EFFECT OF FLOW RATE ON DIGESTION.....	176

5.3.4	LOWER SAMPLE AMOUNTS	178
5.3.5	EFFECT OF ELUENT	180
5.4	BAND BROADENING CONSIDERATIONS.....	182
5.4.1	THEORETICAL BAND BROADENING IN THE MULTICHANNEL CHIP.....	184
5.4.2	EFFECT OF FLOW RATE ON BAND BROADENING	186
5.4.3	EFFECT OF THE ESI INTERFACE ON BAND BROADENING	188
5.5	RESISTANCE TO FLOW WITHIN THE MULTICHANNEL SYSTEM	192
5.6	REFERENCES	207
CHAPTER 6:	CONCLUSIONS AND FUTURE WORK INVOLVING THE MULTICHANNEL DEVICE	208
6.1	SAMPLE INTRODUCTION.....	209
6.1.1	FRACTIONATION "STAR"	209
6.1.2	SAMPLE LOAD	210
6.2	BED REGION	210
6.2.1	DIGESTION BEDS.....	210
6.2.2	SPE BEDS.....	211
6.2.3	BED DESIGN	212
6.3	VARIABLE REGION	213
6.3.1	DELAY LINE.....	213
6.3.2	VALVES	214
6.4	COLLECTION REGION.....	214
6.5	SYSTEM FLOW RATE	215
6.6	APPLICATION TO PROTEOMICS	215
6.7	ALTERNATIVE APPLICATIONS	220
6.8	REFERENCES	221
APPENDIX	SUPPLIERS OF REAGENTS AND EQUIPMENT	223

LIST OF TABLES

Table 2.1	Experimental and theoretical detection limits for a competitive solution-phase estradiol assay	51
Table 2.2	Theoretical minimum DLs for competitive immunoassays at various K and CV ₀ based on the Jackson and Ekins model.....	61
Table 3.1	Empty SPE bed volumes and protein digest concentration capacity	83
Table 3.2	Empty trypsin bed volumes and protein digestion capacity	83
Table 3.3	Delay line calculations.....	89
Table 3.4	Theoretical elution times and peak widths for sample travelling through the variable region of the multichannel device	93
Table 3.5	Sample loading volumes	94
Table 3.6	Cross-sectional areas of the ESI interface	109
Table 4.1	Cytochrome c charge states.....	157
Table 4.2	Cytochrome c peptides.....	158
Table 4.3	Trypsin autodigestion peaks.....	159
Table 4.4	BSA peptides (disulphides not reduced)	160
Table 4.5	BSA peptides (disulphides reduced and capped).....	160
Table 4.6	Lysozyme peptides (disulphides reduced and capped).....	162
Table 5.1	Experimental and theoretical inlet flow distribution within the multichannel device.....	200

LIST OF FIGURES

Figure 1.1	Immunoassay configurations.....	7
Figure 1.2	Illustration of electroosmotic and electrophoretic forces.....	10
Figure 1.3	Proteolysis by trypsin	15
Figure 1.4	Illustration of the focusing process in CIEF	18
Figure 1.5	Illustration of one-step CIEF	20
Figure 1.6	Nine channel chip-ESI-MS device published by Figeys <i>et al.</i>	24
Figure 1.7	96 individual channels and ESI tip array device published by Liu <i>et al.</i>	25
Figure 1.8	96-well plate coupled to chip-ESI-MS published by Zhang <i>et al.</i>	26
Figure 2.1	Graphical interpretation of the detection limit (DL) calculation for a competitive immunoassay	45
Figure 2.2	Confocal epifluorescence optical set-up.....	47
Figure 2.3	Microfluidic device layout	49
Figure 2.4	Typical on-chip electropherogram for a competitive assay of estradiol.....	51
Figure 2.5	Experimental and theoretical calibration curves for a competitive assay of estradiol	52
Figure 2.6	Ultracentrifuge optical cell	54
Figure 2.7	Ultracentrifuge Rayleigh interference optical system.....	55
Figure 2.8	Structure of fluorescently labelled estradiol.....	57
Figure 2.9	MS/MS data of the molecular ion peak for fluorescently labelled estradiol.....	58
Figure 2.10	Saturation analysis for the determination of labelled estradiol concentration.....	59

Figure 2.11	Effect of antibody concentration on theoretical dose-response curves.....	63
Figure 2.12	Effect of reagent molar ratio (Ab:Ag*) on theoretical dose-response curves.....	64
Figure 2.13	Effect of K on theoretical dose-response curves.....	65
Figure 2.14	Theoretical plot of DL as a function of antibody concentration.....	66
Figure 2.15	Theoretical precision plots of RSD _o as a function of antibody concentration.....	68
Figure 3.1	Illustration of the channels in the bottom wafer of the multichannel device.....	79
Figure 3.2	Schematic illustrating electrokinetic fractionation.....	80
Figure 3.3	Cross-sectional view of the bed region in the multichannel device.....	82
Figure 3.4	Schematic illustrating sequential elution.....	85
Figure 3.5	Single channel details.....	87
Figure 3.6	Sources of dispersion in an open tube.....	90
Figure 3.7	Theoretical elution profile from the variable region of the multichannel device based on even flow distribution.....	92
Figure 3.8	Final multichannel chip design.....	95
Figure 3.9	Illustration of a transparency optical mask.....	96
Figure 3.10	Illustration of the device fabrication process.....	98
Figure 3.11	Cartoon side-view of the bed region with the septa and electrodes in place.....	99
Figure 3.12	Electrode assembly.....	99
Figure 3.13	Initial chip holder design. Top view.....	100
Figure 3.14	Final chip holder design. Bottom view.....	100
Figure 3.15	Final chip holder. Side view.....	101
Figure 3.16	Nanoport™ assembly attached to the inlet of the device.....	101

Figure 3.17	Electrical fractionation system.....	102
Figure 3.18	Ohm's law calculation for the fractionation pathway.....	103
Figure 3.19	Drilling procedure for chip-ESI coupling	105
Figure 3.20	Initial ESI liquid junction design (LJ-1).....	107
Figure 3.21	Second ESI interface (SS-1)	109
Figure 3.22	Final platform assembled for pressure driven flow	112
Figure 3.23	Final platform assembled for electrical fractionation.....	113
Figure 4.1	Typical CIEF experiment performed on a commercial CE instrument	121
Figure 4.2	Gel IEF separation of the IEF standard mixture	121
Figure 4.3	Effect of electric field strength on CIEF	122
Figure 4.4	Effect of ampholyte concentration on CIEF	123
Figure 4.5	Ampholyte absorbance at 280 nm.....	124
Figure 4.6	Effect of formic acid as anolyte on CIEF	125
Figure 4.7	Effect of ammonium bicarbonate as catholyte on CIEF.....	126
Figure 4.8	Effect of ammonium hydroxide as catholyte on CIEF.....	127
Figure 4.9	TIC of pressure infused cytochrome c into the platform without packing material in the beds.....	130
Figure 4.10	Cytochrome c spectrum extracted from Figure 4.9.....	130
Figure 4.11	TIC and extracted spectrum of pressure infused cytochrome c into the platform with the trypsin beds packed	132
Figure 4.12	Effect of acidic buffer conditions on trypsin digestion	133
Figure 4.13	TIC and XIC _{589.5} of loading, washing and elution of a cytochrome c sample using the multichannel device with both beds packed	134
Figure 4.14	Spectrum extracted from the loading phase of Figure 4.13.....	135
Figure 4.15	Resulting cytochrome c peptide spectrum during the elution phase of the TIC in Figure 4.13.....	136

Figure 4.16	Cytochrome c peptide XICs extracted from the TIC in Figure 4.13	137
Figure 4.17	TIC and XIC _{589.5} for loading, washing and elution of a cytochrome c sample using 50% ACN as eluent	138
Figure 4.18	Cytochrome c peptide XICs extracted from the TIC in Figure 4.17	139
Figure 4.19	Effect of ampholytes on cytochrome c signal	141
Figure 4.20	Selective ampholyte passage through the platform, XIC _{575.0} (ampholyte) and XIC _{634.5} (cytochrome c peptide)	142
Figure 4.21	Typical ampholyte spectrum extracted from the loading phase of Figure 4.20	143
Figure 4.22	Extracted cytochrome c peptide spectrum from the elution phase of Figure 4.20	143
Figure 4.23	Cytochrome c peptide XICs from loads of 0.1 and 1 nmol cytochrome c.....	144
Figure 4.24	Spectra from 0.1 nmol and 1 nmol cytochrome c loading.....	146
Figure 4.25	Spectrum of a 0.1 nmol BSA load, disulphide bonds unreduced	148
Figure 4.26	BSA peptide XICs resulting from a 0.1 nmol load, disulphide bonds unreduced.....	148
Figure 4.27	Spectrum of a 0.37 nmol BSA load, disulphide bonds reduced with DTT and capped with iodoacetamide.....	149
Figure 4.28	Spectrum of a 0.1 nmol BSA load, disulphide bonds reduced with DTT and capped with iodoacetamide, 1% ampholytes added prior to sample introduction	150
Figure 4.29	Spectrum and XICs of a 1 nmol lysozyme load, disulphide bonds reduced with DTT and capped with iodoacetamide.....	151
Figure 4.30	Electrokinetic fractionation into four channels on the multichannel device.....	154
Figure 5.1	Schematic of the experimental set-up used for LIF observation of electrokinetic fractionation.....	167

Figure 5.2	Frames extracted from a video illustrating electrokinetic fractionation and a photo of the injector region in full light.....	168
Figure 5.3	Schematic illustrating siphoning effects during electrokinetic fractionation.....	171
Figure 5.4	Rough sketch of a sheath flow sample introduction system	172
Figure 5.5	Photo illustrating the effect of negative pressure on the single outlet with one of the twenty channels containing fluorescein	173
Figure 5.6	Peptide XICs and spectrum from a 0.16 nmol load of cytochrome c analyzed with single channel device A	175
Figure 5.7	Effect of flow rate on protein digestion explored with single channel device A.....	177
Figure 5.8	Peptide spectrum resulting from a 8 pmol load of cytochrome c analyzed with single channel device A.....	179
Figure 5.9	Effect of MeOH concentration on peptide elution profiles explored with single channel device A	181
Figure 5.10	Theoretical elution profiles from the multichannel device using two different ESI interfaces	185
Figure 5.11	Effect of flow rate on band broadening explored with single channel device A.....	186
Figure 5.12	Theoretical elution profiles from the single channel device at two different flow rates	187
Figure 5.13	Effect of electrospray interfaces on elution profiles explored with single channel device A.....	190
Figure 5.14	Theoretical elution profiles for three ESI interfaces.....	192
Figure 5.15	Theoretical plot of peaks eluting from the variable region of the multichannel device based on even flow distribution.....	193
Figure 5.16	Theoretical plot of peaks eluting from the variable region of the multichannel device based on a resistance biased flow distribution.....	197
Figure 5.17	Photos of dye pressure driven through a multichannel device with no beds	199

Figure 5.18	Volume contained within the entire multichannel device	202
Figure 5.19	Observation of pressure driven flow throughout the sealed multichannel device, including beds	203
Figure 5.20	XIC _{634.5} , peptide elution profile collected with the same multichannel device as was used for the study in Figure 5.19	205
Figure 6.1	Proposed on-line microfluidic platform for proteomics.....	217
Figure 6.2	Proposed off-line microfluidic platform for proteomics.....	219

LIST OF ABBREVIATIONS AND UNITS

σ	standard deviation	LJ	liquid junction
σ^2	variance	m/z	mass-to-charge ratio
μ -TAS	Micro Total Analysis Systems	MALDI	matrix-assisted laser desorption/ionization
2D-E	two dimensional electrophoresis	MC	missed cleavage
2D-GE	two dimensional gel electrophoresis	MEKC	micellar electrokinetic chromatography
Ab	antibody	MeOH	methanol
ACN	acetonitrile	Met-ox	methionine oxidized
AFU	arbitrary fluorescence units	MS	mass spectrometer
Ag	antigen	MS/MS	tandem MS
APCE	affinity probe CE	MW	molecular weight
API	atmospheric pressure ionization	o.d.	outer diameter
BSA	bovine serum albumin	PEEK	poly ether ether ketone
c.p.s.	counts per second	pl	isoelectric point
C ₁₈	C ₁₈ H ₃₇ bonded to a silica support	RPLC	reverse phase liquid chromatography
CA-IEF	carrier ampholyte isoelectric focusing	RSD	relative standard deviation
CCD	charge coupled device	SEC	size exclusion chromatography
CE	capillary electrophoresis	SCX	strong cation exchange
CEIA	capillary electrophoretic immunoassay	HPLC	high pressure liquid chromatography
CIEF	capillary isoelectric focusing	SPE	solid-phase extraction
CV	coefficient of variation	SS	stainless steel
PMT	photo-multiplier tube	TIC	total ion chromatogram
DL	detection limit	UV	ultra violet
DTT	dithiothreitol	TOF	time-of-flight
EOF	electroosmotic flow	XIC	extracted ion chromatogram
EPM	electrophoretic mobility	Mathematical prefixes	
ESI	electrospray ionization	k	kilo (10 ³)
i.d.	inner diameter	c	centi (10 ⁻¹)
ICAT	isotope-coded affinity tags	m	milli (10 ⁻³)
IEF	isoelectric focusing	μ	micro (10 ⁻⁶)
IPG-IEF	immobilized pH gradient isoelectric focusing	n	nano (10 ⁻⁹)
LC	liquid chromatography	Å	angstrom (10 ⁻¹⁰ m)
LIF	laser induced fluorescence	p	pico (10 ⁻¹²)

CHAPTER 1: LITERATURE REVIEW AND TOPIC INTRODUCTION

1.1	INTRODUCTION	2
1.2	IMMUNOASSAYS	4
1.2.1	PHASE.....	5
1.2.2	CONFIGURATION.....	6
1.2.3	LABELS, SEPARATION AND DETECTION.....	7
1.2.4	IMMUNOASSAY TECHNIQUES UTILIZED IN THIS STUDY.....	8
1.2.5	CE BACKGROUND	9
1.2.6	IMMUNOASSAYS ON-CHIP.....	11
1.3	PROTEOMICS.....	12
1.3.1	CONVENTIONAL TECHNIQUES	13
1.3.2	ALTERNATIVE SEPARATION TECHNIQUES.....	16
1.3.2.1	CIEF.....	17
1.3.3	DEVELOPMENT OF MICROCHIP MS.....	20
1.3.4	MICROCHIPS FOR PROTEOMICS	27
1.3.4.1	PROTEIN SEPARATIONS ON-CHIP	27
1.3.4.2	PROTEIN DIGESTION AND PEPTIDE SEPARATION	27
1.4	OBJECTIVES OF THIS THESIS	28
1.5	REFERENCES	30

1.1 INTRODUCTION

The desire to understand the human body and its idiosyncratic routines continues to be the driving force behind many scientific endeavours. The field of medical research is continually placing a higher demand on analytical techniques. At the forefront of demand is speed and sensitivity, as well as innovative new techniques, that yield both. Medical research stems from a desire to both improve current techniques as well as to develop new techniques with which to explore the many unknown processes that perpetuate human life. Solutions to these queries will require the design and implementation of new analysis systems and experimental techniques. The development of μ -TAS (Micro Total Analysis Systems)¹ has often been geared towards medical research.² μ -TAS has the potential to combine several elements of analysis on to a single planar wafer while affording enhanced performance due to the reduction in size. Such systems could contain components to allow for sample injection, a variety of separation techniques, mixing either pre- or post-separation and product detection. Many more components could also be integrated into the system based on the demands of the analyst. In fact, since both design and fabrication of such systems is relatively straight forward, the possibilities are only limited by imagination. Miniaturization of conventional systems to yield μ -TAS affords many benefits. First, the small channel size (10-50 μm) allows for fast, diffusion-based mixing. Reduced cross-sectional area and the ease of defining a short channel length allows for the application of high electric fields allowing for fast, electrically driven separations. Smaller channel size has the potential to yield a higher mass sensitivity, as the injection and detection volumes can be minimized. Small volume processing also reduces sample consumption as well as process waste. The ability to reproducibly pattern such channels lends itself to densely arrayed, multiplexed fluid networks, thereby increasing sample throughput. The small footprint of the μ -TAS creates the possibility of portability allowing for point-of-care test results as opposed to remote lab testing. The most obvious and realized advantage of μ -TAS is the ability to integrate so many

sample processing steps onto a single device, thereby greatly increasing automation.

The focus of this thesis research has been the application of μ -TAS to the field of medical research. The first half of this work describes the adaptation of a conventional estradiol immunoassay to the microchip format. This study was undertaken to determine the lower limit of detection achieved on-chip using a solution-phase reaction assay. Separation was achieved using capillary electrophoresis (CE)³ and detection using laser induced fluorescence (LIF)⁴. This study resulted in a comparison of on-chip and theoretical detection limits for competitive solution-phase immunoassays.

The second half of this work explores the application of μ -TAS to the field of profiling proteomics. It is hoped that through the identification and comparison of all proteins within healthy and abnormal organisms, some conclusion can be drawn as to the source of disease as well as the treatment of it. There are estimated to be 20,000 to 50,000 proteins in a typical mammalian cell^{5,6} and approximately 216 different types of cells within the body⁷. Furthermore, protein expression will be dependent on cell age and history. This is an overwhelming challenge and solutions as how to best approach it are continually being suggested. One thing is clear though, the solution will require high throughput and multiplexed capabilities. It was with this in mind that this work was undertaken. The work presented in this thesis is based on the design of a multiplexed, microfluidic device for use in proteomics. This device was intended to fractionate incoming protein samples which are then processed allowing for identification. Processing steps involve protein digestion, peptide concentration and finally mass spectrometric identification. A first prototype of this device was constructed and tested.

1.2 IMMUNOASSAYS

The high selectivity of antibody-antigen interactions have made immunoassays one of the most widely used techniques in chemical, pharmaceutical and clinical analyses. An immunoassay can be broadly defined as an assay that utilizes antibodies as analytical reagents for the detection of analytes. Antibodies are a class of proteins referred to as immunoglobulins and are produced within the immune system as a response to a foreign macromolecule, the antigen. The immune response pathway leading to the production of antibodies is quite complex and beyond the scope of this thesis. The result of the natural immune response is the production of several different types of antibodies with varying affinities for the antigen. There are five different classes of antibodies, all of which have the same basic structure. IgD, IgE and IgG antibodies can be simplistically described as having a "Y" shape where the ends of the two arms, the variable region, is responsible for binding the antigen. Thus, if not sterically hindered, each antibody, of the above three classes, can bind two antigens. The remaining two classes are composed of multiple "Y" units, IgM being a pentamer and IgA a monomer, dimer or trimer. All of the classes are seen as a result of natural immune response, and in their entirety are referred to as polyclonal antibodies. Typically, the antigen is a large molecule and the various antibodies will each recognize and bind to different regions. Each specific binding site on the antigen is referred to as an epitope. A solution of polyclonal antibodies will contain a mixture of antibodies with varying affinities to various epitopes.

The production of polyclonal antibodies is accomplished by immunization of an animal with the antigen of interest and then bleeding the animal some time later. Through a more complicated process it is possible to select one of the antibodies for further production, leading to monoclonal antibodies. In this manner, one antibody can be selected which has a high affinity for the epitope of interest. As mentioned, usually antigens are large molecules, however it is often desirable to create antibodies which are reactive towards smaller molecules,

such as hormones, for use in immunoassays. In this case the smaller analyte, referred to as a hapten, can be linked to a larger carrier protein, usually bovine serum albumin (BSA), and be used to induce the production of antibodies. Some care must be taken to select an antibody that is specific to the hapten and not to an epitope on the carrier protein. Once the antibodies have been produced they can be used to recognize the hapten alone, without the carrier protein. In general, an immunoassay involves interaction of the antibody with the antigen of interest and detection of the free and/or bound immunoreagents. In this way the antibody is used to determine the amount of antigen present. There are many different immunoassay configurations, some of which will be discussed in the following sections.

1.2.1 PHASE

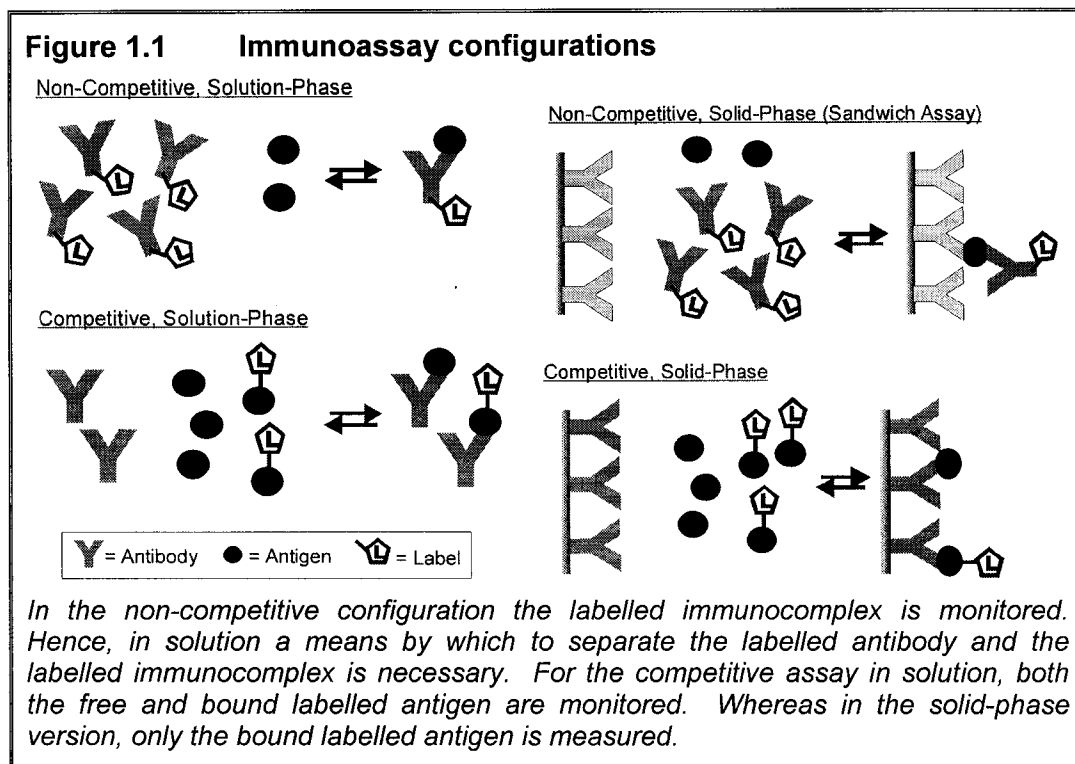
Immunoassays can be run in either solution or solid-phases. This refers to the actually physical state of the reagents used. In solution-phase assays all reagents remain in solution, necessitating a means by which to identify separately bound and free immunoreagents. A further distinction in phase can be added through the terms homogeneous and heterogeneous. Heterogeneous assays require separation of bound and free immunoreagents prior to detection, as both will be labelled. Homogeneous assays do not require immunoreagent separation as the basis for detection is immunoreaction-related signal modulation, allowing only one species to be detected. Only heterogeneous phase assays will be considered in the following discussion as the work presented in Chapter 2 focused on such assays. Both solution-phase separations and solution-phase kinetics occur rapidly, leading to an overall reduction in assay time. In solid-phase assays one of the immunoreagents is immobilized on a solid surface. The advantage of this technique is that the un-immobilized reagent can be concentrated at the surface, which will lead to an enhanced concentration response. Furthermore, separation of the free and bound immunoreagents is achieved simply by washing the surface. However,

the use of a solid-phase will slow reaction kinetics, thereby extending the time needed to achieve static equilibrium. There is also the possibility that immobilization of one of the reagents will disturb binding affinities due to steric crowding at the surface or changes in native protein conformation. This configuration requires additional experimental steps as the reagent immobilization must be accomplished before the assay, in what can be a time consuming procedure.

1.2.2 CONFIGURATION

There are two basic immunoassay configurations: competitive and non-competitive.⁸ The non-competitive configuration involves the direct reaction of the antibody and the antigen of interest. This method commonly involves the use of two antibodies which simultaneously bind to different epitopes on the antigen, allowing for greater specificity. This method is also referred to as a “reagent excess” assay, in that all of the analyte molecules will generally be in the bound state due an excess of antibody. In this configuration one of the antibodies is labelled, allowing for detection of the immunocomplex. This method presents some difficulties for haptens, which are often too small to allow for multiple epitope binding.⁹ Furthermore, separation challenges may arise when trying to distinguish between the free antibody and the hapten-antibody complex, due to the small difference in size between the two species. This is particularly a problem in capillary electrophoretic (CE) separations, as size is an important separation parameter. This separation process will be discussed further in Section 1.2.5. This technique has the potential for high sensitivity. The ultimate limit of sensitivity is restricted only by non-specific signal.^{10,11} In the competitive immunoassay the antigen and a labelled antigen compete for a limited number of antibody binding sites. Detection of the free labelled antigen and the bound labelled antigen can be related to initial unlabelled antigen concentration. The sensitivity of this method is ultimately limited by the affinity constant of the antibody used for binding. These assays are referred to as “limited reagent”

assays. Figure 1.1 illustrates the simplest versions of both configurations in solution and solid-phase arrangements.



1.2.3 LABELS, SEPARATION AND DETECTION

Many different labelling and detection schemes have been explored for use with immunoassays.¹² The use of radioactive labels was one of the first strategies employed and remains one of the most sensitive.¹³ However, for safety reasons this method is being abandoned for nonisotopic strategies. The use of enzymes as labels has been explored thoroughly and is the most popular choice for routine immunoassays.¹⁴ The catalytic behaviour of the enzyme leads to high sensitivity through signal amplification. The method of detection depends on the specific enzyme and substrate coupling. Fluorescent¹⁵ and chemiluminescent^{16,17} detection strategies have also seen extensive use, once again due to the sensitivity of the technique. Electrochemical detection schemes have seen increased use in the recent years due to the simplicity of the detection

system and the lack of interference due to sample turbidity.¹⁸ Most often this technique has been coupled with an enzymatic label, allowing for heightened sensitivity. Many other labelling and detection schemes continue to be developed, all with sensitivity and high throughput in mind. A full overview of immunoassay technique would be overwhelming and only a brief introduction to the common techniques is given here.

Separation techniques are required for solution-phase immunoassays in order to be able to quantify the free and bound species. Two techniques have been used for this purpose, almost exclusively: capillary electrophoresis and various immunochromatographic techniques^{12,19}. Capillary electrophoretic immunoassays (CEIA) have been well studied and are a popular choice for solution-phase immunoassays.²⁰⁻²³ This technique was utilized in the work presented in Chapter 2. The separation mechanism will be presented in Section 1.2.5 and a historical overview in the introduction to Chapter 2.

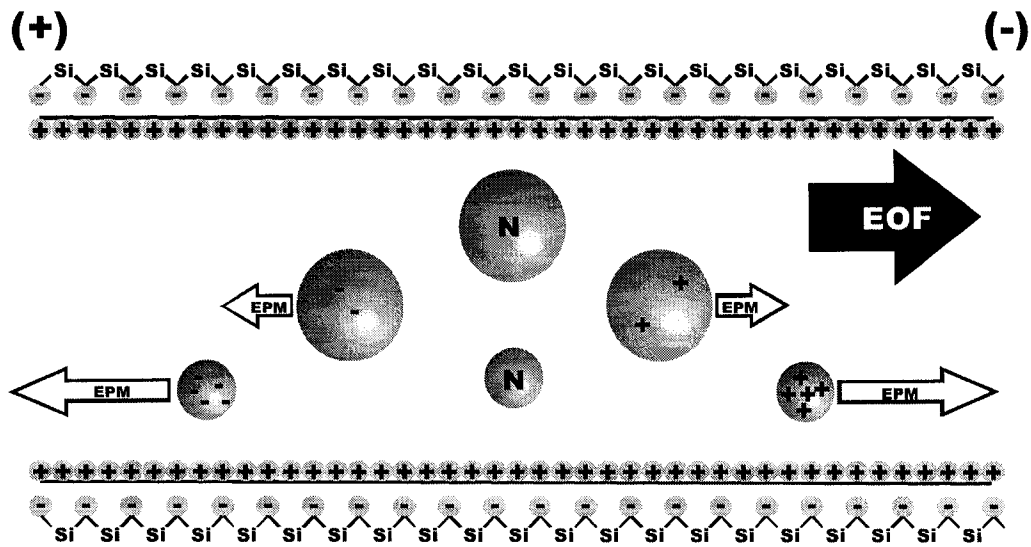
1.2.4 IMMUNOASSAY TECHNIQUES UTILIZED IN THIS STUDY

This study utilizes a competitive CEIA. The mode of detection was laser induced fluorescence (LIF). In part these choices were made as they are the most compatible to the chip format. But these techniques also have several advantages over conventional techniques, predominately speed and sensitivity. These issues are addressed in Chapter 2. One of the initial goals of this work was to transfer a conventional solution-phase CEIA to the microchip format, as such, a historical perspective of this application is given in Section 1.2.6.

1.2.5 CE BACKGROUND

The driving separation force behind CE arises from a combination of electroosmotic flow (EOF) and electrophoretic mobility (EPM). The surface of a silica capillary or glass surface is inherently negatively charged due to the exposed silanol groups. In order to satisfy the constraints of charge balance, positive charges from the buffer solution will collect along the channel wall. In the presence of an electric field, this surplus of positive charges will begin to migrate towards the negative terminal. Due to viscous drag forces the entire cross-section of the channel will be driven towards the negative terminal as well. This method of fluid movement creates a near flat flow profile as opposed to the parabolic profile generated with pressure driven flow, leading to a reduction in band broadening during separation. This is one of the advantages of capillary electrophoresis as a separation technique. This net movement of solution towards the negative terminal is the EOF. Charged analyte molecules also possess their own mobility. Positive ions will migrate towards the negative terminal and negative to the positive terminal, this is called EPM. A molecule's EPM is dependent on both its charge and size. Smaller, more highly charged molecules will migrate faster, while larger, less charged molecules will migrate slower. The net mobility of an analyte during separation will be the vector sum of the EPM and the EOF. These effects result in a separation, as shown in Figure 1.2. The above description of CE is an oversimplification, for mathematical details the reader is directed to the Handbook of CE.²⁴

Figure 1.2 Illustration of electroosmotic and electrophoretic forces



Positively charged molecules will travel in the same direction as the EOF to arrive at the detector first. Neutrals (N) will travel with the EOF to arrive next and negatively charged molecules will migrate against the EOF and arrive last. The size of the arrows illustrating EPM is indicative of the magnitude of the velocity.

1.2.6 IMMUNOASSAYS ON-CHIP

The first successful on-chip immunoassay was developed by Harrison *et al.* in 1995.²⁵ A competitive assay for BSA was reported using LIF detection. The device consisted of a mixing chamber, an injector and a separation channel. Shortly thereafter, Koutney *et al.*²⁶ reported a similar on-chip, competitive assay for serum cortisol. This system demonstrated high throughput by repeated injection and separation every 35 s. Chiem *et al.* reported the development of a device that also integrated sample mixing and incubation onto the device.²⁷ Few examples of multiplexed immunoassay devices have been reported. A six channel microfluidic device allowing for reagent mixing, incubation, injection and separation has been reported.²⁸ In a less conventional use of microfluidics, polymeric open channels were used to pattern antigens in one direction (x) and antibodies in another (y), on to a second surface.²⁹ In this case, the microfluidic channels act as guides for reagent immobilization and were removed from the surface in between patterning directions. The intersection represents the immuno-active region and in its entirety this patterning resulted in the formation of an array. Several solid-phase immunoassays have been presented in the chip format. Some use the channel walls as the surface for immobilization as was reported by Dodge *et al.*³⁰ In this example, a surface modified chamber was used as the reaction site for a competitive assay. An interesting example was recently published which utilized autonomous transport of the immunoreagents to the region of immobilization for utilization of a sandwich assay.³¹ This technique avoids the need for pumps or electrical control as all fluid transport is controlled through capillary forces. Beads have also been used for immobilization of reagents.^{32,33} A particularly ambitious example of this approach utilizing two different sets of beds was recently reported by Roos *et al.*³⁴ Examples of multi-analyte^{35,36}, electrochemical³⁶, enzyme linked chemiluminescent³⁷ and continuous monitoring³⁸ immunoassays, have all been reported on-chip, just to mention a few examples. Two recent reviews serve to give a broad overview of the field.^{2,39}

1.3 PROTEOMICS

The field of proteomics is one that has seen tremendous growth over the past ten years. In a recent review of the field it was stated that over 1300 papers were published in 2002 alone⁴⁰ and there are four journals specifically dedicated to the field. As such, a full review of the field is well beyond the scope of this thesis. The author directs readers to the following review articles.^{40,41} The term “proteome” was coined in 1994 at the first 2 dimensional electrophoresis (2D-E) meeting in Siena, Italy. Originally, it was defined as the protein complement of the genome, that is, all proteins expressed by the genome. Since then its meaning has changed somewhat and the field itself has divided into several branches. A clear cut definition is no longer applicable. The field is basically divided into three branches: profiling proteomics which consists of identifying all proteins present in a biological sample, functional proteomics explores protein function and lastly structural proteomics which explores tertiary protein structure. It is profiling proteomics that is the focus of this thesis. By profiling all proteins expressed by an organism, tissue or cell, it is hoped that some connection can be made between protein expression and the onset of disease. In this sense, most of the actual applications of this technique consist of differential analysis between two samples. The undertaking of such a task is not trivial. It has been projected that a human cell will contain 20,000 to 50,000 proteins with a dynamic range covering five orders of magnitude.^{5,6} Furthermore, protein abundance is dependent on cell type, age and history. This makes the challenge of profiling immense.

1.3.1 CONVENTIONAL TECHNIQUES

The general protocol for proteome analysis consists of the following steps:

1. Protein content is extracted from the biological sample of interest
2. Proteins are separated using a 2 or 3 dimensional technique
3. Enzymatic digestion of the individual separated proteins is performed resulting in a peptide mixture
4. Mass spectrometric (MS) analysis of the resulting peptides in combination with a database search should lead to identification if the protein has been documented
5. If the above does not succeed, a second dimension of MS is run in order to assess the sequence of the resulting peptides.

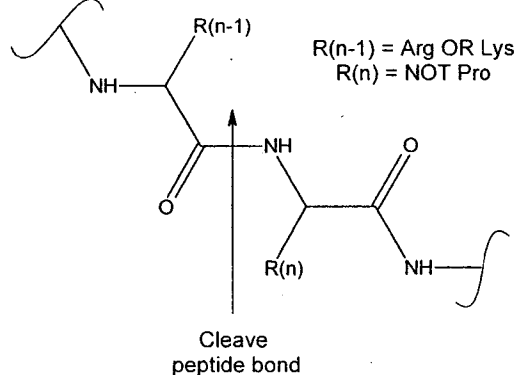
Steps 2 and 3 are somewhat interchangeable depending on the approach to be utilized. Traditionally, mixed protein samples have been separated before digestion, however several recent publications have explored the reverse, where the protein mixture is first digested and then the resulting peptide mixture undergoes a 2 or 3D separation, as will be discussed in Section 1.3.2. The majority of efforts towards protein profiling in the past have utilized 2 dimensional gel electrophoresis (2D-GE) as a means of protein separation followed by MS identification.⁴²

In brief, 2D-GE is a two step procedure, the first step is isoelectric focusing (IEF) where proteins are separated on the basis of their isoelectric points (pI).⁴³ The isoelectric point is the pH at which the protein has a net charge of zero. This process will be described in detail in Section 1.3.2.1. The proteins are then separated in a second dimension based on their mass. The result is a two dimensional distribution of proteins. The resulting gel is stained in order to visualize the protein spots. The spots are excised, destained and digested usually while in the gel. The resulting peptides are extracted from the gel and are ready for MS analysis. A historical overview of this technique is presented by

Issaq *et al.*⁶ Despite the success of this technique, it has several shortcomings. Since the proteins are immobilized within the gel, a means by which to extract them from the gel before further processing is necessary. Furthermore, in order to visualize the proteins, it is necessary to first stain the gel and then to destain the proteins before processing. Both of the above steps result in extended processing time. In order to run a complete sample (gel separation, staining, excision etc.) including MS analysis, a full day is needed. If the peptides are not identified by database searching, a second dimension of MS must be run, extending analysis time to a week.⁴⁴ Besides the lengthy analysis time, this technique has other more dramatic shortcomings. The technique has a limited dynamic range and relatively low sensitivity due mostly to the types of visualization methods used. A recent study has shown that only the most abundant proteins are identified by staining.⁴⁵ Furthermore, the resolution of this technique, although good, is still not sufficient to profile all proteins in a biological sample. On the best gels, 10,000 different spots may be resolved.⁴⁶ A recent paper concluded that if a typical mammalian cell produced 50,000 proteins and 3000-10,000 spots could be visualized using a 2-D gel then only 7-24 % of the most abundant proteins would be recognized.⁵ Proteins exhibiting more extreme characteristics (i.e. high or low pI and high molecular weights) are often not seen, as well as proteins with low solubility such as membrane proteins. Despite these issues, this technique still remains the most successful method of proteome analysis.

Protein digestion has been a fairly standard procedure. A variety of proteolytic digestion enzymes can be used in order to cleave proteins at specific sites. They are broadly categorized into two groups, exopeptidases which cleave specific terminal peptide bonds and endopeptidases which cleave specific internal peptide bonds. Trypsin is one of the most specific endopeptidases and as such has been widely used. It functions to cleave the peptide bond on the carboxyl side of arginine and lysine, provided that proline is not the neighbouring residue, as is illustrated in Figure 1.3.

Figure 1.3 Proteolysis by trypsin



Protein digestion after 2D-GE can be accomplished in several ways. Proteins can be extracted from the gel and then digested in solution, although extraction often requires the use of detergents which may interfere with digestion. A membrane can be used to adsorb proteins from the gel and then digestion can be performed on the membrane. However, transfer is often not complete and may be selective, leading to reduced sample transmission. More commonly, proteins are digested while still in the separation gel.⁴⁷⁻⁴⁹ Protein bands are excised, transferred to vials and digested. When protein separation is achieved using non-gel methods, several options are available. Both protein and trypsin can remain in solution, although sometimes this leads to trypsin autolysis, where trypsin will begin to digest adjacent trypsin molecules. This usually occurs at high trypsin concentrations or low sample concentrations. Alternatively, the trypsin can be immobilized on a surface or in a bed structure. This has been demonstrated and was seen to be effective in reducing digestion time.⁵⁰⁻⁵² Sample immobilization while the trypsin remains in solution has also been explored. This technique has been very effective for the digestion of low concentration samples.⁵³

For many years, mass spectrometers have been the detector of choice for the field of proteomics. When used in a single dimension, MS analysis can provide accurate peptide masses, which can be used for a database search in order to identify the protein of interest. If this fails, a second dimension of MS

can be used in order to fragment the parent peptide into smaller pieces. Peptides fragment in a predictable pattern and analysis of the resulting spectra will yield the sequence of the peptide. This technique is referred to as MS/MS or tandem MS. No other means of detection will yield this information in such a simple and straight forward manner. Two review articles outline recent developments in MS based proteomics.^{54,55}

1.3.2 ALTERNATIVE SEPARATION TECHNIQUES

In order to overcome the aforementioned problems associated with 2D-GE, attempts have been made to develop alternative multidimensional separation techniques. As mentioned previously, there have been two approaches to this. In the first, the protein mixture is separated and then digested, while in the second, the proteins are digested and then the resulting peptides are separated. The advantage of this second technique, which is referred to as shotgun proteomics, is that in general, peptides exhibit higher solubility and more uniform behaviour than proteins. A variety of techniques have been used in combination in an attempt to provide adequate resolution to allow for accurate protein identification. Many 2D separation techniques have been explored including: IEF/reverse phase liquid chromatography (RPLC)⁵⁶, capillary-IEF/RPLC⁵⁷, capillary-IEF/CE⁵⁸, size exclusion (SEC)/RPLC⁵⁹ and 2D-high performance liquid chromatography (HPLC)⁶⁰. A recent publication by J.R. Yates III, who is essentially the pioneer of shotgun proteomics, compared protein identification for digested samples separated by one, two and three dimensions.⁶¹ The three dimensions were all liquid phase and in order were: RPLC, strong cation exchange (SCX) and RPLC. One issue with this approach is that the massive amount of peptides generated, even with prior separation, can overwhelm data collection.⁶² As such, recent approaches have focused on the use of an affinity selector to specifically capture unique proteins that can be used for protein identification.⁶³ Labelling of proteins, via isotope-coded affinity tags (ICAT), has allowed for more quantitative detection.⁶⁴ The above mentioned

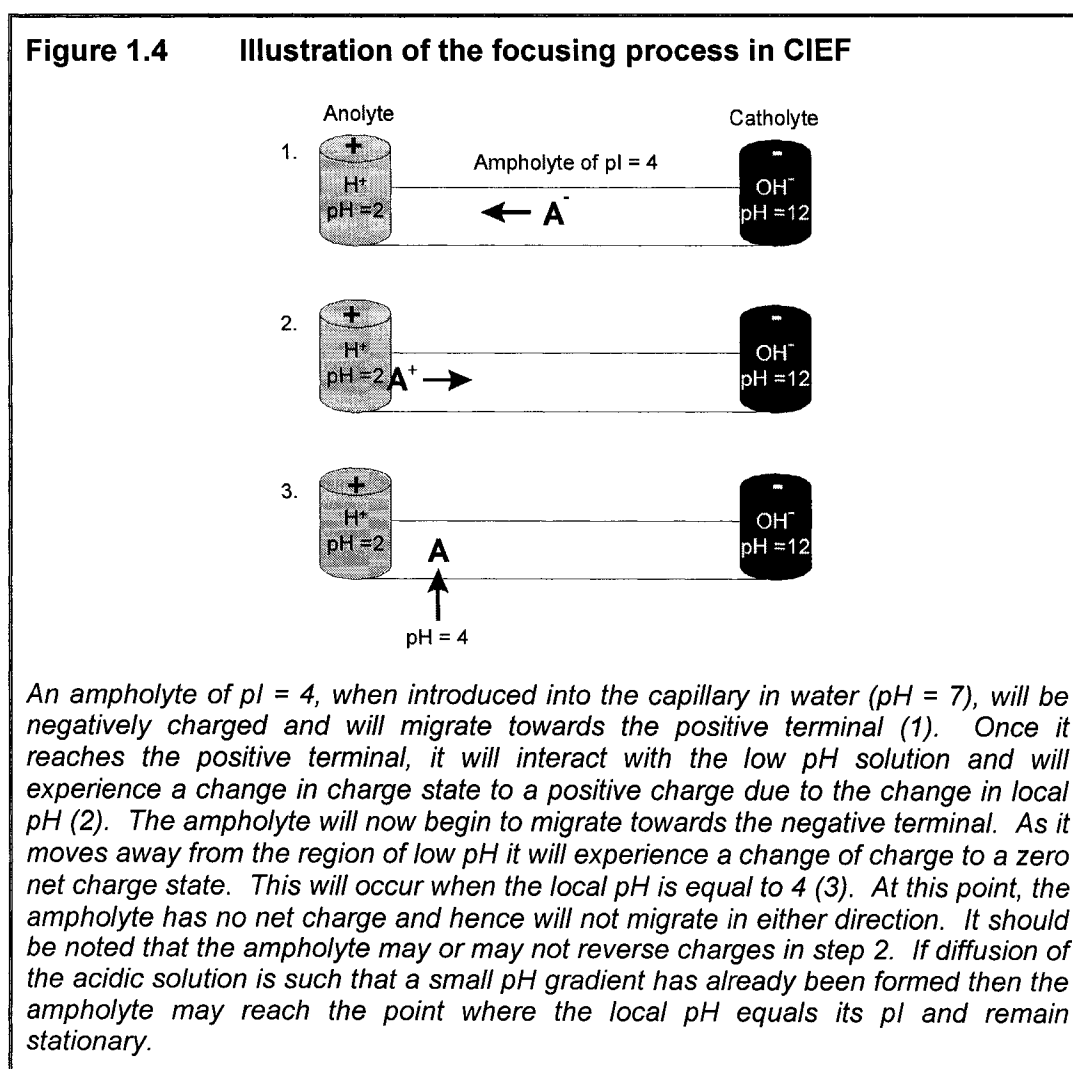
references are merely examples of methods that have been suggested in order to approach the issue of proteomics. The complexity of the field has driven the production of increasingly sophisticated and impressive solutions. An overview of multidimensional separations techniques and general proteomics strategies is provided in the following references.^{41,65,66}

One of the most important considerations when designing a multidimensional technique is the peak capacity achievable by each step. Peak capacity is defined as the maximum number of peaks that can be resolved side-by-side in a defined separation space. According to Giddings⁶⁷, the total peak capacity of a system is defined as the product of the individual peak capacities of each step. Hence, if the goal is the separation of 20,000 to 50,000 proteins, then the separations should be orthogonal and the product of their individual peak capacities should yield this number. In this regard, capillary-IEF (CIEF) has been considered one of the more promising techniques. CIEF is one of the highest efficiency single dimension separation techniques. Peak capacity has been predicted to be as high as 1000 for a single one dimensional run.⁶⁸ As this is the case, the next section will describe the general mechanism of this technique.

1.3.2.1 CIEF

As mentioned briefly before, IEF is based on the separation of samples by their pI values. The separation is facilitated by the presence of a pH gradient and an electric field. The pH gradient is formed using ampholytes, which are synthetic amphoteric (containing both acidic and basic moieties) molecules. The pI values of the ampholytes span a defined pH range. At its pI, a molecule will have no net charge, at a pH above the pI the species is negatively charged and below the pI, positively charged. The following explanation is geared towards CIEF, as this is of relevance to the thesis.^{69,70} The ampholytes are loaded into a capillary which is flanked by a high pH solution (catholyte) at one end and a low pH solution (anolyte) at the other. In most cases the EOF of the capillary is eliminated (or reduced) so that the main driving force is electrophoretic mobility

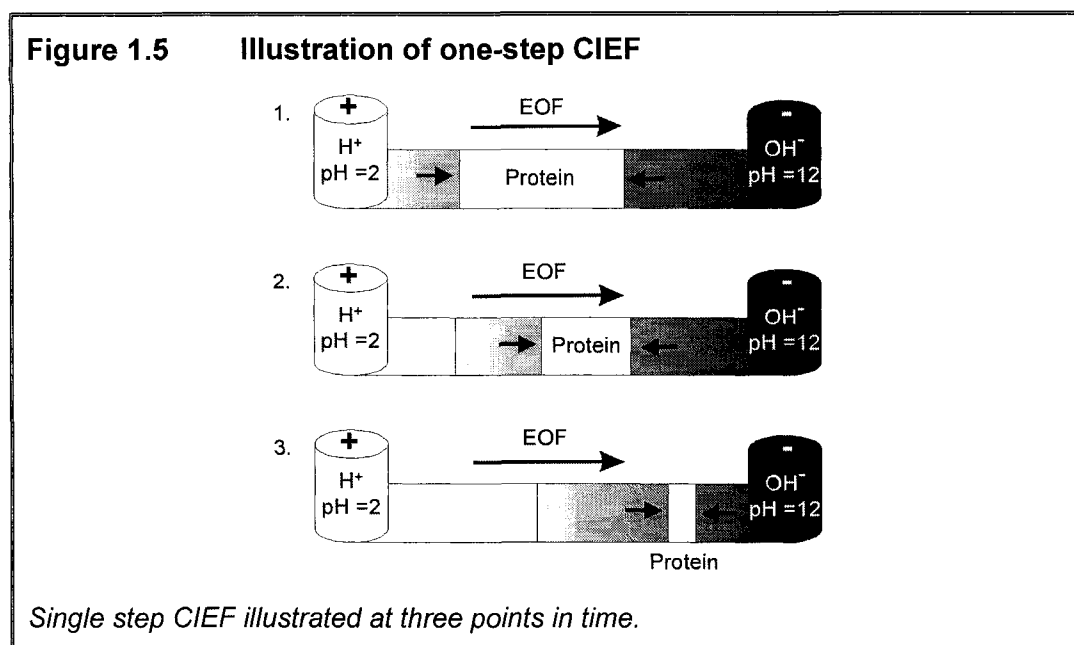
(EPM). When an electric field is applied, the charged ampholytes will begin to migrate toward the electrode of opposite charge. The positive terminal is located at the low pH end and the negative terminal at the high pH end. However, the ampholytes will not exit the capillary as interaction with the high (or low) pH solution will cause a change in charge, which will in turn cause the ampholyte to remain stationary if net charge is zero or migrate in the opposite direction if the charge is reversed. This process is best explained through the use of a diagram, Figure 1.4, and consideration of one molecule.



All of the ampholytes undergo this same process and are distributed through the capillary on the basis of their pIs. Since the ampholytes also have a buffering capacity they will maintain the pH in their local region. The final result is a stable pH gradient. IEF can be accomplished using carrier ampholytes (CA-IEF), where the ampholytes are free to move around in solution (as described), or using an immobilized pH gradient (IPG-IEF), where the ampholytes are immobilized. Traditionally, IEF was performed in gels to reduce sample convection and to act as a support for sample staining. The development of CE has allowed the process to be carried out in a capillary using high voltages for rapid focusing and allowing for UV detection, thereby eliminating the need for a gel support. CIEF uses carrier ampholytes and as this is the focus of this thesis, no discussion of IPG-IEF will be presented. The author directs readers to the following review article.⁷²

The basic procedure for CIEF is as follows. A mixture of ampholytes and proteins are introduced into the capillary. The voltage is initiated and the ampholytes rapidly establish a pH gradient. The proteins undergo the process outlined in Figure 1.4 at a slower rate due to their reduced electrophoretic mobility (EPM). While the focusing is occurring, the current across the capillary is monitored. As the focusing nears completion a drop in current is seen, as there are fewer charge carriers in solution, leading to a lower conductivity. Once the focusing is complete, the proteins are mobilized in order to be detected or collected. Mobilization can be achieved by several methods. The samples can be hydraulically mobilized by changing the liquid levels in the end reservoirs, relative to one another. Voltage is maintained during mobilization so that the focused bands are not disturbed. Another alternative is to use chemical mobilization. In this case, a salt is added to one of the end reservoirs resulting in a pH shift as the salts migrate into the capillary. Both of these options are used in the absence of EOF and this procedure is referred to as two-step CIEF, one step for focusing and one for mobilization. CIEF has also been achieved in the presence of EOF and is referred to as one-step CIEF. In this case, the proteins

are simultaneously focused and mobilized, as illustrated by Figure 1.5. For the sake of simplicity, one-step CIEF was used for the work presented in this thesis. Since it was already intended that several protein processing steps were to be performed on-chip, the CIEF step was left off-chip, although many groups have explored the transfer of CIEF to the microchip format with success.⁷³⁻⁷⁷



1.3.3 DEVELOPMENT OF MICROCHIP MS

MS for proteomics has focused on two main types of ionization: matrix-assisted laser desorption/ionization (MALDI)⁷⁸ and electrospray ionization (ESI)⁷⁹. The two techniques are inherently different, with MALDI being a discrete time event whereas ESI is a continuous flow technique. The focus of work presented in this thesis has been the application of microchips to the field of proteomics. Hence, the coupling of microchips and MS will be discussed, but the general development of MS techniques will be left to more thorough reviews.⁵⁴ The continuous flow of the ESI source is particularly amenable to microfluidic devices and will be the focus of future discussions. Some excellent work has

recently been presented exploring the coupling of microfluidics to MALDI, but this topic will not be explored in detail.⁸⁰

Electrospray ionization was proposed as a means of sample introduction to the mass spectrometer in the late 1960's. It was postulated that by electro spraying analyte molecules in solution, the molecules may be liberated to the gas phase and further introduced into a mass spectrometer.⁸¹ However, it was not until the mid 1980's that this technique was actually utilized as such. Work by Yamashita and Fenn explored the application of the phenomenon as a means of sample introduction.⁷⁹ The actual process of electrospray ionization is quite complicated and has been explored in depth. The process is generally thought to consist of four steps. Charged droplets are first formed by application of an electric field across an emitter containing the liquid of interest and an oppositely charged counter electrode. This first step initiates the formation of a Taylor cone, where the solution is drawn out into a cone formation as the charged molecules migrate towards the counter electrode. Charged droplets will break away from tip of this cone and travel towards the counter electrode. The charged droplets undergo evaporation leading to shrinkage and repeated droplet disintegration. Finally, the formation of gas phase ions from the reduced droplets occurs. The last step in the process has been explored in depth and is still not fully understood. A full explanation of these processes is beyond the scope of this thesis and the reader is directed to the following review by Kebarle and Tang.⁸² Electrospray ionization was originally developed for use with flow rates in the range of 0.5 – 5 $\mu\text{L}/\text{min}$. Pneumatically assisted interfaces, ionspray, were designed to be used with the higher flow rates associated with most liquid phase separations. However, with the development of CE and micro-bore liquid chromatography, micro-electrospray (0.2 - 4 $\mu\text{L}/\text{min}$) and nano-electrospray (low nL/min) techniques began to emerge. Caprioli and co-workers originally defined micro-electrospray to describe an on-line miniaturized electrospray source they had designed utilizing a sprayer i.d. of 10-20 μm .⁸³ The term nano-electrospray was used by Wilm and Mann to describe an offline technique that used a tip i.d.

of 1-2 μm .⁸⁴ The terms have been used somewhat interchangeably in recent years.

It was the development of CE ESI interfaces as well as nano-ESI that facilitated chip to MS coupling. The coupling of CE and ESI developed through the late 1980's and resulted in three main types of interfaces.⁸⁵ The coaxial sheath interface was developed by Smith *et al.*⁸⁶ in 1988. This interface usually consists of three concentric tubings, the innermost is the separation capillary, the second carries the sheath liquid and the outermost, a nebulizing gas. ESI voltage is applied through the sheath liquid which is in contact with the analyte solution at the end of the capillary. The second interface is referred to as a liquid junction and was introduced by Lee *et al.*⁸⁷ and Minard *et al.*⁸⁸, independently. In this case the CE capillary is decoupled from the ESI source by a small gap allowing for electrical contact. The third is the so-called sheathless interface. Electrical contact is made through a conductive tubing at the end of the capillary without the use of sheath liquid.⁸⁹ Lastly, the development of nano-ESI has allowed for the elimination of the sheath gas through the use of low flow rates. Electrical contact is made through a conductive coating at the end of the emitter⁸⁴, which is usually tapered, or through the use of stainless steel emitters⁹⁰. All four of these interfaces have in some variation been applied to the chip format. A full review of the development of MS interfaces for liquid-phase separations is given by Gelpí.⁹¹

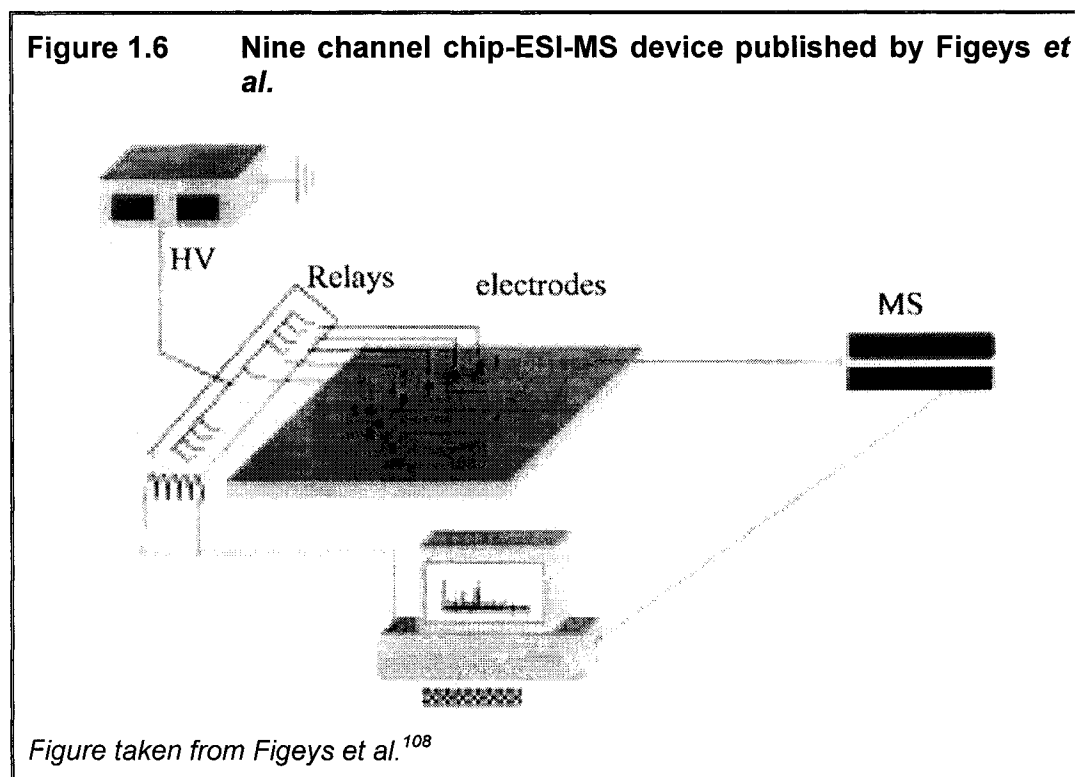
Karger's group was the first to explore the coupling of microchips to the mass spectrometer.⁹² The first attempt focused on initiating electrospray directly from the end of the chip. In this work, the electrospray voltage was applied across the chip channel and the MS interface. The device was fabricated in glass and the EOF created from the glass surface served as the mobilization force. Shortly thereafter, similar work was published by Ramsey which illustrated the formation of the Taylor cone from the edge of the chip.⁹³ Although samples were effectively ionized, the liquid exiting the channel was seen to wet the surface of the chip edge, leading to the formation of relatively large droplets

excluding the coupling of this approach to separation techniques. Hydrophobic coatings applied to the edge of the chip served to reduce this problem somewhat. Furthermore, Karger's group integrated a nebulizer on-chip in order to reduce this problem.⁹⁴ Work published by Aebersold's group focused on the use of a transfer line for coupling the chip to a conventional liquid junction ESI source.⁹⁵ This means of sample transfer from the chip to the MS proved robust and over the next years many examples of similar couplings were seen. The main concern for this type of interface is the formation of a low dead volume junction.⁹⁶ From these initial efforts many different coupling configurations have been explored.

Several designs were mentioned above in relation to conventional CE-ESI interfaces and most of these have been translated to microchip equivalents. Single component interfaces achieve electrospray directly from the fabricated microchip. This is either done from the flat edge of the chip, as was illustrated in some of the first designs, or from an integrated electrospray tip defined during fabrication.^{73,97-99} Voltage can be applied in the chip channel^{100,101} or at the end of the channel or emitter through the use of a conductive coating¹⁰². Multi-component interfaces are of varied designs. The simplest involves a tapered electrospray emitter coupled directly to the device through a low dead volume junction⁹⁶, allowing for nano-ESI.^{103,104} Electrospray voltage for nano-ESI can be applied through the use of a conductive coating on the emitter¹⁰⁵, directly in the case of stainless steel emitters¹⁰⁶ or as a liquid junction on chip¹⁰⁴. In most cases, the liquid junction is formed as a side channel on the device and as such does not really decouple the separation from the ESI process as was stated for CE-ESI interfaces. However, in one design, the liquid junction was integrated as a large channel on-chip, intersecting the end of the separation channel and the ESI emitter.⁹⁴ In this example, the liquid junction is more conventional in its behaviour and use. Other multi component interfaces involve the use of external microsyringes¹⁰⁷, subatmospheric ionization chambers⁹⁴, external liquid junctions⁹⁵ and conventional sheath flow interfaces¹⁰³. In all of these cases, the

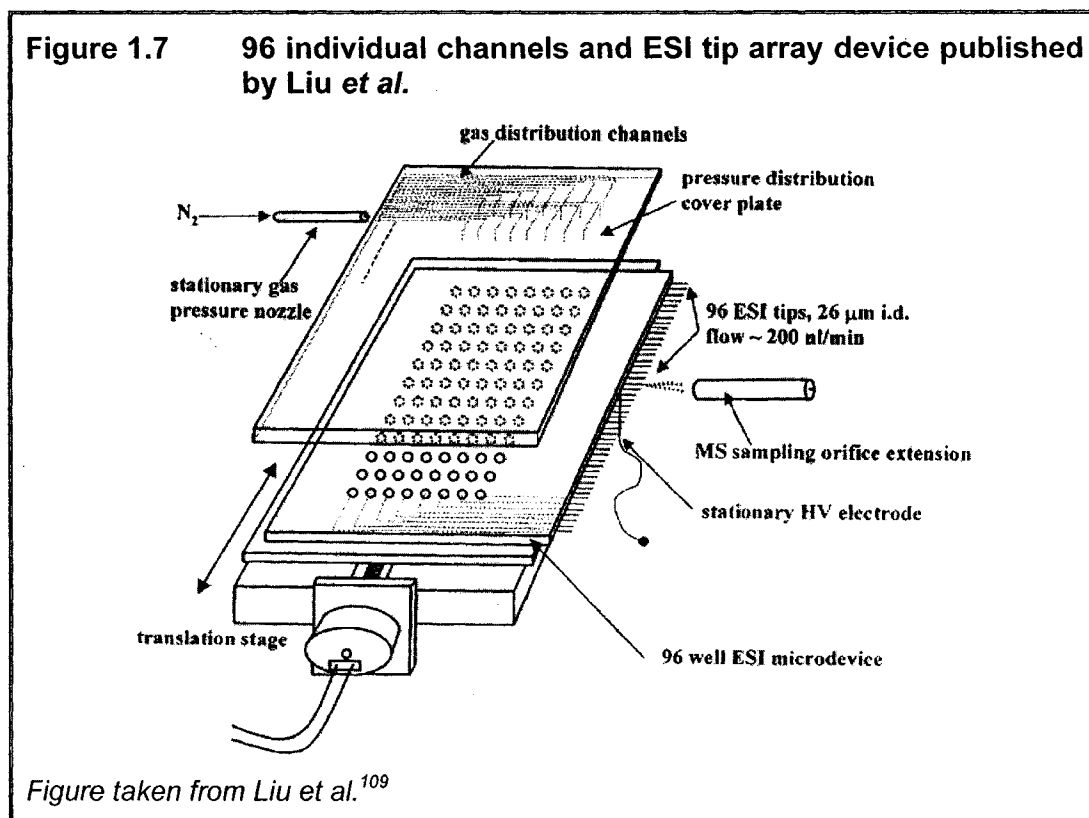
chip is interfaced to the external component through a transfer capillary of some sort.

Multiplexed examples of chip-ESI-MS have also been seen. Figeys *et al.* interfaced nine parallel channels to a single ESI tip for use in proteomic analysis.¹⁰⁸ In this work protein samples were separated using 2D-GE, digested in-gel, concentrated and then transferred to the microfluidic device. Each of the channels was individually directed to the ESI-MS interface using electrical control. A schematic of the design is shown in Figure 1.6.



Liu *et al.* have designed a complex interface consisting of 96 individual ESI tips.¹⁰⁹ The device consisted of two microfluidic devices, both of which are shown, schematically, in Figure 1.7. The first contained 96 channels all with an entrance on one side of the device and exiting through the bottom of the device at a position in-line with the arrangement of a 96-well plate. This is used as the

cover plate for the bottom device which contains 96 wells each with an integrated electrode and a fluidic channel leading to an individual ESI tip. The top device is used in conjunction with a gas source to drive solution from the reservoir in the bottom device to its own electrospray tip.



Continuing from this work the same group has designed a platform which samples from a 96-well plate and transfers to a microfluidic device, allowing for injection and CE separation, as illustrated in Figure 1.8.¹¹⁰ The device contained an integrated liquid junction allowing for application of the ESI voltage, as shown in the top picture of Figure 1.8. The device was coupled to a subatmospheric ESI chamber allowing for sample introduction in the MS and was located between the 96-well plate and the ESI interface as shown in the lower schematic of Figure 1.8. The platform was used for the analysis of tryptic peptides. Although not directly applicable to work done in this thesis, microfabricated arrays of standalone nanospray emitters have been fabricated for use in coupling to

capillaries and are now commercially available.^{111,112} Several reviews of the developments of chip-MS are available.¹¹³⁻¹¹⁵

Figure 1.8 96-well plate coupled to chip-ESI-MS published by Zhang *et al.*

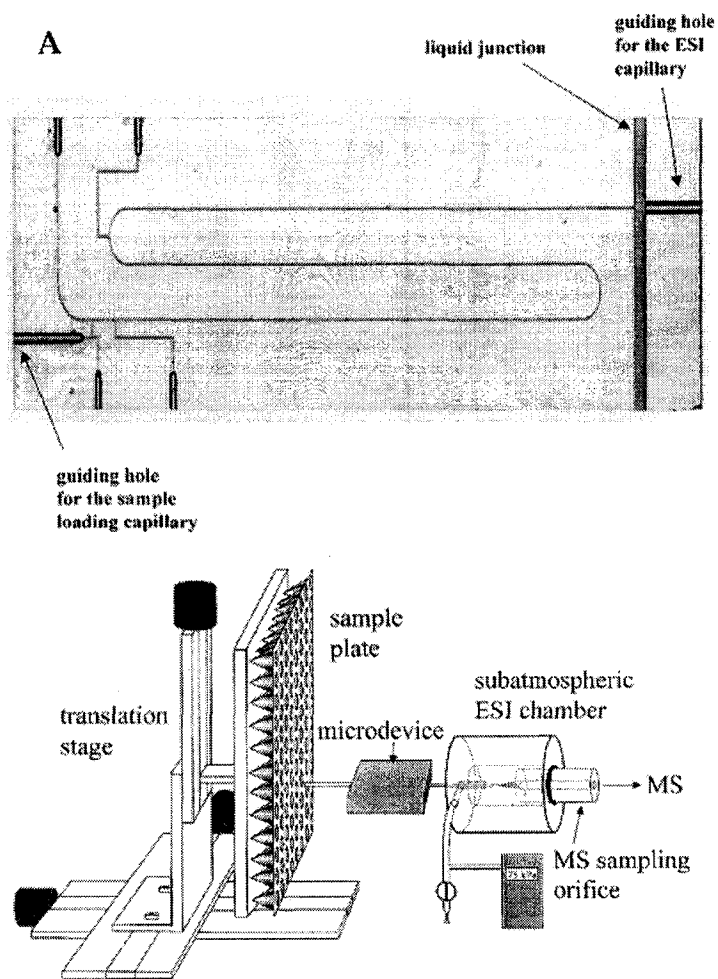


Figure taken from Zhang *et al.*¹¹⁰

1.3.4 MICROCHIPS FOR PROTEOMICS

Over the past several years, many advances have been made in the development of microchips for application to the field of proteomics. Microfluidics are well suited to the present challenges of proteomics, as integration of several separation techniques or sample processing techniques on a single device is possible. Most recent examples have focused on protein digestion and peptide separation as opposed to protein separation techniques. The following discussion will be geared towards examples in which more than one protein or peptide processing step have been integrated on-chip. Examples involving only one protein processing step are now too numerous to be fully reviewed. The reader is directed to the following review articles.^{113,116-118}

1.3.4.1 PROTEIN SEPARATIONS ON-CHIP

Only a few examples of multidimensional protein separations on-chip have been seen in recent years. The Whitesides group has attempted to convert the traditional 2D-GE to the microfluidic platform using a set of orthogonal channels integrated onto a polymeric device.¹¹⁹ This has been the most ambitious work to date in the attempt to replace 2D-GE by microfluidics. Herr *et al.* explored the coupling of CIEF and CE for separation of fluorescently labelled proteins.⁷⁵ Results indicated a concentration enhancement of 70 times and the potential for relatively high peak capacity.

1.3.4.2 PROTEIN DIGESTION AND PEPTIDE SEPARATION

Several examples of trypsin digestion followed by CE separation of the resulting peptides have been presented. Wang *et al.* reported the integration of protein digestion and peptide CE separation followed by ESI-MS detection.⁵² In this example protein digestion was achieved using trypsin immobilized beads trapped in a column on-chip. Similar work was recently presented using trypsin immobilized in a sol-gel matrix for protein digestion, followed by CE separation

and LIF detection.¹²⁰ Ramsey's group has explored high efficiency peptide separations following off-chip protein digestion.¹²¹ Tryptic digests were separated using micellar electrokinetic chromatography (MEKC) followed by CE using LIF detection. Peak capacities of 4200 were determined. Recent work by Regnier's group illustrated the integration of three processing steps on a single device.¹²² Protein samples were digested on-chip, followed by copper-immobilized metal affinity chromatography and reverse-phase electrochromatography of the selected peptides. Detection was achieved using laser induced fluorescence. Work done in collaboration with our lab and Pierre Thibault's group has focused on utilizing the microfluidic device as a peptide preconcentrator and selector after conventional 2D-GE and in-gel digestion. In this work tryptic digests were concentrated by a reverse phase column on the device. Alternatively, the column was packed with an affinity phase to selectively trap peptides of interest.¹²³ This work was further extended to incorporate two columns on the device allowing for on-chip protein digestion, peptide preconcentration and CE separation before introduction to the MS through a chip-ESI coupling.¹²⁴ This is one of the more ambitious, integrated proteomics systems to date and was the basis for work presented in this thesis.

1.4 OBJECTIVES OF THIS THESIS

The first objective of this thesis was the conversion of a conventional competitive, solution-phase CEIA to the microchip format. This work developed to include a comparison of the experimentally achievable detection limits and the theoretically predicted values. Results of this work are presented in Chapter 2.

The second aim of this work was to develop a multiplexed microfluidic platform for use in proteomics. This was to include off-chip CIEF, on-chip fractionation of the incoming focused protein bands, protein digestion, peptide concentration and finally, sequential introduction of each fraction to the MS via a chip-ESI interface. The first prototype of this device had twenty channels. Design of this prototype is introduced in Chapter 3, followed by evaluation of the

platform in Chapter 4 and finally, analysis of the individual components in Chapter 5. Suggestions for future work and design optimization are presented in Chapter 6.

1.5 REFERENCES

- (1) Manz, A.; Graber, N.; Widmer, H. M. *Sens. Actuators, B* **1990**, *B1*, 244-248. "Miniaturized total analysis systems: A novel concept for chemical sensing"
- (2) Khandurina, J.; Guttman, A. *J. Chromatogr. A* **2002**, *943*, 159-183. "Bioanalysis in microfluidic devices"
- (3) Jorgenson, J. W.; Lukas, K. D. *Anal. Chem.* **1981**, *53*, 1298-1302. "Zone electrophoresis in open-tubular glass capillaries"
- (4) Cheng, Y.-F.; Dovichi, N. J. *Science* **1988**, *242*, 562-564. "Subattomole amino acid analysis by CZE and LIF"
- (5) Vuong, G. L.; Weiss, S. M.; Kammer, W.; Priemer, M.; Vingron, M.; Nordheim, A.; Cahill, M. A. *Electrophoresis* **2000**, *21*, 2594-2605. "Improved sensitivity proteomics by postharvest alkylation and radioactive labelling of proteins"
- (6) Issaq, H. J.; Conrads, T. P.; Janini, G. M.; Veenstra, T. D. *Electrophoresis* **2002**, *23*, 3048-3061. "Methods for fractionation, separation and profiling of proteins and peptides"
- (7) Medical Research Council, "Research in focus: Stem cell therapy" **2001**, www.mrc.ac.uk
- (8) Christopoulos, T. K.; Diamandis, E. P. "Chapter 10: Immunoassay Configurations" In *Immunoassay*; Eds.: Diamandis, E. P., Christopoulos, T. K.; Academic Press: San Diego, 1996, pp 227-236.
- (9) Buscarlet, L.; Grassi, J.; Créminon, C.; Pradelles, P.; Dupret-Carruel, J.; Jolivet, M.; Mons, S. *Anal. Chem.* **1999**, *71*, 1002-1008. "Cross-linking of 17 β -estradiol to monoclonal antibodies by direct UV irradiation: Application to an enzyme immunometric assay"
- (10) Jackson, T. M.; Ekins, R. P. *J. Immunol. Methods* **1986**, *87*, 13-20. "Theoretical limitations on immunoassay sensitivity"
- (11) Qu, Y.; Berghman, L. R.; Vandesande, F. *Anal. Biochem.* **1998**, *259*, 167-175. "An electrochemical enzyme immunoassay for chicken lutenizing hormone: Extension of the detection limit by adequate control of the nonspecific adsorption"
- (12) Hage, D. S.; Thomas, D. H.; Chowdhuri, A. R.; Clarke, W. *Anal. Chem.* **1999**, *71*, 2965-2975. "Development of a theoretical model for chromatographic-based competitive binding immunoassays with simultaneous injection of sample and label"
- (13) Chard, T. "Chapter 12: Radioimmunoassay" In *Immunoassay*; Eds.: Diamandis, E. P., Christopoulos, T. K.; Academic Press: San Diego, 1996, pp 269-285.
- (14) Gosling, J. P. "Chapter 13: Enzyme Immunoassay" In *Immunoassay*; Eds.: Diamandis, E. P., Christopoulos, T. K.; Academic Press: San Diego, 1996, pp 287-308.
- (15) Christopoulos, T. K.; Diamandis, E. P. "Chapter 14: Fluorescence Immunoassay" In *Immunoassay*; Eds.: Diamandis, E. P., Christopoulos, T. K.; Academic Press: San Diego, 1996, pp 309-335.

- (16) Kricka, L. J. "Chapter 15: Chemiluminescence Immunoassay" In *Immunoassay*; Eds.: Diamandis, E. P., Christopoulos, T. K.; Academic Press: San Diego, 1996, pp 337-351.
- (17) Roda, A.; Pasini, P.; Guardigli, M.; Baraldini, M.; Musiani, M.; Mirasoli, M. *Fresenius J. Anal. Chem.* **2000**, 366, 752-759. "Bio- and chemiluminescence in bioanalysis"
- (18) Warsinke, A.; Benkert, A.; Scheller, F. W. *Fresenius J. Anal. Chem.* **2000**, 366, 622-634. "Electrochemical immunoassays"
- (19) Weller, M. G. *Fresenius J. Anal. Chem.* **2000**, 366, 635-645. "Immunochemical techniques - A critical review"
- (20) Schmalzing, D.; Buonocore, S.; Piggee, C. *Electrophoresis* **2000**, 21, 3919-3930. "CE-based Immunoassays"
- (21) Schmalzing, D.; Nashabeh, W. *Electrophoresis* **1997**, 18, 2184-2193. "CE based Immunoassays: A critical review"
- (22) Bao, J. J. *J. Chromatogr. B* **1997**, 699, 463-480. "Review: CEIA"
- (23) Heegaard, N. H. H.; Kennedy, R. T. *J. Chromatogr. B* **2002**, 768, 93-103. "Antigen-antibody interactions in CE"
- (24) *Handbook of Capillary Electrophoresis*, 2nd Edition; Ed.: Landers, J. P.; CRC Press, Inc.: New York, 1997.
- (25) Harrison, D. J.; Fluri, K.; Chiem, N.; T., T.; Fan, Z. H. "Micromachining chemical and biochemical analysis and reaction systems on glass substrates" In *Digests of Technical Papers of the 5th International Conference on Solid-State Sensors and Actuators, and Eurosensors IX*, Stockholm, Sweden, June 25-29, **1995**; 752-755.
- (26) Koutney, L. B.; Schmalzing, D.; Taylor, T. A.; Fuchs, M. *Anal. Chem.* **1996**, 68, 18-22. "Microchip electrophoretic immunoassay for serum cortisol"
- (27) Chiem, N. H.; Harrison, D. J. *Clin. Chem.* **1998**, 44, 591-598. "Microchip systems for immunoassay: an integrated immunoreactor with electrophoretic separation for serum theophylline determination"
- (28) Cheng, S. B.; Skinner, C. D.; Taylor, J.; Attiya, S.; Lee, W. E.; Picelli, G.; Harrison, D. J. *Anal. Chem.* **2001**, 73, 1472-1479. "Development of a multichannel microfluidic analysis system employing affinity CE for immunoassay"
- (29) Bernard, A.; Michel, B.; Delamarche, E. *Anal. Chem.* **2001**, 73, 8-12. "Micromosaic immunoassays"
- (30) Dodge, A.; Fluri, K.; Verpoorte, E.; de Rooij, N. F. *Anal. Chem.* **2001**, 73, 3400-3409. "Electrokinetically driven microfluidic chips with surface-modified chambers for heterogeneous immunoassays"
- (31) Jüncker, D.; Schmid, H.; Drechsler, U.; Wolf, H.; Wolf, M.; Michel, B.; de Rooij, N.; Delamarche, E. *Anal. Chem.* **2002**, 74, 6139-6144. "Autonomous microfluidic capillary system"
- (32) Jemere, A. B.; Oleschuk, R.; Taylor, J.; Harrison, D. J. "Microchip-based selective preconcentration using protein A immunoaffinity chromatography" In

Proceedings of the μ TAS 2001 Symposium, Monterey, CA, USA, October 21-25, **2001**; Kluwer Academic Publishers; 501-502.

- (33) Hayes, M. A.; Polson, N. A.; Phayre, A. N.; Garcia, A. A. *Anal. Chem.* **2001**, *73*, 5896-5902. "Flow-based microimmunoassay"
- (34) Roos, P.; Skinner, C. D. *Analyst* **2003**, *128*, 527-531. "A two bead immunoassay in a microfluidic device using a flat laser intensity profile for illumination"
- (35) Xue, Q. F.; Wainright, A.; Gangakhedkar, S.; Gibbons, I. *Electrophoresis* **2001**, *22*, 4000-4007. "Multiplexed enzyme assays in CE single-use microfluidic devices"
- (36) Wang, J.; Ibanez, A.; Chatrathi, M. P. *J. Am. Chem. Soc.* **2003**, *125*, 8444-8445. "On-chip integration of enzyme and immunoassays: Simultaneous measurements of insulin and glucose"
- (37) Yakovleva, J.; Davidsson, R.; Lobanova, A.; Bengtsson, M.; Eremin, S.; Laurell, T.; Emneus, J. *Anal. Chem.* **2002**, *74*, 2994-3004. "Microfluidic enzyme immunoassay using silicon microchip with immobilized antibodies and chemiluminescence detection"
- (38) Roper, M. G.; Shackman, J. G.; Dahlgren, G. M.; Kennedy, R. T. *Anal. Chem.* **2003**, *75*, 4711-4717. "Microfluidic chip for continuous monitoring of hormone secretion from live cells using an electrophoresis-based immunoassay"
- (39) Guijt, R. M.; Baltussen, E.; van Dedem, G. W. K. *Electrophoresis* **2002**, *23*, 823-835. "Use of bioaffinity interactions in electrokinetically controlled assays on microfabricated devices"
- (40) Figeys, D. *Anal. Chem.* **2003**, *75*, 2891-2905. "Proteomics in 2002: A year of technical development and wide-ranging applications"
- (41) Patterson, S. D.; Aebersold, R. H. *Nat. Genet.* **2003**, *33*, 311-323. "Proteomics: The first decade and beyond"
- (42) Beranova-Giorgianni, S. *Trends Anal. Chem.* **2003**, *22*, 273-281. "Proteome analysis by 2D-GE and MS: Strengths and limitations"
- (43) Garfin, D. E. *Trends Anal. Chem.* **2003**, *22*, 263-272. "2D-GE: An overview"
- (44) Hille, J. M.; Freed, A. L.; Watzig, H. *Electrophoresis* **2001**, *22*, 4035-4052. "Possibilities to improve automation, speed and precision of proteome analysis: A comparison of two-dimensional electrophoresis and alternatives"
- (45) Gygi, S. G.; Corthals, G. L.; Zhang, Y.; Rochon, Y.; Aebersold, R. *Proc. Nat. Acad. Sci. USA* **2000**, *97*, 9390-9395. "Evaluation of 2D-GE-based proteome analysis technology"
- (46) Hoving, S.; Voshol, H.; van Oostrum, J. *Electrophoresis* **2000**, *21*, 2617-2621. "Towards high performance 2D-GE using ultrazoom gels"
- (47) Rosenfeld, J.; Capdevielle, J.; Guillemot, J. C.; Ferrara, P. *Anal. Biochem.* **1992**, *203*, 173-179. "In-gel digestion of proteins for internal sequence-analysis after 1-D or 2-D-GE"
- (48) Eckerskorn, C.; Lottspeich, F. *Electrophoresis* **1990**, *11*, 554-561. "Combination of 2D-GE with microsequencing and amino acid-composition analysis - Improvement of speed and sensitivity in protein characterization"

- (49) Hellman, U.; Wernstedt, C.; Góñez, J.; Heldin, C.-H. *Anal. Biochem.* **1995**, *224*, 451-455. "Improvement of an "In-Gel" digestion procedure of the micropreparation of internal protein fragments for amino acid sequencing"
- (50) Cobb, K. A.; Novotny, M. *Anal. Chem.* **1989**, *61*, 2226-2231. "High-sensitivity peptide mapping by CZE and microcolumn LC, using immobilized trypsin for protein digestion"
- (51) Slys, G. W.; Schriemer, D. C. *Rapid Commun. Mass Spectrom.* **2003**, *17*, 1044-1050. "On-column digestion of proteins in aqueous-organic solvents"
- (52) Wang, C.; Oleschuk, R.; Ouchen, F.; Li, J. J.; Thibault, P.; Harrison, D. J. *Rapid Commun. Mass Spectrom.* **2000**, *14*, 1377-1383. "Integration of immobilized trypsin bead beds for protein digestion within a microfluidic chip incorporating CE separations and an electrospray MS interface"
- (53) Craft, D.; Doucette, A.; Li, L. *J. of Prot. Res.* **2002**, *1*, 537-547. "Microcolumn capture and digestion of proteins combined with MS for protein identification"
- (54) Aebersold, R.; Mann, M. *Nature* **2003**, *422*, 198-207. "MS-based proteomics"
- (55) Godovac-Zimmermann, J.; Brown, L. R. *Mass Spectrom. Rev.* **2001**, *20*, 1-57. "Perspectives for MS and functional proteomics"
- (56) Wall, D. B.; Kachman, M. T.; Gong, S.; Hinderer, R.; Parus, S.; Misek, D. E.; Hanash, S. M.; Lubman, D. M. *Anal. Chem.* **2000**, *72*, 1099-1111. "IEF nonporous RP HPLC: A 2-D liquid-phase separation method for mapping of cellular proteins with identification using MALDI-TOF MS"
- (57) Chen, J.; Balgley, B. M.; DeVoe, D. L.; Lee, C. S. *Anal. Chem.* **2003**, *75*, 3145-3152. "CIEF-based multidimensional concentration/separation platform for proteome analysis"
- (58) Mohan, D.; Paša-Tolić, L.; Masselson, C. D.; Tolić, N.; Bogdanov, B.; Hixson, K. K.; Smith, R. D.; Lee, C. S. *Anal. Chem.* **2003**, *75*, 4432-4440. "Integration of electrokinetic-based multidimensional separation/concentration platform with ESI-Fourier transform ion cyclotron resonance-MS for proteome analysis of *Shewanella oneidensis*"
- (59) Opiteck, G. J.; Ramirez, S. M.; Jorgenson, J. W.; Moseley, M. A. *Anal. Biochem.* **1998**, *258*, 349-361. "Comprehensive two-dimensional high-performance liquid chromatography for the isolation of overexpressed proteins and proteome mapping"
- (60) Wagner, K.; Miliotis, T.; Marko-Varga, G.; Bischoff, R.; Unger, K. K. *Anal. Chem.* **2002**, *74*, 809-820. "An automated on-line multidimensional HPLC system for protein and peptide mapping with integrated sample preparation"
- (61) McDonald, W. H.; Ohi, R.; Miyamoto, D. T.; Mitchison, T. J.; Yates, J. R. *Int. J. Mass Spectrom.* **2002**, *219*, 245-251. "Comparison of three directly coupled HPLC MS/MS strategies for identification of proteins from complex mixtures"
- (62) Nesvizhskii, A. I.; Keller, A.; Kolker, E.; Aebersold, R. *Anal. Chem.* **2003**, *75*, 4646-4658. "A statistical model for identifying proteins by tandem MS"
- (63) Ren, D.; Penner, N. A.; Slentz, B. E.; Mirzaei, H.; Regnier, F. E. *J. of Prot. Res.* **2003**, *2*, 321-329. "Evaluating immobilized metal affinity chromatography for the selection of histidine-containing peptides in comparative proteomics"

- (64) Gygi, S. G.; Rist, B.; Gerber, S. A.; Turecek, F.; Gelb, M. H.; Aebersold, R. *Nat. Biotech.* **1999**, *17*, 994-999. "Quantitative analysis of complex protein mixtures using isotope-coded affinity tags"
- (65) Wang, H.; Hanash, S. *J. Chromatogr. B* **2003**, *787*, 11-18. "Multi-dimensional liquid phase based separations in proteomics"
- (66) Romijn, E. P.; Krijgsveld, J.; Heck, A. J. R. *J. Chromatogr. A* **2003**, *1000*, 589-608. "Recent liquid chromatographic-(tandem) mass spectrometric applications in proteomics"
- (67) Giddings, J. C. *J. High Resolut. Chromatogr.* **1987**, *10*, 319-323. "Concepts and comparisons in multidimensional separation"
- (68) Shen, Y. F.; Smith, R. D. *Electrophoresis* **2002**, *23*, 3106-3124. "Proteomics based on high-efficiency capillary separations"
- (69) Rodriguez-Diaz, R.; Wehr, T.; Zhu, M.; Levi, V. "Chapter 4: Capillary Isoelectric Focusing" In *Handbook of Capillary Electrophoresis*, 2nd Edition ed.; Ed. Landers, J. P.; CRC Press, Inc.: New York, 1997, pp 101-138.
- (70) Shimura, K. *Electrophoresis* **2002**, *23*, 3847-3857. "Recent advances in CIEF: 1997-2001"
- (71) Tan, A.; Pashkova, A.; Zang, L.; Foret, F.; Karger, B. L. *Electrophoresis* **2002**, *23*, 3599-3607. "A miniaturized multichamber solution IEF device for separation of protein digests"
- (72) Choe, L. H.; Lee, K. H. *Electrophoresis* **2000**, *21*, 993-1000. "A comparison of three commercially available IEF units for proteome analysis"
- (73) Wen, J.; Lin, Y. H.; Xiang, F.; Matson, D. W.; Udseth, H. R.; Smith, R. D. *Electrophoresis* **2000**, *21*, 191-197. "Microfabricated IEF device for direct ESI-MS"
- (74) Hofmann, O.; Che, D. P.; Cruickshank, K. A.; Muller, U. R. *Anal. Chem.* **1999**, *71*, 678-686. "Adaptation of CIEF to microchannels on a glass chip"
- (75) Herr, A. E.; Molho, J. I.; Drouvalakis, K. A.; Mikkelsen, J. C.; Utz, P. J.; Santiago, J. G.; Kenny, T. W. *Anal. Chem.* **2003**, *75*, 1180-1187. "On-chip coupling of IEF and free solution electrophoresis for multidimensional separations"
- (76) Li, Y.; DeVoe, D. L.; Lee, C. S. *Electrophoresis* **2003**, *24*, 193-199. "Dynamic analyte introduction and focusing in plastic microfluidic devices for proteomic analysis"
- (77) Huang, T. M.; Pawliszyn, J. *Electrophoresis* **2002**, *23*, 3504-3510. "Microfabrication of a tapered channel for IEF with thermally generated pH gradient"
- (78) Karas, M.; Bachmann, D.; Bahr, U.; Hillenkamp, F. *Int. J. Mass Spectrom. Ion Processes* **1987**, *78*, 53-68. "Matrix-assisted ultraviolet-laser desorption of nonvolatile compounds"
- (79) Yamashita, M.; Fenn, J. B. *J. Chem. Phys.* **1984**, *88*, 4451-4459. "Electrospray ion-source - Another variation on the free-jet theme"

- (80) Ekström, S.; Önnérjörd, P.; Nilsson, J.; Bengtsson, M.; Laurell, T.; Marko-Varga, G. *Anal. Chem.* **2000**, *72*, 286-293. "Integrated microanalytical technology enabling rapid and automated protein identification"
- (81) Dole, M.; Mach, L. L.; Hines, R. L.; Mobley, R. C.; Ferguson, L. P.; Alice, M. B. *J. Chem. Phys.* **1968**, *49*, 2240-2249.
- (82) Kebarle, P.; Tang, L. *Anal. Chem.* **1993**, *65*, 972A-986A. "From ions in solution to ions in the gas phase"
- (83) Andren, E.; Emmett, M. R.; Caprioli, R. M. *J. Am. Soc. Mass Spectrom.* **1994**, *5*, 867-869. "Micro-electrospray - Zeptomole-attomole per microliter sensitivity for peptides"
- (84) Wilm, M.; Mann, M. *Anal. Chem.* **1996**, *68*, 1-8. "Analytical properties of the nanoelectrospray ion source"
- (85) von Brocke, A.; Nicholson, G.; Bayer, E. *Electrophoresis* **2001**, *22*, 1251-1266. "Recent advances in CE/ESI-MS"
- (86) Smith, R. D.; Barinaga, C. J.; Udseth, H. R. *Anal. Chem.* **1988**, *60*, 1948-1952. "Improved ESI interface for CZE-MS"
- (87) Lee, E. D.; Muck, W.; Henion, J. D.; Covey, T. R. *Biomed. Environ. Mass Spectrom.* **1989**, *18*, 844-850. "Liquid junction coupling for CZE ESI-MS"
- (88) Minard, R. D.; Luckenbill, D.; Curry, P. J.; Ewing, A. G. *Adv. Mass Spectrom.* **1988**, *11A*, 436-437. "CE/Flow FAB/MS"
- (89) Olivares, J. A.; Nguyen, N. T.; Yonker, C. R.; Smith, R. D. *Anal. Chem.* **1987**, *59*, 1230-1232. "On-line MS detection for CZE"
- (90) Ishihama, Y.; Katayama, H.; Asakawa, N.; Oda, Y. *Rapid Commun. Mass Spectrom.* **2002**, *16*, 913-918. "Highly robust stainless steel tips as micro electrospray emitters"
- (91) Gelpí, E. *J. Mass Spectrom.* **2002**, *37*, 241-253. "Interfaces for coupled liquid-phase separation/MS techniques"
- (92) Xue, Q. F.; Foret, F.; Dunayevskiy, Y. M.; Zavracky, P. M.; McGruer, N. E.; Karger, B. L. *Anal. Chem.* **1997**, *69*, 426-430. "Multichannel microchip ESI-MS"
- (93) Ramsey, R. S.; Ramsey, J. M. *Anal. Chem.* **1997**, *69*, 1174-1178. "Generating electrospray from microchip devices using electroosmotic pumping"
- (94) Zhang, B.; Liu, H.; Karger, B. L.; Foret, F. *Anal. Chem.* **1999**, *71*, 3258-3264. "Microfabricated devices for CE ESI-MS"
- (95) Figeys, D.; Ning, Y. B.; Aebersold, R. *Anal. Chem.* **1997**, *69*, 3153-3160. "A microfabricated device for rapid protein identification by micro-ESI ion trap MS"
- (96) Bings, N. H.; Wang, C.; Skinner, C. D.; Colyer, C. L.; Thibault, P.; Harrison, D. J. *Anal. Chem.* **1999**, *71*, 3292-3296. "Microfluidic devices connected to fused-silica capillaries with minimal dead volume"
- (97) Licklider, L.; Wang, X. Q.; Desai, A.; Tai, Y. C.; Lee, T. D. *Anal. Chem.* **2000**, *72*, 367-375. "A micromachined chip-based ESI source for MS"
- (98) Kim, J. S.; Knapp, D. R. *Electrophoresis* **2001**, *22*, 3993-3999. "Miniaturized multichannel ESI emitters on PDMS microfluidic devices"

- (99) Yuan, C. H.; Shiea, J. *Anal. Chem.* **2001**, *73*, 1080-1083. "Sequential electrospray analysis using sharp-tip channels fabricated on a plastic chip"
- (100) Gobry, V.; van Oostrum, J.; Martinelli, M.; Rohner, T. C.; Reymond, F.; Rossier, J. S.; Girault, H. H. *Proteomics* **2002**, *2*, 405-412. "Microfabricated polymer injector for direct MS coupling"
- (101) Kameoka, J.; Orth, R.; Ilic, B.; Czaplewski, D.; Wachs, T.; Craighead, H. G. *Anal. Chem.* **2002**, *74*, 5897-5901. "An ESI source for integration with microfluidics"
- (102) Svedberg, M.; Pettersson, A.; Nilsson, S.; Bergquist, J.; Nyholm, L.; Nikolajeff, F.; Markides, K. *Anal. Chem.* **2003**, *75*, 3934-3940. "Sheathless electrospray from polymer microchips"
- (103) Li, J. J.; Thibault, P.; Bings, N. H.; Skinner, C. D.; Wang, C.; Colyer, C.; Harrison, J. *Anal. Chem.* **1999**, *71*, 3036-3045. "Integration of microfabricated devices to CE-ESI MS using a low dead volume connection: Application to rapid analyses of proteolytic digests"
- (104) Lazar, I. M.; Ramsey, R. S.; Sundberg, S.; Ramsey, J. M. *Anal. Chem.* **1999**, *71*, 3627-3631. "Subattomole-sensitivity microchip nanoelectrospray source with TOF-MS detection"
- (105) Li, J. J.; Wang, C.; Kelly, J. F.; Harrison, D. J.; Thibault, P. *Electrophoresis* **2000**, *21*, 198-210. "Rapid and sensitive separation of trace level protein digests using microfabricated devices coupled to a quadrupole-TOF MS"
- (106) Shui, W. Q.; Yu, Y. L.; Xu, X. J.; Huang, Z. Y.; Xu, G. B.; Yang, P. Y. *Rapid Commun. Mass Spectrom.* **2003**, *17*, 1541-1547. "Micro-electrospray with stainless steel emitters"
- (107) Deng, Y. Z.; Zhang, N. W.; Henion, J. *Anal. Chem.* **2001**, *73*, 1432-1439. "Chip-based quantitative CE/MS determination of drugs in human plasma"
- (108) Figeys, D.; Gygi, S. P.; McKinnon, G.; Aebersold, R. *Anal. Chem.* **1998**, *70*, 3728-3734. "An integrated microfluidics-tandem MS system for automated protein analysis"
- (109) Liu, H. H.; Felten, C.; Xue, Q. F.; Zhang, B. L.; Jedrzejewski, P.; Karger, B. L.; Foret, F. *Anal. Chem.* **2000**, *72*, 3303-3310. "Development of multichannel devices with an array of electrospray tips for high-throughput MS"
- (110) Zhang, B. L.; Foret, F.; Karger, B. L. *Anal. Chem.* **2001**, *73*, 2675-2681. "High-throughput microfabricated CE/ESI-MS: Automated sampling from a microwell plate"
- (111) Griss, P.; Melin, J.; Sjodahl, J.; Roeraade, J.; Stemme, G. *J. Micromech. Microeng.* **2002**, *12*, 682-687. "Development of micromachined hollow tips for protein analysis based on nano-ESI MS"
- (112) Schultz, G. A.; Corso, T. N.; Prosser, S. J.; Zhang, S. *Anal. Chem.* **2000**, *72*, 4058-4063. "A fully integrated monolithic microchip electrospray device for mass spectrometry"
- (113) Limbach, P. A.; Meng, Z. J. *Analyst* **2002**, *127*, 693-700. "Integrating micromachined devices with modern MS"

- (114) de Mello, A. J. *Lab on a Chip* **2001**, *1*, 7N-12N. "Chip-MS: Coupling the large with the small"
- (115) Oleschuk, R. D.; Harrison, D. J. *Trends Anal. Chem.* **2000**, *19*, 379-388. "Analytical microdevices for MS"
- (116) Mouradian, S. *Current Opin. Chem. Bio.* **2001**, *6*, 51-56. "Lab-on-a-chip: Applications in proteomics"
- (117) Figeys, D.; Pinto, D. *Electrophoresis* **2001**, *22*, 208-216. "Proteomics on a chip: Promising developments"
- (118) Figeys, D. *Proteomics* **2002**, *2*, 373-382. "Adapting arrays and lab-on-a-chip technology for proteomics"
- (119) Chen, X.; Wu, H.; Mao, C.; Whitesides, G. M. *Anal. Chem.* **2002**, *74*, 1772-1778. "A prototype 2-D CE system fabricated in PDMS"
- (120) Sakai-Kato, K.; Kato, M.; Toyo'oka, T. *Anal. Chem.* **2003**, *75*, 388-393. "Creation of an on-chip enzyme reactor by encapsulating trypsin in sol-gel on a plastic microchip"
- (121) Ramsey, J. D.; Jacobson, S. C.; Culbertson, C. T.; Ramsey, J. M. *Anal. Chem.* **2003**, *75*, 3758-3764. "High-efficiency, 2D separations of protein digests on microfluidic devices"
- (122) Slentz, B. E.; Penner, N. A.; Regnier, F. E. *J. Chromatogr. A* **2003**, *984*, 97-107. "Protein proteolysis and the multi-dimensional electrochromatographic separation of histidine-containing peptides on a chip"
- (123) Li, J. J.; LeRiche, T.; Tremblay, T. L.; Wang, C.; Bonneil, E.; Harrison, D. J.; Thibault, P. *Mol. Cell. Proteomics* **2002**, *1*, 157-168. "Application of microfluidic devices to proteomics research - Identification of trace-level protein digests and affinity capture of target peptides"
- (124) Wang, C. *Ph.D. Thesis*, "Integrated protein analysis on microchips for CE-ESI-MS" University of Alberta, Edmonton, Alberta, Canada, **2001**.

CHAPTER 2: AN EVALUATION OF THE DETECTION LIMITS POSSIBLE FOR COMPETITIVE CAPILLARY ELECTROPHORETIC IMMUNOASSAYS

2.1	INTRODUCTION	39
2.2	IMMUNOASSAY THEORY	41
2.3	MATERIALS AND METHODS	46
2.3.1	SOLUTIONS AND REAGENTS	46
2.3.2	INSTRUMENTATION.....	46
2.3.3	DEVICE FABRICATION.....	48
2.3.4	COMPETITIVE ESTRADIOL IMMUNOASSAY.....	49
2.4	RESULTS	50
2.4.1	ESTRADIOL ASSAY RESULTS	50
2.4.2	DETERMINATION OF REAGENT QUALITY.....	53
2.4.3	THEORETICAL PREDICTIONS FROM THE JACKSON AND EKINS MODEL	60
2.4.4	EFFECT OF CONCENTRATION AND AFFINITY ON DETECTION LIMITS ..	62
2.4.5	MINIMUM DETECTION LIMIT FROM THE DOSE-RESPONSE FUNCTION	65
2.4.6	EXPERIMENTAL VS. THEORETICAL	69
2.5	CONCLUDING REMARKS	70
2.6	REFERENCES	72

A version of this chapter has been published. Taylor, J.; Picelli, G.; Harrison, D.J. *Electrophoresis* **2001**, 22, 3699-3708. "An evaluation of the detection limits possible for competitive capillary electrophoretic immunoassays"

2.1 INTRODUCTION

Utilization of capillary electrophoresis (CE) as a separation technique for immunoassays (collectively CEIA) is a field that sprung from initial work done by Grossman *et al.*¹ in the late eighties. From this work Kennedy went on to combine CEIA with laser-induced fluorescence (LIF) detection to develop the first truly successful CE immunoassay.² Karger, also using CEIA combined with LIF, coined the term affinity probe CE shortly thereafter³, and in the past ten years the field has expanded rapidly.⁴⁻⁹ The union of the two techniques (CE and IA) offers several advantages over conventional solid-phase methods. Since separation by CE occurs without immobilization the immunoreaction can be run in a single phase, allowing for rapid solution-phase kinetics. Solution-phase reactions also reduce problems associated with the reproducibility of the immobilization step and with non-specific adsorption that are often seen in solid-phase assays. CE separation can be achieved rapidly, reducing the likelihood of complex dissociation often seen when using solid-phase separation methods. When coupled with LIF detection¹⁰, CEIA offers an enhanced mass sensitivity. The procedure itself is simple and could be easily adapted to an automated system.¹¹ Although the separation itself is serial, it is possible to multiplex using either capillary bundles¹²⁻¹⁵ or microfluidic devices¹⁶. The added dimension of separation allows for the simultaneous analysis of multiple analyte systems, provided that individual analyte peaks are resolved.¹⁷ And lastly, the smaller volume of the capillary itself is less demanding of sample size.

Unfortunately, CEIA generally exhibits a poorer concentration sensitivity than the more commonly used solid-phase techniques, especially for competitive assays.^{5,18} This can be attributed in part to the smaller detection volume associated with CE, but more importantly, to the preconcentration that solid-phase techniques provide. However, the use of a solid-phase slows down reaction kinetics, thereby lengthening analysis time. The theoretical detection limits (DL) that may be achieved in immunoassay have been examined by a number of authors.¹⁹⁻²³ The methods used and the results obtained were specific

to the type of immunoassay performed: competitive vs. direct²⁴, homogeneous vs. immunosorptive, chromatographic²⁵, etc.²⁶⁻²⁸ Some optimization of CEIA parameters such as pH, incubation time, reagent concentrations, temperature and applied voltage has been previously performed.²⁹⁻³¹ However, a specific theoretical analysis of the detection limits achievable by CEIA has not been reported previously, yet it is clearly important to understand the factors that can be adjusted to optimize the DL.

Detailed analysis of the detection limits obtained in solution-phase competitive radioimmunoassays has been presented previously.¹⁹⁻²³ This approach was adapted to estimate a DL for competitive CEIA, and to select the optimal reagent concentrations and reagent ratios for achieving the best DL and precision. Previous analyses have used functional relationships and iterative calculations to correlate error in the measurement with reagent concentration and the percent bound antigen, based upon the specifics of detecting radioactive labels.^{20,22,23} In this first analysis of CEIA with LIF detection, a simplified approach was used, assigning a fixed standard deviation to measurements at any concentration as a first approximation, since the radioimmunoassay model for errors may not be wholly appropriate. DL estimates were easily obtained using spreadsheet calculations, without a need for the complex programming that more detailed error modeling has required.^{20,21} The results confirm the extreme importance of a high affinity constant for solution-phase CEIA, which lacks the preconcentration step in immunosorbent assays. Furthermore, the model presented allows the experimentalist to predict the optimum antibody and labelled antigen concentrations.

The calculated DL predictions have been compared with experimental results from microfluidic chip CEIA for estradiol using anti-estradiol and fluorescently labelled estradiol as a competitor. Estradiol is one of the more important estrogens and as such the need to monitor serum levels is essential.³² Estradiol levels are most commonly monitored during pregnancy to assess the health of the foetus, however it has also been linked to breast cancer, prostate

cancer and ovarian tumours. During menopause, women will experience a decrease in estradiol levels which often leads to uncomfortable side effects. Hormone replacement therapies use estradiol to relieve these symptoms. This decrease has also been linked to the onset of osteoporosis and hence, the need to monitor estradiol levels at this time is crucial. Furthermore, estradiol has been seen to be a vital biomarker and can be used to monitor the health of the environment through its adsorption into water animals.³³ For endocrinological purposes, the range of estradiol values of interest is 5-1000 pg/mL. The lowest reported DL was 0.49 pg/mL for a solid-phase, competitive, chemiluminescent assay.³⁴ The lowest DL using CEIA was 9 pg/mL, by means of a competitive, solution-phase assay for estradiol in conjunction with a direct assay for the anti-estradiol antibody using a fluorescently labelled second antibody.³⁰ Direct assays are capable of higher sensitivities than competitive assays, as was outlined in Section 1.2.2. This work used a hydrogel as a separation matrix in order to improve reproducibility and resolution of the separation technique. As an interesting aside, a recent publication reported the simultaneous use of two antibodies with varying affinities for the analyte, as a means of dynamic range extension.³⁵ In this work, high and low affinity antibodies were used simultaneously leading to an additive signal-response curve covering a larger range of analyte concentrations. For estriol, a related estrogen, the additive dynamic range was 10 pM to 1 μ M, covering five orders of magnitude. The goal of the present work was to determine if analyte detection in the endocrinological range of interest was experimentally or theoretically possible using a solution-phase, competitive assay.

2.2 IMMUNOASSAY THEORY

Immunoassays can be broadly categorized into two groups: non-competitive and competitive.²⁶⁻²⁸ A labelled antibody reacting with the analyte of interest would result in a non-competitive assay. Although non-competitive assays have the potential to yield lower detection limits, there are several

technical drawbacks inherent to the format that makes the competitive format the frequently preferred choice for CEIA. A competitive immunoassay is based on the competition between an analyte (Ag) and a labelled analyte (Ag*) for a limited number of antibody (Ab) binding sites. Typical protocol holds Ab and Ag* concentrations fixed for various concentrations of the analyte of interest, Ag. The assay is governed by two equilibria:



where K and K* are the resulting equilibrium constants for the reaction of Ab with Ag and Ag*, respectively. The result of the two reactions is that there will be five species in solution, only two of which are fluorescently labelled and therefore observable. By monitoring Ag* and Ab-Ag*, the amount of Ag initially present can be quantified. Both of these reactions can be defined by equilibrium or mass-action expressions:

$$K = \frac{B}{F(N - B - B^*)} \quad (2.3)$$

$$K^* = \frac{B^*}{F^*(N - B - B^*)} \quad (2.4)$$

where B is the concentration of bound antigen, F the concentration of free antigen, N the concentration of antibody binding sites and the superscript * refers to the labelled antigen. The reaction between antibody and antigen is often multivalent. Here we assume that the two binding sites on IgG do not interact and have the same affinity, so that N represents antibody concentration multiplied by the valency. Therefore, Equations 2.1 and 2.2, which are for univalent reactions, may be employed using N as the binding site concentration. Throughout this chapter, the antibody concentration is stated, not the binding site

concentration, and a valency of two is assumed for the antibody-antigen interaction in all calculations. The native and labelled antigens may have different affinity constants for the antibody. Here, the assumption is made that the two affinity constants are equal ($K = K^*$), so that the following relationships can be derived:

$$\frac{B}{F} = \frac{B^*}{F^*} \quad (2.5)$$

$$\frac{B}{T} = \frac{B^*}{T^*} = y \quad (2.6)$$

where T is the total analyte concentration, be it either labelled (T^*) or unlabeled (T). The response, y, can be experimentally determined by taking the ratio of the bound Ag^* signal (B^*) to the total signal ($T^* = Ag^* + Ab-Ag^*$ or $T^* = B^* + F^*$). Using these equations, a theoretical dose-response expression can be defined by:

$$T + T^* = \frac{N}{y} - \frac{1}{K(1-y)} \quad (2.7)$$

This expression predicts the behaviour of the system for various values of N, T^* and K, using $y = B^*/T^*$ as the response and T as the dose.^{22,23} This equation is valid when all binding sites are equivalent and have the same affinity for the antigen. Further assumptions made in defining the above equations are outlined by Campfield.²⁶

Plots of response versus analyte concentration were generated in two ways. Experimentally, the response, y, was defined as the ratio of the area of the B^* peak to the total peak area ($B^* + F^*$), and this was analyzed versus T, which was the estradiol concentration. Theoretical data was generated by substituting chosen values for N, K, y and T^* into the dose-response expression, Equation 2.7, and obtaining values for T. In both cases, the resulting data sets were

plotted as response versus analyte concentration (T) and fit using the four parameter logistic model shown below:

$$y = d + \frac{a - d}{1 + \left(\frac{T}{c}\right)^b} \quad (2.8)$$

where a, b, c and d are fitted parameters.³⁶

Undoubtedly, one of the most important assay parameters is the detection limit. Jackson and Ekins¹⁹ stated that experimental error and antibody affinity constant would ultimately define detection limits for competitive immunoassays. They constructed the following expression:

$$(\sigma)_{\min,0} = \frac{CV_0}{K} \quad (2.9)$$

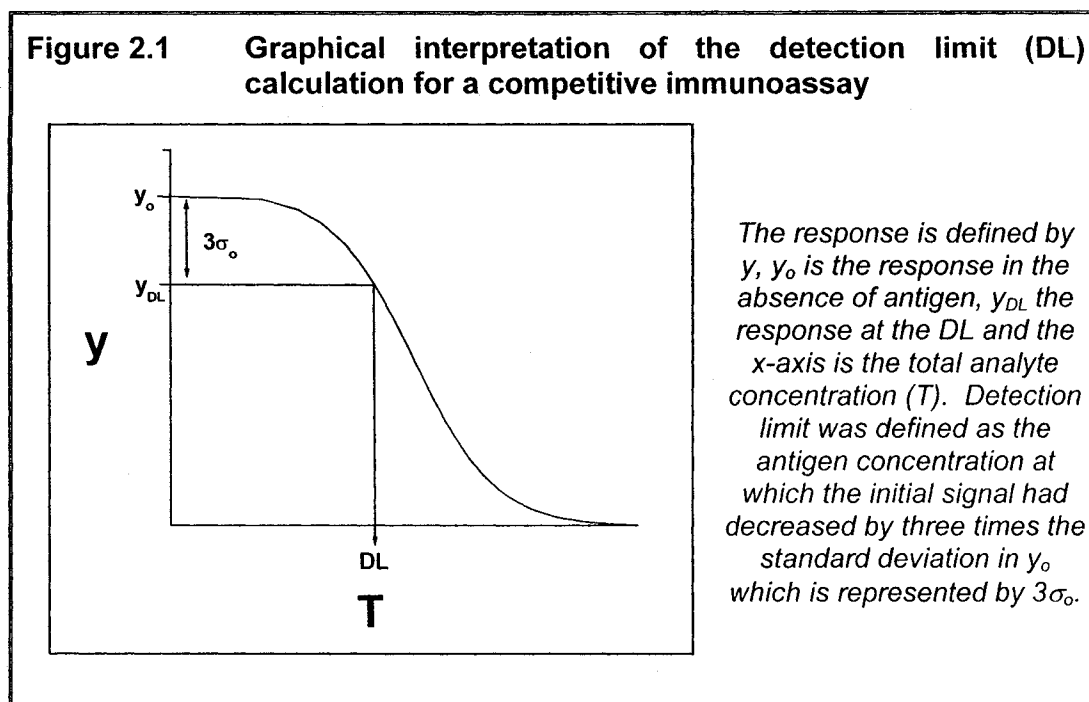
where $(\sigma)_{\min,0}$ is the theoretical minimum standard deviation of the response in the presence of zero analyte, CV_0 is the coefficient of variation of the response at zero analyte and K is again the affinity constant. This definition assumes there is no signal measurement error contribution to the CV, and that all other errors have a constant relative error. Constant relative error implies that the absolute standard deviation will continually decrease as reagent concentrations are lowered. This is not experimentally possible, as standard deviation will ultimately be limited to a finite value, probably dictated by detector noise. As a result, Equation 2.9 provides an essentially unobtainable lower limit for the DL. It is necessary to look to the theoretical dose-response expressions in order to evaluate the optimal concentrations of N and T* required for the lowest possible DL.

For this study, detection limits were calculated from the curves obtained by fitting the experimental or calculated response to the logistic equation (Equation 2.8). The analyte concentration at the point where the initial signal had decreased by three times its standard deviation was determined from the logistic

fit. This concept is mathematically described by Equation 2.10, and is graphically illustrated in Figure 2.1.

$$y_0 - y_{DL} = 3\sigma_0 \quad (2.10)$$

where y_0 is the response in the presence of zero analyte, y_{DL} is the response at the DL and σ_0 is the standard deviation in the response at zero dose.



Substitution of logistic equations for y_0 and y_{DL} lead to the following definition:

$$DL = c \left(\frac{a-d}{a-d-3\sigma_0} - 1 \right)^{\frac{1}{b}} \quad (2.11)$$

The value of σ_0 used was the standard deviation obtained experimentally from the variation in replicate measurements of y_0 . A value of $3\sigma_0$ was chosen to represent the point at which y_0 and y_{DL} were statistically different for a single sample measurement. This method of calculating DL assumes that the standard deviation at the DL is the same as the standard deviation at zero dose. This may

not always be the case. Theoretical dose-response detection limits were determined as above, using a standard deviation estimated from the experimental relative standard deviation (RSD_o) and the response at zero dose as predicted by the theoretical curve, $y_o(\text{theory})$.

$$\sigma_o(\text{theory}) = \sigma_o(\text{exp.}) \frac{y_o(\text{theory})}{y_o(\text{exp.})} \quad (2.12)$$

These predictions of DL are defined as arising from the dose-response expression.

2.3 MATERIALS AND METHODS

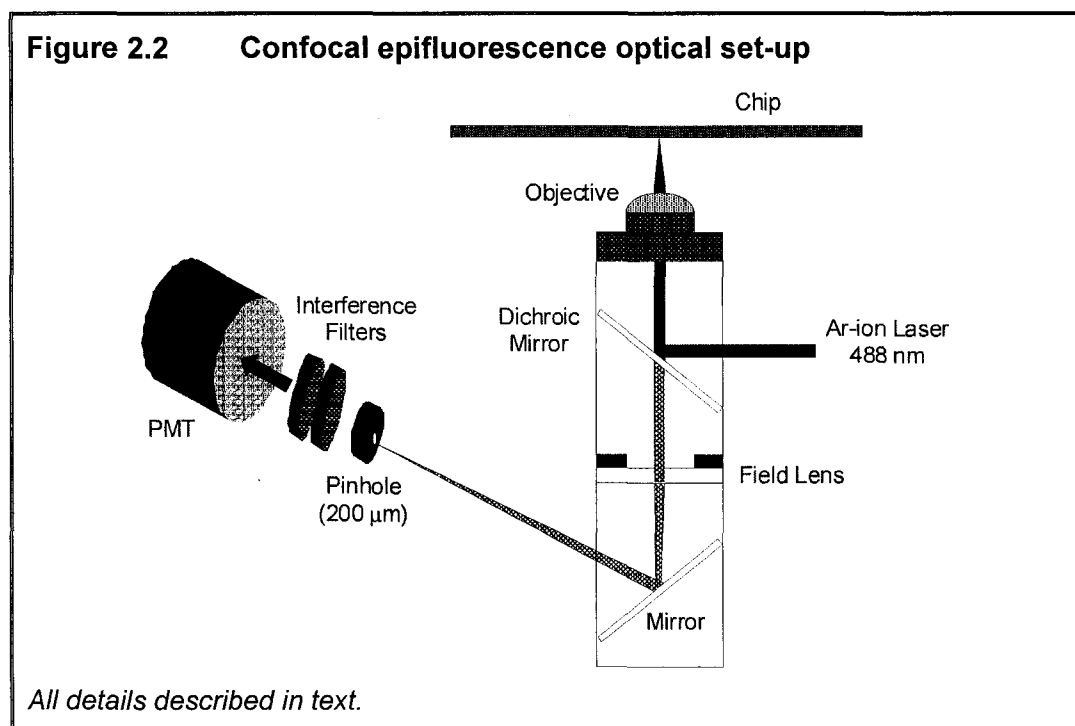
2.3.1 SOLUTIONS AND REAGENTS

All studies were performed in 20 mM boric acid (BDH Inc.) buffer prepared in ultrapure water (Millipore Canada) with pH adjusted to 8.2 using 1 M NaOH (BDH Inc.), with 20 mM NaCl (BDH Inc.) and 0.01% Tween-20 (Sigma-Aldrich), added to reduce protein adsorption. Estradiol, monoclonal anti-estradiol antibody (10G6D6, mouse IgG1(λ), $K = 2 \times 10^9 \text{ M}^{-1}$, $k_{\text{association}} = 1.2 \times 10^6 \text{ M}^{-1}\text{s}^{-1}$, $k_{\text{dissociation}} = 5.5 \times 10^{-4} \text{ s}^{-1}$)^{37,38} and the fluorescently labelled estradiol were prepared at bioMérieux, Marcy l'Étoile, France. All buffer solutions were filtered through a Nylon syringe filter (0.2 μm pore size, Chromatographic Specialties Inc.) and degassed prior to use. Final protein solutions were not filtered.

2.3.2 INSTRUMENTATION

The power supply and relay system used to control the electrophoretic voltages necessary for liquid handling on-chip have been described previously.³⁹ LabVIEW programs (National Instruments), written in-house, were used for computer control of the voltage system and for data acquisition.

The confocal epifluorescence detection system described previously was used with some modifications.⁴⁰ Briefly, excitation light from an argon ion laser (488 nm, JDS Uniphase 2214-10SL) operated at 6.6–7.6 mW was reflected by a dichroic mirror (505DRLP, Omega Optical) and then focused on the device using a 40x, 0.6 N.A. microscope objective (Planachromat LDN 1.2-A, Carl Zeiss Jena). The fluorescence emission was collected by the same objective, passed through the dichroic mirror and focused by a tube lens (achromat, $f = 200\text{mm}$, Newport PAC064) onto a 200 μm pinhole. This corresponded to a detection volume of 216 fL. Signal was collected using two 530 nm bandpass filters (530DF30, Omega Optical) and a photomultiplier tube (Hamamatsu HC-120-05) biased at 725–735 V. The analog signal was amplified (10^7 gain trans-impedance amplifier), filtered (25 Hz low-pass filter) and converted to digital data with a National Instruments NB-MIO16 A/D board at a sampling frequency of 20 Hz. The optical path is illustrated in Figure 2.2. The chip was held above the confocal detection system on a Plexiglass platform. The position of this platform could be controlled through the use of three translation stages (Newport #423).



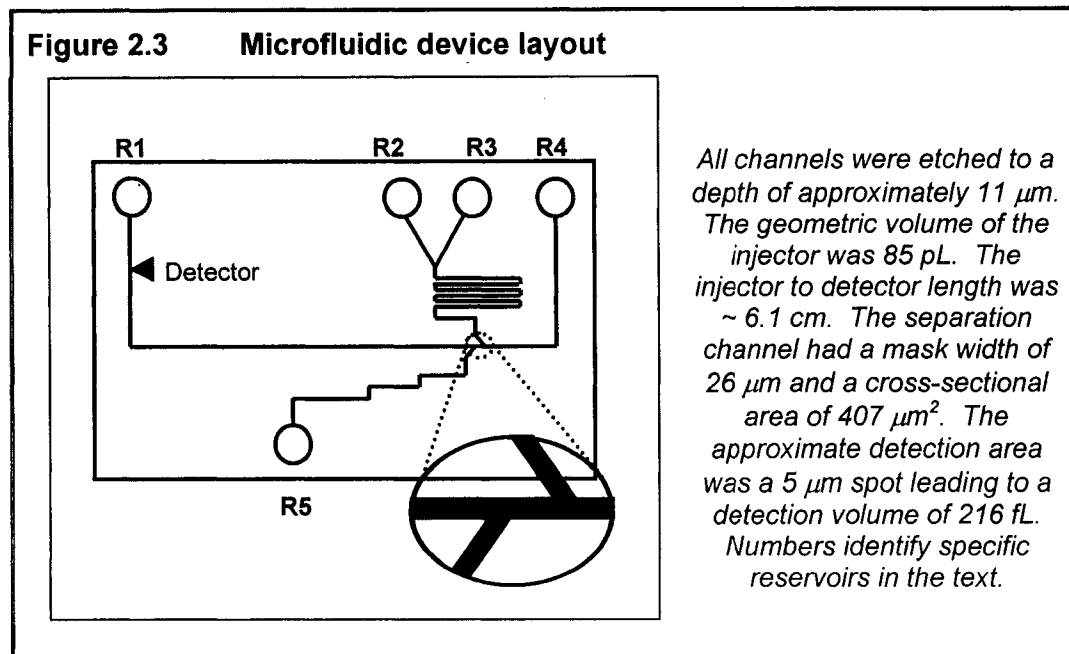
Platinum electrodes were suspended in the chip reservoirs and connected to the power supply via electrical contacts embedded in the platform. Some care was taken to ensure that the excitation beam made a 90° angle with the device. This was done by first aligning the beam perpendicular to the optical table using a set of cross-hairs. One set was positioned directly above the microscope and the second at a distance of approximately two feet above the microscope. This ensured that the beam traveled directly perpendicular to the table. Next, a mirror was placed on the Plexiglass platform in order to ensure that this platform was level with the table. If the mirror is perpendicular to the incoming beam, then the reflected beam will travel exactly the path of the incoming beam, if not the reflected beam would be offset from the incoming beam. The Plexiglass stage was shimmed in order to level it to the table. This procedure has been described in part previously.⁴⁰

The detection set-up was aligned daily as previously described.⁴⁰ The process involved first focusing the channel in the centre of the field of view using a 10X eyepiece (Melles Griot). A 1 nM solution of fluorescein (Sigma-Aldrich) was then drawn through the channel using vacuum. The laser spot was aligned in the centre of the channel and the x and y translation stages were locked. The eyepiece was then replaced with a pinhole focused on the laser spot and a PMT. The z stage was incrementally raised and lowered while simultaneously stopping and starting the flow at each increment. The z stage was locked in the position that afforded the greatest difference between the flowing solution and the stopped flow signals.

2.3.3 DEVICE FABRICATION

The device was fabricated in 4-in. square photomask glass (Agfa-Gevaert, Belgium) by Micralyne (Formerly the Alberta Microelectronic Corporation), using previously published procedures.⁴¹ A full description of the steps involved with chip fabrication is presented in Section 3.3.8. The device layout and relevant parameters are shown in Figure 2.3. The device was initially wet with water and

then conditioned with 0.1 – 0.2 M NaOH daily or as needed for experimentation. Only one device was required for the entire course of this work (approximately 18 months).



2.3.4 COMPETITIVE ESTRADIOL IMMUNOASSAY

Stock solutions of estradiol (1 mg/mL in ethanol), anti-estradiol (7.44 mg/mL) and fluorescently labelled estradiol (0.25 mg/mL) received from bioMérieux, were diluted as needed in borate buffer. Estradiol and fluorescently labelled estradiol were mixed and vortexed for 10 s, then the anti-estradiol was added. The solution was vortexed for 10 s and the reaction incubated for 10 min before introduction into reservoirs R2 and R3 of the device. (NOTE: The incubation time was arbitrarily chosen and does not reflect the actual reaction rate. However, it is known that by this point the reaction had reached steady state.) The sample was initially flushed through the injector region to waste (R5) by grounding R2 and R3 and holding R5 at -1.5 kV for 80 s. The separation channel was then flushed with buffer by holding R4 at ground and waste reservoir R1 at -6 kV. R2, R3 and R5 were held at -0.63 kV during separation to

inhibit leakage from the side channels. Repeated sample injection was performed by holding R2 and R3 at ground and R5 at -1.5 kV for 2 s. Separation was then achieved by holding R4 at ground, R2, R3 and R5 at -0.63 kV and R1 at -6 kV. Before introducing a new sample all reservoirs and channels were flushed with buffer.

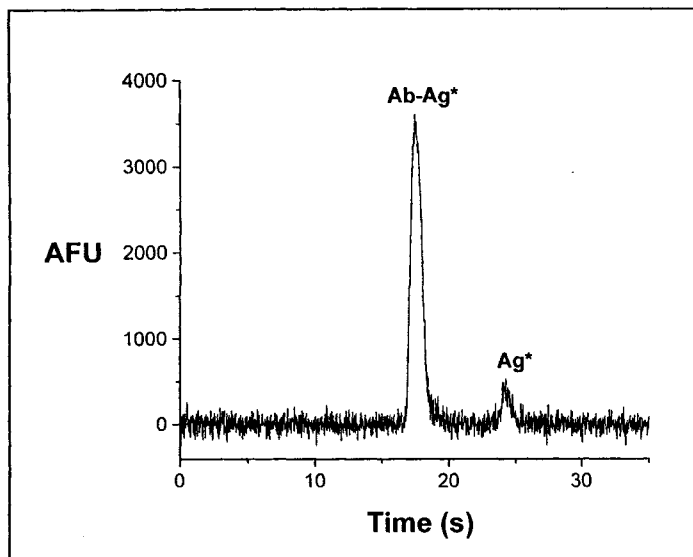
2.4 RESULTS

2.4.1 ESTRADIOL ASSAY RESULTS

Initial migration order of the reagents was determined using a conventional CE instrument (Beckman PACE 5000) with LIF detection (Argon Ion laser: Excitation at 488 nm and emission monitored at 532 nm). Using 20 mM borate buffer at pH = 8.3, it was determined that the Ab-Ag* complex preceded the free Ag*. This is to be expected based on the charges on the species of interest. Monoclonal IgG has a pI of 7.5-7.9⁴² and at a pH above the pI, it can be expected to be negatively charged. The estradiol alone is neutral and the label, 4,5-carboxyfluorescein, will also be negatively charged. Considering that all species are negatively charged, differences in migration are expected to arise from size differences. The free labelled estradiol, being much smaller than the antibody-antigen complex, will have a higher mobility. Both migrate towards the positive terminal, thereby opposing the EOF. Hence, the free labelled estradiol will migrate more strongly against the EOF and as such will arrive at the detector second (see Section 1.2.5 for further discussion of EOF and mobility).

Using the microchip device, data was gathered for the immunoassay. A sample electropherogram is shown in Figure 2.4.

Figure 2.4 Typical on-chip electropherogram for a competitive assay of estradiol



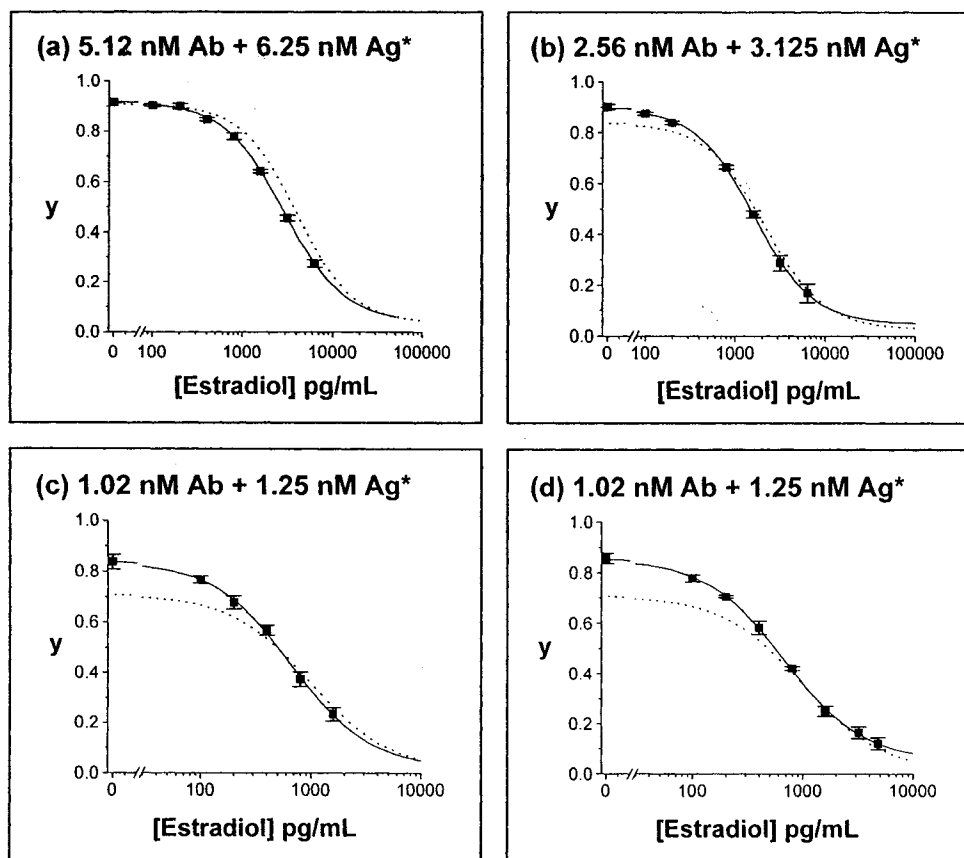
Obtained for 5.12 nM Ab and 6.25 nM Ag in 20 mM borate, 20 mM NaCl, 0.01% Tween-20, pH = 8.2 buffer solution, with an electric field of 770 V/cm during separation.*

Using peak areas, the response, y , was plotted versus estradiol concentration, then fit using the four parameter logistic model, Equation 2.8. The resulting calibration curves are shown in Figure 2.5. Detection limits were calculated using the parameters from the logistic fit and Equation 2.11. Experimental concentration parameters for the assay as well as the resulting detection limits, RSD_o values and theoretical predictions are shown in Table 2.1.

Table 2.1 Experimental and theoretical detection limits for a competitive solution-phase estradiol assay

[Ab] nM	[Ag*] nM	Experimental RSD_o	Experimental DL (pM)	Theoretical DL (pM)
5.12	6.25	0.32%	310 (84 pg/mL)	593 (162 pg/mL)
2.56	3.125	1.1%	490 (130 pg/mL)	673 (183 pg/mL)
1.02	1.25	3.5%	440 (120 pg/mL)	740 (202 pg/mL)
1.02	1.25	2.4%	320 (87 pg/mL)	530 (144 pg/mL)

Figure 2.5 Experimental and theoretical calibration curves for a competitive assay of estradiol



A comparison of theoretical predictions and experimental results at three different concentrations. The response, y , is defined as the ratio of bound Ag^* to total Ag^* , calculated using peak areas. The solid lines show the logistic fit of the experimental data and the dashed lines represent the logistic fit to the theoretical predictions. Theoretical predictions were made by substitution of experimental conditions into the dose-response expression. Each data point represents the average of 5 replicate injections except for the first data point at zero analyte which is the average of 10 replicate injections. Plots (c) and (d) were replicate trials run under the same conditions.

The lowest experimental DL achieved was 310 pM, which corresponds to a mass DL of approximately 2100 molecules passing through the detection volume. Further optimization of the detector might have given a lower concentration DL, however this study was not undertaken.

Reagent concentrations presented in this section were confirmed through analysis of the stock solutions, the results of which are presented in Section 2.4.2.

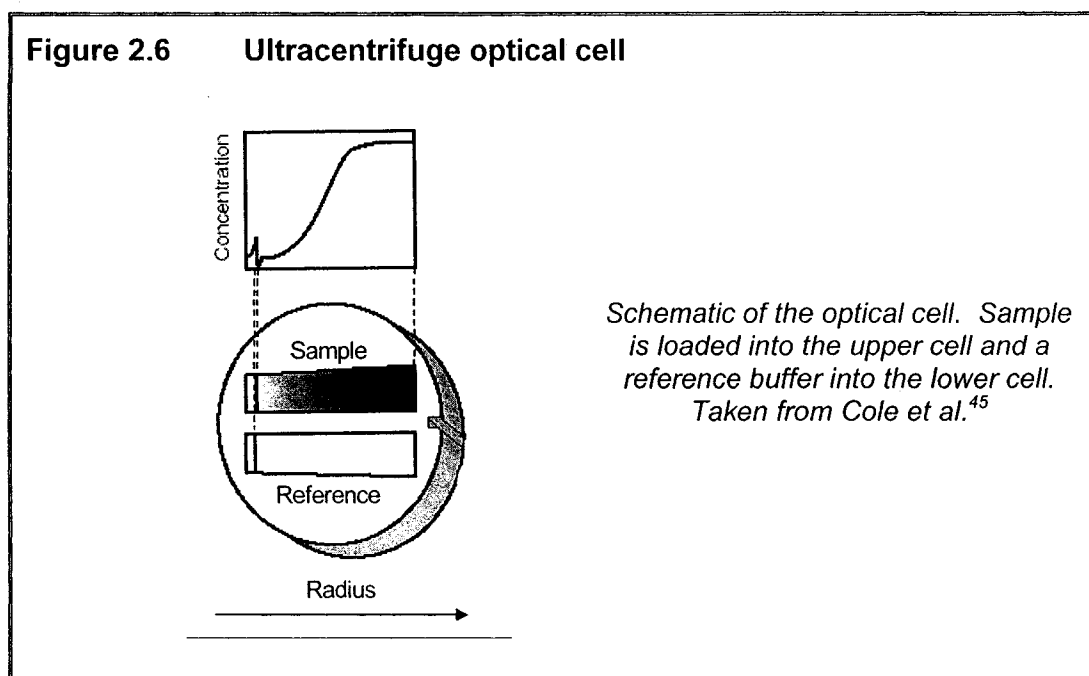
2.4.2 DETERMINATION OF REAGENT QUALITY

In the past, estimates of antibody concentration have been made by measuring UV absorbance at 280 and 260 nm and using the following equation for the determination of general protein concentration:⁴³

$$[\text{Protein}](\text{mg/mL}) = 1.55 * A_{280} - 0.76 * A_{260} \quad (2.13)$$

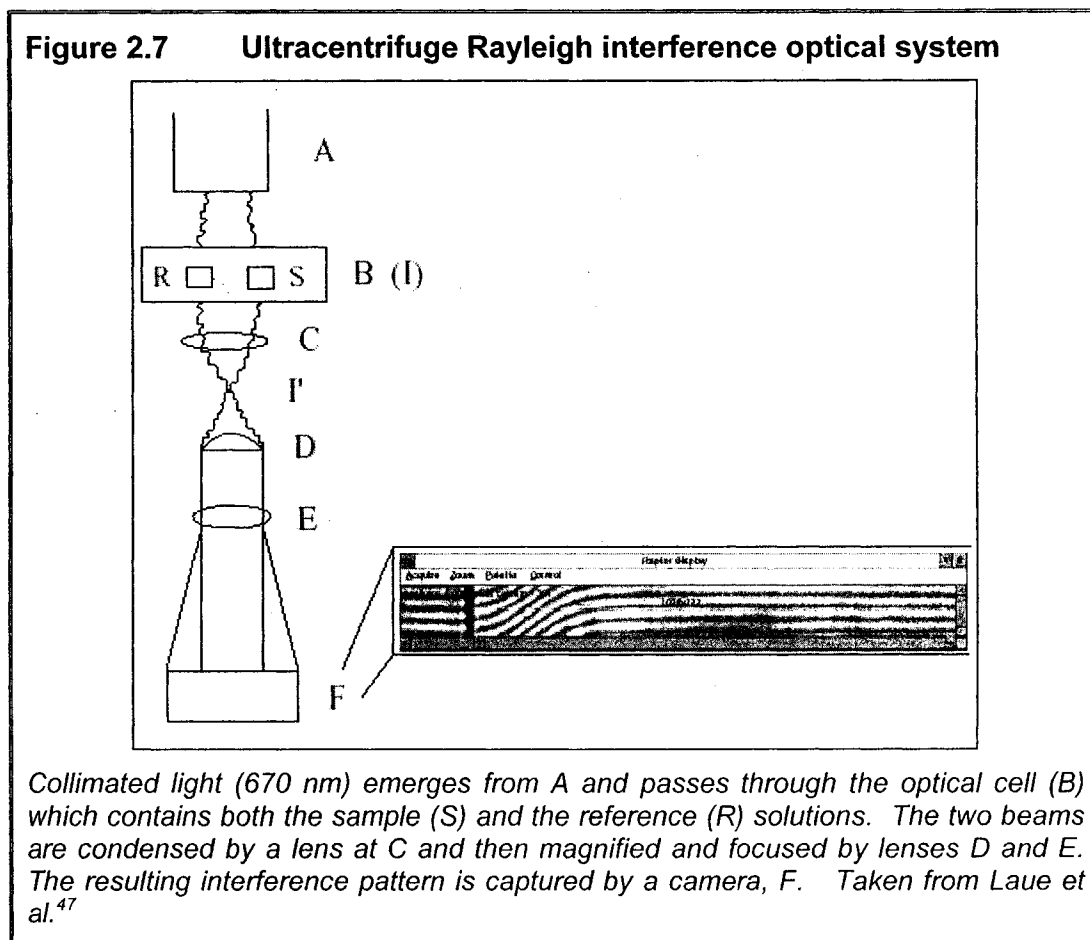
However, Equation 2.13 is largely dependent on the number of aromatic residues (tyrosine and tryptophan) present in the antibody. Since all antibodies contain a variable region which is specific to the antigen of interest and hence contain varying numbers of aromatic residues, this method should only be used as a rough estimate of concentration. Furthermore, secondary protein structure has also been seen to affect absorbance. A slightly more rigorous method was undertaken involving a standard protein assay kit (Bio-RAD cat. # 500-0006) based on the Bradford method.⁴⁴ Coomassie® Brilliant Blue G-250 experiences a shift in absorbance maximum from 465 nm to 595 nm when bound to protein. It binds primarily basic and aromatic residues, in particular arginine. This method assigns antibody concentration by comparing the signal at 595 nm of the antibody of interest to a standard curve prepared using a standard IgG antibody solution. The downfall of this method is that small changes in the amino acid sequence in the variable region will affect the amount of dye that binds to the antibody. Hence, comparing two different IgG antibodies may not yield an accurate concentration for the unknown. Since accurate antibody concentration

was essential for this study, a more accurate method of concentration determination was undertaken. The method of Fringe count analysis was used to determine both the concentration and the absorptivity coefficient of the specific antibody that was studied. This method involves the use of an analytical ultracentrifuge fitted with both UV absorbance and Raleigh interference optics. The refractive increment (change in refractive index per change in concentration) of a protein is thought to be largely independent of amino acid composition and hence can be used for accurate concentration determination.⁴⁵⁻⁴⁷ In brief, there are two detection cells parallel to one another and perpendicular to the optical path. One contains the reference buffer and one the sample as illustrated in Figure 2.6.



When the rotor is started, a gradient is developed in the sample cell. Both absorbance and interference measurements are made along the radial length of the cell. The result is a sigmoidal curve that will shift down the radial axis with time. However, the height of the upper plateau will remain constant. The absorbance measurement simply measures the difference in absorbance between the reference and the sample. This was performed at 280 nm.

Absorbance is determined by taking the difference between the upper and lower plateaus of the sigmoidal curve. The interference measurement arises from differences in the refractive indices of the reference and the sample. The incident rays that pass through the sample and reference, individually, are recombined after passing through the cell, as illustrated in Figure 2.7.



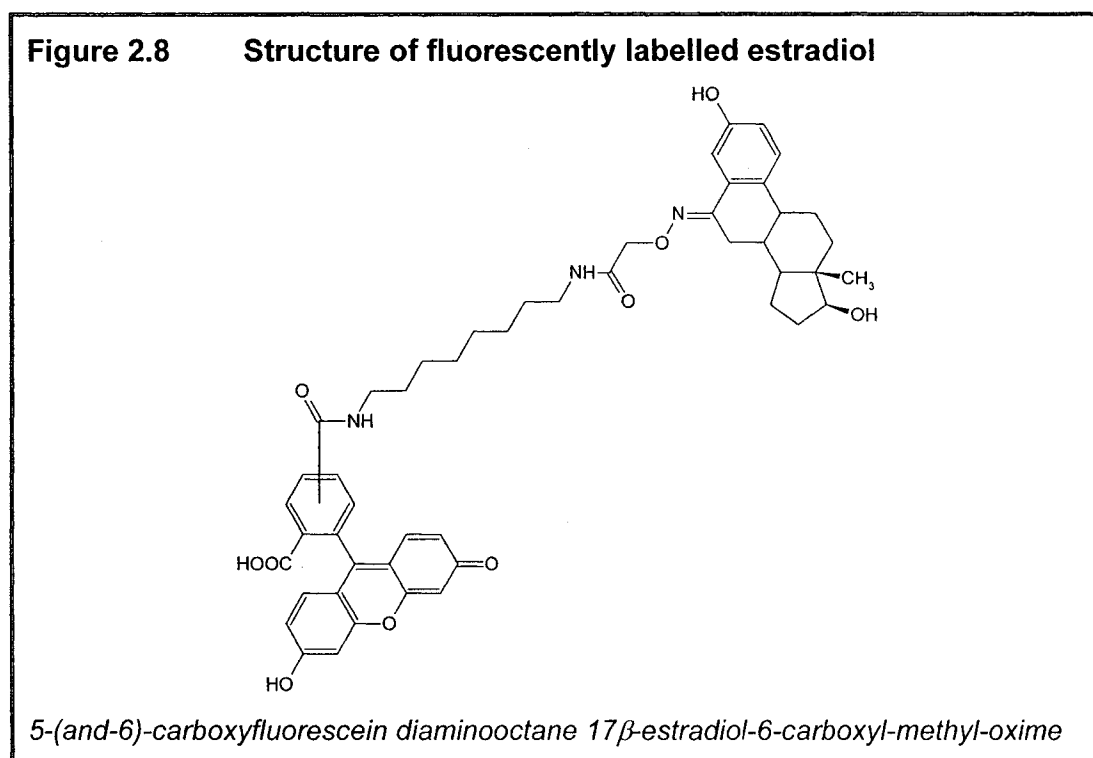
Due to refractive index differences, there will be a displacement of the interference pattern or fringes resulting from the interaction of the two beams. Fringe displacement is measured at all points along the radial axis and is then plotted on the y-axis as the vertical height of the sigmoidal curve and can be converted to a concentration measurement using a known coefficient for refractive increments. The concentration of the antibody of interest was calculated using Equation 2.14.

$$\text{Concentration} = \frac{\lambda \Delta J}{L \left(\frac{dn}{dt} \right)} \quad (2.14)$$

Where L is the path length (1.0 cm), λ is the wavelength (670 nm), ΔJ is the fringe displacement (10.1031 fringes) and dn/dt the specific refractive increment, which for human IgG was 0.187 mL/g.⁴⁸ Knowing the concentration of the solution of interest as well as the absorbance, one can then accurately calculate an absorptivity coefficient. The final antibody concentration was determined to be 7.44 mg/mL and the absorptivity coefficient was 1.51 AU/(mg/mL). The labelled concentration supplied from bioMérieux was 7.27 mg/mL. Thanks are extended to Prof. C. Kay for use of the ultracentrifuge and Les Hicks who performed this work.

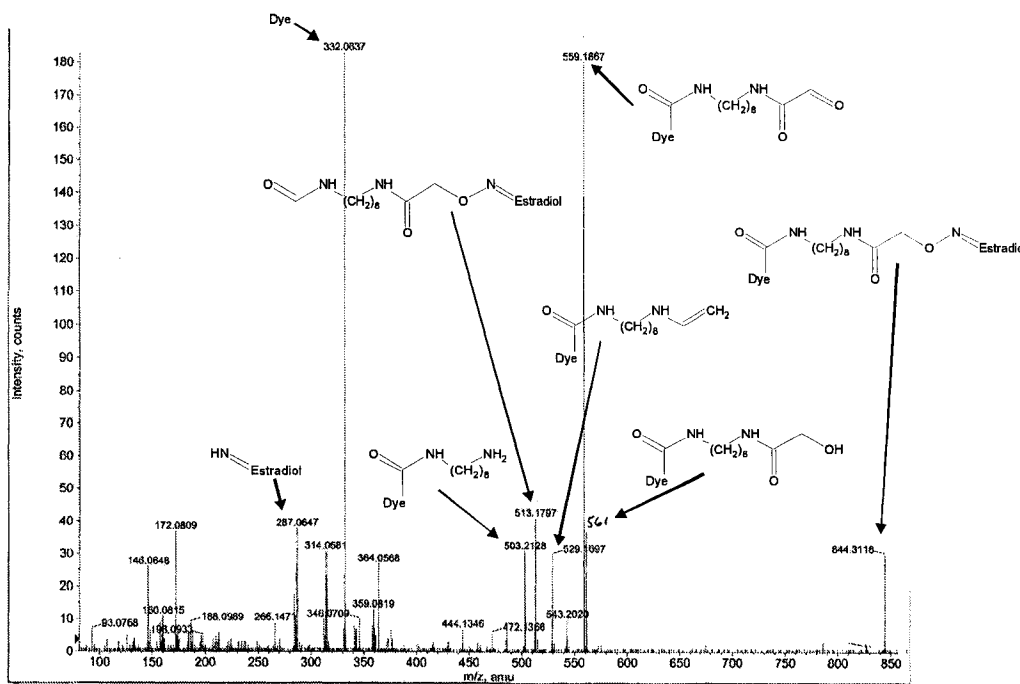
Concentration determination of the fluorescently labelled estradiol proved to be more difficult. An IgG antibody has two reactive sites at which to bind antigen, as was shown in the introduction to this chapter. Hence, reaction between an IgG antibody and its antigen used in a ratio of 1:2 should result in three species; Ab-Ag, Ab and Ag. The amount of free species will be dependent on the concentration of reagents and the affinity constant of the antibody. At this ratio, LIF detection with a fluorescently labelled antigen should yield two fluorescent peaks, Ab-Ag* and Ag*. However, it was not until a ratio of 1:5 (Ab:Ag*) was used that a free Ag* peak was seen, using the concentrations as provided by bioMérieux. This suggested that the concentration of the Ag* was incorrect (Ab concentration having already been determined). A CE separation of the compound provided only one peak using both UV and LIF detection, which disproved the notion of free dye or free hormone. However, an HPLC separation of the compound with UV detection revealed two peaks [C₁₈ column (3.9 x 150 mm), mobile phase: 60% 0.1 M formic acid, 40% ACN, isocratic, Flow rate: 1.5 mL/min, detection at 220 and 280 nm]. The ratio of the area of the two peaks was 1:3. At this point, it was revealed by bioMérieux that the labelled compound had been synthesized using a mixed isomer, 4,5-carboxyfluorescein, as the

fluorescent dye. Further LC/MS [C_{18} column (2 x 150 mm), mobile phase: 0.1% acetic acid with gradient: 80% H_2O to 90% ACN in 10 min, Flow rate: 0.25 mL/min, MS: Single Quad., API-ESI positive mode] results confirmed that both peaks had the same molecular weight, 843 g/mol. MALDI-TOF MS/MS fragmentations patterns in conjunction with published results from bioMérieux using a similar hormone linking system^{37,38}, led to the structure in Figure 2.8.



The molecular formula of this structure was confirmed by high resolution ESI-TOF which lead to an elemental composition of $C_{49}H_{54}N_3O_{10}$ for the molecular ion peak identified as $[M+H]^+ = 844.380381$, with an error of only 0.6 ppm. The sodium adduct was also studied resulting in 0.4 ppm error for the formula $C_{49}H_{53}N_3O_{10}Na$ as compared to the identified peak $[M+Na]^+ = 866.363195$. The structure was further confirmed by MS/MS analysis of the molecular ion, the result of which is shown in Figure 2.9. A description of some of the identified peaks is given in the figure caption.

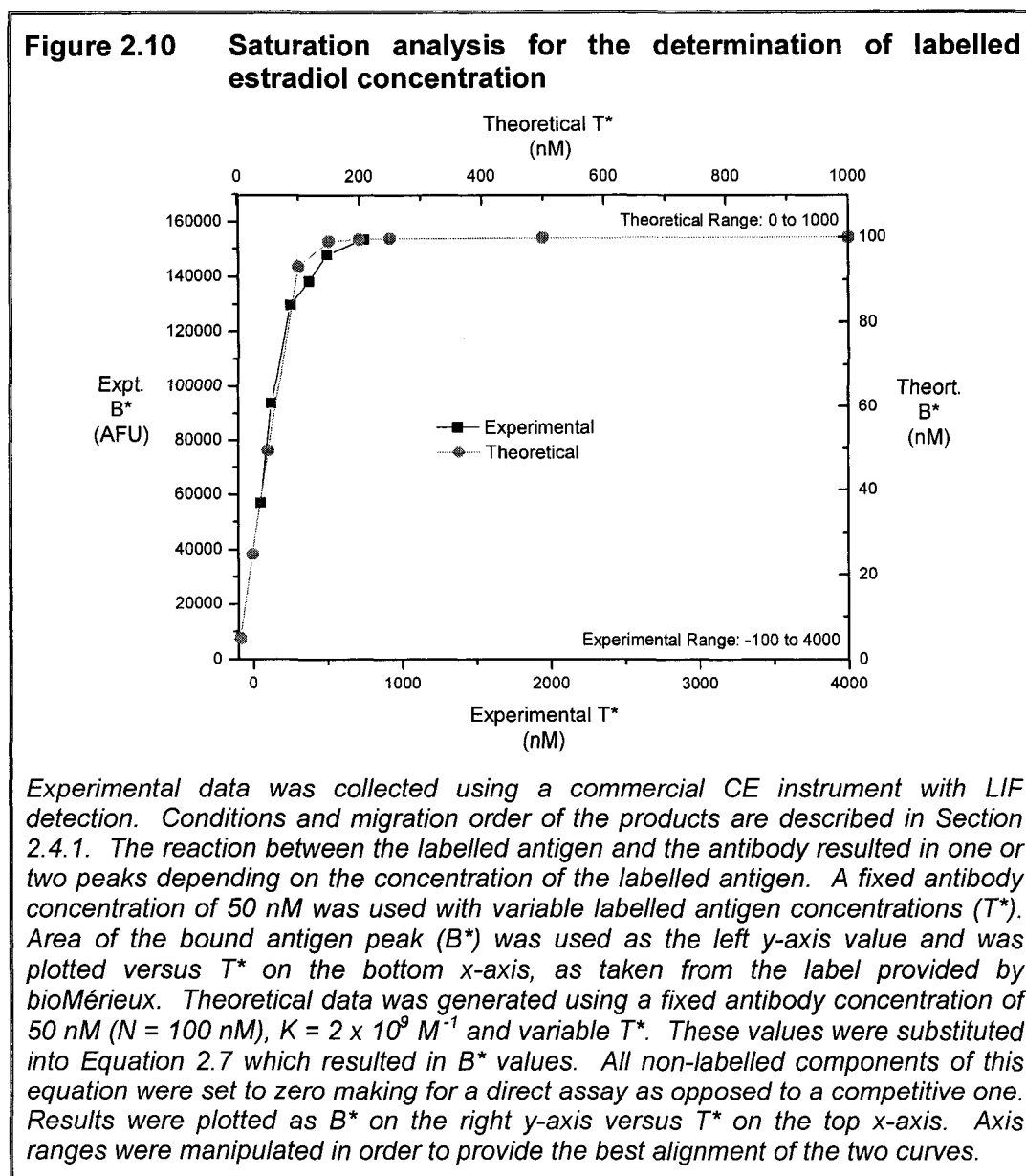
Figure 2.9 MS/MS data of the molecular ion peak for fluorescently labelled estradiol



The molecular ion peak ($m/z = 844$, $[M+H]^+$) was chosen for MS/MS analysis. Cleavage of the oxime N-O bond led to peaks at 559 and 561, for the unreduced and reduced fragment containing the dye and linker, and the complimentary estradiol fragment was seen at 287. Loss of water from 561 led to 543 and loss of both carbonyl groups from 559 resulted in 529. Loss of ethylene from 529 resulted in 503. Cleavage of the dye resulted in 332 and the complimentary linker and estradiol fragment at 513.

At this point, it was postulated that one of the two isomers might be inactive, thereby, reducing the apparent concentration. An attempt was made to immobilize the antibody to examine if a preferential interaction with one of the two isomers occurred. However, the results were inconclusive due to excessive non-specific binding and difficulties with the immobilization process. Using a commercial CE instrument a saturation curve was constructed in order to attempt to extrapolate the true antigen concentration. The curve was generated by holding antibody concentration constant and varying the labelled estradiol concentration, no unlabelled estradiol was used for this experiment. The results

were plotted as labelled estradiol bound (B^*) versus total labelled estradiol (T^*). The curve plateaus when all of the antibody binding sites have been occupied by antigen. The resulting curve is shown in Figure 2.10, as black squares. A theoretical plot was generated using Equation 2.7 and the values presented in the caption to Figure 2.10.



It was suspected that the smaller of the two peaks seen in the LC-MS work was the active isomer and as such, the theoretical data was generated for a labelled estradiol concentration range equal to one quarter of the experimental values. The theoretical curve is plotted as grey circles in Figure 2.10. By overlaying the two curves, it is evident that they correlate well and that the theoretical T^* value is approximately 25% of the experimental value. This confirms the suspicion that the larger of the two peaks seen in the HPLC separation was inactive making the active antigen concentration 25% of the stated value. Hence, this value was used to determine Ag^* concentrations for the study.

2.4.3 THEORETICAL PREDICTIONS FROM THE JACKSON AND EKINS MODEL

In the context of competitive immunoassays, the DL is often defined as the analyte dose resulting in a signal change that is equivalent to three times the standard deviation in the response at zero dose (σ_0). Using this definition and Equation 2.9, predictions can be made as to the theoretical minimum detection limits based on the Jackson and Ekins model. Table 2.2 presents a series of theoretical detection limits for various antibody affinity constants, assuming either a 1% or 3% coefficient of variation. For an affinity constant of $2 \times 10^9 \text{ M}^{-1}$, which is the affinity constant of the antibody studied, a minimum DL of 15-45 pM is predicted.

Table 2.2 Theoretical minimum DLs for competitive immunoassays at various K and CV_o based on the Jackson and Ekins model

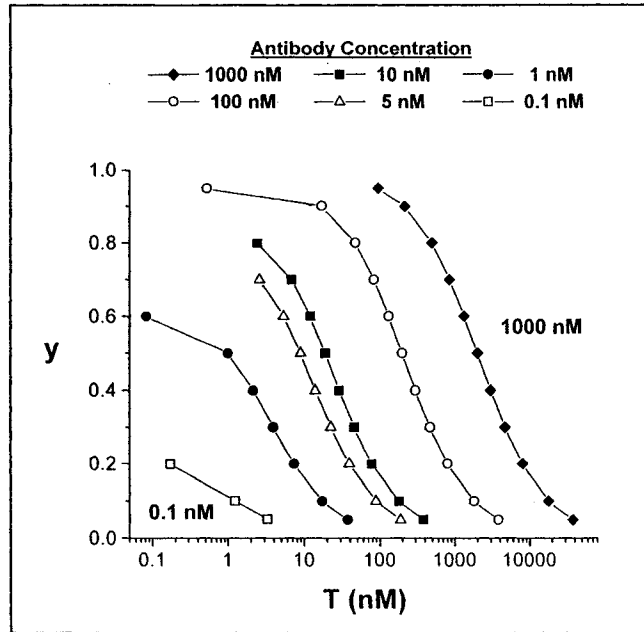
K (M⁻¹)	DL (CV_o = 1%)	DL (CV_o = 3%)
10 ¹²	30 fM	90 fM
10 ¹⁰	3 pM	9 pM
2 x 10⁹	15 pM	45 pM
10 ⁸	300 pM	900 pM
10 ⁷	3 nM	9 nM
10 ⁶	30 nM	90 nM
10 ⁵	300 nM	900 nM

2.4.4 EFFECT OF CONCENTRATION AND AFFINITY ON DETECTION LIMITS

From Equation 2.7 there are three factors which may affect the DL: antibody binding site concentration (N), labelled analyte concentration (T^*) and the affinity constant of the antibody (K). Using Equation 2.7, several theoretical dose-response curves were constructed, in order to demonstrate the effect of each of these parameters. It should be noted that extensive modeling has been done in the past in order to optimize experimental conditions for immunoassays.²¹ However, the majority of this work relies on complex computer simulations which attempt to optimize all parameters simultaneously. The method that we present is much simpler and focuses on each parameter individually, to examine general trends.

Figure 2.11 illustrates the effect of changing the antibody concentration for an antibody with $K = 2 \times 10^9 \text{ M}^{-1}$. All references to antibody concentration refer to intact antibodies and not binding sites. As antibody concentration is lowered the midpoint of the dose-response curve shifts to lower analyte concentrations, making it possible to achieve lower detection limits. However, as we lower the antibody concentration, the dynamic range of the response becomes limited, as is seen for the two traces at the lowest antibody concentrations. Limiting the dynamic range demands a lower standard deviation in order to achieve the same precision. At 1 nM Ab, the response is approximately 60% of the maximum. Hence, use of still lower antibody concentrations may not serve to improve the DL, since the standard deviation that is required for high precision may become experimentally unobtainable.

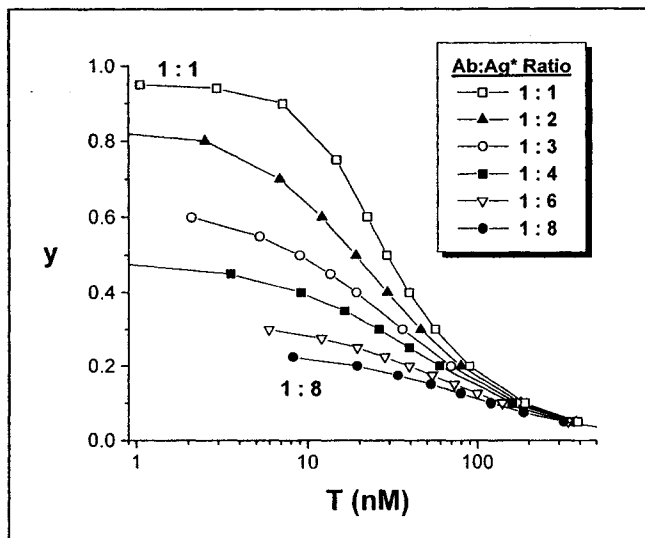
Figure 2.11 Effect of antibody concentration on theoretical dose-response curves



Plot calculated for an antibody with $K = 2 \times 10^9 \text{ M}^{-1}$ and fixed molar Ab:Ag ratio = 1:2. The response, y , is defined as the ratio of bound Ag* to total Ag* and T represents the total analyte concentration. Antibody concentration refers to the intact antibody and not individual binding sites.*

Figure 2.12 illustrates the effect of changing the molar ratio of antibody to labelled analyte, for a fixed concentration of 10 nM intact antibody (corresponding to 20 nM binding sites). As the concentration of the labelled analyte is increased, the dynamic range of the response becomes limited. This result is again undesirable. This same effect was seen experimentally by Ou *et al.*²⁹, using a competitive assay for BSA. However, a second limitation arises at the lowest labelled analyte concentration. The plot of molar ratio 1:1 has a slope that approaches zero in the low T region meaning that the response is relatively insensitive to small changes in analyte concentration. This is obviously undesirable. It was concluded that using an antibody to labelled analyte molar ratio of 1:2 will maximize the dynamic range of response and result in a minimum DL. A molar ratio of 1:2 results in one antibody with two binding sites and two available antigens. It should be noted that an experimental ratio of 1:1.2 was employed. This was due to difficulties in determining an accurate labelled antigen concentration, as was explained in Section 2.4.2.

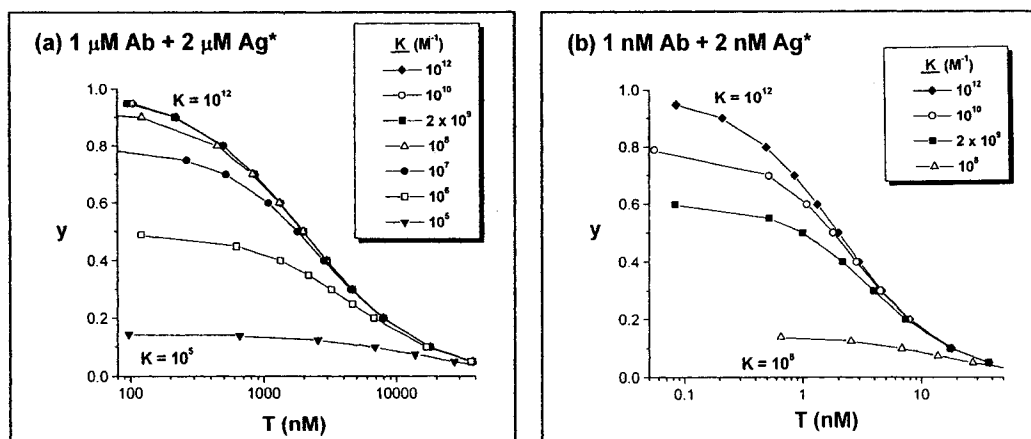
Figure 2.12 Effect of reagent molar ratio (Ab:Ag*) on theoretical dose-response curves



Calculated for an antibody with $K = 2 \times 10^9 \text{ M}^{-1}$ at a fixed antibody concentration of 10 nM. The response, y , is defined as the ratio of bound Ag to total Ag* and T represents the total analyte concentration.*

The effect of the affinity constant on the dose-response curves is significant, although one often has no control over the affinity constant of the antibody to be utilized.^{49,50} Figure 2.13a illustrates the effect of K on the response to analyte, for an antibody concentration of 1 μM . At this concentration, increasing the value of K above 10^8 M^{-1} does not further improve the dynamic range. However, at lower antibody concentrations, the effect of variation in large values of K becomes significant, as is illustrated in Figure 2.13b using 1 nM antibody. Thus, in order to work with low antibody concentrations to improve detection limits, the affinity constant must be high.

Figure 2.13 Effect of K on theoretical dose-response curves



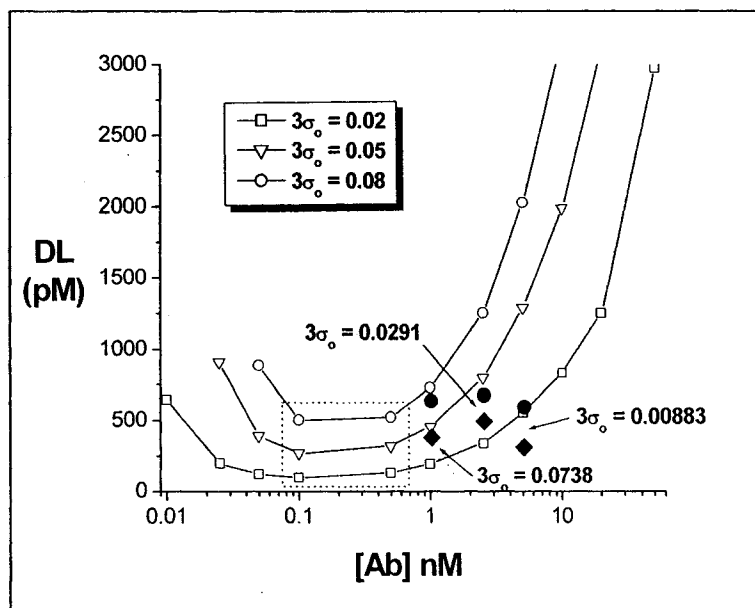
Calculations for (a) 1 μM Ab and 2 μM Ag^* and (b) 1 nM Ab and 2 nM Ag^* . The response, y , is defined as the ratio of bound Ag^* to total Ag^* and T represents the total analyte concentration.

2.4.5 MINIMUM DETECTION LIMIT FROM THE DOSE-RESPONSE FUNCTION

For a given reagent molar ratio and affinity constant, Figure 2.11 shows the DL should be improved by lowering antibody concentration. However, since the RSD of the detection system will increase at lower reagent concentrations, the theoretical DL will not decrease to zero. A minimum theoretical DL can be predicted for specific values of affinity constant, reagent molar ratio and standard deviation. Using a method similar to that used by Rodbard²³, the calculations described below lead to an approximation for the minimum DL. The analysis is based on an affinity constant of $2 \times 10^9 \text{ M}^{-1}$ and Ab to Ag^* molar ratio of 1:2.

Theoretical dose-response data was produced for various different antibody concentrations using Equation 2.7. This data was plotted as response versus analyte concentration and fit with the logistic model, Equation 2.8. Detection limits were calculated for arbitrary values for $3\sigma_0$ using the logistic parameters and Equation 2.11. For these calculations, values for $3\sigma_0$ were chosen to be similar to the experimentally observed values. Results were plotted as DL versus antibody concentration and are shown in Figure 2.14.

Figure 2.14 Theoretical plot of DL as a function of antibody concentration



Calculations were done for three different values of $3\sigma_0$: 0.02 , 0.05 and 0.08. A valency of two was assumed for the Ab:Ag interaction. Conditions for the three traces were: Ab:Ag* = 1:2, $K = 2 \times 10^9 \text{ M}^{-1}$. The dashed box emphasizes the zone of lowest detection limits for these conditions. Solid circles (●) represent the theoretically predicted detection limits presented in Table 2.1, calculated using the experimental conditions (Ab:Ag* = 1:1.2, $K = 2 \times 10^9 \text{ M}^{-1}$). The solid diamonds (◆) show the experimentally determined detection limits. The $3\sigma_0$ values for the experimental results and corresponding theoretical predictions are shown next to the data points.

The resulting plots were U-shaped, where the bottom portion of the “U” indicates the minimum DL. Minimum theoretical detection limits were approximately 125, 300 and 525 pM for $3\sigma_0$ values of 0.02, 0.05 and 0.08 respectively. The U-shaped curves exhibit a broad minimum across a range of antibody concentrations. The range covers approximately one order of magnitude and is highlighted by the dashed box in Figure 2.14. It should be noted that in order to experimentally achieve these detection limits, it is necessary that the indicated standard deviation be achievable within the antibody concentration range of interest (i.e. within the dashed box).

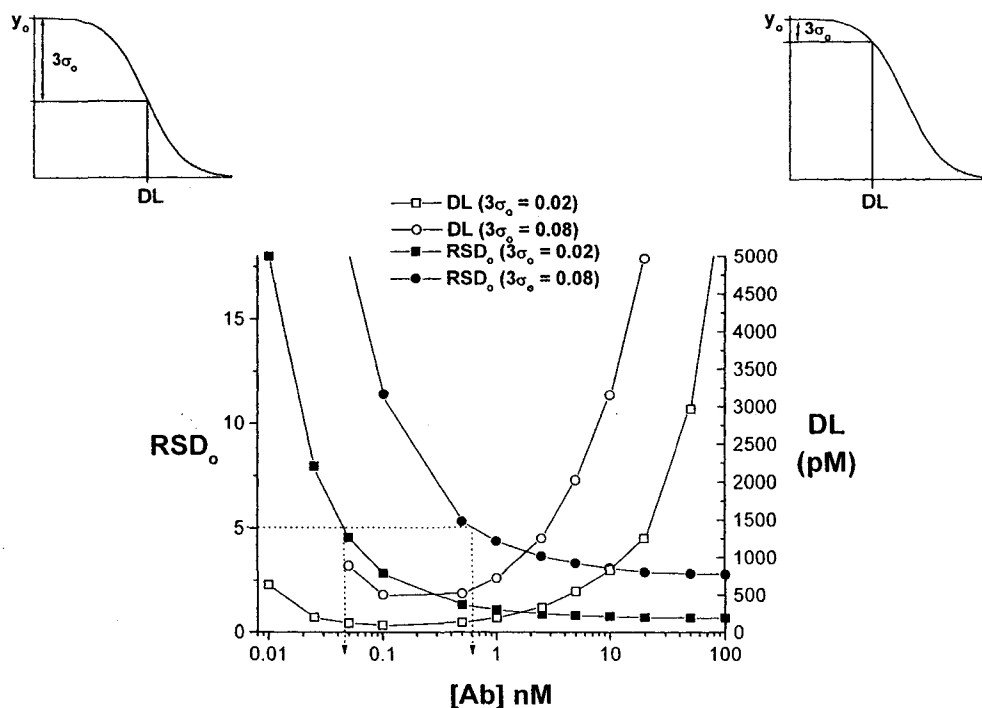
There were two assumptions made in the construction of these curves. First, for any one curve, the value of $3\sigma_0$ was taken to be constant for all antibody concentrations. In reality, $3\sigma_0$ would vary for different antibody concentrations. At higher antibody concentrations σ_0 would decrease to a minimum value most likely limited by pipetting errors.^{19,20} This would allow for a lower DL and shift those data points slightly downwards. Hence, at high antibody concentration the curve would most closely resemble the $3\sigma_0 = 0.02$ curve. Conversely, for lower antibody concentrations σ_0 would increase, thereby shifting the data points slightly upwards, most closely resembling the $3\sigma_0 = 0.08$ curve. One could imagine that if a unique σ_0 was used for each antibody concentration the resulting plot would roughly resemble a collage of the three curves. Our method should provide a reasonable estimate of the ultimate DL and a good guide to optimizing reagent concentrations. As a means of comparison, Ezan *et al.*²², using a similar method with a variable σ_0 , estimated a minimum DL of 200 pM for the same reagent conditions ($K = 2 \times 10^9 \text{ M}^{-1}$ and Ab to Ag* molar ratio of 1:2). The method presented herein is much simpler and although it does make some assumptions, yields an acceptable approximation of minimum DL.

Another point of interest, shown in Figure 2.15, is the fraction of the initial response that is occupied by $3\sigma_0$. At high antibody concentration, $3\sigma_0$ is small when compared to y_0 , as shown by the inset in Figure 2.15. However, at lower antibody concentrations, y_0 becomes smaller and $3\sigma_0$ then occupies a significant fraction of the response. The $3\sigma_0$ value can be manipulated to represent an RSD value by:

$$\text{RSD}_0 = \frac{3\sigma_0}{3y_0} \tag{2.15}$$

The above term can be directly compared to experimental RSD_0 values.

Figure 2.15 Theoretical precision plots of RSD_o as a function of antibody concentration



RSD_o calculations for two values of $3\sigma_o$: 0.02 (■) and 0.08 (●). As a reference the plots of DL from Figure 2.14 are also shown for $3\sigma_o = 0.02$ (□) and $3\sigma_o = 0.08$ (○). These plots were calculated using the same conditions as for Figure 2.14 ($Ab:Ag^ = 1:2$ and $K = 2 \times 10^9 M^{-1}$). A valency of two was assumed for the $Ab:Ag$ interaction. The dashed lines indicate the intersection of the RSD_o plots and the $RSD_o = 5\%$ line. The vertical dashed lines extrapolate to the antibody concentration that should yield 5% RSD_o for a given value of $3\sigma_o$.*

As antibody concentration decreases and $3\sigma_o$ begins to occupy a significant fraction of the response, the RSD_o will increase. Plots of RSD_o vs. antibody concentration are shown in Figure 2.15 for specific values of $3\sigma_o$. Plots of RSD vs. concentration or signal are referred to as precision plots and were pioneered by Ekins.⁵¹ The experimentalist sets a limit as to the maximum RSD that will be accepted. Setting this value to 5%, Figure 2.15 shows that the limiting antibody concentration ranges from 45 to 600 pM depending on the value $3\sigma_o$, as indicated by the dashed lines. Use of antibody concentrations lower than these

limits would lead to unacceptable RSD values. Returning to the dashed box in Figure 2.14, it can be seen that working at the highest antibody concentration within this box will yield the best RSD. Once entering the flat portion of these DL vs. [Ab] curves, there is virtually no improvement in DL on moving to lower antibody concentration, only a rise in RSD.

2.4.6 EXPERIMENTAL VS. THEORETICAL

Experimental and theoretical curves are compared in Figure 2.5, where solid traces represent the logistic fit to the experimental data and dashed lines the logistic fit to the theoretical data obtained from the dose-response function, Equation 2.7. In all cases, the theoretical predictions fit the experimental results reasonably well. There are several factors that could account for the small discrepancies seen. First and foremost, in defining the theoretical dose-response expression, it was assumed that the affinity constants for the labelled and unlabelled analytes were equal. This is likely not true, since the fluorescent label may change the affinity for the antibody-binding pocket. Second, it may be possible that the binding sites are not independent of one another. Lastly, separation of the bound and free fractions will disturb the equilibrium and as a result, some complex dissociation will occur. However, on the basis of the dissociation constant for the antibody ($k_{\text{diss}} = 5.5 \times 10^{-4} \text{ s}^{-1}$, provided by bioMérieux), it was calculated that during the 17 seconds it takes for the complex to migrate to the detector, only 1% of the complex will dissociate.

$$\frac{[AbAg^*]}{[AbAg^*]_0} = e^{-tk_{\text{dissociation}}} = e^{-(20\text{s})(5.5 \times 10^{-4} \text{ s}^{-1})} = 0.989 \quad (2.16)$$

Comparing the theoretical and experimental detection limits in Table 2.1, one can see that in all cases the experimental results were somewhat better than the theoretical predictions, validating the need for experimentation. Possible sources of error in the theory were outlined above. The lowest experimental DL was achieved at the highest antibody concentration, where the RSD was the

lowest. When optimizing experimental conditions in order to achieve low detection limits, it is important to note the synergy between low reagent concentrations and acceptable RSD values. Both the experimental DL (◆) and the theoretical DL (●), as calculated using the experimental conditions, were plotted in Figure 2.14. The theoretical values (●) were calculated for the experimentally employed molar ratio of 1:1.2 and the observed experimental standard deviations, in order to directly compare to the experimental results. These values were not identical to those used to obtain the family of curves shown.

2.5 CONCLUDING REMARKS

We have presented a simple method by which to estimate the theoretical minimum DL for any competitive CEIA. Theoretical dose-response curves were used to optimize experimental conditions. It was determined that low antibody concentration and a reagent molar ratio of 1:2 should lead to a lower DL. However, the limited dynamic range of response seen at low reagent concentrations limits the achievable DL. For any affinity constant and reagent molar ratio, there will be a range of antibody concentrations that lead to a minimum DL. Using three different values for standard deviation, theoretical minimum detection limits, as predicted from the dose-response expression, ranged from 125 to 525 pM, as shown in Figure 2.14. At any given absolute standard deviation, it is advantageous to use the upper limit of the antibody concentration range within the broad minimum observed in DL versus antibody concentration plots in order to achieve the lowest RSD. The analysis of Jackson and Ekins predicts that for a competitive assay using an antibody with $K = 2 \times 10^9 \text{ M}^{-1}$, the theoretical minimum DL should be 15-45 pM. Even using an optimistically low standard deviation with the dose-response function, leading to DL = 125 pM, it was impossible to reach the theoretical minimum detection limits predicted by Jackson and Ekins.¹⁹ This is explained by considering that the Jackson and Ekins predictions are based on a constant relative error that

depends upon an ever decreasing absolute error at lower concentration, which is not experimentally possible. Experimental CEIA results yielded a lowest DL of 310 pM, corresponding to approximately 2100 estradiol molecules passing through the detection zone. At this concentration, the detector noise limited detection, however, we note that simply by increasing the detection volume the concentration DL could have been lowered. Doubling the detection volume by doubling the channel depth would reduce the DL by half. Such a value approaches the predicted theoretical minimum of 125 pM. Furthermore, use of reagent molar ratio of 1:2 as opposed to 1:1.2, should also serve to improve the detection limit somewhat. We have shown that there are some limitations on the possible detection limits of CEIA that arise from the thermodynamic properties of solution-phase assays as well as experimental error. In the present case, detector performance and the small channel volumes ultimately established the DL, but these values are within easy striking distance of the theoretical limits suggested by the dose-response function. We conclude that for assays requiring low detection limits (i.e. hormone assays) a preconcentration step⁵² such as is used in immunosorbent assays, will be necessary in CEIA.

2.6 REFERENCES

- (1) Grossman, P. D.; Colburn, J. C.; Lauer, H. H.; Nielsen, R. G.; Riggin, R. M.; Sittampalam, G. S.; Rickard, E. C. *Anal. Chem.* **1989**, *61*, 1186-1194. "Application of free-solution CE to the analytical scale separation of proteins and peptides"
- (2) Schultz, N. M.; Kennedy, R. T. *Anal. Chem.* **1993**, *65*, 3161-3165. "Rapid immunoassays using CE with fluorescence detection"
- (3) Shimura, K.; Karger, B. L. *Anal. Chem.* **1994**, *66*, 9-15. "APCE: Analysis of recombinant human growth hormone with a fluorescent labelled antibody fragment"
- (4) Bao, J. J. *J. Chromatogr. B* **1997**, *699*, 463-480. "Review: CEIA"
- (5) Heegaard, N. H. H.; Kennedy, R. T. *Electrophoresis* **1999**, *20*, 3122-3133. "Identification, quantitation and characterization of biomolecules by CE analysis of binding interactions"
- (6) Heegaard, N. H. H.; Nilsson, S.; Guzman, N. A. *J. Chromatogr. B* **1998**, *715*, 29-54. "Affinity CE: Important application areas and some recent developments."
- (7) Schmalzing, D.; Buonocore, S.; Piggee, C. *Electrophoresis* **2000**, *21*, 3919-3930. "CE-based Immunoassays"
- (8) Schmalzing, D.; Nashabeh, W. *Electrophoresis* **1997**, *18*, 2184-2193. "CE based Immunoassays: A critical review"
- (9) Heegaard, N. H. H.; Kennedy, R. T. *J. Chromatogr. B* **2002**, *768*, 93-103. "Antigen-antibody interactions in CE"
- (10) Cheng, Y.-F.; Dovichi, N. J. *Science* **1988**, *242*, 562-564. "Subattomole amino acid analysis by CZE and LIF"
- (11) Tao, L.; Aspinwall, C. A.; Kennedy, R. T. *Electrophoresis* **1998**, *19*, 403-408. "On-line competitive immunoassay based on CE applied to monitoring insulin secretion from a single islet of Langerhans"
- (12) Zagursky, R. J.; McCormick, R. M. *BioTechniques* **1990**, *9*, 74-79. "DNA sequencing report - DNA sequencing separations in capillary gels on a modified commercial DNA sequencing instrument"
- (13) Huang, X. C.; Quesada, M. A.; Mathies, R. A. *Anal. Chem.* **1992**, *64*, 967-972. "Capillary array electrophoresis using laser-excited confocal fluorescence detection"
- (14) Zhang, J.; Voss, K. O.; Shaw, D. F.; Roos, K. P.; Lewis, D. F.; Yan, J.; Jiang, R.; Ren, H.; Hou, J. Y.; Fang, Y.; Puyang, X.; Ahmadzadeh, H.; Dovichi, N. J. *Nucleic Acids Res.* **1999**, *27*, E36: i-vii. "A multiple-CE system for small-scale DNA sequencing and analysis"
- (15) Gong, X.; Yeung, E. S. *Anal. Chem.* **1999**, *71*, 4989-4996. "An absorption detection approach for multiplexed CE using a linear photodiode array"
- (16) Cheng, S. B.; Skinner, C. D.; Taylor, J.; Attiya, S.; Lee, W. E.; Picelli, G.; Harrison, D. J. *Anal. Chem.* **2001**, *73*, 1472-1479. "Development of a"

multichannel microfluidic analysis system employing affinity CE for immunoassay"

- (17) Chen, F. T.; Evangelista, R. A. *Clin. Chem.* **1994**, *40*, 1819-1822. "Feasibility studies for simultaneous immunochemical multianalyte drug assay by CE with LIF"
- (18) Wang, Q.; Luo, G.; Ou, J.; Yeung, S. B. *J. Chromatogr. A* **1999**, *848*, 139-148. "Noncompetitive immunoassays using protein G affinity capillary chromatography and CE with LIF detection"
- (19) Jackson, T. M.; Ekins, R. P. *J. Immunol. Methods* **1986**, *87*, 13-20. "Theoretical limitations on immunoassay sensitivity"
- (20) Keilacker, H.; Besch, W.; Woltanski, K. P.; Diaz-Alonso, J. M.; Kohnert, K. D.; Ziegler, M. *Eur. J. Clin. Chem. Clin. Biochem.* **1991**, *29*, 555-563. "Mathematical modelling of competitive labelled-ligand assay systems"
- (21) Yanagishita, M.; Rodbard, D. *Anal. Biochem.* **1978**, *88*, 1-19. "Computerized optimization of radioimmunoassays for hCG and estradiol: An experimental evaluation"
- (22) Ezan, E.; Tiberghien, C.; Dray, F. *Clin. Chem.* **1991**, *37*, 226-230. "Practical method for optimizing radioimmunoassay detection and precision limits"
- (23) Rodbard, D. *Anal. Biochem.* **1978**, *90*, 1-12. "Statistical estimation of the minimal detectable concentration ("sensitivity") for radioligand assays"
- (24) Ohmura, N.; Lackie, S. J.; Saiki, H. *Anal. Chem.* **2001**, *73*, 3392-3399. "An immunoassay for small analytes with theoretical detection limits"
- (25) Hage, D. S.; Thomas, D. H.; Chowdhuri, A. R.; Clarke, W. *Anal. Chem.* **1999**, *71*, 2965-2975. "Development of a theoretical model for chromatographic-based competitive binding immunoassays with simultaneous injection of sample and label"
- (26) Campfield, L. A. "Mathematical Analysis of Competitive Protein Binding Assays" In *Principles of Competitive Protein-Binding Assays*, 2 ed.; Eds.: Odell, W. D., Franchimont, P.; John Wiley & Sons, Inc.: New York, USA, 1983, pp 125-148.
- (27) Christopoulos, T. K.; Diamandis, E. P.; Grojtan, H. E.; Keel, B. A. "Chapter 3 - Theory of Immunoassays" In *Immunoassay*; Eds.: Diamandis, E. P., Christopoulos, T. K.; Academic Press: San Diego, 1996, pp 25-92.
- (28) Tiberghien, C.; Dray, F. "3.3.1 Competition Methods" In *Methods of Immunological Analysis*; Eds.: Masseyeff, R. F., Albert, W. H., Staines, N. A.; VCH Publishers Inc.: New York, USA, 1993; Vol. 1, pp 214-227.
- (29) Ou, J. P.; Wang, Q. G.; Cheung, T. M.; Chan, S. T. H.; Yeung, W. S. B. *J. Chromatogr. B* **1999**, *727*, 63-71. "Use of CE-based competitive immunoassay for a large molecule"
- (30) Wang, Y. C.; Su, P.; Zhang, X. X.; Chang, W. B. *Anal. Chem.* **2001**, *73*, 5616-5619. "Enhancement of the sensitivity of a CEIA for estradiol with LIF based on a fluorescein-labeled secondary antibody"

- (31) Su, P.; Wang, Y. C.; Zhang, X. X.; Sun, L.; Chang, W. B. *Anal. Chim. Acta.* **2000**, *418*, 137-143. "Thermally reversible hydrogel modified CEIA of estradiol with LIF detection"
- (32) Giese, R. W. *J. Chromatogr. A* **2003**, *1000*, 401-412. "Measurement of endogenous estrogens: Analytical challenges and recent advances"
- (33) Lopez del Alda, M. J.; Barcelo, D. *Fresenius J. Anal. Chem.* **2001**, *371*, 437-447. "Review of analytical methods for the determination of estrogens and progestogens in waste waters"
- (34) England, B. G.; Parsons, G. H.; Possley, R. M.; McConnell, D. S.; Midgley, A. R. *Clin. Chem.* **2002**, *48*, 1584-1586. "Ultrasensitive semiautomated chemiluminescent immunoassay for estradiol"
- (35) Ohmura, N.; Tsukidate, Y.; Shinozaki, H.; Lackie, S. J.; Saiki, H. *Anal. Chem.* **2003**, *75*, 104-110. "Combinatorial use of antibody affinities in an immunoassay for extension of dynamic range and detection of multiple analytes"
- (36) Raab, G. M. *Clin. Chem.* **1983**, *29*, 1757-1761. "Comparison of a logistic and a mass-action curve for radioimmunoassay data"
- (37) Bettsworth, F.; Monnet, C.; Watelet, B.; Battail-Poirot, N.; Gilquin, B.; Jolivet, M.; Menez, A.; Arnaud, M.; Ducancel, F. *J. Mol. Recog.* **2001**, *14*, 99-109. "Functional characterization of two anti-estradiol antibodies as deduced from modelling and site-directed mutagenesis experiments"
- (38) Monnet, C.; Bettsworth, F.; Stura, E. A.; Le Du, M.-H.; Ménez, R.; Derrien, L.; Zinn-Justin, S.; Gilquin, B.; Sibai, G.; Battail-Poirot, N.; Jolivet, M.; Ménez, A.; Arnaud, M.; Ducancel, F.; Charbonnier, J. B. *J. Mol. Biol.* **2002**, *315*, 699-712. "Highly specific anti-estradiol antibodies: Structural characterisation and binding diversity"
- (39) Seiler, K.; Harrison, D. J.; Manz, A. *Anal. Chem.* **1993**, *65*, 1481-1488. "Planar glass chips for CE: Repetitive sample injection, quantitation, and separation efficiency"
- (40) Ocvirk, G.; Tang, T.; Harrison, D. J. *Analyst* **1998**, *123*, 1429-1434. "Optimization of confocal epifluorescence microscopy for microchip-based μ -TAS"
- (41) Fan, Z. H.; Harrison, D. J. *Anal. Chem.* **1994**, *66*, 177-184. "Micromachining of CE injectors and separators on glass chips and evaluation of flow at capillary intersections"
- (42) Righetti, P. G.; Caravaggio, T. *J. Chromatogr.* **1976**, *127*, 1-28. "Isoelectric points and molecular weights of proteins: A table"
- (43) Layne, E. *Methods Enzymol.* **1957**, *3*, 447. "Spectrophotometric and turbidimetric methods for measuring proteins"
- (44) Bradford, M. *Anal. Biochem.* **1976**, *72*, 248-254. "Rapid and sensitive method for quantitation of microgram quantities of protein utilizing principle of protein-dye binding"
- (45) Cole, J. L.; Hansen, J. C. *J. Biomol. Tech.* **1999**, *10*, 163-176. "Analytical ultracentrifugation as a contemporary biomolecular research tool"

- (46) Gray, R. A.; Stern, A.; Bewley, T.; Shire, S. J. *Beckman Application Information Monograph* **1995**, "Rapid determination of spectrophotometric absorptivity by analytical ultracentrifugation", A-1821A
- (47) Laue, T. M. *Beckman Application Information Monograph* **1996**, "Choosing which optical system of the Optima™ XL-I analytical ultracentrifuge to use", A-1821A
- (48) Van Holde, K. E. In *Physical Biochemistry*; Prentice Hall, Inc.: Englewood Cliffs, NJ, 1971, pp 94-95.
- (49) O'Conner, T.; Gosling, J. P. *J. Immunol. Methods* **1997**, *208*, 181-189. "The dependence of radioimmunoassay detection limits on antibody affinity"
- (50) O'Conner, T.; Gosling, J. P. *Biochem. Soc. Trans.* **1998**, *26*, 104. "Antibody affinity and the detection limit of solid-phase enzyme immunoassay"
- (51) Ekins, R. P. In *Radioimmunoassay*; Ed. Bizollon, C. A.; Elsevier North Holland Biomedical Press: Amsterdam, 1979, pp 239-255.
- (52) German, I.; Kennedy, R. T. *Anal. Chem.* **2000**, *72*, 5365-5372. "RP capillary LC coupled on-line to CEIA"

CHAPTER 3: DESIGN OF A MUTIPLICED PLATFORM FOR PROTEOMICS

3.1	INTRODUCTION	77
3.2	PROJECT GOALS.....	78
3.3	CHIP DESIGN	78
3.3.1	SAMPLE INTRODUCTION – ELECTRICAL FRACTIONATION AREA	79
3.3.2	BED REGION	81
3.3.2.1	BOTTOM WAFER.....	81
3.3.2.2	TOP WAFER.....	81
3.3.3	VARIABLE REGION	84
3.3.4	COLLECTION REGION.....	86
3.3.5	SINGLE CHANNELS	86
3.3.5.1	BOTTOM WAFER.....	86
3.3.5.2	TOP WAFER.....	86
3.3.6	CHANNEL WIDTH	88
3.3.7	MATERIALS AND METHODS - FABRICATION DETAILS.....	95
3.4	HOLDER AND FLUIDIC INTERFACES.....	98
3.5	ELECTRICAL FRACTIONATION SYSTEM.....	102
3.6	ESI INTERFACE.....	104
3.7	FINAL PLATFORM	111
3.8	REFERENCES	114

3.1 INTRODUCTION

As the field of proteomics continues to expand, a greater stress is placed on the search for analytical techniques with which to process the massive amount of samples generated. The conventional approach to this problem is extremely time consuming and laborious as was outlined in the introduction of this thesis. The question arises as to how this process might be streamlined to increase sample throughput. Several approaches to this problem have been suggested and in this thesis, microfluidics has been studied as a potentially useful method. As mentioned previously, the basis for protein analysis relies on being able to efficiently and precisely separate a mixture of proteins or peptides. For proteins this is most effectively accomplished using 2D-GE.^{1,2} The major disadvantage of this technique is the immobilization of the proteins in the gel, which adds several post-separation processing steps to the overall procedure. If this separation could be achieved while allowing the proteins to remain in solution, a great reduction in sample preparation time would be achieved. Separation by isoelectric point is easily accomplished in solution-phase via CIEF and separation by mass via solution-phase methods can be achieved using size exclusion chromatography. Several research groups have explored various solution-phase separation techniques in an attempt to replace 2D-GE, as was outlined in the introductory chapter. The approach undertaken by this research group was to use CIEF as the first dimension of protein separation and couple this to a fraction collector. Each fraction was to undergo protein digestion and peptide concentration followed by MS analysis. Fractionation, digestion, concentration and sequential injection into the MS was to be done on-chip. In this first attempt, it was assumed that the high resolving powers of the mass spectrometer would function as the mass separation step. If a single fraction were to contain several proteins, the peptides could be analyzed by tandem MS/MS in order to identify the parent proteins.³ Research done in this lab only has the capabilities of single quadrupole MS, however, in theory this analysis could be done by the much more sophisticated tandem MS approach.

3.2 PROJECT GOALS

The focus of this project was to design a multiplexed microfluidic based platform for use in proteomics. This project was an extension of work done previously in our lab involving a single channel proteomic platform.^{4,5} The overall design was to include the following:

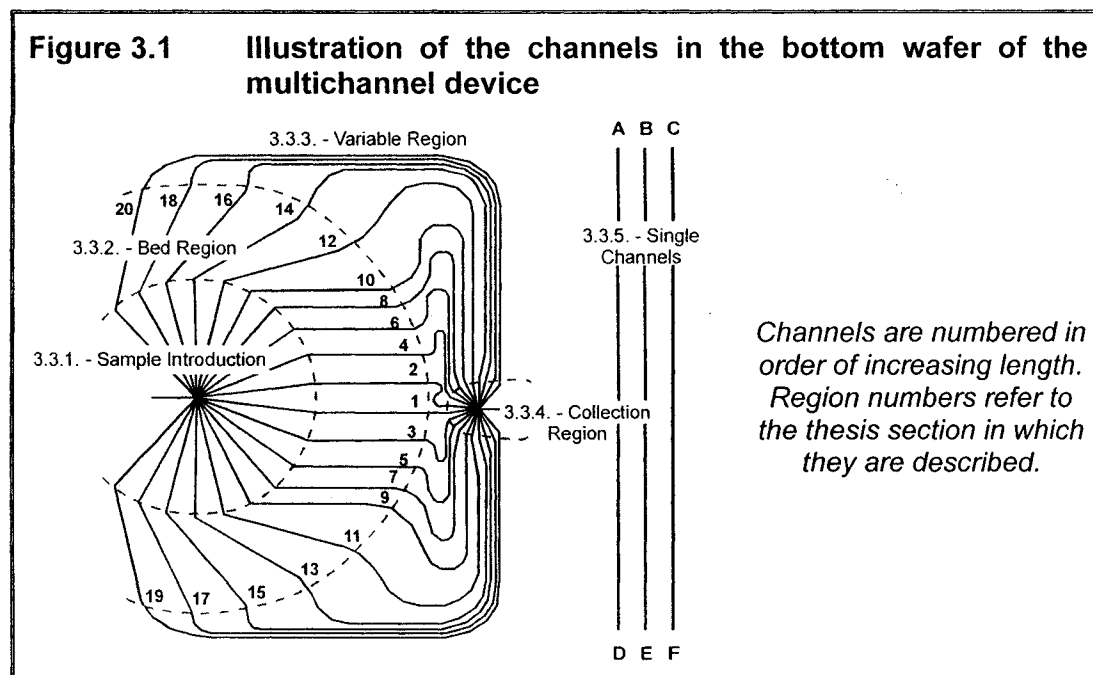
- An inlet capillary to be used for CIEF
- A means by which to fractionate the incoming flow into 20 separate channels within the microchip
- A digestion column or “bed” containing immobilized trypsin beads for protein digestion
- A SPE bed containing a C₁₈ phase for peptide concentration
- A means by which to sequentially elute the peptides from each SPE bed
- A chip-ESI interface allowing for MS detection of the resulting peptides

There were several design challenges that needed to be met in order to allow this platform to function. Each issue is addressed separately below.

3.3 CHIP DESIGN

The first issue addressed was the design of the microchip. The chip was to have a single inlet, 20 parallel channels and a single outlet. The bottom wafer of the device contained the main channel network that comprised the flow path for the multichannel chip, as well as several straight single channels. Two beds were incorporated into each flow path for protein digestion and peptide preconcentration. Continuing from Can Wang's previous work in this lab, the beds were located in the cover plate of the device.⁴ Short, deep channels were etched into the top wafer such that they could be aligned with the bottom wafer,

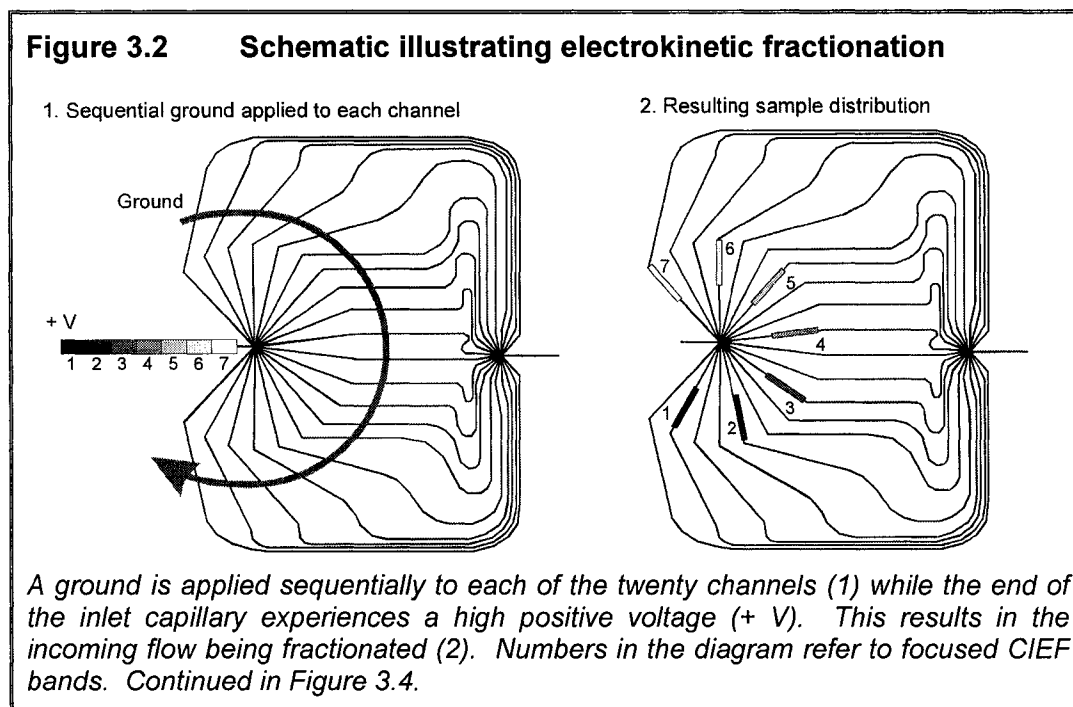
allowing the beds to sit over top of the channels in the bottom wafer. By packing the bed with beads that were larger than the channels on the bottom wafer, the beads were effectively trapped in the bed. From this point, the wafer containing the channel network will be referred to as the bottom wafer and the wafer containing the beds and the access holes will be referred to as the top. The finished bottom wafer design is shown in Figure 3.1. Each region will be discussed in detail.



3.3.1 SAMPLE INTRODUCTION – ELECTRICAL FRACTIONATION AREA

The inlet of the microchip was to be coupled to a CIEF column used in single-step mode, such that the proteins would be simultaneously focused and mobilized. Fractionation of the incoming flow was achieved on-chip using electrokinetic effects. Simply, the end of the inlet capillary experienced a high positive voltage while one of the channels on the chip was at ground, creating a net flow of solution from the capillary on to the chip, driven by electroosmotic forces. In order to accomplish this it was necessary to sequentially apply a ground to each of the twenty channels. In sequence, flow would move from the

capillary into channel 1 which was held at ground, the ground was then switched to channel 2 and flow was introduced into that channel, and so on. Using this method, the incoming flow from the capillary was fractionated into the twenty channels on-chip. This is illustrated in Figure 3.2.



In order for the fractionation process to occur identically in each channel the flow paths must have the same electrical resistance. This was most easily accomplished by placing the electrical contacts for each channel on the radius of a circle with the inlet at the approximate center, ensuring that the channels lengths were equal. This concept is illustrated in Figure 3.1, where the innermost dashed circular line marks the ends of the individual arms. The radius for the circle was limited by the spacing between the ends of the arms which needed to be far enough apart to allow for drilling. It was assumed that the reservoirs would be approximately 1 mm in diameter and a spacing of at least 5mm between reservoirs was desirable to avoid any problems with the glass cracking during the drilling process. A radius of 2 cm provided adequate separation between the ends of the arms. The actual reservoirs, which were located at the head of the

first bed, were placed 5 mm further down the flow path from the end of the introductory radius, as shown in Figure 3.3. This was done because space allowed for it.

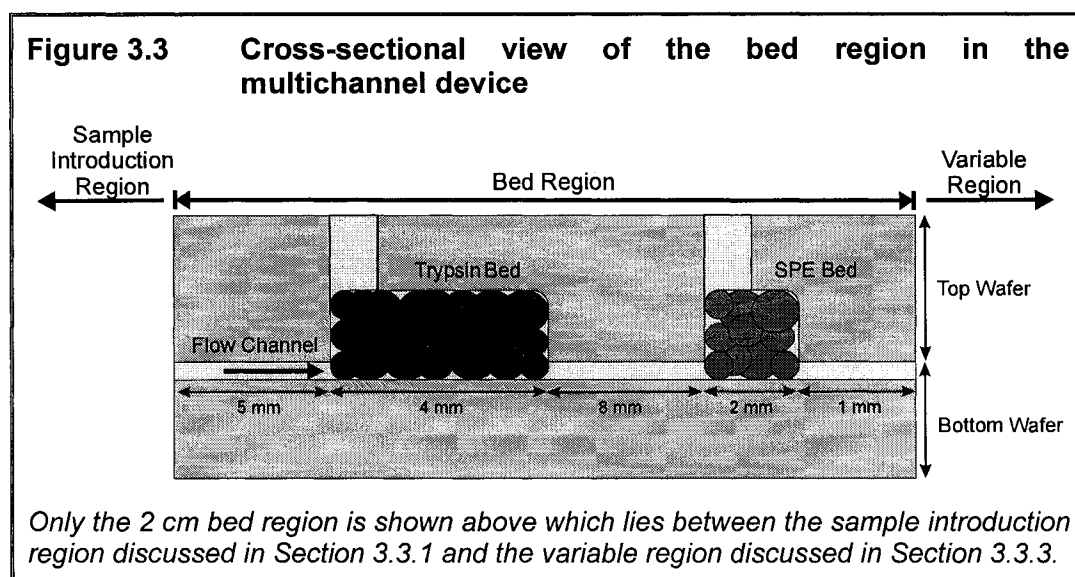
3.3.2 BED REGION

3.3.2.1 BOTTOM WAFER

Since the beds were etched into the top wafer, this region in the bottom wafer simply consisted of a straight channel long enough to accommodate the lengths of the beds that would sit above. A length of 2 cm easily accommodated the initial bed lengths that were to be used and allowed some leeway should we decide to use variable bed lengths or insert additional beds in the future. This region is shown in Figure 3.1 and is referred to as “3.3.2 – Bed Region”.

3.3.2.2 TOP WAFER

Work done previously on a single channel device served as the basis for the determination of bed volumes.⁵ As described previously, the beds were etched in the top wafer and aligned with the flow channels in the bottom wafer. A cross section of the bed region is shown in Figure 3.3 to illustrate this concept. The cross sectional view illustrates the problem with this design. Since the incoming flow enters the bottom of the bed from a relatively small cross-sectional area, problems with flow distribution throughout the bed were expected. A similar design was recently modeled and sample bands passing through the structure were seen to experience a significant amount of dispersion.⁶ Previous work on the single channel device was successful despite this potential problem and hence this method was used in this project. It was understood that this may lead to more diffuse analyte peaks, thereby reducing detection sensitivity.



In previous work, the single channel trypsin digestion bed had a volume of 1.214 μL and the SPE bed, 0.441 μL .⁵ For the SPE bed, it was determined that 0.15 mg of beads were needed to fill the 0.441 μL bed. As stated by the manufacturer (Oasis® HLB Plus, 60 μm , #1860001323, Waters), 18 μg of protein digest would be concentrated by 0.5 mg of beads. Hence, the single channel chip has the potential to concentrate 5.4 μg of protein digest. The beds on the multichannel device were intended to handle an incoming CIEF separation and as such it was required that all twenty beds hold enough beads to concentrate all of the CIEF column proteins. If the entire CIEF column holds a maximum of 10 μg of protein (an overestimate, 10 times greater than predicted⁷), each bed should be able to concentrate 0.5 μg of protein digest, assuming that the incoming flow is distributed evenly. This is not always the case, as some fractions may contain more proteins than others depending on the CIEF separation. From these considerations, each SPE bed on the multichannel device could be 10 times smaller than the single channel SPE bed. However, reduction of the bed volume may induce packing issues due to the relatively large size of the beads (60 μm diameter), leading to some of the beds exhibiting lower activity. On the basis of the above two points, the final SPE bed mask width was 400 μm with a bed

length of 2 mm. Protein digest capacities are listed in Table 3.1 as a function of etch depth.

Table 3.1 Empty SPE bed volumes and protein digest concentration capacity

Etch Depth (μm)	Cross Section Area (μm^2)	Bed Volume (μL)	Bead Capacity (mg)	Protein Digest Capacity (μg)
100	55,708	0.111	0.0379	1.36
125	74,544	0.149	0.0507	1.82
150	95,343	0.191	0.0648	2.33

These values would be sufficient for our needs.

For the trypsin beds, a length of 4 mm and a 400 μm mask width was used for the multichannel device. The manufacturer of the trypsin beads (Immobilized TPCK Trypsin, 20230, Pierce Chemical Company) suggested that 0.1 – 0.25 mL of beads be used per mg of protein to be digested. If we assume that the volume of the bed is equivalent to the volume of beads used, values for maximum protein load can be calculated based on etch depth. The resulting values are presented in Table 3.2.

Table 3.2 Empty trypsin bed volumes and protein digestion capacity

Etch Depth (μm)	Cross Section Area (μm^2)	Bed Volume (μL)	Protein Capacity (μg)
100	55,708	0.223	0.891 – 2.23
125	74,544	0.298	1.19 – 2.98
150	95,343	0.381	1.53 – 3.81

It should be noted that all bed volumes presented in this section are the result of volume calculations assuming a “D” shaped channel cross-sectional area due to the isotropic etching of the glass. The etching process results in an aspect ratio of 1:1 meaning, that the channel is etched equally in all directions resulting in a “D” shaped cross-section with the curved sections forming quarter circles on each side with a radius equal to the etch depth. The cross-sectional area can be calculated using Equation 3.1.

$$A = wd + \frac{1}{2}\pi d^2 \quad (3.1)$$

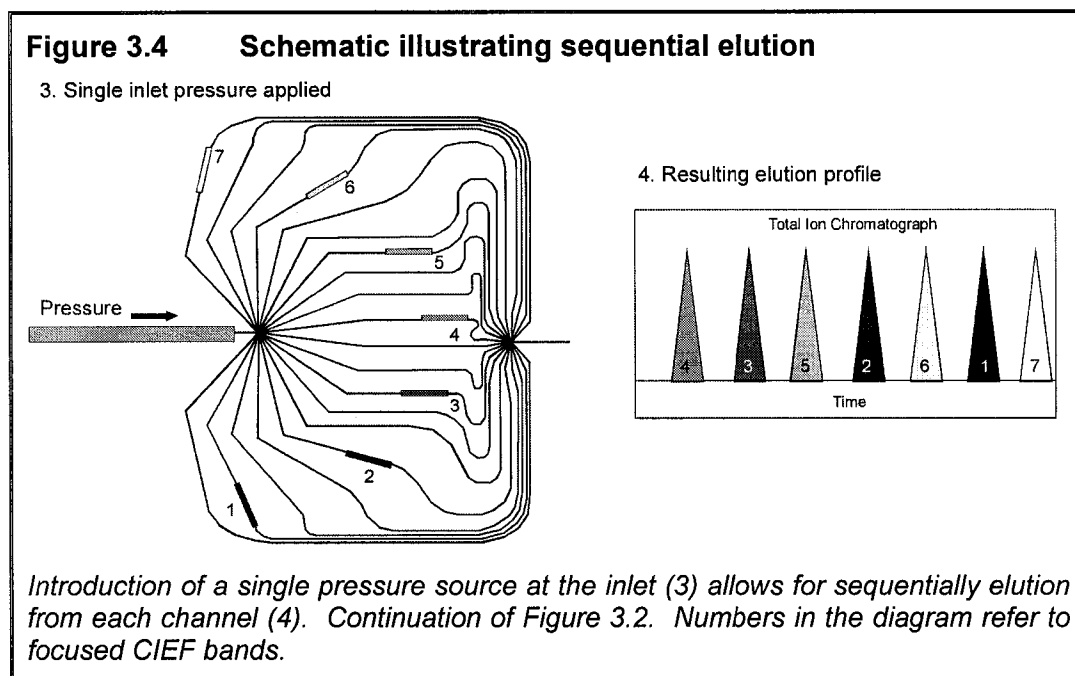
where A is the cross sectional area of the etched channel, w is the mask width and d is the etch depth. The aforementioned volume calculations do not take into account the longitudinal etching that would extend the length of the bed by isotropically etching outwards. A calculation showed this additional volume to be negligible. The additional volume added by the access reservoirs, shown in Figure 3.3, was not included in the bed volume calculation, as it was expected that this region would not contain beads.

One can see that the capacity of the trypsin and SPE beds are compatible with each other and readily able to accept 1/20 to 1/10 of an estimated total 10 μg protein sample. The exact positions of the beds with respect to the straight channel on the bottom wafer are illustrated in Figure 3.3. These positions were chosen arbitrarily.

3.3.3 VARIABLE REGION

Work done on the single channel device incorporated a CE separation of the resulting peptides after digestion, prior to MS detection. Early in the design process, it was determined that incorporating a CE separation following the peptide concentration step would be too challenging to design and test within the first multichannel prototype. Incorporating injectors and separation channels of equal length, having already mapped out space for sample introduction, digestion and preconcentration beds proved complicated. It can be assumed that the high resolving power of a tandem mass spectrometer should overcome the need for a CE peptide separation. This assumption is valid provided that an accurate and unique peptide mass can be determined and that the parent protein is entered in a database.^{3,8-10} The reader is directed to the introductory chapter for a discussion of these issues. Thus, it was concluded that flow following the SPE elution step should be pressure driven towards the MS. A delay line was used to

facilitate the sequential introduction of each channel into the MS using a single pressure source. This was accomplished by varying channel length, such that each channel was longer than the previous. Hence, when a single pressure was applied at the inlet of the sealed system, the result was sequential introduction of each of the 20 channels, from shortest to longest, to the MS. This concept is illustrated in Figure 3.4 (a continuation of Figure 3.2).



Numbers in Figure 3.4 refer to focused CIEF bands and are not related to channel length. Channels were numbered in order of their length in Figure 3.1. The size of the wafer (4" x 4") ultimately limited the length of the longest channel. A length difference of 0.5 cm between channels was most compatible with the wafer size. For channel #1, as defined in Figure 3.1, the distance from the bed region to the collection region was 0.25 cm, for channel #2 it was 0.75 cm, channel #3: 1.25 cm and so on to channel #20 which had a variable region length of 9.75 cm. Time delay calculations, which were dependent on the delay line as well as channel cross-section, are presented in Section 3.3.6.

3.3.4 COLLECTION REGION

Flow from the 20 channels was united at the outlet of the device, which leads to the MS. The same radius concept was used for collection as was outlined in Section 3.3.1 for sample introduction. This ensured that only the variable region, located between the packed beds and the outlet “star”, altered the length of each flow path. An arbitrary radius of 5 mm was chosen for this collection region.

3.3.5 SINGLE CHANNELS

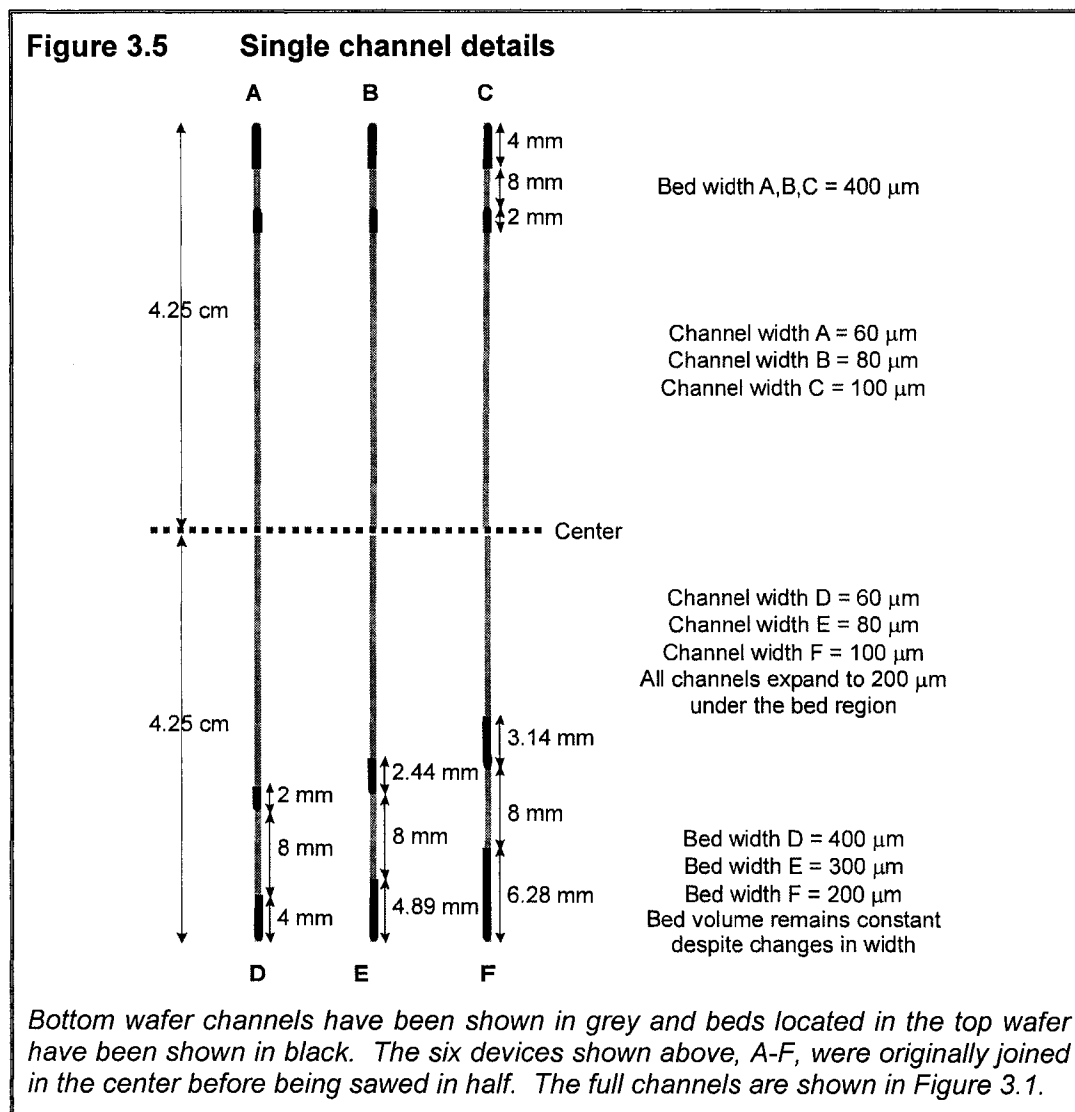
3.3.5.1 BOTTOM WAFER

In order to explore the behaviour of the isolated bed region, three single straight channels (right side of Figure 3.1) were incorporated into the bottom wafer to serve as single channel devices. The channels were 8.5 cm long with the expectation that they be sawed in half to be used as six separate devices. The six devices have been labelled as A-F in Figure 3.1 and the pertinent details of each individual device are shown in Figure 3.5. Devices A, B and C have mask widths of 60, 80 and 100 μm , respectively, on the bottom wafer. Devices D, E and F start from the center with the same mask widths as A, B and C, but widen to 200 μm at the bed-end of the device. The widening occurs over 0.5 cm starting 1.25 cm from the center. The remaining 2.5 cm are straight at 200 μm . It was suspected that this would allow for a more uniform distribution of sample throughout the packed bed.

3.3.5.2 TOP WAFER

Several different bed designs were incorporated into the single channels to allow for testing of certain parameters. Devices A, B and C had the same bed parameters as the multichannel device, only the width of the channels in the bottom wafer varied. Beds in devices D, E and F varied quite substantially as shown in Figure 3.5. In the three devices the beds have been designed to hold

the same volume despite changes in bed width. This was accomplished by increasing the bed length while making the bed narrower. Exact volumes depend on the etch depth used.



3.3.6 CHANNEL WIDTH

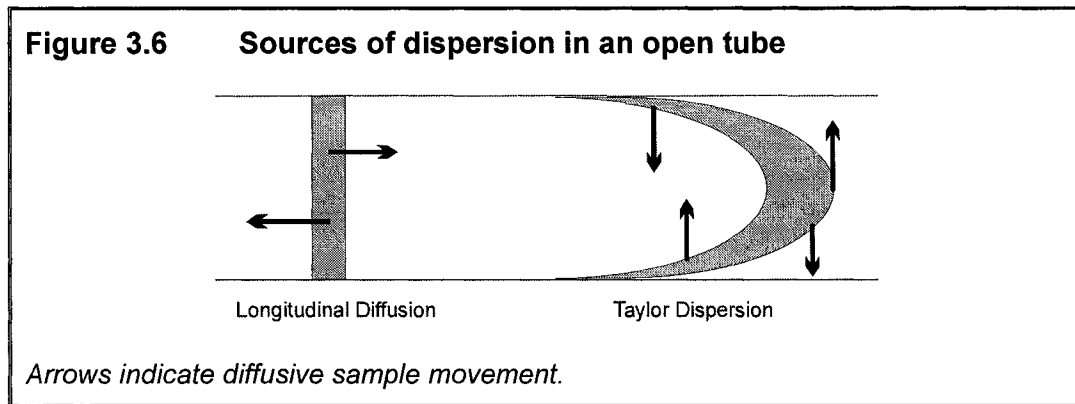
Determining the channel width to define on the optical mask took careful consideration. Having already set the delay line length to 0.5 cm, the time delay was now a function of cross-sectional area and flow rate. The experimental channel cross-section is adaptable even after mask fabrication by changing the etch depth defined during fabrication. Thus, a mask channel width was defined that would allow leeway in both directions. Considering that the inlet flow rate would need to be compatible with the ESI interface (inlet flow rate = outlet flow rate), a range of 0.1 to 0.5 $\mu\text{L}/\text{min}$ was considered. The flow within each individual channel would be 1/20 of the total flow at the inlet, assuming that the inlet flow is distributed evenly to each of the twenty channels. Since the channels vary in length, it is expected that the longest channel should have a higher resistance to flow and hence the inlet flow should not be distributed evenly. However, it was assumed that the effects of the packed bed at the beginning of each flow channel would dominate flow resistance and thereby the effects of the variable channel lengths following this region would be negligible. This issue will be explored further in Section 5.5. Using a volumetric flow rate equal to 1/20 of the incoming flow and the volume defined by the cross-sectional area of the channel multiplied by 0.5 cm (the delay line length), time delays were calculated and the results are presented in Table 3.3. The time delay represents the time between eluting peaks from each of the twenty channels, assuming an equal flow rate in all channels. Cross sectional areas were calculated assuming a D-shaped cross-section as defined by Equation 3.1. A mask width of 60 μm was chosen since a time delay of 44 s between eluting fractions at an inlet flow rate of 0.25 $\mu\text{L}/\text{min}$ served as a good starting point. Furthermore, the cross-sectional area of a channel with a mask of 60 μm , etched to a depth of 20 μm , matches well with the cross-section of a 50 μm i.d. capillary. The importance of this will be discussed in Section 3.6.

Table 3.3 Delay line calculations

Mask Width = 60 μm		Time Delay at Various Inlet Flow Rates (s)		
Etch Depth (μm)	Cross Section Area (μm^2)	0.1 $\mu\text{L}/\text{min}$	0.25 $\mu\text{L}/\text{min}$	0.5 $\mu\text{L}/\text{min}$
10	757	45.4	18.2	9.08
20	1828	110	43.9	21.9
30	3214	193	77.1	38.6
Mask Width = 80 μm				
10	957	57.4	23.0	11.5
20	2228	134	134	26.7
30	3814	229	91.5	45.8

As a means of visualization, a theoretical plot was generated to illustrate the effects of diffusion and the time delay. The resulting plot is a representation of what would be seen at the end of the variable region, at the collection “star”, as each channel undergoes sequential elution. The sample in channel 1 only travels a distance of 0.25 cm before reaching the collection “star” whereas the sample in channel 20 must travel 9.75 cm before reaching the “star”. The following section explores the effect this variable travel distance has on the sample plug.

As a pressure driven sample plug travels down an open channel, it will undergo dispersion. Two processes dominate dispersion in an open tube. The first is longitudinal diffusion which is the diffusion of molecules in the lengthwise direction of the channel as they move down the tube. The second is Taylor dispersion which involves the movement of molecules in the other two dimensions of the channel, across the flow stream lines of the parabolic concentration profile induced by pressure mobilization. The variation of velocities also causes a dispersion of the sample. The two processes are illustrated in Figure 3.6.



The width of the sample plug at any point in time is defined by Equation 3.2.¹¹

$$\sigma_x^2 = 2kt \quad (3.2)$$

Where σ_x^2 is the sample peak variance, k is the effective dispersivity of the sample and t is time for dispersion to occur. The effects of both dispersion processes are included in k . The square root of the variance is referred to as standard deviation. For a Gaussian peak, the width at 60.7% of the maximum peak height is 2σ . By taking tangents to the inflection points of a Gaussian curve, the peak can be approximated by a triangle. The base of this triangle will be 4σ . The result of Equation 3.2 is a length based variance value. In order to convert this to a time value, σ_t^2 , Equation 3.3 is used.¹¹

$$\sigma_t^2 = \frac{\sigma_x^2 t^2}{L^2} = \frac{2kt^3}{L^2} \quad (3.3)$$

The length of the channel is defined by L . Furthermore, t can be defined by the volume of the channel (V) divided by the volumetric flow rate (F). The volume is further defined as cross-sectional area (A) multiplied by length (L), leading to Equation 3.4.

$$\sigma_t^2 = \frac{2kA^3L}{F^3} \quad (3.4)$$

Equation 3.4 can be used to calculate theoretical peak widths based on channel cross-section, channel length and volumetric flow rate. The implication of Equation 3.4 is that as L increases, so does peak width and hence, the peaks that travel further will be more diffuse. The effective dispersivity has been defined for flow in a tube as shown in Equation 3.5.¹²

$$k = D \left[1 + \frac{1}{48} \left(\frac{Ur}{D} \right)^2 \right] \quad (3.5)$$

Where D is the molecular diffusion coefficient, U is the average linear velocity and r is the tube radius. A more general solution to this equation was also presented for any channel geometry as shown in Equation 3.6.¹³

$$k = D \left[1 + \frac{1}{210} \left(\frac{Ud}{D} \right)^2 f \left(\frac{d}{w} \right) \right] \quad (3.6)$$

Where, d is the channel depth and f(d/w) is a function dependent on the exact geometry of the channel. The value of f(d/w) has been determined for a variety of channel geometries, including isotropically etched "D" cross-sections.¹⁴ Dutta *et al.* plotted f(d/w) vs. aspect ratio (d/w) for both rectangular channels and isotropic etched channels, and concluded that the dispersivity of isotropic channels is approximately equal to the dispersivity of rectangular channels of the same area and aspect ratio. From this plot, a f(d/w) value of 5.8 was predicted for a isotropically etched channel with an aspect ratio of d/w = 0.214 (determined by experimental values: mask width = 60 μm, etch depth = 22.5 μm, total width = 105 μm). Furthermore, the average linear velocity can be defined by the volumetric flow rate (F) divided by the cross-sectional area (A). These substitutions led to Equation 3.7.

$$k = D \left[1 + \frac{5.8}{210} \left(\frac{Fd}{AD} \right)^2 \right] \quad (3.7)$$

Equations 3.7 and 3.4 were used to calculate σ_t values for each of the twenty channels. Channel cross-sectional area (A) was defined by choosing an etch depth of $d = 22.5 \mu\text{m}$ with a mask width of $60 \mu\text{m}$, resulting in $A = 2145 \mu\text{m}^2$. An inlet flow rate of $0.25 \mu\text{L}/\text{min}$ was chosen, resulting in an individual channel flow rate of $1/20$ of this value ($F = 0.0125 \mu\text{L}/\text{min}$), assuming the incoming flow is evenly distributed. A diffusion coefficient (D) of $5 \times 10^{-6} \text{cm}^2/\text{s}$ was chosen to represent a relatively small, fast peptide. By choosing a slightly larger diffusion coefficient, any diffusion related band-broadening effects will be exaggerated (analytes with higher D, will result in larger σ_t^2). Elution time (t) was calculated by dividing the volume of each channel ($A \times L$) by the volumetric flow rate in the channel (F). The eluted peaks were approximated by triangles with a base equal to 4σ . Triangle area was constant, as it should be for a constant amount of sample, and was arbitrarily set to one. Peak heights were calculating using the base of 4σ and the formula for the area of triangle ($\text{Area} = \frac{1}{2} \text{base} \times \text{height}$). The peak of the triangle was located at the elution time (t) and the time points at $t-2\sigma$ and $t+2\sigma$ were assigned a y-value of zero in order to define the triangle shape. Table 3.4 presents the values resulting from these calculations and Figure 3.7 illustrates the plotted values.

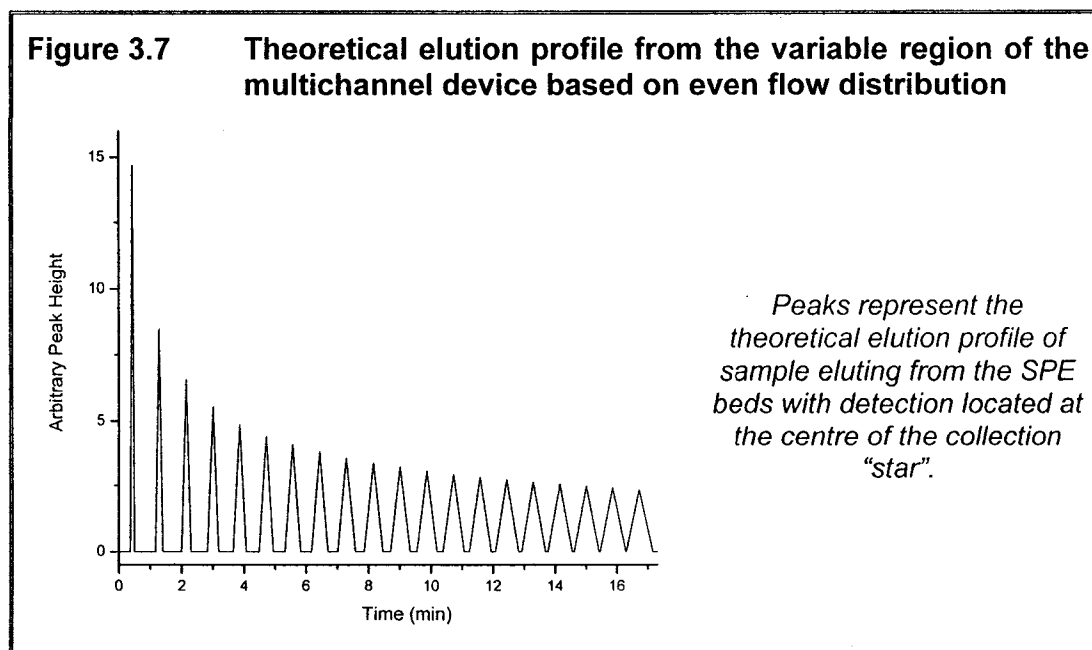


Table 3.4 Theoretical elution times and peak widths for sample travelling through the variable region of the multichannel device

Channel	Length (L) (cm)	Volume (A x L) (nL)	Elution Time (t) (min)	σ_t (min)	Peak Height
1	0.25	5.36	0.429	0.0340	14.694
2	0.75	16.09	1.287	0.0589	8.484
3	1.25	26.81	2.145	0.0761	6.571
4	1.75	37.54	3.003	0.0900	5.554
5	2.25	48.26	3.861	0.1021	4.898
6	2.75	58.99	4.719	0.1129	4.430
7	3.25	69.71	5.577	0.1227	4.075
8	3.75	80.44	6.435	0.1318	3.794
9	4.25	91.16	7.293	0.1403	3.564
10	4.75	101.89	8.151	0.1483	3.371
11	5.25	112.61	9.009	0.1559	3.207
12	5.75	123.34	9.867	0.1632	3.064
13	6.25	134.06	10.725	0.1701	2.939
14	6.75	144.79	11.583	0.1768	2.828
15	7.25	155.51	12.441	0.1832	2.729
16	7.75	166.24	13.299	0.1895	2.639
17	8.25	176.96	14.157	0.1955	2.558
18	8.75	187.69	15.015	0.2013	2.484
19	9.25	198.41	15.873	0.2070	2.416
20	9.75	209.14	16.731	0.2125	2.353

The results of this theoretical study illustrate that the peaks eluting from the longest channels will experience more diffusion. At this flow rate, the peaks do remain separated, justifying the theoretical basis of the delay line concept. However, at slower flow rates the later eluting peaks will begin to overlap. For this reason experimental flow rate was kept above 0.25 $\mu\text{L}/\text{min}$. It should be noted that the above theoretical calculations assume that the sample elutes from the SPE bed as an infinitely narrow plug. This is not the case. The width of the plug eluting from the SPE bed would need to be added to the above peak widths.

Considering this, lower flow rates will most likely not lead to peak resolution and hence should be avoided.

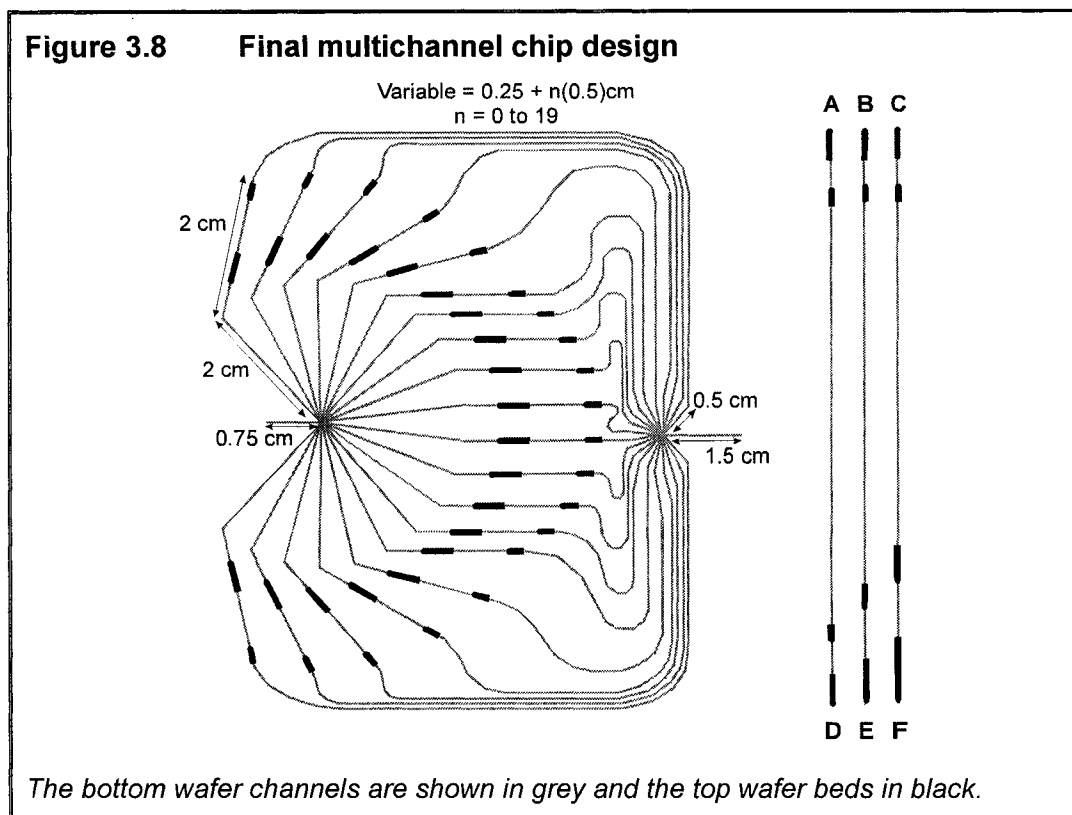
Having defined a mask width, an estimate of the loading volumes could be made based on etch depths. The loading volume for each fraction was defined as the volume contained between the center of the introductory “star” and the electrode used for fractionation. This region had a length of 2.5 cm. Volumes were calculated for etch depths of 10, 20 and 30 μm . The volume contained in this region was multiplied by twenty and correlated with the length of a 50 μm i.d. capillary that would contain this volume. This represented the maximum load that could be fractionated by the device. The results are shown in Table 3.5.

Table 3.5 Sample loading volumes

Etch Depth (μm)	Volume in one fraction (nL)	Total volume (x 20) (μL)	Length of corresponding 50 μm i.d. capillary (cm)
10	18.9	0.379	19.3
20	45.7	0.914	46.6
30	80.3	1.61	81.8

Sample loading for CIEF can vary drastically simply by changing the inner diameter of the capillary. The total loading volumes shown above were compatible with most CIEF-ESI-MS based experiments that were seen in the literature.^{15,16} Most examples of high loading volumes were concerned with a second dimension of separation and thus it was necessary to ensure that enough sample was introduced to be carried on to the next dimension.¹⁷ Efforts continue to reduce sample loads while retaining a high level of sensitivity.^{18,19}

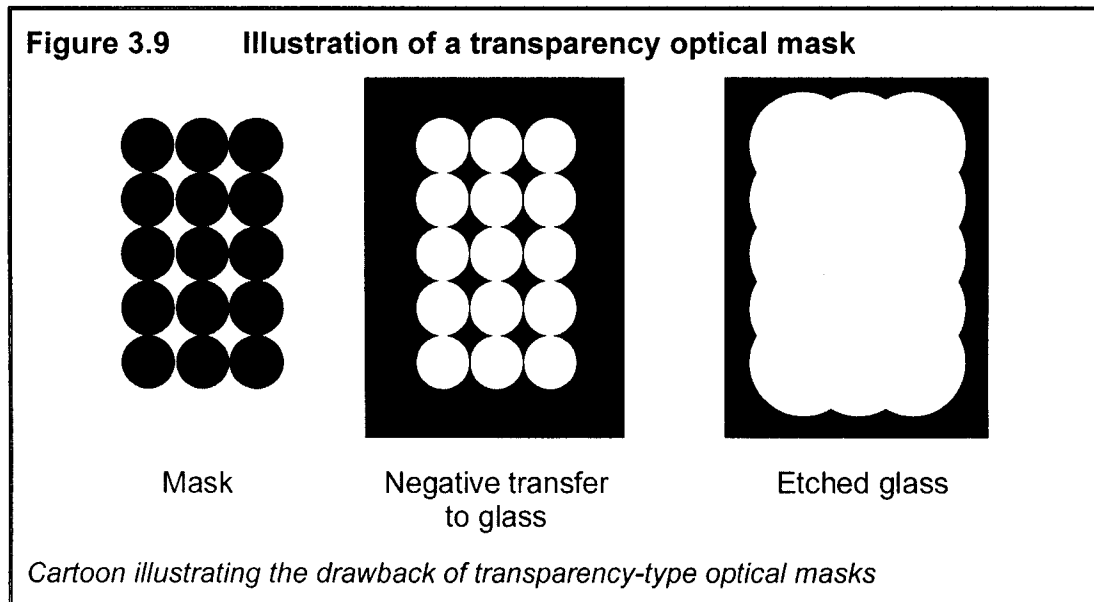
The device is shown in its entirety in Figure 3.8.



3.3.7 MATERIALS AND METHODS - FABRICATION DETAILS

The first step in the fabrication procedure was to obtain an optical mask of the device to be used in the lithographic process. The mask for the bottom wafer was made of glass coated with chrome in all but the area to be defined, the channel region. This mask was made commercially by Adtek. Masks made by this process are costly (approximately \$300-\$500), but do provide high resolution results, allowing channels of small dimensions to be defined. An alternative to this approach is to use a transparency printed by a high resolution printer as the optical mask. The drawback of this technique is that it leads to rough channel walls due to the ink dots formed by the printing process. This concept is illustrated in Figure 3.9. Due to the limited resolution of this process, it is not recommended for features under $50 \mu\text{m}$. Since the top wafer contained only the beds, which were quite large, the transparency printing process was used for the

creation of this mask. As the beds were to be quite deep (100-150 μm), the etch procedure would remove this roughness.



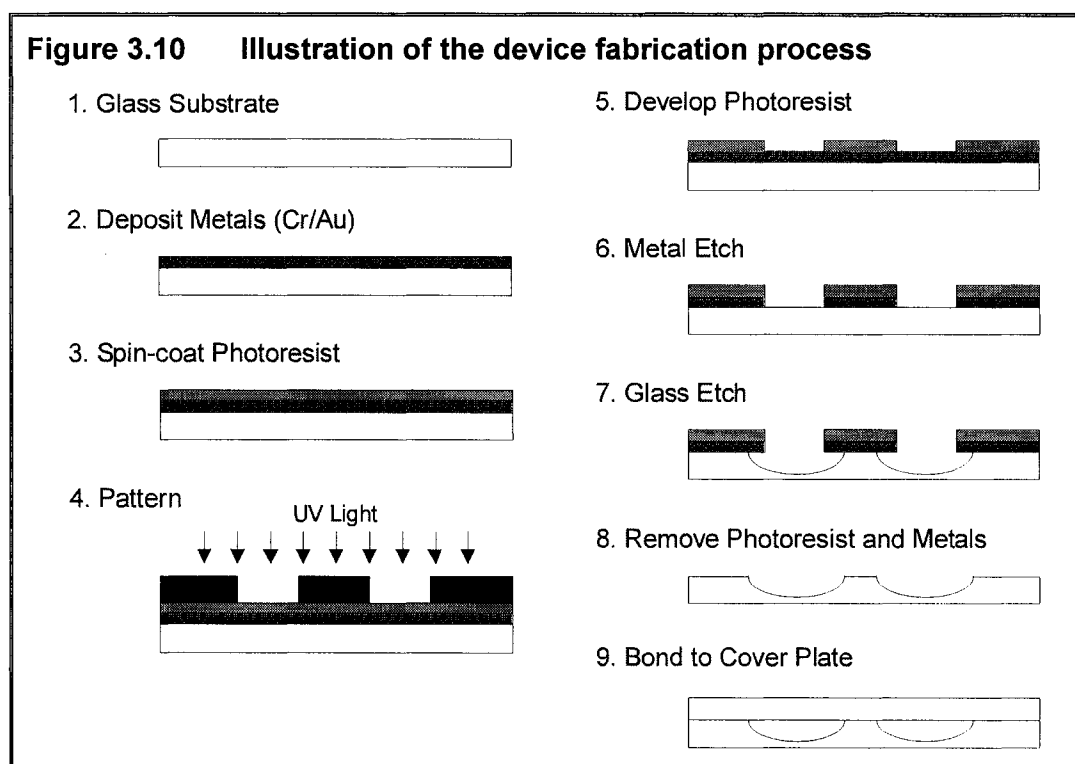
Devices were fabricated using standard lithographic techniques, which have been described previously.^{20,21} The entire process is illustrated at the end of this section in Figure 3.10. Metalized (200 \AA chrome, 1200 \AA gold) borofloat substrates were purchased from Micralyne. A layer of photoresist (HPR 504, OCG Microelectronic Materials) was spin-coated on top of the metal surface (500 rpm for 10 s, 4000 rpm for 40 s, Solitec). The substrates were then baked to strengthen the photoresist (115 $^{\circ}\text{C}$ for 30 min). The substrate and photomask defining the pattern of channels were aligned using a mask aligner (AB-M Inc). The commercial photomask was easily mounted in the mask aligner, but the transparency had to be taped onto the bottom of a piece of glass before it could be mounted. A short burst of UV exposure (4 s, $\lambda = 365 \text{ nm}$) served to weaken the exposed areas of photoresist. The weakened photoresist was removed using developer (25 s, Microposit[®] Developer 354, Shipley Company, L.L.C.). This was followed by gold etching (KI : I₂ at 4:1 in H₂O), chrome etching (HNO₃, (NH₄)₂Ce(NO₃)₆ and H₂O, Arch Chemicals, Inc.) and finally glass etching (HF:HNO₃:H₂O at 20:14:33). The glass etching proceeded at a rate of 0.71

$\mu\text{m}/\text{min}$ in borofloat glass. The bottom wafer was etched to an average depth of $22.5 \mu\text{m}$ and the top wafer to a depth of approximately $120 \mu\text{m}$. Any attempt to etch deeper than this resulted in further increase of the channel width with no significant change in depth ($120 \mu\text{m}$). The reason for this was not determined, but similar results were obtained by others in this group in the same time period.

At this point, holes were drilled in the cover plate to allow for the fluidic and electrical contacts. Referring to Figure 3.8, a hole was drilled at the head of each bed and at the single outlet using a diamond plated drill bit (0.027" OD, 200/240 Grit, #98-0668, Lunzer, Inc.) and immersing the wafer in water while drilling (Drill model: 7010, Servo Products Company). The position of these access holes relative to the beds is illustrated in cross-section in Figure 3.3. A smaller hole was drilled at the single inlet with a diameter more compatible to the $360 \mu\text{m}$ inlet capillary ($399 \mu\text{m}$, Kyocera Tycom). By leaving the photoresist and metal layers on the wafer during the drilling, visual alignment of the drill bit to the head of the beds was simple. Prior to drilling, the wafer was mounted on a scrap piece of glass using Crystalbond™ (#509, Aremco Products Inc.), in order to reduce the amount of break-out as the drill passed through the glass. Since the hole was drilled within the bed structure previously etched on the wafer, it was unnecessary to use a scrap piece of glass on top of the device as this surface would not contact the bottom wafer. Each cover plate was drilled individually.

The remaining photoresist was removed with acetone from both the top and bottom wafers. By quickly immersing the wafer in piranha solution (H_2SO_4 : H_2O_2 at 3:1, add H_2SO_4 to H_2O_2 slowly), it was found that the gold and chrome layers were easily and completely removed using the gold and chrome etchants, respectively. The entire glass substrate was cleaned with piranha (30 min while hot), rinsed with water, scrubbed with soap (Sparkleen 1, Fisher Scientific) and rinsed with water extensively. The wafers were dried and mounted in a single wafer ring holder. The wafers were individually rinsed (5 cycles) and dried (10 cycles) in a high pressure washer (Micro Automation 2066). The top and bottom wafer were aligned and pressed gently together to start the cold bond

(electrostatic interactions). After the initial cold bonding process, the glass sandwich was thermally bonded in the oven (room temperature to 550 °C @ 10 °C/min hold 30 min, 550 °C to 610 °C @ 10 °C/min hold 30 min, 610 °C to 635 °C @ 10 °C/min hold 30 min, 635 °C to 650 °C @ 5 °C/min hold 6 hrs). This process served to form a covalent bond between adjacent silanol groups on opposing wafers through the exclusion of water. The device was then ready for use.



3.4 HOLDER AND FLUIDIC INTERFACES

In order to allow for pressure driven flow throughout the system, it was necessary to seal all of the access reservoirs once the beds had been packed and to create an inlet driving pressure. Furthermore, a means by which to position and seal the grounding electrodes was also necessary. This was originally done using a Plexiglass clamp, where the reservoirs were sealed with septa (Supelco Thermogreen LB-2, Division of Sigma-Aldrich). The top piece of

Plexiglass contained small holes in order to align the electrodes to the chip reservoirs. Each electrode pierced through a septum to make electrical contact with the channel below, as is shown in Figure 3.11. The electrode assembly is shown in Figure 3.12 and the first holder design is shown in Figure 3.13, with the chip and electrodes in place.

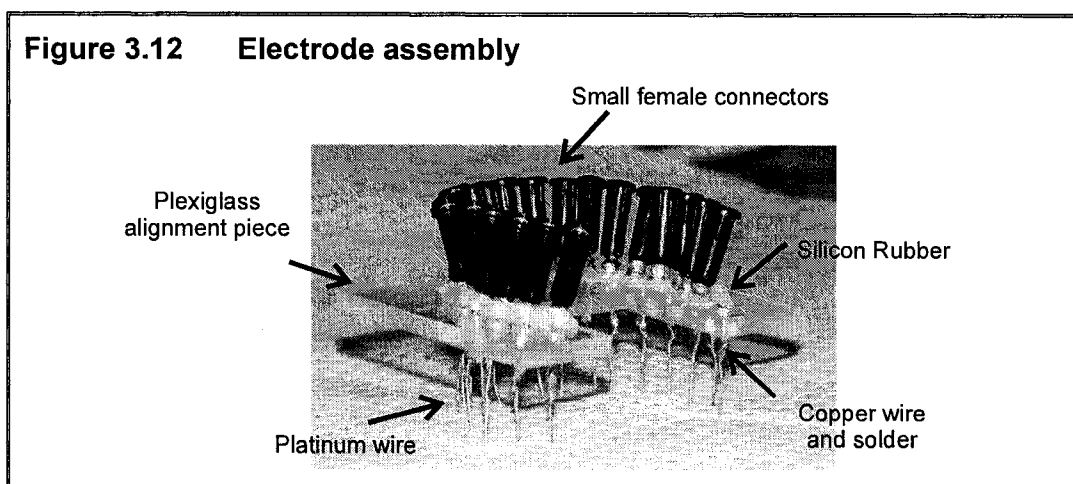
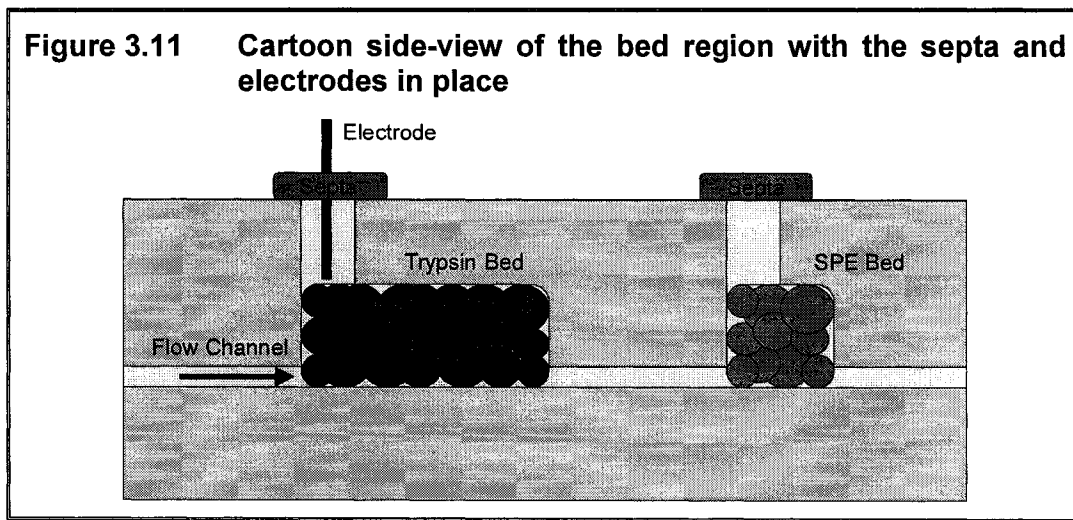
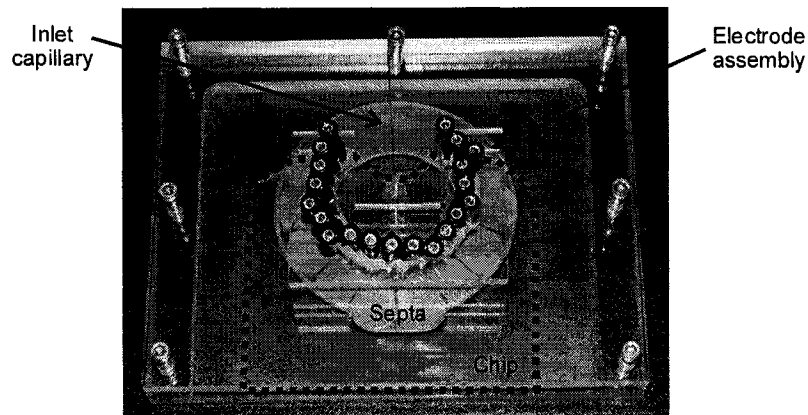
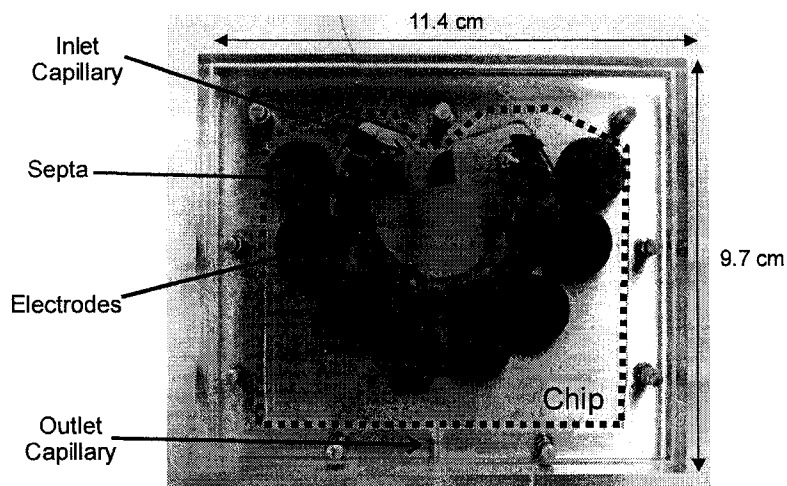


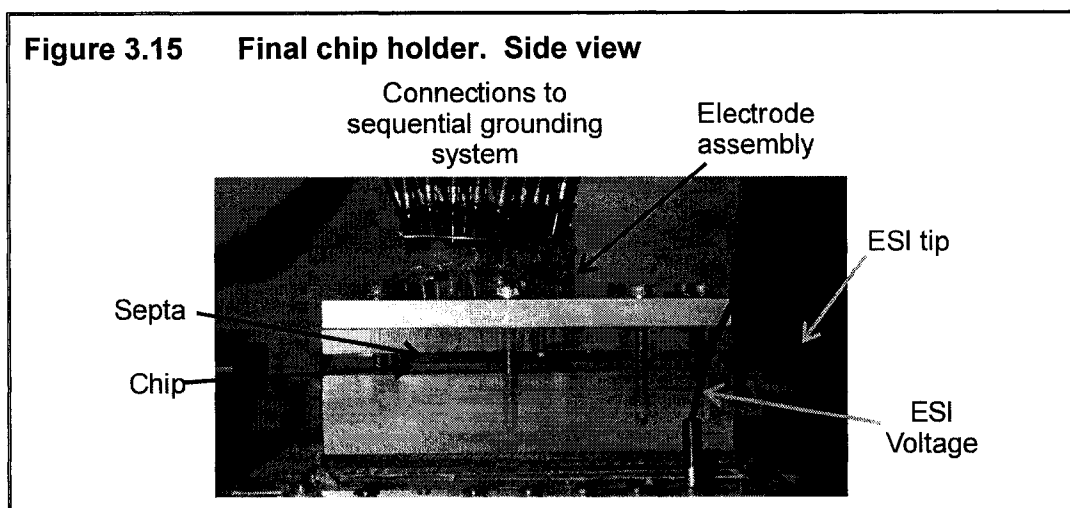
Figure 3.13 Initial chip holder design. Top view



From the original design, it was determined that Plexiglass was too flexible to properly seal the device and that it was important to localize the pressure above the reservoirs to be sealed. A second clamp was designed that had a metal top plate and a thicker (1") Plexiglass bottom plate. Furthermore, the edges of the chip were sawed off in order to minimize the surface area, giving a device with dimensions of 7.0 cm by 8.9 cm, although as seen in Figure 3.14, not necessarily square. A smaller clamp was designed to fit more closely to the shape of the chip. The bottom view and cross-section of the entire assembly are shown in Figures 3.14 and 3.15.

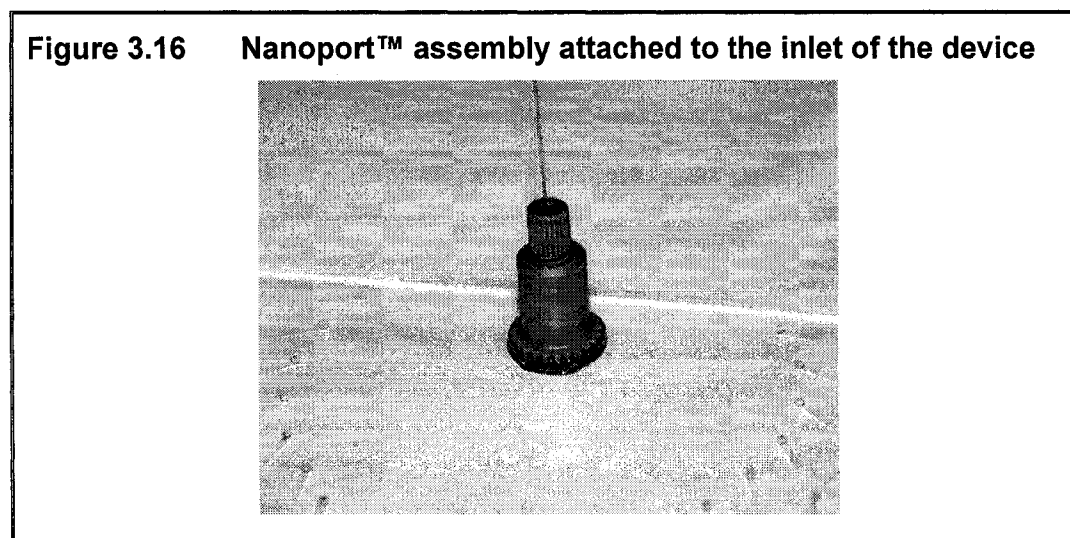
Figure 3.14 Final chip holder design. Bottom view





This holder sealed the device well and could be used with flow rates up to 2 $\mu\text{L}/\text{min}$.

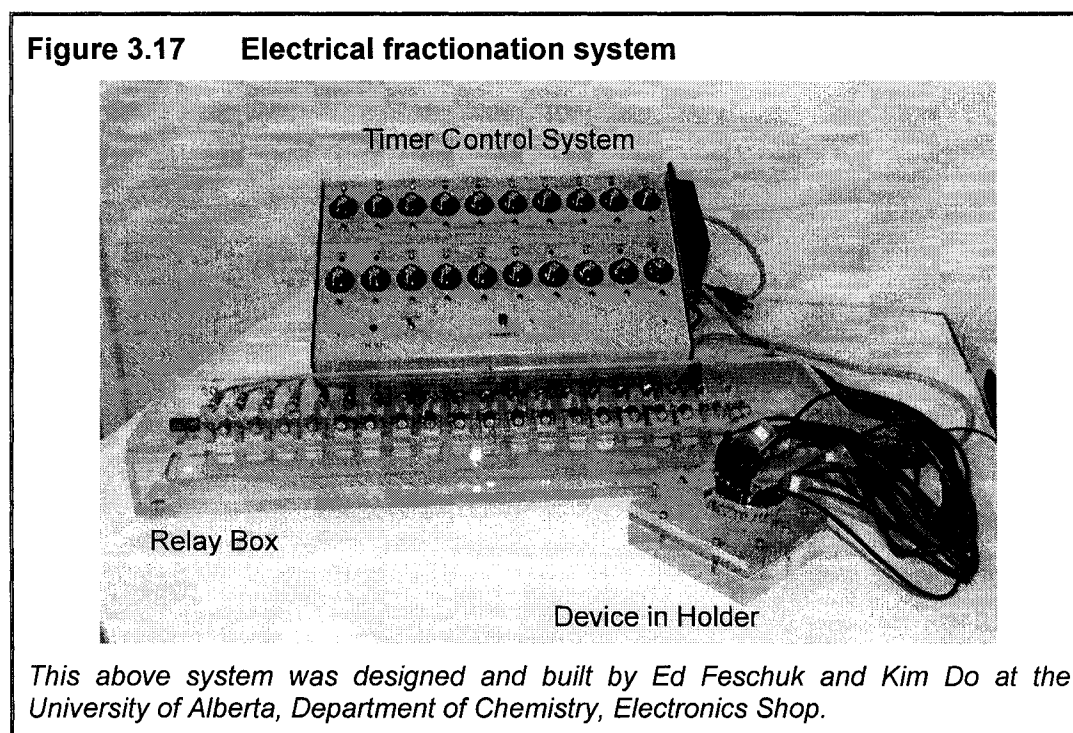
As seen in both Figures 3.13 and 3.14, the inlet capillary was originally coupled to the device simply by piercing a capillary through a septum and inserting it into the inlet reservoir. This reservoir had a diameter of 399 μm so it fit the capillary well. However, this led to difficulties in exchanging the inlet capillary. For this reason, commercially available Nanoports™ (N-124H, Upchurch Scientific) were used to couple the 365 μm capillary directly to the chip, as is shown in Figure 3.16.



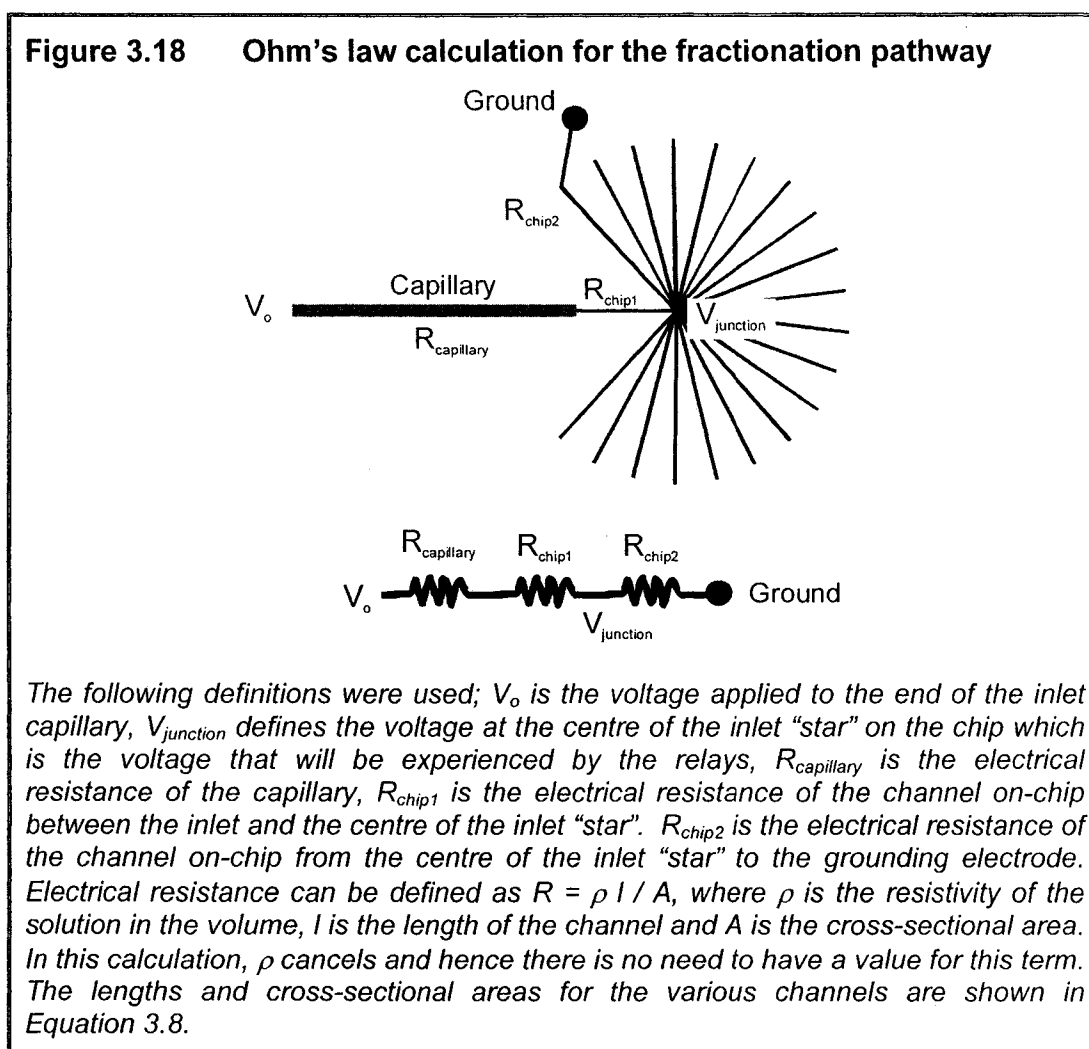
These devices allowed the inlet capillary to be easily exchanged. They were also easy to attach and remove when using silicon rubber as the adhesive as opposed to the adhesive ring provided (shown in Figure 3.16). By this means they could be recycled. To test the durability of the seal, the device was used as shown in Figure 3.16 (reservoirs NOT sealed) up to a flow rate of 200 $\mu\text{L}/\text{min}$ without failure.

3.5 ELECTRICAL FRACTIONATION SYSTEM

In order to facilitate the fractionation process, an electrical system was designed to perform the sequential grounding process. The system consisted of timers, relays (S05LTA235, Kilovac Corporation) and electrodes for each channel and a high voltage source (Spellman®). As was explained in Section 3.3.1., a high voltage was applied to the end of the inlet capillary and a sequential ground applied to each of the twenty channels. The electrical components are shown in Figure 3.17; the high voltage source is not pictured here.



The timer control system controlled the entire electrical sequence. The dwell time is set individually for each channel; the sequence can be initiated at any timer and runs to the last timer. The relay box is connected to ground and hence when a relay is activated it provides a path to ground. The timer control system is connected to the relay box and the high voltage source. Initiating the grounding sequence also initiates the high voltage and when the sequence is finished the high voltage is disengaged. This ensures that one channel is always at ground. Fluidic pathways can be compared to electrical resistors, and as such a simple Ohm's law calculation was used to calculate the voltage that would be experienced by the relays. This calculation is illustrated in Figure 3.18 and numerical values follow in Equation 3.8.



$$V_{\text{junction}} = \frac{R_{\text{chip2}}}{R_{\text{chip1}} + R_{\text{capillary}} + R_{\text{chip2}}} V_o$$

$$R_{\text{chip1}} = \frac{\rho(0.75 \text{ cm})}{2145 \mu\text{m}^2}$$

$$R_{\text{chip2}} = \frac{\rho(2.5 \text{ cm})}{2145 \mu\text{m}^2}$$

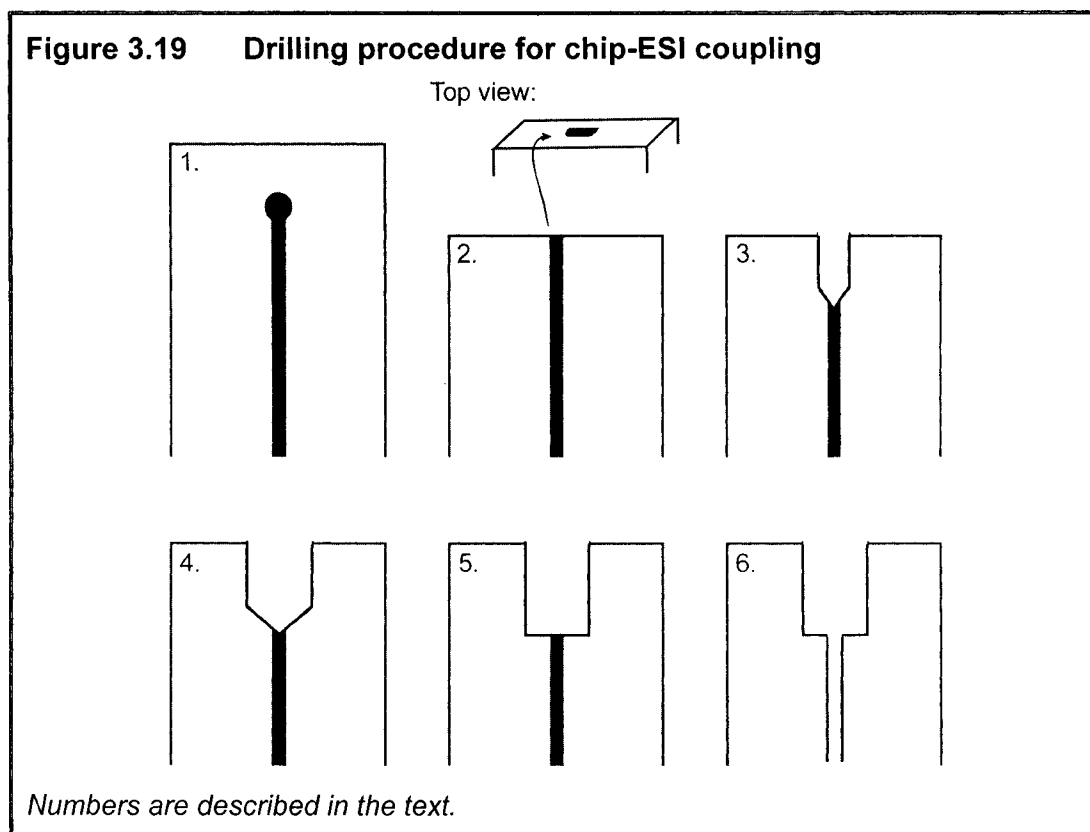
$$R_{\text{capillary}} = \frac{\rho l_{\text{capillary}}}{1963 \mu\text{m}^2}$$
(3.8)

Using a 20 cm inlet capillary, which is a short estimate, $V_{\text{junction}} = 0.1V_o$. At the maximum voltage of 30 kV, V_{junction} will be 3 kV which justifies the use of high voltage relays. The relays used had a rating of 10 kV, which was more than sufficient.

3.6 ESI INTERFACE

Previous work done in this research group involved a study of low dead volume capillary-microchip coupling.²² In brief, the optimal procedure was as follows; bracketed numbers refer to steps illustrated in Figure 3.19. The outlet of the microchip was first filled with CrystalbondTM in order to minimize the possibility of any glass shards entering the channel during the sawing and drilling procedure (1). The edge of the chip was removed using a glass saw so that the outlet channel was exposed at the end (2). The end of the chip was polished in order to be able to visualize the channel. A drill bit (Kyocera Tycom) was aligned parallel to the channel and a hole was drilled to accommodate the electrospray tip. In the case of the multichannel work, a 368 μm drill bit (#79 series 225) was used to accommodate a 360 μm electrospray tip. The hole was first drilled using a 201 μm drill bit (#92 series 225) which allowed for easy alignment with the channel as the drill bit and the channel were of comparable sizes (3). The hole was widened with a 368 μm drill bit to accommodate the ESI tip (4). Finally, the hole was drilled with a 368 μm drill bit that had been flattened at the tip (5). The tip was manually flattened by sanding the end of the drill bit and observing the tip

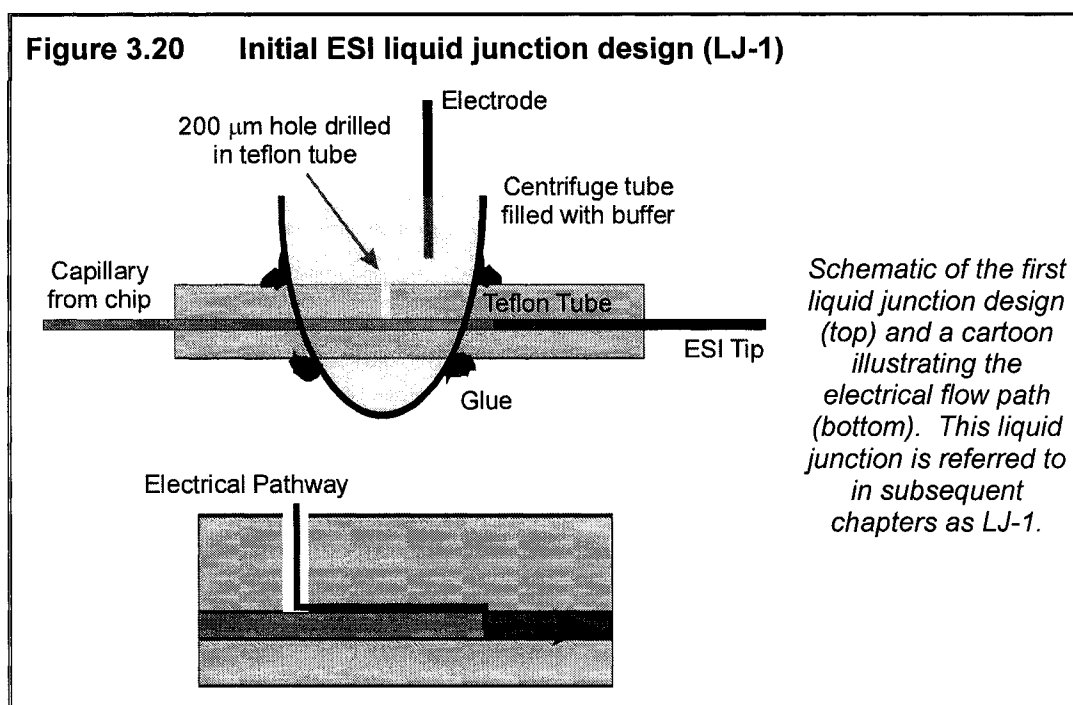
under magnification. This last step allowed for the creation of a low dead volume connection. This process is illustrated in Figure 3.19.



The chip was soaked in water overnight to allow the glass shards to be removed via gravity. Using gentle heat the Crystalbond™ was removed from the channel by applying a vacuum to the outlet (6). The chip was placed in acetonitrile in order to remove the Crystalbond™ that collected in the hole after application of the vacuum. Acetonitrile, methanol and water were pulled through the channels by vacuum to remove any remaining Crystalbond™. It was noted that after the use of organic solvents, the natural capillary forces of the channels were disturbed. This was easily visualized by placed a single drop of water at the inlet of the multichannel device. Before the use of organic solvents the capillary forces drew the liquid into each of the twenty channels evenly. However, after exposure to organic solvents, the flow was not evenly distributed. Initially, we attempted to solve this problem by conditioning the channels with sodium

hydroxide. Surprisingly, this did not solve the problem. Suspecting that the problem resided in lingering organic residues on the channel surfaces, we tried to remedy the problem by ashing the chip. This consisted of putting the device in the oven, set on a shorter version of the bonding program that was presented in Section 3.3.7 (the last stage at 650 °C was shortened to 2 hrs). This solved the problem, and from this point on, was incorporated into the standard preparation procedure.

Originally, the electro spray tip was coupled directly to the microchip and fixed with an adhesive, as was done in previous work.²³ However, problems with the stability of the metallic coating of the commercially available electro spray tips (New Objective, Inc.) made this unfeasible. Previous work had used ESI tips that were prepared by collaborators at the National Research Council, Ottawa, Ontario, Canada. Those tips were metalized by first sputtering a seed layer of gold and then electroplating a second layer of gold. This process lead to tips that were exceptionally stable and conductive; allowing a voltage to be applied directly to the tip to drive the electro spray. Due to the stability of the electroplating procedure these tips could be used for great lengths of time. However, the commercially available tips that were used for this work were metalized using a sputtering procedure only. When an electro spray voltage was applied to the tip, more often than not, the metal layer degraded somewhat and was no longer conductive, meaning that the tip had to be replaced.²⁴⁻²⁶ Having fixed the tip with an adhesive, removal of the tip was difficult. In order to avoid these problems, an external liquid junction was designed, allowing for easy exchange of the emitter.^{27,28} A discussion of chip-MS interfaces was presented in Section 1.3.3. The initial design is shown in Figure 3.20.



A short piece of fused silica capillary (length = 2 cm, 365 μm o.d., 50 μm i.d., Polymicro) was coupled to the chip through the low dead volume junction. The end of this capillary was cut to be very blunt and straight. This was inserted into one end of a larger piece of Teflon tubing (300 μm i.d., 1.58 mm o.d., #58702, Supelco). The electrospray tip (360 μm o.d., 50 μm i.d., 15 μm at tip, length ≈ 4 cm, FS360-50-15, New Objective), which also had a blunt end, was inserted into the other end and the two capillaries were butted against one another. The Teflon tubing had a small hole drilled in it perpendicular to the flow path. The tubing was then inserted through a centrifuge tube that had a hole drilled into it to accommodate the Teflon tubing. The edges of the holes (in the centrifuge tube) were sealed with silicone rubber (GE Silicones) and the tube was filled with a conductive solution (0.1 M formic acid). An electrode was placed into the tube. Using this device, the electrospray voltage was supplied to the tip through the small hole in the Teflon tube. It was important that the actual interface between the two capillaries was offset from the drilled hole as to avoid leakage of the solution travelling inside of the capillaries. If the interface was placed directly below the hole, the solution within the capillaries would leak out the hole. One

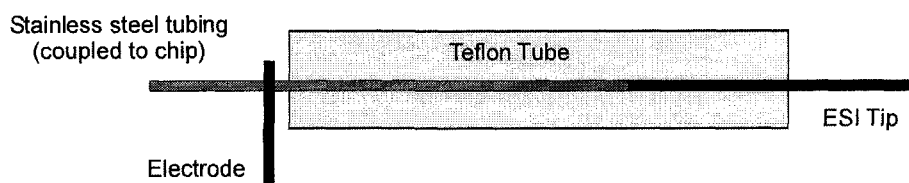
can think of this design as a controlled leak. The actual electrical pathway is through the hole, down the side of the capillary to the interface between the two capillaries, as is shown in Figure 3.20. There must be some amount of solution that leaks along the side of the capillary to allow for the electrical contact.

This design provided a stable electrospray signal that could be run for hours. It also allowed for easy exchange of the electrospray tip should it become clogged. Furthermore, this design did not rely on a metallic coating for the tip, avoiding the problems associated with such tips. However, great care needed to be taken when inserting the fused silica capillary from the chip into the Teflon tube. More often than not, the capillary broke off in the chip, creating great difficulties. In order to avoid this problem, PEEK tubing with the same dimensions as the capillary (360 μm o.d., 50 μm i.d., length = 2 cm, #1570, Upchurch Scientific) was used in its place. This tubing was flexible, thereby avoiding the aforementioned problem. However, inserting the PEEK tubing into the relatively tight fitting Teflon tubing became tedious. This aside, the design provided a stable ESI signal for extended periods of time.

The only drawback of this assembly was the so-called controlled leak. Eventually the Teflon tubing of the original device became stretched and began to leak at the ends. When a new piece tubing was used the fit between the tubing and the capillaries was too tight. Hence, there was no leakage at the small drilled hole and no electrical contact. Achieving the correct Teflon tube fit proved difficult. For this reason, another method with which to provide the electrical contact was explored.

It was suggested that electrical contact could be easily achieved if a short piece of graphite was used to couple the chip to the electrospray tip.²⁹ No graphite tubing with the correct dimensions could be found, however, stainless steel (SS) tubing of the correct dimensions was available. The design for this interface is shown in Figure 3.21.

Figure 3.21 Second ESI interface (SS-1)



Cartoon of the SS ESI design (top) and the resulting product (left). This interface is referred to in subsequent chapters as SS-1.

Originally, SS tubing of the correct dimensions to match the hole that had been drilled in the microchip was used. This required that we used tubing of dimensions: 360 μm o.d. and 175 μm i.d.. This created a large mismatch in cross-sectional area between the internal dimensions of the microchip, the SS tubing and the electro spray tip. Channel dimensions had been designed such that the cross-sectional area matched that of a capillary with a 50 μm i.d.. Cross-sectional areas are noted in Table 3.6.

Table 3.6 Cross-sectional areas of the ESI interface

Component	Cross Sectional Shape	Dimensions (μm)	Cross Sectional Area (μm^2)
Chip channel	Trapezoidal	Mask width = 60 Depth = 22.5	2145
SS tubing	Circular	o.d. = 360 i.d. = 175	24,053
	"	o.d. = 125 i.d. = 50	1963
Electrospray Tip	"	o.d. = 360 i.d. = 50	1963

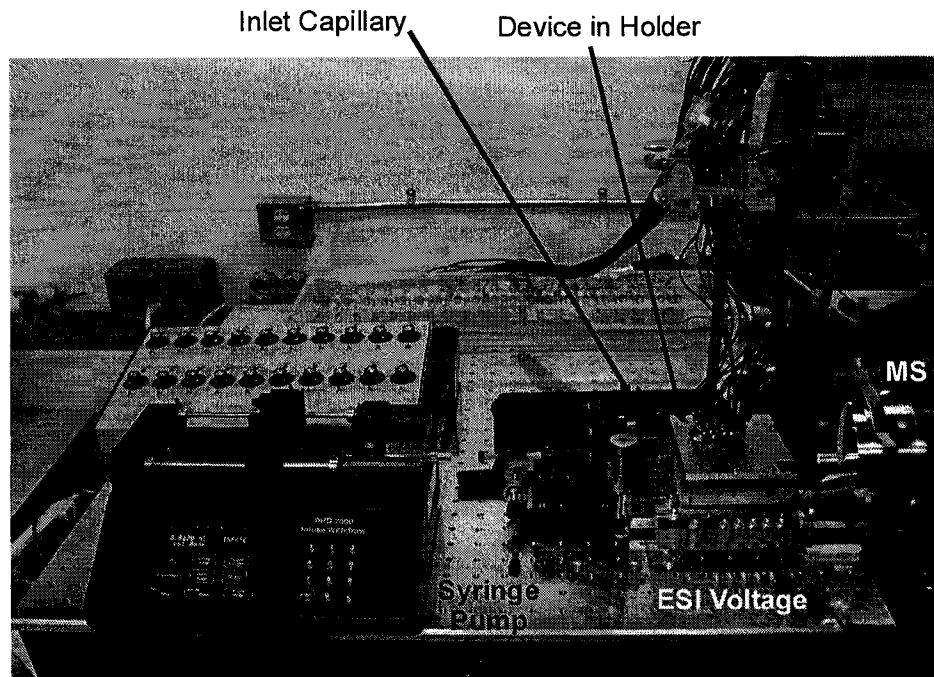
Hence, when the larger diameter SS tubing was used, it has the potential to act like a mixing chamber and contribute a significant amount of band broadening to the system. For this reason, a SS tubing with 125 μm o.d. and 50 μm i.d. was used instead. For this tubing, a smaller hole was drilled into the chip (150 μm) and the SS tubing coupled directly to the device as before. The rest of the design was as per Figure 3.21, except that a small piece of PEEK tubing (360 μm o.d., 150 μm i.d., #1572, Upchurch Scientific) was used inside of the larger Teflon tubing to create a tight fit with the SS tubing. The slightly constricted i.d. of the Teflon tubing (300 μm) created a tight enough fit that no leakage was initially seen. This design will be referred to in future sections as SS-2. However, this design was not stable and soon began to leak. A different means by which to couple the SS tubing and the electrospray tip will have to be explored either through the use of an actual low dead volume commercial junction or by using an ESI tip with a smaller o.d..

It was discovered at this point that electrospray directly from the end of the smaller SS tubing was possible; this configuration is referred to as SS-3 in future sections. Several recent publications have explored the use of SS tubing as direct electrospray emitters.^{24,26,30-32} The ability to achieve electrospray without the need of a tapered outlet was explored in a recent publication²⁶ through examining the mechanism of micro-ESI with SS emitters. In this work, the authors achieve electrospray directly from a blunt SS emitter of large dimensions, 100 μm i.d. and 400 μm o.d.. They propose that the greater hydrophobicity of the SS emitter allows the ESI Taylor cone to remain well formed despite the large emitter o.d.. This recent work also couples a SS emitter directly to a polymeric microfluidic device. The work presented by Ishihama *et al.*²⁴ has sources for SS tubing of a variety of sizes, many of which would be ideal for our needs. These should be explored in the future.

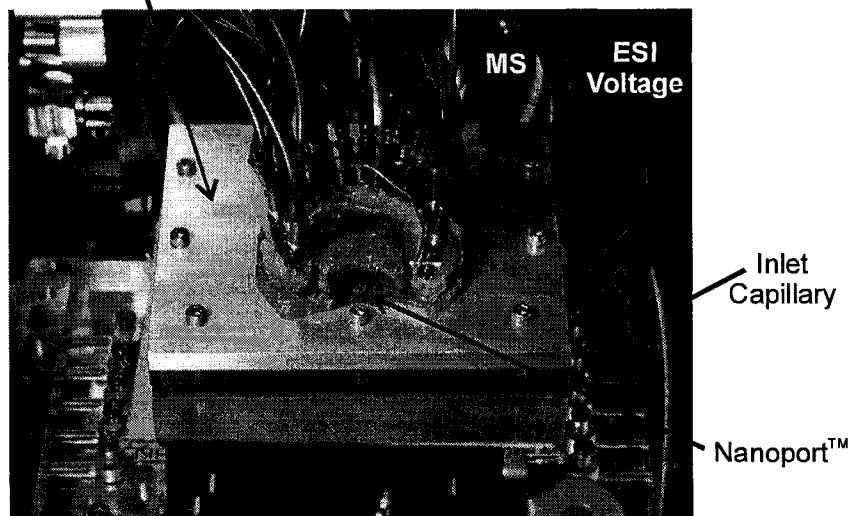
3.7 FINAL PLATFORM

All of the above mentioned components were assembled to form the final platform. The system was used in two modes, pressure driven and electrical fractionation. The final pressure driven system is shown in Figure 3.22. For electrically driven flow, the syringe pump was removed and the inlet capillary was placed in a vial containing the high voltage electrode. This vial was kept at the same level as the chip to avoid any siphoning effects. The entire system is shown in Figure 3.23.

Figure 3.22 Final platform assembled for pressure driven flow

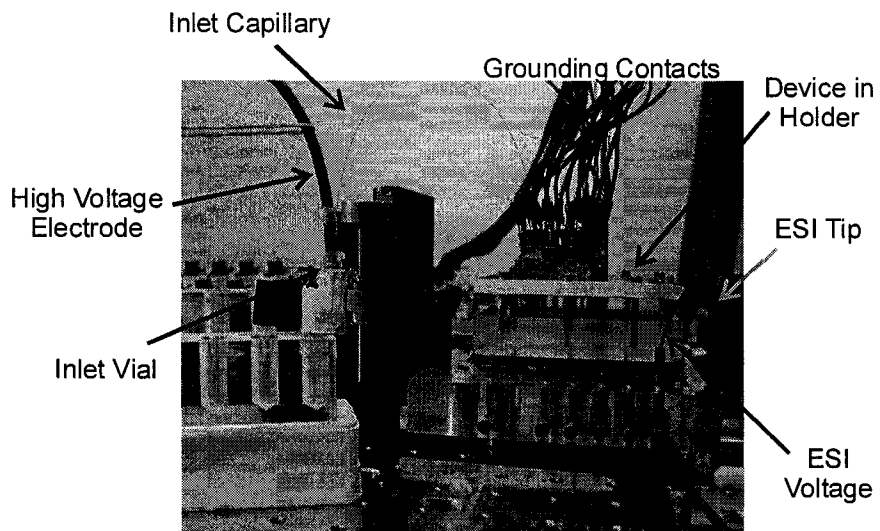
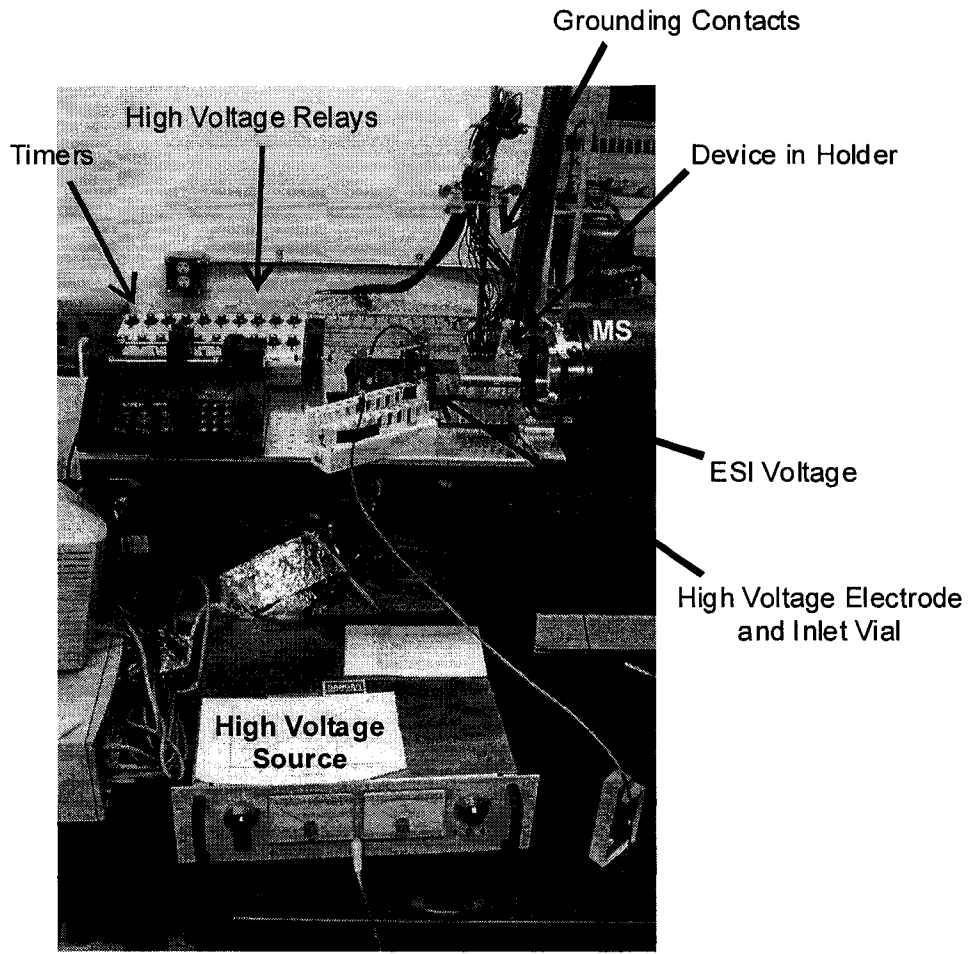


Device in Holder



Entire assembled platform (top) and a closer view of the inlet region (bottom).

Figure 3.23 Final platform assembled for electrical fractionation



3.8 REFERENCES

- (1) Beranova-Giorgianni, S. *Trends Anal. Chem.* **2003**, *22*, 273-281. "Proteome analysis by 2D gel electrophoresis and MS: Strengths and limitations"
- (2) Garfin, D. E. *Trends Anal. Chem.* **2003**, *22*, 263-272. "2D gel electrophoresis: An overview"
- (3) Yates, J. R. *J. Mass Spectrom.* **1998**, *33*, 1-19. "MS and the age of the proteome"
- (4) Wang, C.; Oleschuk, R.; Ouchen, F.; Li, J. J.; Thibault, P.; Harrison, D. J. *Rapid Commun. Mass Spectrom.* **2000**, *14*, 1377-1383. "Integration of immobilized trypsin bead beds for protein digestion within a microfluidic chip incorporating CE separations and an ESI-MS interface"
- (5) Wang, C. *Ph.D. Thesis*, "Integrated protein analysis on microchips for CE-ESI-MS" University of Alberta, Edmonton, Alberta, Canada, **2001**.
- (6) Bergkvist, J.; Ekström, S.; Wallman, L.; Löfgren, M.; Marko-Varga, G.; Nilsson, J.; Laurell, T. *Proteomics* **2002**, *2*, 422-429. "Improved chip design for integrated solid-phase microextraction in on-line proteomic sample preparation"
- (7) Shen, Y. F.; Smith, R. D. *Electrophoresis* **2002**, *23*, 3106-3124. "Proteomics based on high-efficiency capillary separations"
- (8) Smith, R. D.; Anderson, G. A.; Lipton, M. S.; Paša-Tolić, L.; Shen, Y. F.; Conrads, T. P.; Veenstra, T. D.; Udseth, H. R. *Proteomics* **2002**, *2*, 513-523. "An accurate mass tag strategy for quantitative and high-throughput proteome measurements"
- (9) Washburn, M. P.; Wolters, D.; Yates, J. R. *Nat. Biotechnol.* **2001**, *19*, 242-247. "Large-scale analysis of the yeast proteome by multidimensional protein identification technology"
- (10) Conrads, T. P.; Anderson, G. A.; Veenstra, T. D.; Paša-Tolić, L.; Smith, R. D. *Anal. Chem.* **2000**, *72*, 3349-3354. "Utility of accurate mass tags for proteome-wide protein identification"
- (11) Cantwell, F. F. *Lecture Notes, Chem 421: Analytical Separations*; University of Alberta, Department of Chemistry: Edmonton, Alberta, Canada, **1998**.
- (12) Taylor, G. I. *Proc. Roy. Soc. (London)* **1953**, *219*, 186-203. "Dispersion of soluble matter in solvent flowing slowly through a tube"
- (13) Chatwin, P. C.; Sullivan, P. J. *J. Fluid Mech.* **1982**, *120*, 347-358. "The effect of aspect ratio on longitudinal diffusivity in rectangular channels"
- (14) Dutta, D.; Leighton, J., D.T. *Anal. Chem.* **2001**, *73*, 504-513. "Dispersion reduction in pressure-driven flow through microetched channels"
- (15) Yang, L. Y.; Lee, C. S.; Hofstadler, S. A.; Smith, R. D. *Anal. Chem.* **1998**, *70*, 4945-4950. "Characterization of microdialysis acidification for CIEF microelectrospray ionization MS"
- (16) Kirby, D. P.; Thorne, J. M.; Gotzinger, W. K.; Karger, B. L. *Anal. Chem.* **1996**, *68*, 4451-4457. "A CE/ESI-MS interface for stable, low-flow operation"

- (17) Chen, J. Z.; Balgley, B. M.; DeVoe, D. L.; Lee, C. S. *Anal. Chem.* **2003**, *75*, 3145-3152. "CIEF-based multidimensional concentration/separation platform for proteome analysis"
- (18) Chen, J. Z.; Gao, J.; Lee, C. S. *J. Prot. Res.* **2003**, *2*, 249-254. "Dynamic enhancement of sample loading and analyte concentration in CIEF for proteome studies"
- (19) Mohan, D.; Pašja-Tolić, L.; Masselon, C. D.; Tolić, N.; Bogdanov, B.; Hixson, K. K.; Smith, R. D.; Lee, C. S. *Anal. Chem.* **2003**, *75*, 4432-4440. "Integration of electrokinetic-based multidimensional separation/concentration platform with ESI-Fourier transform ion cyclotron resonance-MS for proteome analysis of *Shewanella oneidensis*"
- (20) Fan, Z. H.; Harrison, D. J. *Anal. Chem.* **1994**, *66*, 177-184. "Micromachining of CE injectors and separators on glass chips and evaluation of flow at capillary intersections"
- (21) Fluri, K.; Fitzpatrick, G.; Chiem, N.; Harrison, D. J. *Anal. Chem.* **1996**, *68*, 4285-4290. "Integrated CE devices with an efficient postcolumn reactor in planar quartz and glass chips"
- (22) Bings, N. H.; Wang, C.; Skinner, C. D.; Colyer, C. L.; Thibault, P.; Harrison, D. J. *Anal. Chem.* **1999**, *71*, 3292-3296. "Microfluidic devices connected to fused-silica capillaries with minimal dead volume"
- (23) Li, J. J.; Wang, C.; Kelly, J. F.; Harrison, D. J.; Thibault, P. *Electrophoresis* **2000**, *21*, 198-210. "Rapid and sensitive separation of trace level protein digests using microfabricated devices coupled to a quadrupole-TOF MS"
- (24) Ishihama, Y.; Katayama, H.; Asakawa, N.; Oda, Y. *Rapid Commun. Mass Spectrom.* **2002**, *16*, 913-918. "Highly robust stainless steel tips as micro-electrospray emitters"
- (25) Jussila, M.; Sinervo, K.; Porras, S. P.; Riekkola, M. L. *Electrophoresis* **2000**, *21*, 3311-3317. "Modified liquid junction interface for nonaqueous CE-MS"
- (26) Shui, W.; Yu, Y.; Xu, X.; Huang, Z.; Xu, G.; Yang, P. *Rapid Commun. Mass Spectrom.* **2003**, *17*, 1541-1547. "Micro-electrospray with stainless steel emitters"
- (27) von Brocke, A.; Nicholson, G.; Bayer, E. *Electrophoresis* **2001**, *22*, 1251-1266. "Recent advances in CE/ESI-MS"
- (28) Gelpí, E. *J. Mass Spectrom.* **2002**, *37*, 241-253. "Interfaces for coupled liquid-phase separation/MS techniques"
- (29) Fadgen, K. *Personal communication*, Waters Corporation, Milford, MA, USA, Nov. 2002
- (30) Wang, H. L.; Lim, K. B.; Lawrence, R. F.; Howald, W. N.; Taylor, J. A.; Ericsson, L. H.; Walsh, K. A.; Hackett, M. *Anal. Biochem.* **1997**, *250*, 162-168. "Stability enhancement for peptide analysis by electrospray using the triple quadrupole MS"
- (31) Chowdhury, S. K.; Chait, B. T. *Anal. Chem.* **1991**, *63*, 1660-1664. "Method for the ESI of highly conductive aqueous solutions"

- (32) Guzzetta, A. W.; Thakur, R. A.; Mylchreest, I. C. *Rapid Commun. Mass Spectrom.* **2002**, *16*, 2067-2072. "A robust micro-ESI technique for high-throughput LC/MS proteomics using a sanded metal needle as an emitter"

CHAPTER 4: PLATFORM PERFORMANCE

4.1	INTRODUCTION	118
4.2	CIEF.....	119
4.2.1	MATERIALS AND METHODS.....	119
4.2.2	RESULTS AND DISCUSSION.....	120
4.3	PRESSURE DRIVEN FLOW THROUGHOUT THE SYSTEM.....	127
4.3.1	MATERIALS AND METHODS.....	127
4.3.2	PRESSURE DRIVEN FLOW – BEDS NOT PACKED	129
4.3.3	PRESSURE DRIVEN FLOW – TRYPSIN BEDS PACKED	131
4.3.4	PRESSURE DRIVEN FLOW – BEDS PACKED.....	134
4.3.5	ELUENT EFFECTS	138
4.3.6	ADDITION OF AMPHOLYTES.....	140
4.3.7	EFFECT OF CONCENTRATION.....	144
4.3.8	METHOD VALIDATION – STANDARD PROTEINS.....	147
4.3.8.1	BSA.....	147
4.3.8.2	LYSOZYME	150
4.4	ELECTRICAL FRACTIONATION	152
4.4.1	METHODS	152
4.4.2	RESULTS AND DISCUSSION.....	153
4.5	REFERENCES	156
4.6	APPENDIX.....	157

4.1 INTRODUCTION

Performance of the platform described in Chapter 3 was initially assessed using the entire sealed system. The experimental procedure allowing for full proteomic analysis was to be as follows:

- The inlet capillary is conditioned and filled with a protein solution to be separated using single-step CIEF, allowing for simultaneous sample focusing and mobilization. During this process, the electrokinetic fractionation system directs the incoming flow to each of the twenty channels.
- A pressure source is introduced and the proteins are driven through the immobilized trypsin beds allowing for digestion. The resulting peptides are then trapped on the SPE beds.
- The beds are washed to remove any unretained components and to ensure that all of the sample has been transferred to the SPE bed.
- Finally, introduction of an organic solvent allows for elution of the peptides, which are then driven towards the MS.

The system was designed such that all steps functioned together, consequently, testing individual components of the system was a challenge. The clamp that had been designed to properly seal the device did not allow for optical detection of any kind, which limited the detection point to the single outlet which led to the MS. For this reason, it seemed more logical to test the system in its assembled form first. Initially, the above procedure was divided into three steps: CIEF, electrical fractionation and pressure driven flow. The CIEF step was tested using a commercial CE instrument, in order to first optimize the separation parameters. Pressure driven flow throughout the system was explored through the introduction of a single sample at the inlet. This allowed for optimization of flow rates as well as the experimental procedure to be used while loading, washing and eluting material from the beds. Lastly, electrokinetic fractionation was examined in the sealed system, followed by pressure driven flow to the detector.

The last step was particularly ambitious, as there was no way to monitor the fractionation process directly or to determine where in the entire flow path there could be problems. These initial tests allowed for possible system and/or design problems to be identified.

4.2 CIEF

Initial CIEF work was done on a commercial CE instrument and stemmed from previously published work done with single step CIEF.¹ In order to keep the experimental procedure as simple as possible, the first study of CIEF conditions was done without coated capillaries and without the use of buffer additives.^{2,3} Usually, neutral capillaries are used so that the EOF is sufficiently suppressed to allow for efficient separation. IEF standards were used as the sample in these initial optimization experiments. Original conditions were not MS compatible, and hence further optimization was necessary, as is described in the next sections.

4.2.1 MATERIALS AND METHODS

All CIEF work was done using a PACE 5010 (Beckman) instrument fitted for UV detection at 280 nm. Fused silica capillaries (50 μm i.d., 360 μm o.d.) were obtained from Polymicro Technologies, and a length of 27 cm was used for all studies. This resulted in 20 cm from the defined inlet to detector and 7 cm from detector to the defined outlet. A positive voltage was applied to the outlet and negative voltage to the inlet, resulting in flow from the outlet to the inlet. This defined a detectable separation length of 7 cm.

Chemicals were obtained from the following sources: formic acid and ammonium bicarbonate (NH_4HCO_3) from Sigma-Aldrich, IEF standards (161-0310) and ampholytes (Bio-Lyte® 3/10) from Bio-Rad, sodium hydroxide (NaOH) and ammonium hydroxide (NH_4OH) from BDH and phosphoric acid (H_3PO_4) from Caledon. All solutions were prepared in ultrapure water (H_2O) (Millipore Canada) and all but the sample solutions were filtered through a nylon syringe filter (0.2

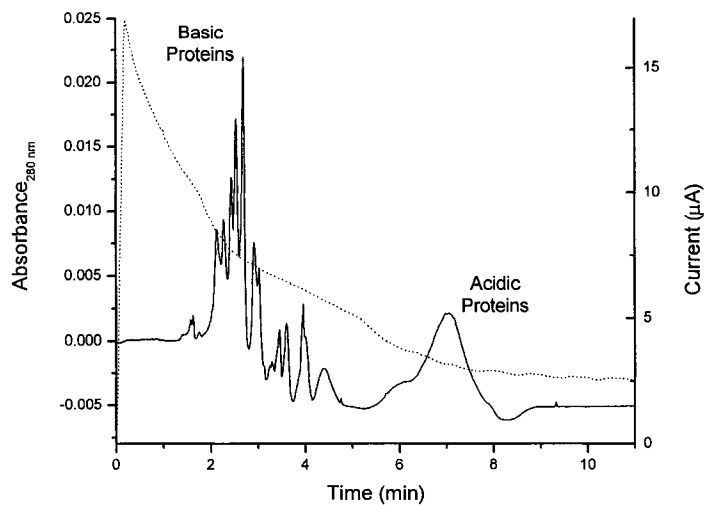
μm , Chromatographic Specialties Inc.). Protein solutions were prepared in siliconized vials (Rose Scientific Ltd.). The capillary was initially conditioned by a high pressure flush with 0.1 M NaOH for 20 min, followed by H₂O for 10 min. In between runs, the capillary was rinsed and the sample loaded using the following procedure: 0.1 M NaOH for 2 min, H₂O for 1 min and sample for 2 min, all done at high, forward pressure (inlet to outlet). The sample consisted of 1.65 mg/mL of the IEF standards with 0-8% (v/v dilution from stock, which was provided as 40% solids) ampholytes made up in H₂O. After loading the sample, the vials were switched such that the anolyte (acid) was at the positive terminal (outlet) and the catholyte (base) was at the negative terminal (inlet), and the voltage was applied, resulting in flow from outlet to inlet.

4.2.2 RESULTS AND DISCUSSION

The first experiments were performed using the conditions presented by Hofmann *et al.*⁴. Figure 4.1 illustrates the typical absorbance signal seen for the IEF standards, as well as the resulting current signal. The result was always the same reproducible pattern of peaks shown in Figure 4.1. No attempt was made to definitively identify each of the peaks in the IEF standard. The manufacturer supplied a typical gel IEF result, which is shown in Figure 4.2.

The separation in Figure 4.1 was achieved with flow traveling from the outlet (+) to the inlet (-), passing by the detector 7 cm from the outlet. Hence, the sample in the 20 cm beyond the detector is not observed. Evaluating the resulting absorbance signal, it appears that the majority of the basic proteins are not seen. As this study was merely qualitative, no steps were undertaken to resolve this problem.

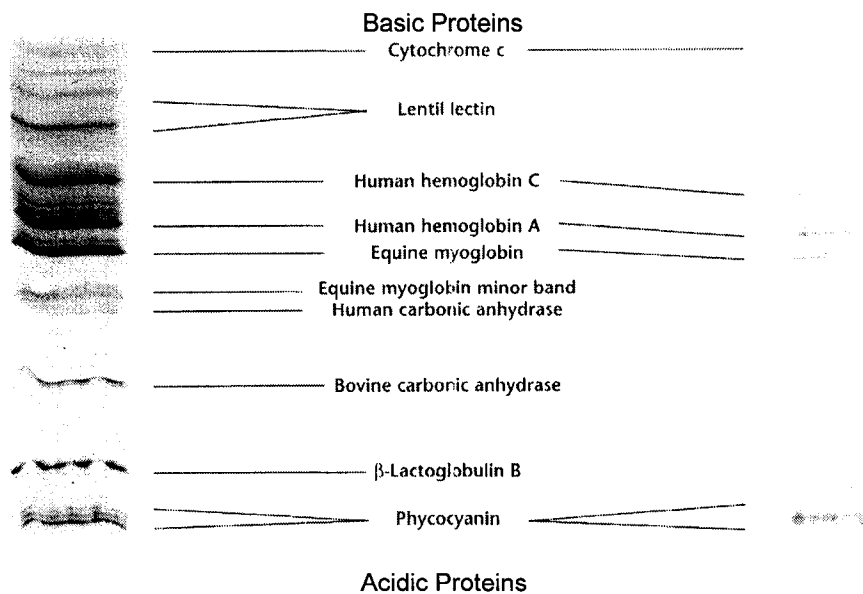
Figure 4.1 Typical CIEF experiment performed on a commercial CE instrument



Sample: 1.65 mg/mL IEF standards + 4% ampholytes in water.
 Separation voltage: 0.5 kV/cm.
 Anolyte: 10 mM H_3PO_4 (pH 2.3).
 Catholyte: 20 mM NaOH (pH 12.3).
 The solid line represents the resulting absorbance signal and the dashed line the observed current.

(Mar. 12, 2001)

Figure 4.2 Gel IEF separation of the IEF standard mixture

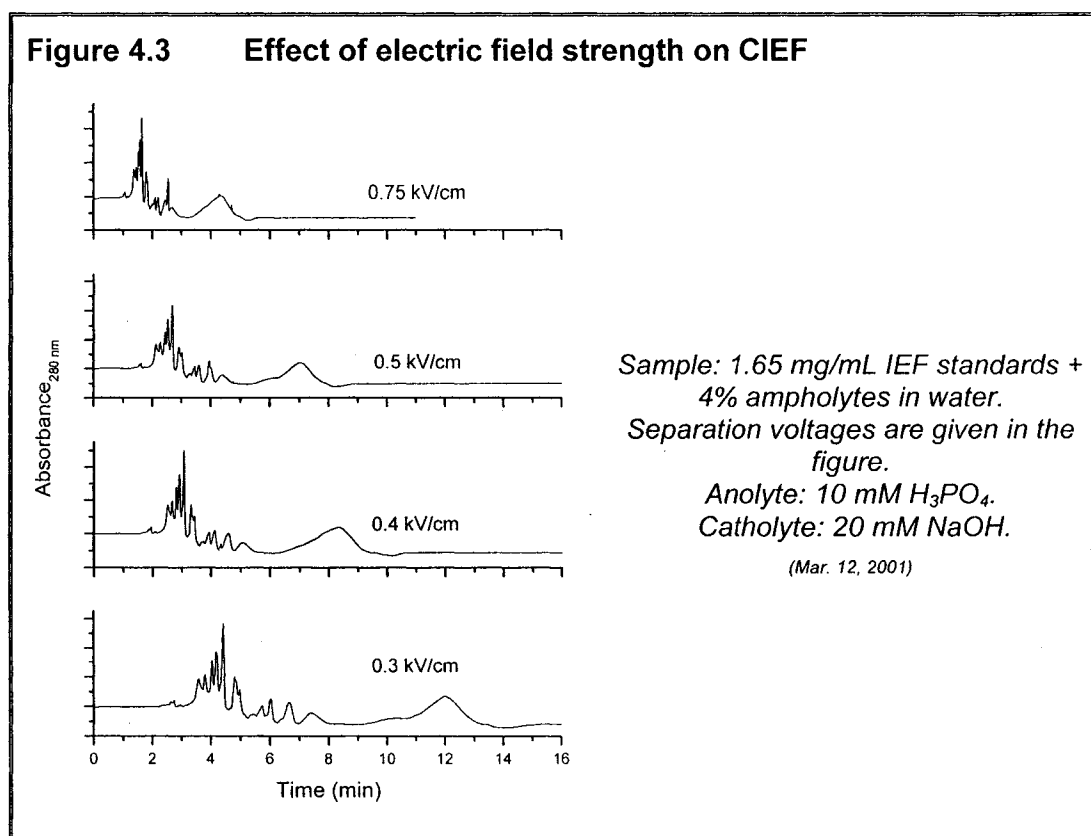


The left side of the above picture illustrates the IEF standards stained with Coomassie blue R-250 and crocein scarlet. The right side shows the unstained proteins. The pH range represented is from 9.6 (cytochrome c) to 4.45 (lowest phycocyanin band). This result was supplied by the manufacturer, Bio-Rad.

Comparing the electropherogram in Figure 4.1 to previous published work using the same mixed sample [see Figure 12 in Rodriguez-Diaz *et al.*¹], definite similarities are seen. By comparing the two results, in this work cytochrome c and the lentil lectins are not observed, hemoglobin A and myoglobin are represented by the tallest peaks in the spectrum and the broad peak at the end is phycocyanin.

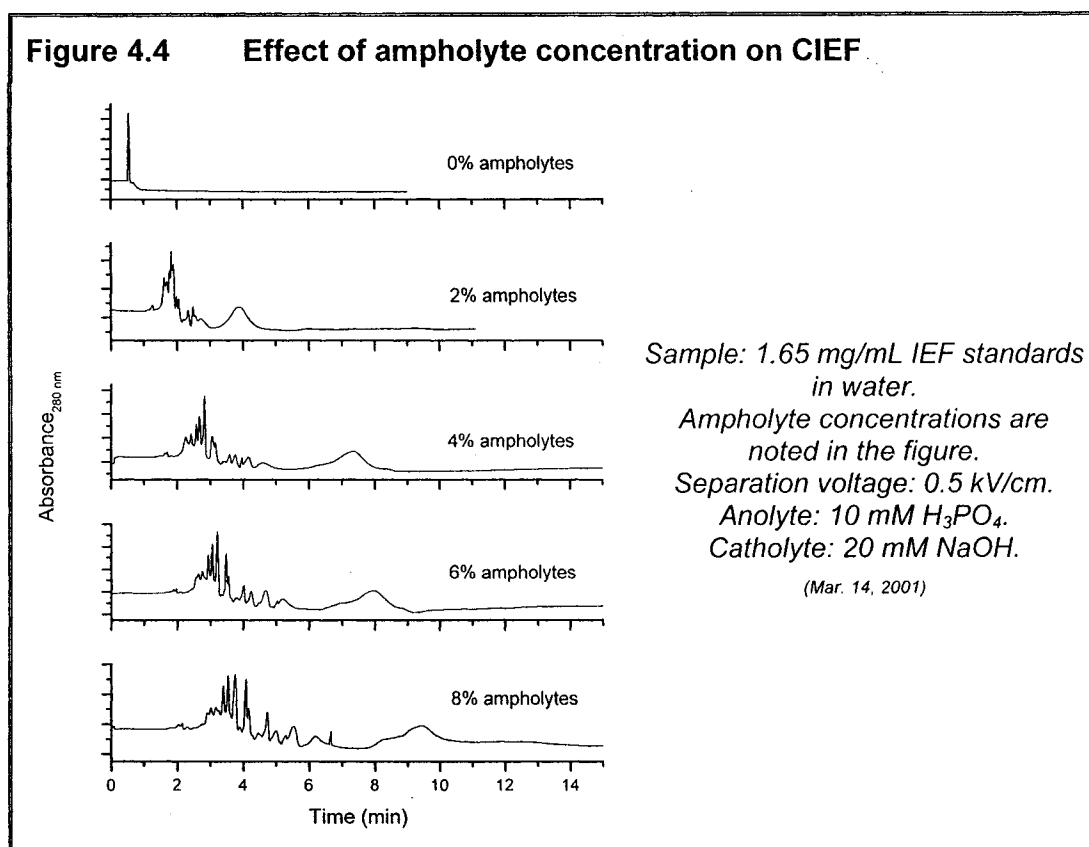
The resulting current seen in Figure 4.1 is typical of CIEF experiments. When the voltage is initially applied, the charged ampholytes and proteins will begin to migrate to their pI positions, as was explained in Section 1.3.2.1. When the various species reach their pI position, they will no longer have a net charge. As focusing progresses, there are fewer charged species in solution and hence a lower current. Focusing is thought to be complete when the current has decreased to 10% of its initial value.

The first parameter explored was electric field, as illustrated in Figure 4.3.



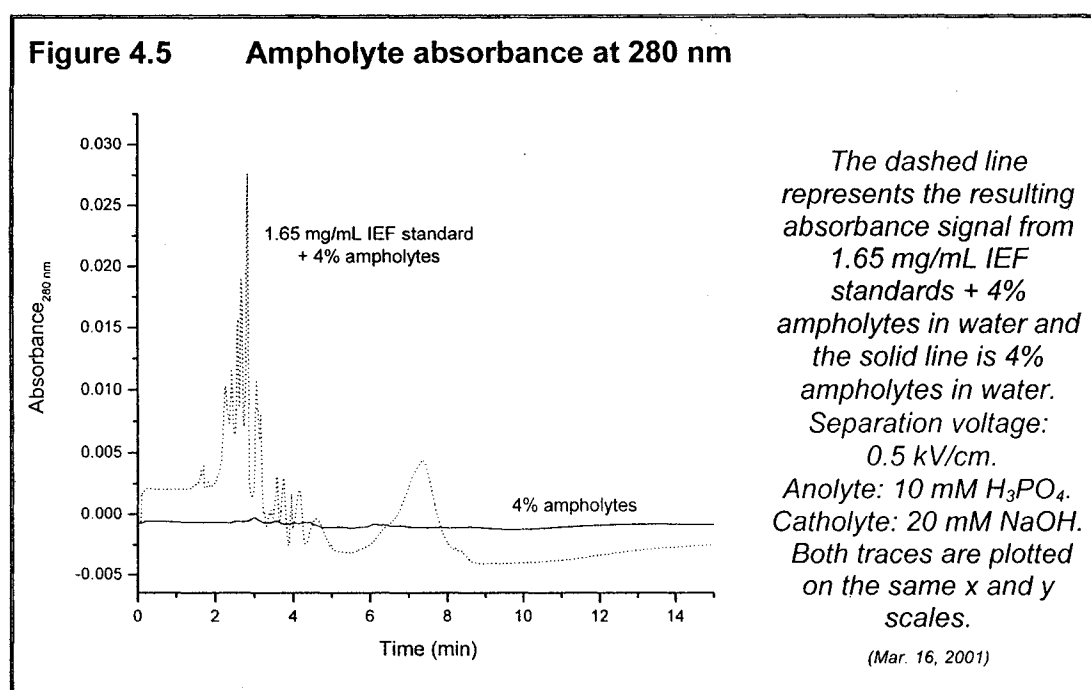
Electric field strength is not thought to affect resolution to a great extent in CIEF.¹ This is supported by the data presented above, in which there is little difference in resolution, though an increase in migration times at lower field strengths is noted. In the case of 0.75 kV/cm, it appears as if the peaks are not well resolved, this is only due to the compressed time scale. The electric field should be high enough to allow for rapid separations, but not so high as to induce Joule heating effects. Hence, 0.5 kV/cm was used for the remainder of this work.

The second parameter explored was ampholyte concentration, as is shown in Figure 4.4.



Choice of ampholyte type and concentration are perhaps the most important CIEF parameters. Many different types of ampholytes are commercially available in a wide range of pH values. Defining a highly linear pH gradient often requires that mixtures of ampholyte systems from different manufacturers be used. In this case, a single broad pH range (3.5-9.5) ampholyte system was chosen to

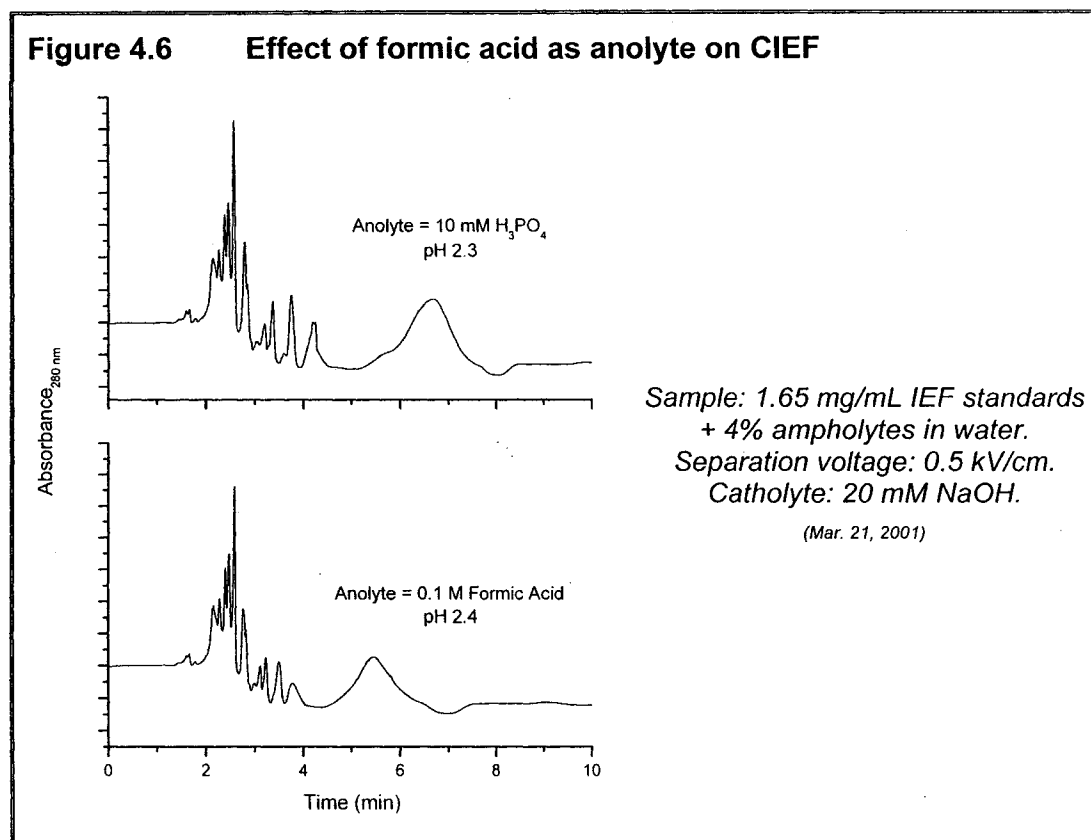
accommodate the sample. Looking at the first trace, in the absence of ampholytes, one can clearly see that no separation occurs, as would be expected. On increasing from 2% to 4% ampholyte, a great improvement in resolution is gained, but beyond this there is little improvement. It was expected that the ampholytes would interfere with the ESI-MS analysis⁵⁻⁷ to be done in subsequent work and, as such, an attempt was made to minimize their concentration. For the remainder of the CIEF study, 4% ampholyte was used. In order to ensure that the ampholytes were not interfering with the resulting absorbance signal, a blank containing only ampholytes was run and detected at 280 nm. The result is shown in Figure 4.5.



The results clearly indicate that the ampholytes were not an interference at this wavelength.

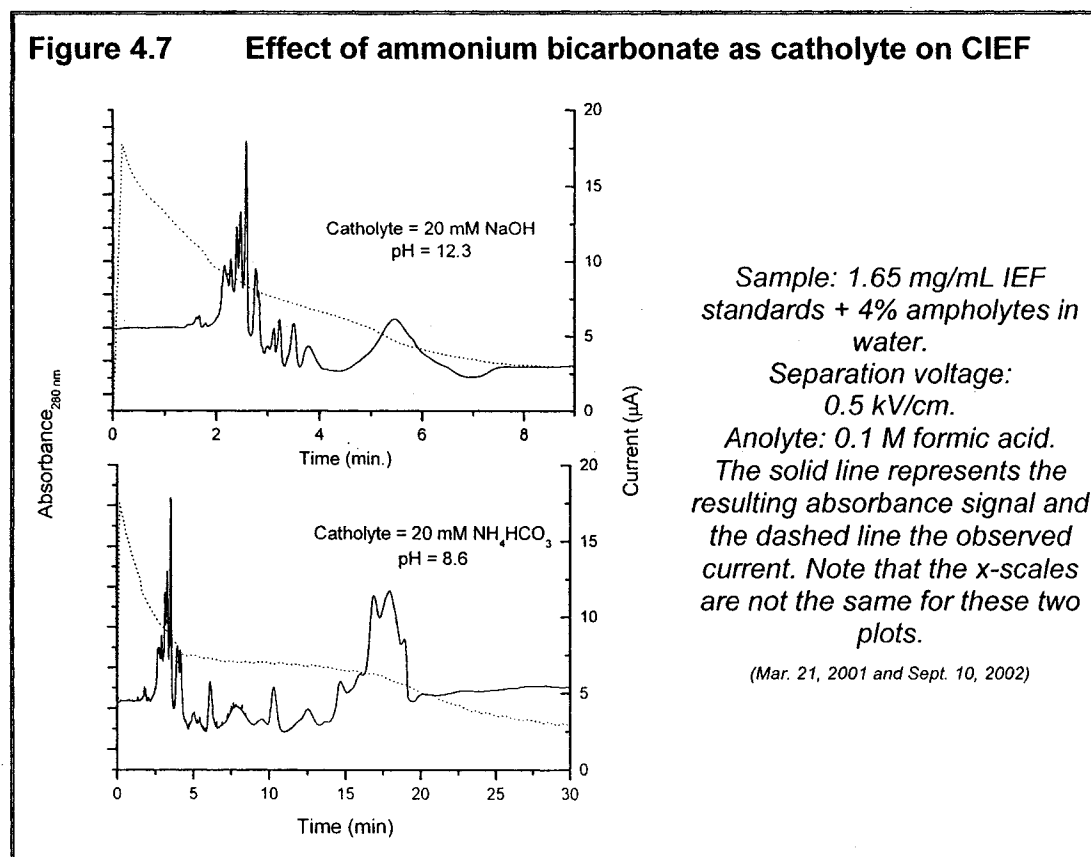
The anolyte and catholyte originally used were not compatible with the MS but provided a good reference point with which to compare our results. Formic acid was to be used in subsequent experiments to facilitate the ESI of the peptides and proteins. Figure 4.6 illustrates the effect of using formic acid as the anolyte for CIEF separation. Few differences were seen in the

electropherograms using either acid. The pH of the phosphoric acid was 2.3 whereas that of the formic acid was 2.4, so little change was expected.

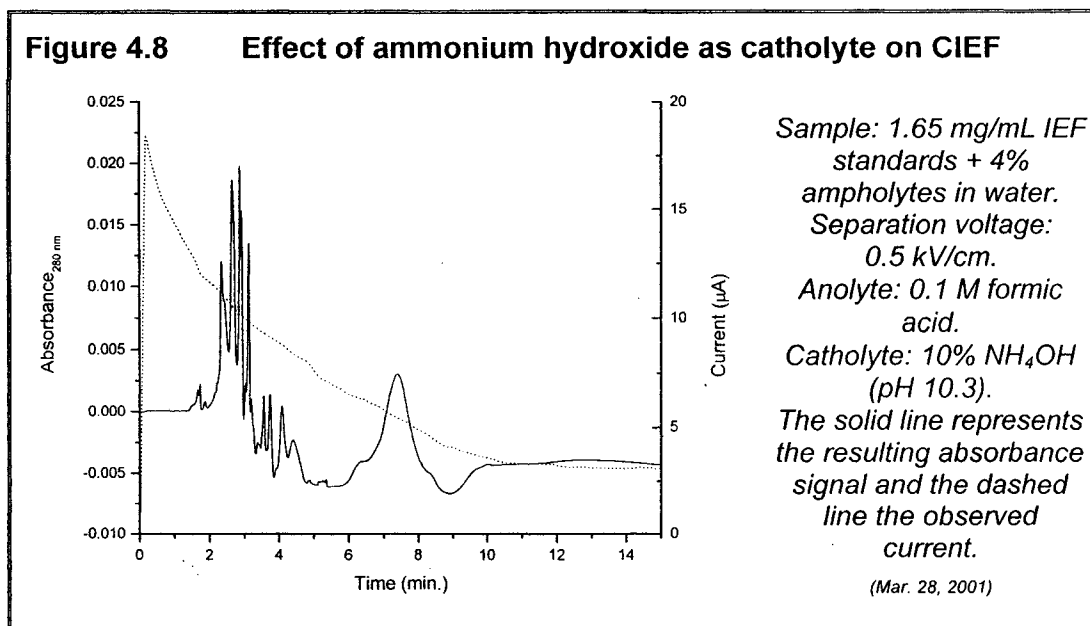


Sodium hydroxide (pH 12.3) was replaced with ammonium bicarbonate (pH 8.6) and the result is shown in Figure 4.7. Ammonium bicarbonate was chosen, as it would be used as the digestion buffer in subsequent work, and is compatible with ESI-MS. Comparing the two traces in Figure 4.7, there are noticeable differences, although the overall pattern of peaks remains similar. Most noticeably, the migration times become much longer using ammonium bicarbonate rather than NaOH. There are two problems related to the use of ammonium bicarbonate as catholyte. First, the low pH of this catholyte will lead to difficulties focusing more basic proteins. Second, it was later discovered that the presence of carbonates can alter the focusing process¹, by disturbing the

local pH. This may explain the bi-modal current trace in the lower plot of Figure 4.7.



Use of ammonium hydroxide as catholyte may be a better choice as it has been used previously for ESI-MS compatible CIEF.⁸ The result of using 10% ammonium hydroxide as catholyte is shown in Figure 4.8. A 10% ammonium hydroxide solution has a pH of 10.3, which is more comparable to the pH of the NaOH (12.3) catholyte originally used. The elution profile in Figure 4.8 is similar to that in the upper plot of Figure 4.7 and justifies the choice of ammonium hydroxide as a replacement for NaOH. It has yet to be determined whether ammonium hydroxide will be compatible with the rest of the platform, specifically the trypsin and SPE beds.



Optimization of CIEF parameters was limited in this thesis as it was also the focus of a collaborating research group at the National Research Council of Canada and as such, further optimization of this component was left in their hands.

4.3 PRESSURE DRIVEN FLOW THROUGHOUT THE SYSTEM

The platform was assembled as described in Chapter 3. For the pressure driven studies, the electrodes were in place but not used. These initial tests were mostly qualitative and as such, the exact amount of material introduced into the system was not always monitored.

4.3.1 MATERIALS AND METHODS

The chip was fabricated as described in Chapter 3. The beads were introduced to the bed region by pipetting them onto the head of the bed and keeping a house vacuum at the end of the bed. For the trypsin bed, the vacuum was applied at the inlet for the SPE bed and for the SPE beds, there was only

one outlet for all of the beds and hence the vacuum was applied there. Bed packing was somewhat inconsistent, as it proceeded sometimes without difficulties and sometimes with excessive problems. The source of these inconsistencies was not determined; however, persistence seemed to overcome these issues. The trypsin beads were prepared by extracting 200 μ L of the suspension supplied by the manufacturer (Immobilized TPCK Trypsin, 20230, Pierce Chemical Company, 2 mL gel suspended in 4 mL aqueous slurry containing 50% glycerol, 0.05% sodium azide) and washing it three times with 1 mL of 20 mM ammonium bicarbonate. The beads were then suspended in the same. The SPE beads were removed from the cartridge in which they came (Oasis® HLB Plus, 60 μ m, #1860001323, Waters) and 0.15 mg of beads were suspended in 0.5 mL of methanol (MeOH). The beads were washed three times with MeOH and three times with water and finally suspended in 0.5 mL of a 50:50, water: MeOH solution. Pressure driven flow into the system was accomplished through the use of a syringe pump (Harvard Apparatus, PHD 2000, syringes from Hamilton Company).

MS work was done using a single quadrupole Sciex API 150EX (Applied Biosystems / MDS Sciex). All experiments were done using positive electrospray ionization with various electrospray voltages depending on the flow rate used. For the work done on-chip, the following experimental parameters were defined using the software accompanying the instrument: nebulizer gas = 0, curtain gas = 8, orifice = 35 V, focusing ring = 175 V, entrance quadrupole = -10 V, inter-quadrupole lens = -11 V, prefilters (stubbies) = -15 V, first resolving quadrupole = -11 V, deflector = -250 V, channel electron multiplier = 2100 V. For data collection, a variety of mass-to-charge (m/z) ranges were used, but the step size was always 0.5 amu and the dwell time 1 ms. The pause time, time between full scans, was varied depending on the resolution required in the resulting chromatogram. Chemicals were obtained from the following sources: lysozyme from chicken egg white (L-6876), dithiothreitol (DTT) (D-5545), bovine serum albumin (BSA) with 0.3% DTT (A-8531), cytochrome c from horse heart (C-

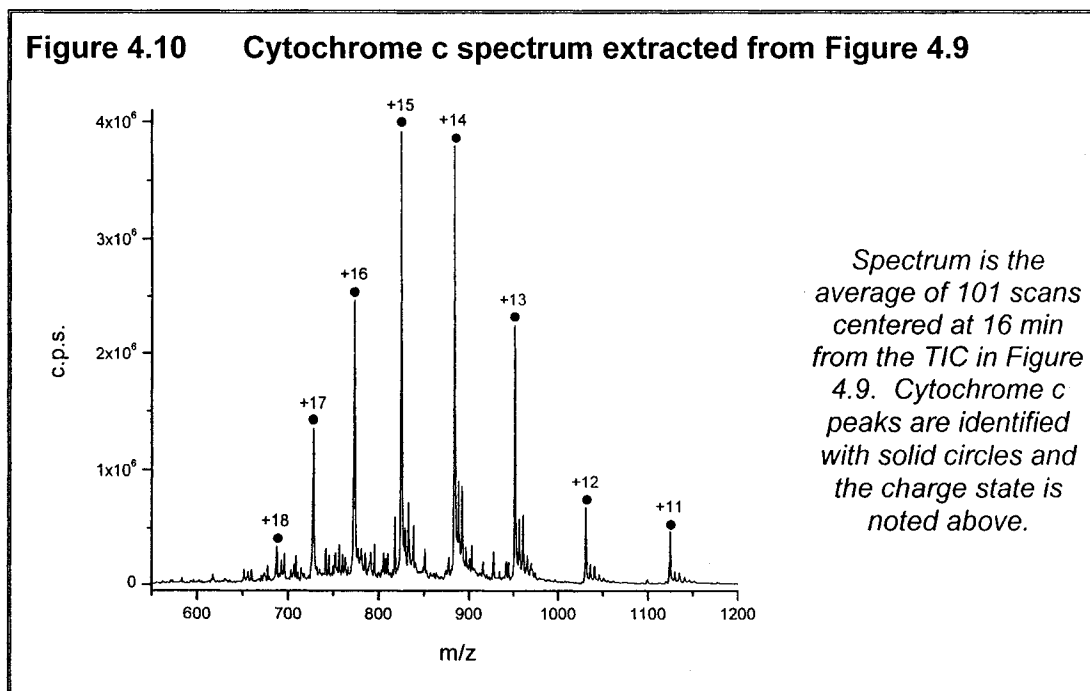
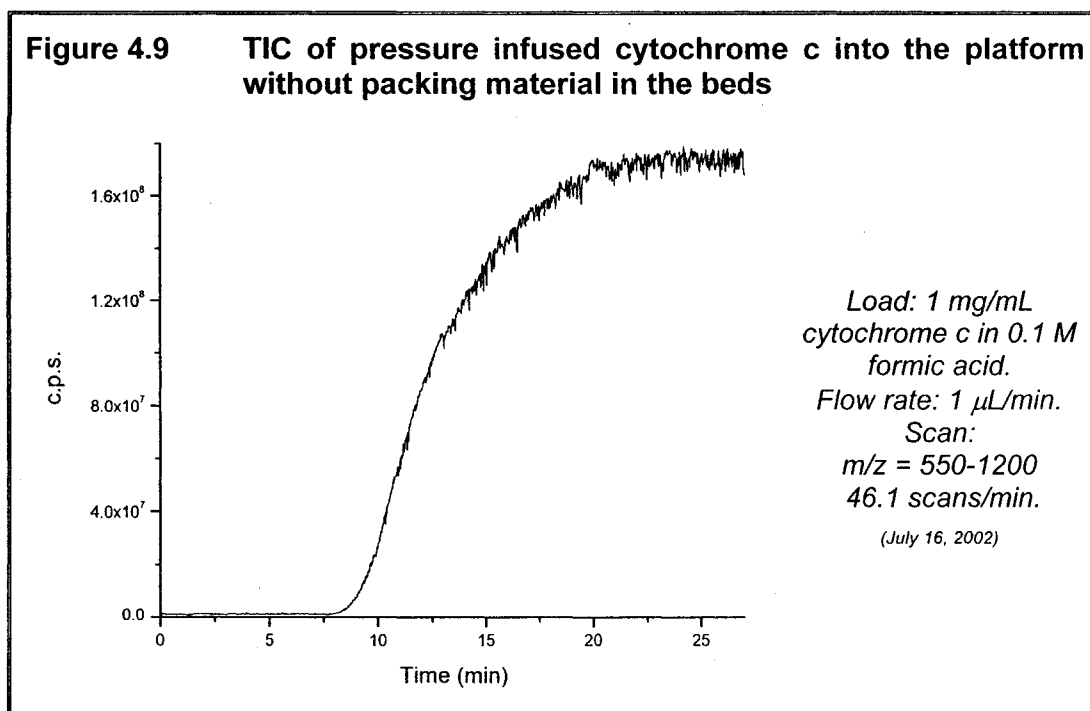
7752), angiotensin II (A-9525), iodoacetamide (Sigma Ultra I-1149), MeOH and acetonitrile (ACN) (both HPLC grade) from Sigma-Aldrich. All solutions were prepared in ultrapure water (Millipore Canada) and all aqueous solutions were filtered through a nylon syringe filter (0.2 μm , Chromatographic Specialties Inc.) before use. Organic solvents and proteins solutions were never filtered. Both the MeOH and ACN were distilled before use. All protein solutions were prepared in siliconized vials (Rose Scientific Ltd.).

Cysteine bonds were reduced using the following protocol. In a siliconized vial, 5 μL of 1 mg/mL protein solution was mixed with 10 μL of 0.1 M NH_4HCO_3 and 5 μL of 45 mM DTT and incubated either for 20 min at 37 $^\circ\text{C}$ or for 1 hour at room temperature. Then, 5 μL of 100 mM iodoacetamide was added and the solution was allowed to stand at room temperature in the dark for 20 min. Concentrations were changed somewhat to accommodate lower protein concentrations, but the molar ratios remained the same.

4.3.2 PRESSURE DRIVEN FLOW – BEDS NOT PACKED

The first measurements with the platform used pressure driven flow into the sealed system with no packing material in the beds. A solution of cytochrome c was introduced at the inlet and driven towards the MS. This first test served to optimize the electrospray conditions, as well as to test whether the system had been sealed properly. Using the final chip holder described in the previous chapter, and the first ESI interface (LJ-1), the following results were obtained. Figure 4.9 shows the total ion chromatogram (TIC) that was obtained. The TIC is the sum of the intensities of all the mass-to-charge (m/z) values scanned. It is represented as counts per second (c.p.s.) versus time. Each time point in the TIC has an m/z spectrum associated with it. These spectra can be extracted and averaged. An extracted spectrum from the TIC in Figure 4.9 is shown in Figure 4.10 depicting a typical ESI-MS spectrum for cytochrome c. The result is an envelope of peaks, each of which represents a different charge state for

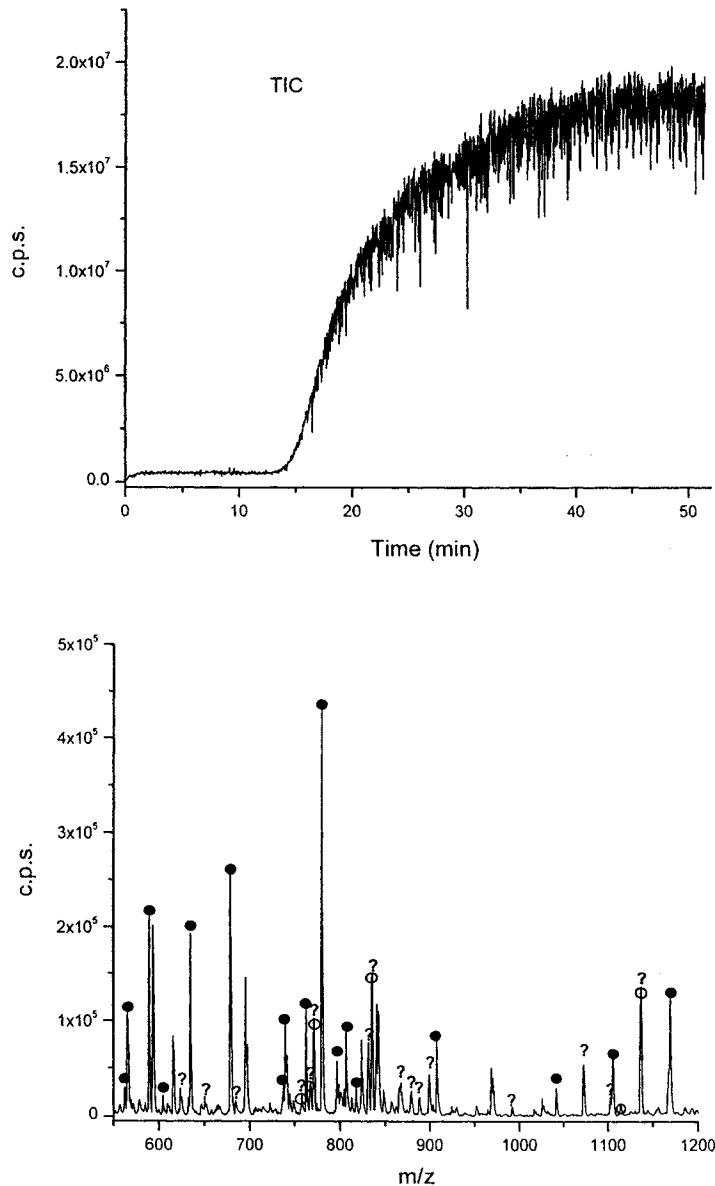
cytochrome c. The various cytochrome c charge states and m/z values are listed in Table 4.1, which can be found in the Appendix to this chapter.



4.3.3 PRESSURE DRIVEN FLOW – TRYPSIN BEDS PACKED

The trypsin beds were packed as described in the experimental section and cytochrome c was introduced in order to test the digestion step. The resulting TIC and extracted spectrum are shown in Figure 4.11. Several cytochrome c peptides were identified and no undigested cytochrome c peaks were seen. Table 4.2 in the Appendix to this chapter lists cytochrome c peptides that were identified throughout the course of this work, not all were seen in every spectrum. Peptides were identified through database searching using a combination of ExPASy (<http://us.expasy.org/>) and Protein Prospector (<http://prospector.ucsf.edu/>) tools. All search parameters are outlined in the Appendix. Sequence coverage was defined as the number of amino acid residues identified in the resulting peptides, divided by the total number of residues in the protein. Several unidentified peaks were seen in Figure 4.11. Some of these were trypsin autodigestion peaks and were identified with hollow circles (see Table 4.3 in the Appendix for a list of trypsin-related peaks), others were not positively identified. As experiments proceeded and techniques developed, many of these non-cytochrome c peaks were no longer seen. New devices were used and bed packings exchanged and the problem did not resurface. Peaks identified with question marks were also seen in the washing phase of later experiments done with packed SPE beds (Figure 4.14). This suggests that whatever the identity of these peaks, they were not retained by the SPE phase, as was confirmed in later trials utilizing the SPE bed.

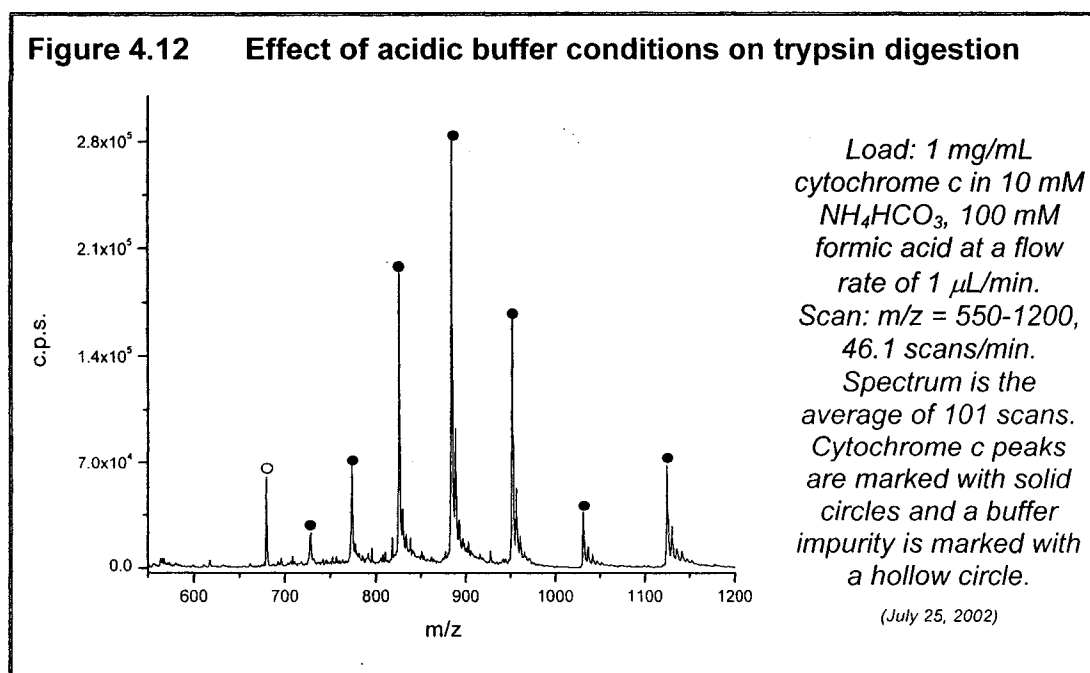
Figure 4.11 TIC and extracted spectrum of pressure infused cytochrome c into the platform with the trypsin beds packed



Load: 1 mg/mL
 cytochrome c in 20 mM
 NH_4HCO_3 at a flow rate
 of 1 $\mu\text{L}/\text{min}$.
 Scan: $m/z = 550-1200$,
 46.1 scans/min.
 Spectrum is the
 average of 101 scans
 centered at 14 min from
 the TIC. Cytochrome c
 peptides are marked
 with solid circles and
 possible trypsin
 autodigestion peaks
 with hollow circles. The
 question marks
 represent unidentified
 peaks that were not
 retained by the SPE
 beds in later trials, they
 are introduced for ease
 of comparison to Figure
 4.14. Sequence
 coverage was 77%.

(July 26, 2002)

This initial run was done using 20 mM ammonium bicarbonate (pH = 8.6) as the digestion buffer. This was the digestion buffer used in previous single channel work done in this lab.⁹ Once the system is used to process input from a CIEF column, a variety of pH values will be associated with the incoming samples. In order to test the ability of the trypsin to afford digestion at more acidic conditions, cytochrome c was introduced in 10 mM ammonium bicarbonate and 100 mM formic acid (pH = 3). The resulting extracted spectrum is shown in Figure 4.12.



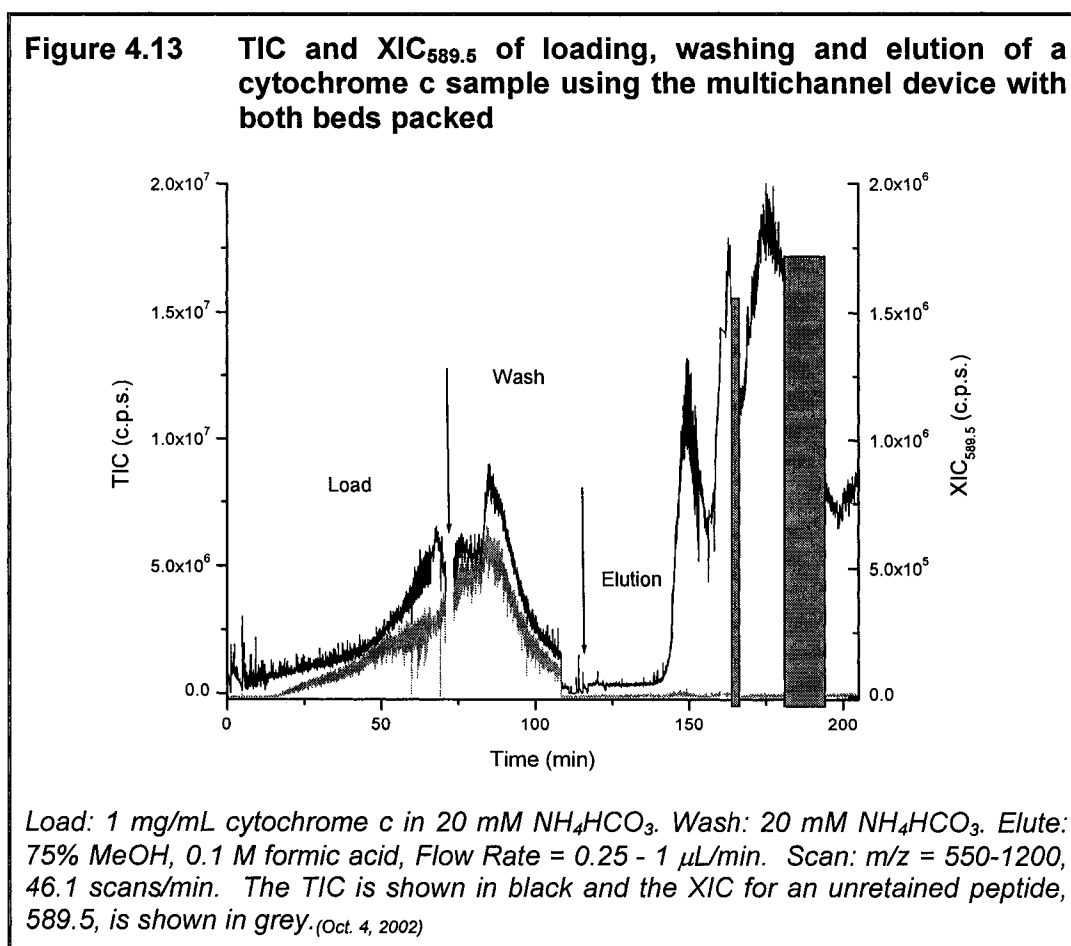
From the above spectrum, it is obvious that no digestion is seen, indicating that the immobilized trypsin will not tolerate acidic pH values.

An incoming CIEF sample plug may be diluted by the digestion buffer already in the bed, serving to normalize the various pH values and allow digestion to proceed. If, however, this problem persists, a sheath flow may be necessary in order to optimize the pH values of the incoming samples. Such a sheath flow could also solve the problem of using ammonium bicarbonate as the catholyte for CIEF separation. If ammonium bicarbonate is introduced post-CIEF as a sheath flow, then ammonium hydroxide could be used as the catholyte. The

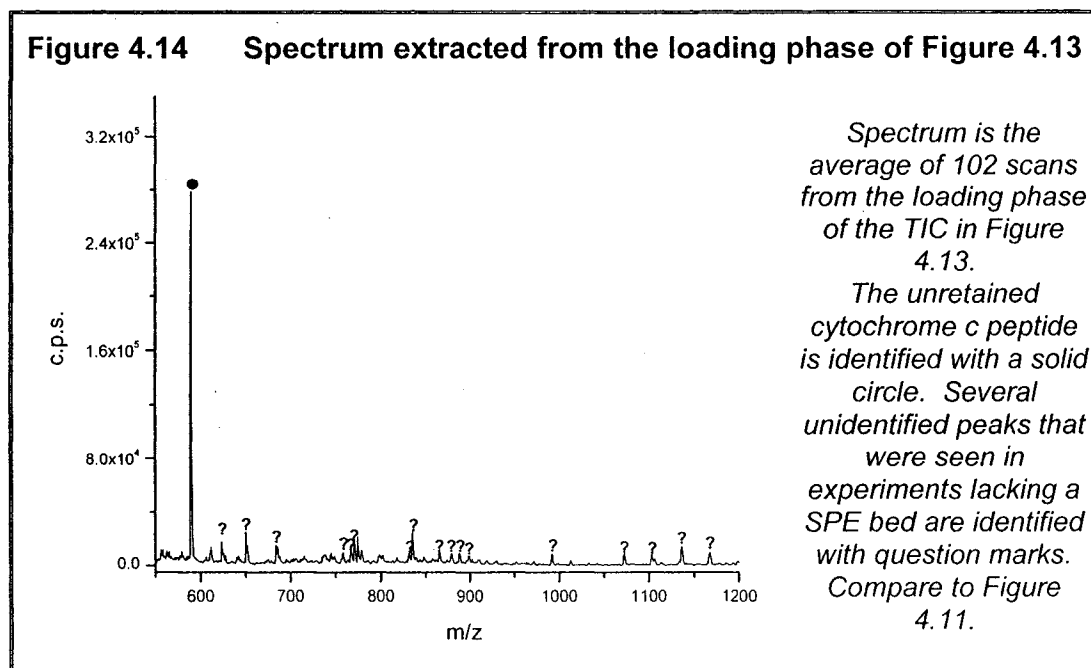
sheath flow could be introduced by an additional channel with the microchip device. This idea is explored further in Section 5.2.2.

4.3.4 PRESSURE DRIVEN FLOW – BEDS PACKED

Both the trypsin and SPE beds were packed and the entire device was tested. Experimental procedure for pressure driven flow within the entire platform consisted of three steps: loading, washing and elution. The first attempt at this procedure is shown in Figure 4.13. The black trace represents the TIC and the grey trace the extracted ion chromatogram (XIC) for $m/z = 589.5$. The XIC represents the intensity versus time plot for the signal at $m/z = 589.5$. This information can be extracted from the TIC.

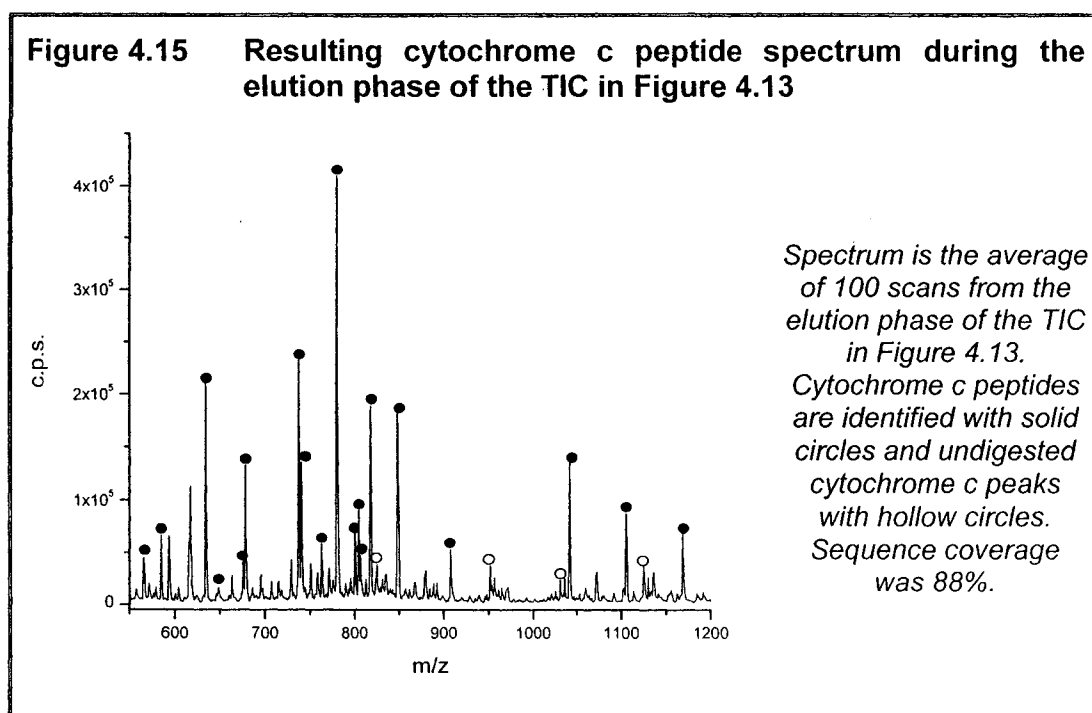


During the loading phase, cytochrome c was pressure driven into the system. A single peak, $m/z = 589.5$, is seen in the resulting spectrum during this phase, as shown in Figure 4.14. The signal at $m/z = 589.5$ is a cytochrome c peptide that is not retained by the SPE beds. The XIC for this peptide is shown in Figure 4.13. This unretained peptide, $m/z = 589.5$, proved to be a useful marker for monitoring the bed loading and washing steps.



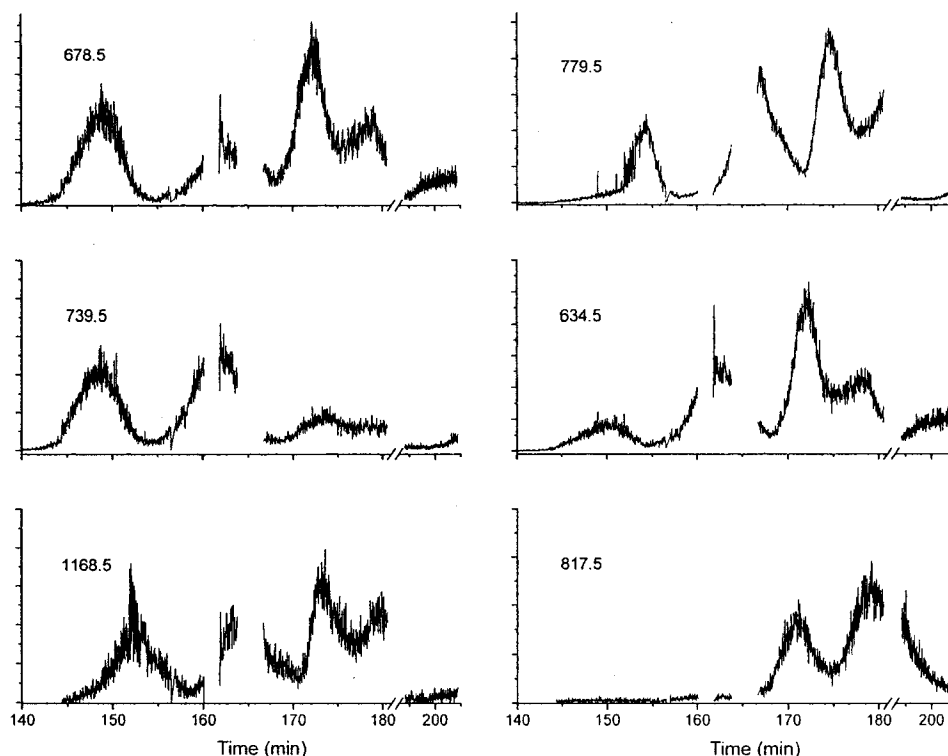
At an arbitrary time, the washing phase was initiated with the introduction of 20 mM ammonium bicarbonate. There is a break in the TIC as the flow was stopped and the solutions exchanged. Once it appeared that the TIC was returning to baseline, the flow was again stopped and the elution buffer was introduced. The two superimposed boxes in Figure 4.13 represent areas of missing data. The first smaller region was due to an instability in the electrospray signal. As the buffer began to switch from 100% aqueous to the organic phase, stabilizing the ESI signal became difficult. Optimal electrospray conditions for aqueous and organic conditions are not the same and it took some time to find conditions amenable to both. The flow rate was changed in order to optimize ionization, as indicated in the caption of Figure 4.13. This approach was later

abandoned as it created difficulties in calculating injected volumes. The second, larger box was due to a computer crash caused by the overwhelming amount of data created. This was avoided in future work by changing the pause time in the scanning parameters, which allowed for a longer wait time between full scans, resulting in fewer scans being collected. A spectrum was extracted from the elution phase of the TIC in Figure 4.13 and is shown in Figure 4.15.



In this case, some undigested cytochrome c was seen in the extracted spectrum. It was noted that peptide (and cytochrome c) signal intensities varied at different time points in the TIC. Extraction of XICs for various peptides resulted in the elution profiles shown in Figure 4.16. One can see that the various peptides exhibit unique behaviours. Several possible reasons were postulated as to why these offset elution traces were seen.

Figure 4.16 Cytochrome c peptide XICs extracted from the TIC in Figure 4.13



All plots use the same x-scale but variable y-scales. The m/z that was extracted is noted above each plot. There is a break in the x-axis from 181 to 193 which represents the missing data referred to in Figure 4.13. Two smaller breaks are also seen which are due to electrospray instabilities. All conditions were noted in Figure 4.13.

It was suspected that there were some chromatographic effects taking place as the peptides eluted from the SPE bed. Thus, it was hoped that use of a stronger eluent should resolve this problem. It was also suspected that some ion suppression was occurring^{10,11}, which is supported by the noticeable offset of peptide 779.5. The effects of stronger eluent were explored using the entire multichannel device, however a more in depth study of the elution profiles was done using a single channel device and is presented in Section 5.3.5.

4.3.5 ELUENT EFFECTS

To understand the apparent chromatographic behaviour that was seen previously, a stronger eluent was used to facilitate a flash elution. In order for the delay line concept to be functional, a flash elution from the SPE beds was necessary. The TIC and XIC_{589.5} for elution with 50% ACN are shown in Figure 4.17. It should be noted that at this point, the second ESI interface (SS-1) from the previous chapter was introduced. This interface consisted of coupling the microchip to the ESI tip using a piece of stainless steel of matching outer diameter (360 μm o.d., 175 μm i.d.). The sharp peak at the beginning of the elution step looks promising, but the XICs shown in Figure 4.18 show similar elution profiles as were seen in Figure 4.16.

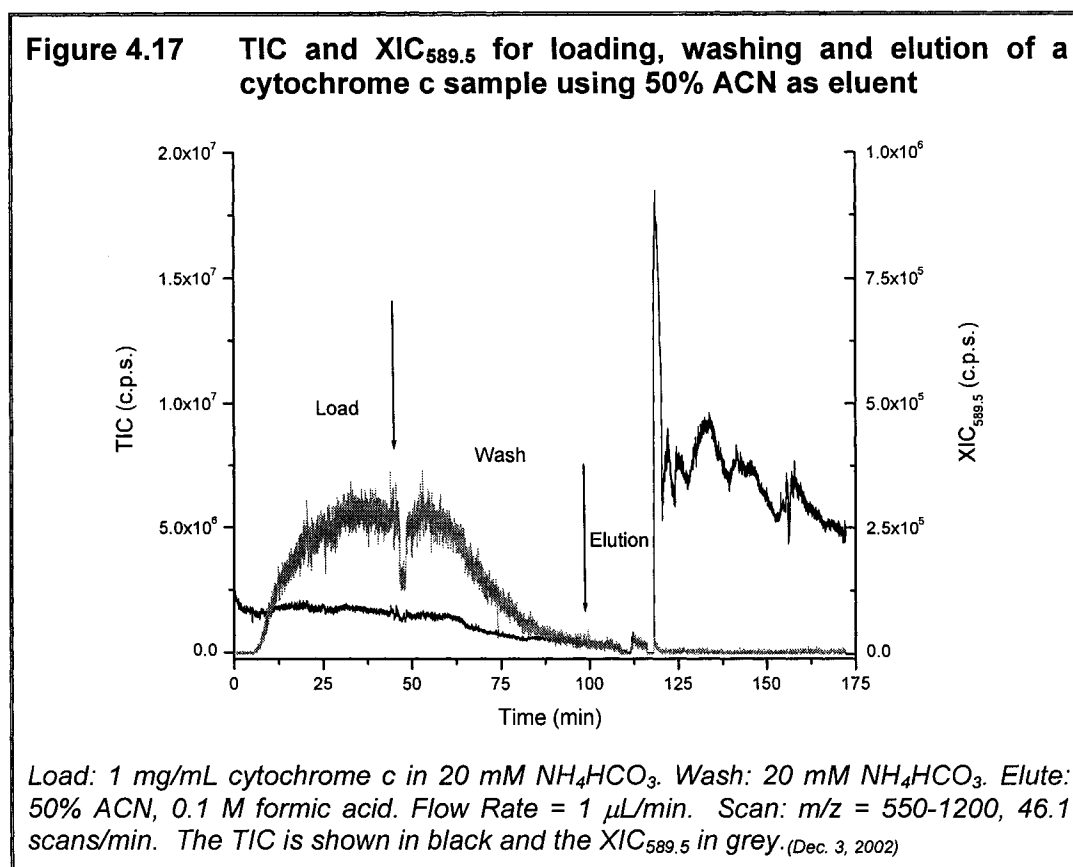
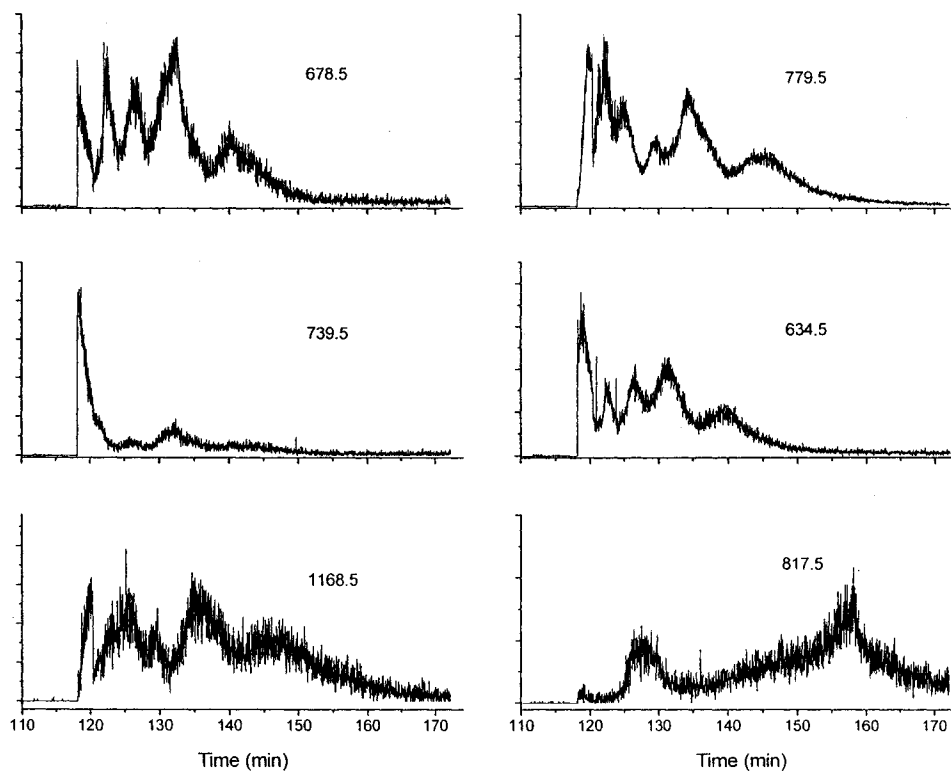


Figure 4.18 Cytochrome c peptide XICs extracted from the TIC in Figure 4.17



All plots are on the same x-scale but variable y-scale. The m/z that was extracted is noted above each plot.

These results do not identify the cause of the problem but do make it clear that simply switching to a stronger eluent does little to resolve it. As mentioned before, the multichannel system had been designed to function as a whole and pinpointing problems within it was difficult. Many of these issues will be explored in the following chapter, which focuses on methods by which to evaluate the individual components of the device. After using ACN as eluent for four runs, the trypsin beds ceased to function. Hence, the use of ACN was not feasible and the remainder of the multichannel work was done with MeOH as the eluent, usually at 50%.

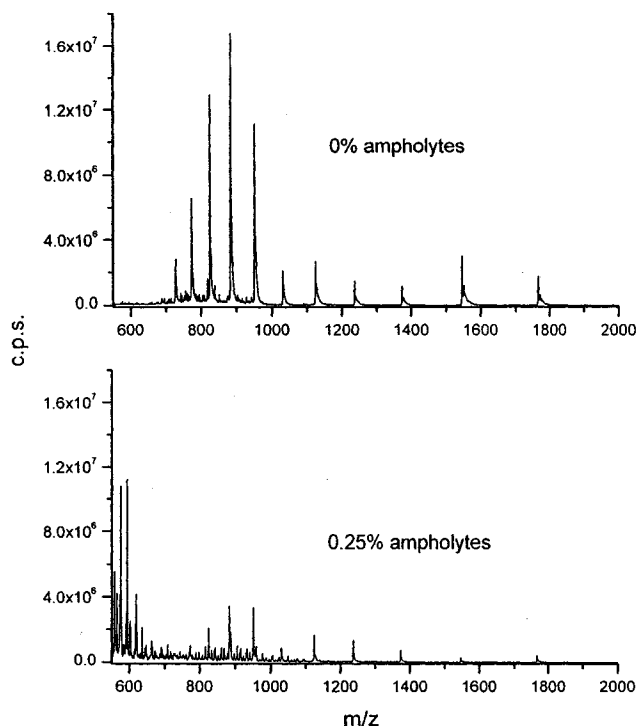
In the TIC in Figure 4.17, one can see that the electrospray signal crashed briefly at the beginning of the elution phase. This was seen often and sometimes

the electrospray tip would be physically clogged and have to be removed and rinsed. It was suspected that some precipitation was occurring as the incoming organic phase met the buffer phase. In order to avoid this problem, a quick rinse with water was done after the first ammonium bicarbonate washing step. This additional step completely solved this problem and was incorporated into subsequent experimental procedures.

4.3.6 ADDITION OF AMPHOLYTES

This platform was designed to handle input from a CIEF column which would contain ampholytes as well as the sample of interest. It is well known that ampholytes suppress protein signal in ESI-MS.⁵⁻⁷ Within an electrospray droplet the species of higher concentration will orient itself on the outside of the droplet which will more readily lead to the formation of gas phase ions. The lower concentration species will resist the transformation to the gas phase and will orient itself in the center of the droplet, leading to the formation of less gas phase ions. Hence, when the ampholyte concentration is high relative to the analyte concentration, the result is the formation of more gas phase ampholyte molecules and less gas phase analyte molecules. This problem has been overcome in the past using several methods: sheath flow to dilute ampholyte concentration⁸, microdialysis junctions^{12,13} to remove them, and free-flow electrophoresis¹⁴ to separate the ampholytes from the sample. In order to test the effects of the ampholytes on ESI-MS, a quick experiment was done using the conventional ionspray source for the instrument. Spectra of cytochrome c alone and in the presence of 0.25% ampholytes are shown in Figure 4.19. The signal is drastically suppressed even in the presence of a small amount of ampholytes. The CIEF study presented in Section 4.2.2 suggests that 0.25% would not be a high enough ampholyte concentration to afford a quality separation.

Figure 4.19 Effect of ampholytes on cytochrome c signal



Spectra were accumulated using the conventional ionspray source and represent the sum of 30 scans.

Sample: 0.1 mg/mL cytochrome c in 50% MeOH, 0.1 M formic acid with (top) and without (bottom) ampholytes.

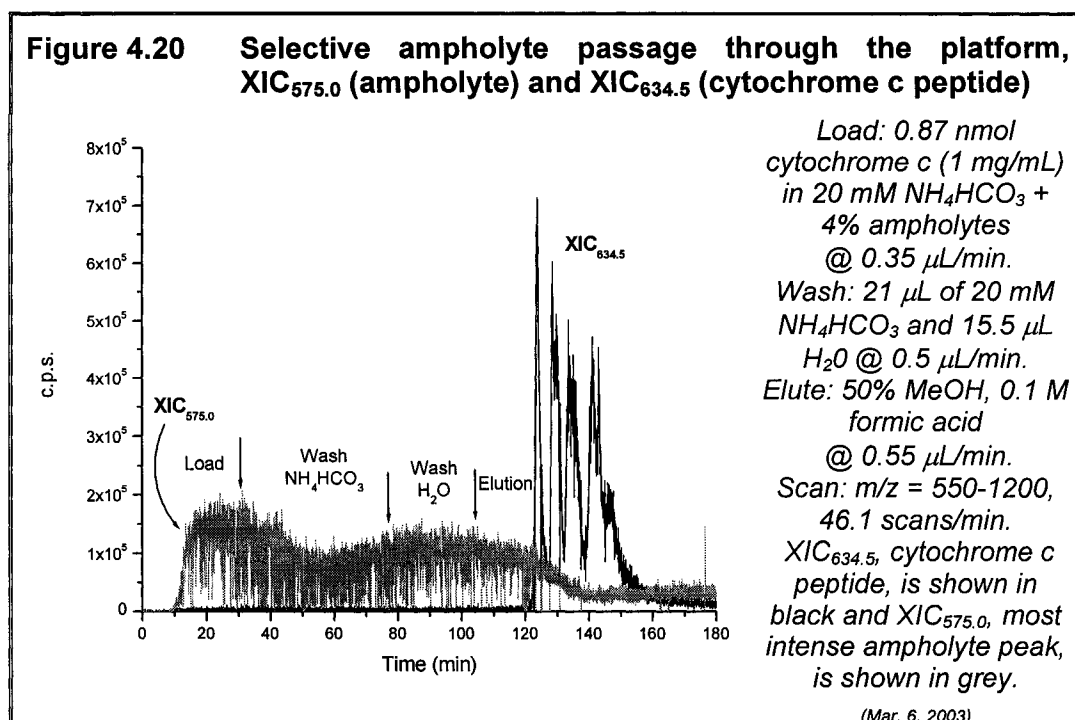
Flow rate = 3 μ L/min.

Scan: m/z = 550-2000, 20.7 scans/min.

Both spectra are on the same scales.

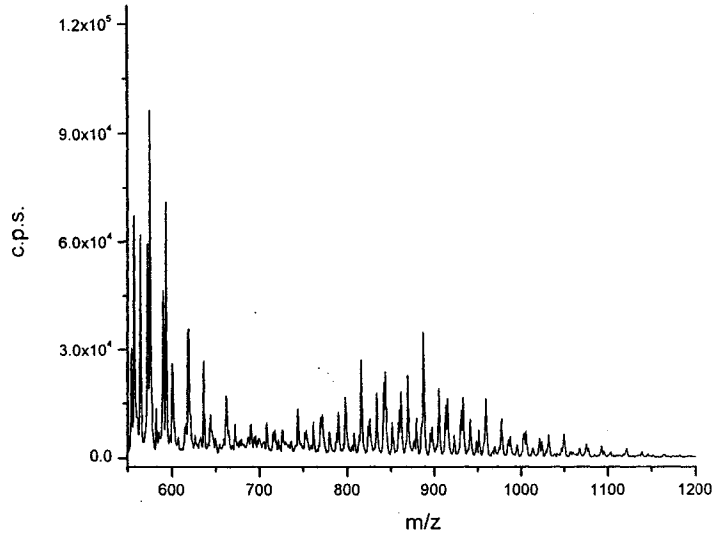
(Apr. 6, 2001)

The SPE beds on the chip were intended to selectively trap the peptides while allowing the ampholytes to pass through to waste. This assumption was tested by running the system as before, but with ampholytes added to the sample. The strongest ampholyte peak, $m/z = 575.0$, and the quickest eluting cytochrome c peptide, $m/z = 634.5$, were monitored and the resulting XICs are shown in Figure 4.20. The resulting plot illustrates that the majority of the ampholyte is removed before the elution step.



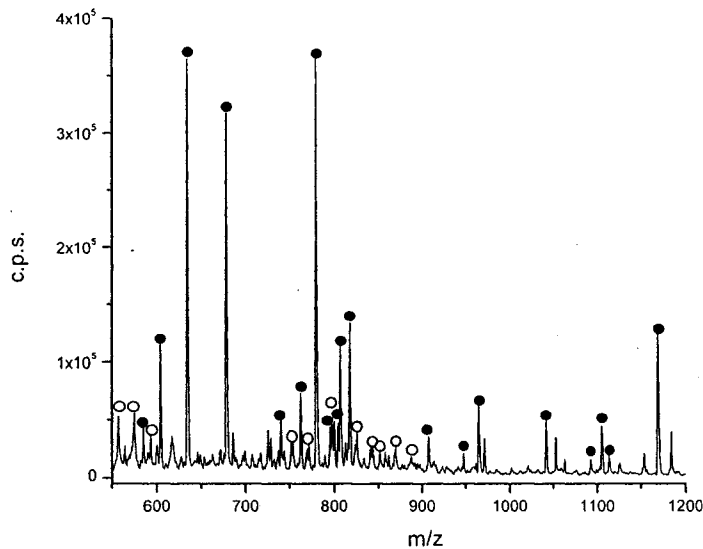
Spectra extracted from the loading phase of Figure 4.20 result in a typical ampholyte spectrum (Figure 4.21), while those extracted from the elution phase result in a spectrum dominated by peptide signals (Figure 4.22). Some ampholyte related chemical noise remains after the SPE step, but does not strongly interfere with peptide ionization or measurement. Only the most prominent of the ampholyte peaks were identified in Figure 4.22, most of the smaller unlabelled baseline peaks could also be attributed to ampholytes. This first experiment was done using 4% ampholytes, as was suggested by previous work done in optimizing the CIEF conditions. However, this project is part of a larger collaborative project in which the other half of the partnership has developed and optimized CIEF conditions leading to high resolution protein separations. They have chosen to use 1% ampholytes in a much longer capillary than was used in the optimization study undertaken in this lab. For the sake of consistency, the remainder of the work presented in this chapter used 1% ampholyte. A lower ampholyte concentration should suppress the analyte signal less, and be easier to reduce by SPE.

Figure 4.21 Typical ampholyte spectrum extracted from the loading phase of Figure 4.20



Spectrum is the average of 103 scans taken during the loading phase of Figure 4.20.

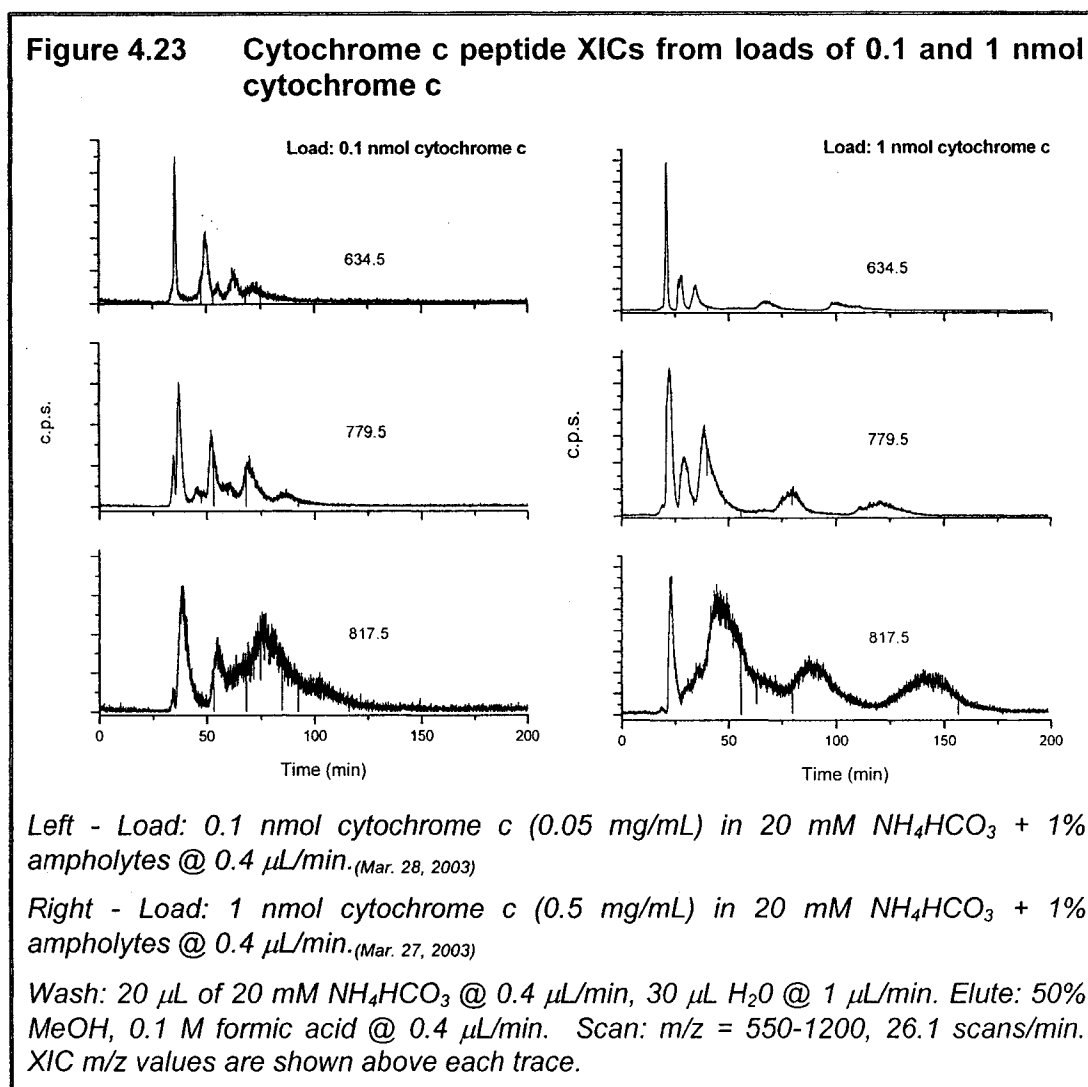
Figure 4.22 Extracted cytochrome c peptide spectrum from the elution phase of Figure 4.20



Spectrum is the average of 103 scans taken from the elution phase of Figure 4.20. Cytochrome c peptides are identified with solid circles and ampholyte peaks with hollow circles. Sequence coverage was 89%.

4.3.7 EFFECT OF CONCENTRATION

The issue of the irregular elution profiles was readdressed. It was considered that sample load may play a role in defining the elution pattern. In order to test this, two experiments were done under the same conditions using a ten fold difference in concentrations. XICs are shown in Figure 4.23 for 0.1 and 1 nmol loads of cytochrome c.

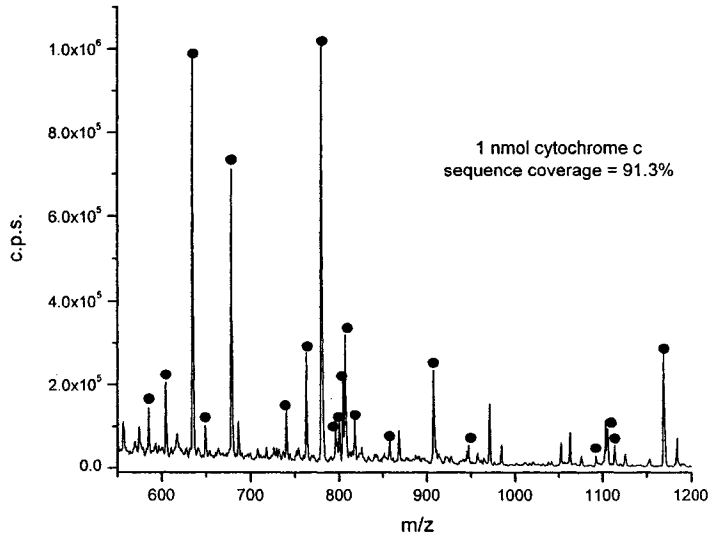


The elution profiles are similar yet not identical, but there is no evidence that loading is a major factor in elution profile distortion. It should be noted that in all elution profiles shown for the protein studies, the time at which elution begins is

arbitrary and hence elution times can not be compared between different runs. There were difficulties in stabilizing the ESI signal while simultaneously initiating the data acquisition, and hence the absolute start time could not be accurately determined. All elution profiles should be compared on the basis of their shape and duration but not on absolute elution time.

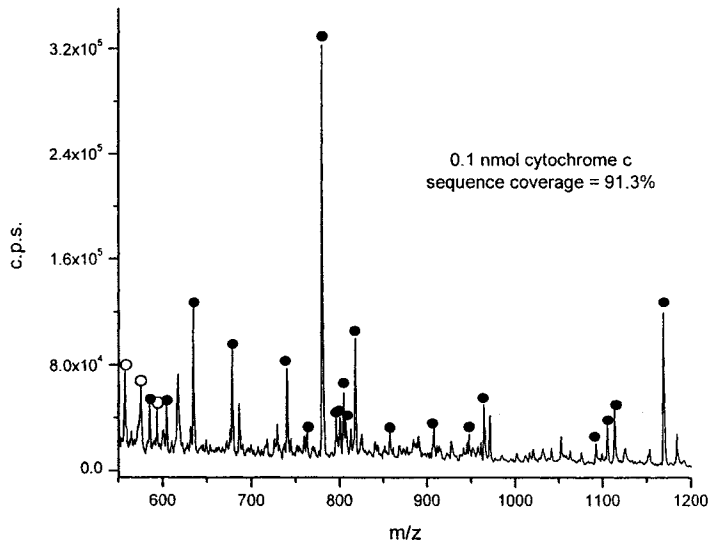
A few other points are worth considering when comparing the extracted spectra for these two runs, which are shown in Figure 4.24. First, as the protein load decreases, the ampholytes become a greater spectral interference, as would be expected. When identifying peptides where ampholytes were used, care was taken not to assign any peptide where there was a high probability of an ampholyte peak. Hence, if ampholyte and peptides peaks were seen at the same m/z , the peak was assumed to be ampholyte. Even assuming this, the sequence coverage is high, 91.3%, and does not decrease at lower loading. This indicates that the system has more than enough sensitivity at a 0.1 nmol load, though it is also a reflection of the ease of analysis of cytochrome c. Second, when comparing these two spectra, which were extracted at different time points from their respective TIC, it is easy to see how the peptide distribution changes depending on where in the elution profile the spectrum is extracted. Lastly, the unknown peaks that were observed earlier are no longer seen. This is most likely due to more thorough washing steps.

Figure 4.24 Spectra from 0.1 nmol and 1 nmol cytochrome c loading



Top: Spectrum is the average of 107 scans taken from the right-hand plots of Figure 4.23, centered at 20 min.

Bottom: Spectrum is the average of 100 scans taken from the left-hand plots of Figure 4.23, centered at 37 min.



Cytochrome c peptides are indicated by solid circles and ampholyte peaks by hollow circles. Plots are on the same m/z scale but different c.p.s. scales.

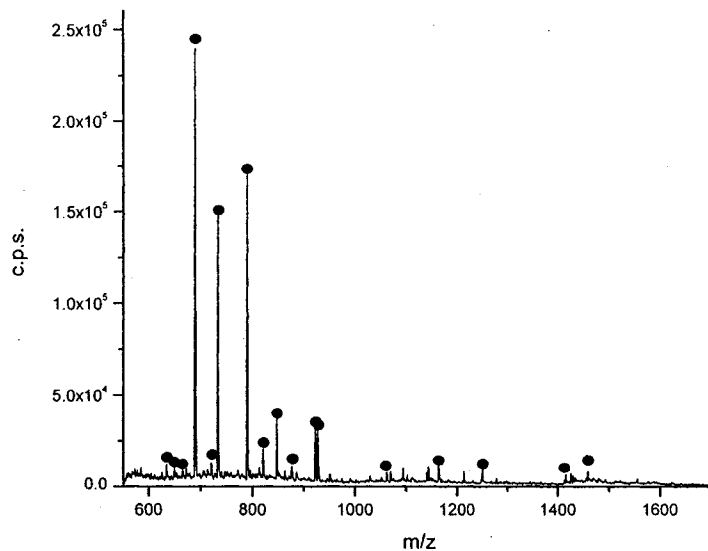
4.3.8 METHOD VALIDATION – STANDARD PROTEINS

In order to test the ability of this system to process actual protein samples, three standard proteins were run. For cytochrome c, the results have already been presented. This protein is easy to work with, digest and identify. The second protein was bovine serum albumin (BSA), which will digest somewhat without modification and is quite large. The third was lysozyme. This was the most challenging, as it will not digest without prior reduction of the disulphide bonds. It is also difficult to work with, as it has a tendency to precipitate. Disulphide reduction is performed using dithiothreitol (DTT) after which the thiols are capped using iodoacetamide. This procedure was outlined in Section 4.3.1.

4.3.8.1 BSA

Initial trials with BSA were done without prior reduction of disulphide bonds, however the BSA sample used did contain 0.3% DTT from the manufacturer. No ampholytes were used initially. The resulting spectrum for a 0.1 nmol load is shown in Figure 4.25 and a list of peptides for the unreduced BSA is presented in Table 4.4 in the Appendix. Even at low loading, the BSA peptides were easily identifiable, although there were not many. In order to confirm that the elution profiles seen with cytochrome c were not sample dependent, XICs were extracted for the most intense BSA peptides and are shown in Figure 4.26. Similar complex elution profiles are seen in this case as well, so the possibility of protein dependence can be ruled out.

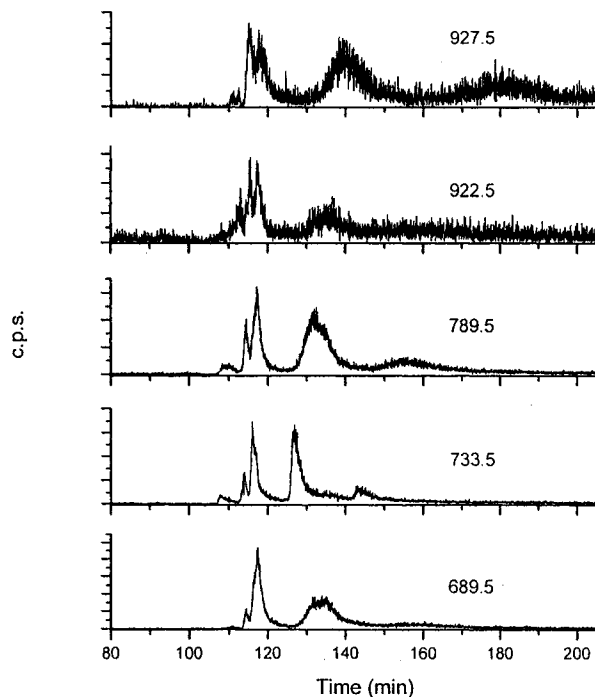
Figure 4.25 Spectrum of a 0.1 nmol BSA load, disulphide bonds unreduced



Load: 0.1 nmol BSA
(0.25 mg/mL) in 20 mM
 NH_4HCO_3 .
Wash: 18.4 μL of 20 mM
 NH_4HCO_3 , 19.2 μL H_2O .
Elute: 50% MeOH,
0.1 M formic acid.
Flow Rate = 0.4 $\mu\text{L}/\text{min}$.
Scan: 550-1700,
28.9 scans/min.
Spectrum is the average
of 104 scans. The
resulting BSA peptides
are indicated by the
solid circles. Sequence
coverage was 24%.

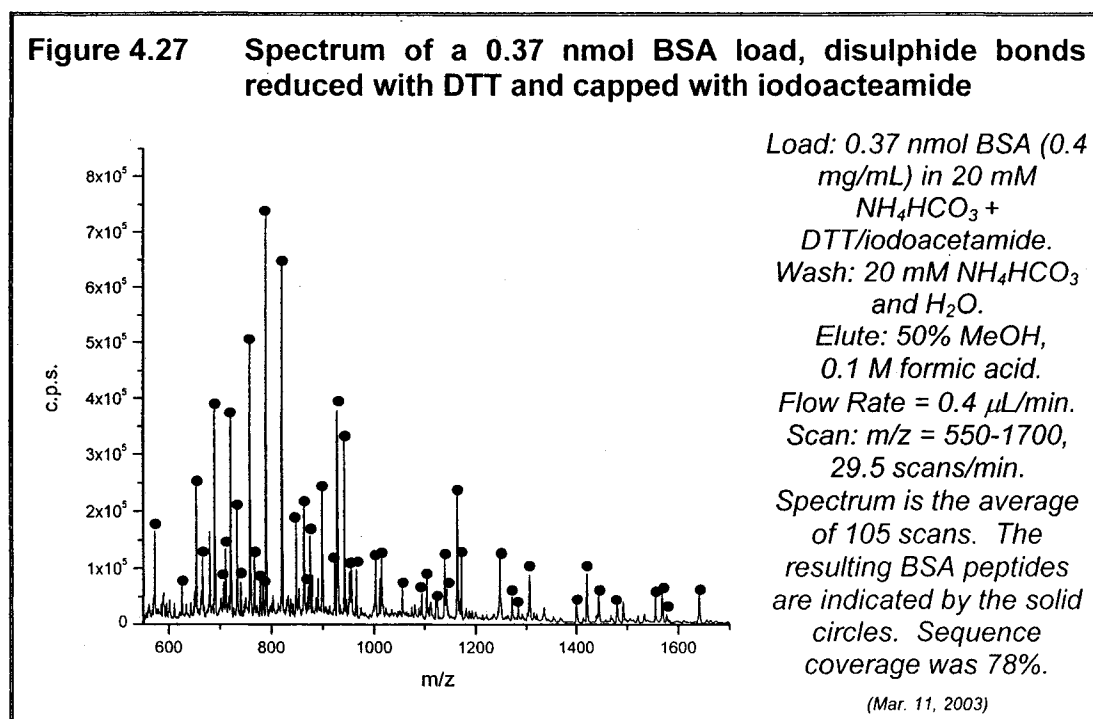
(Mar. 20, 2003)

Figure 4.26 BSA peptide XICs resulting from a 0.1 nmol load, disulphide bonds unreduced



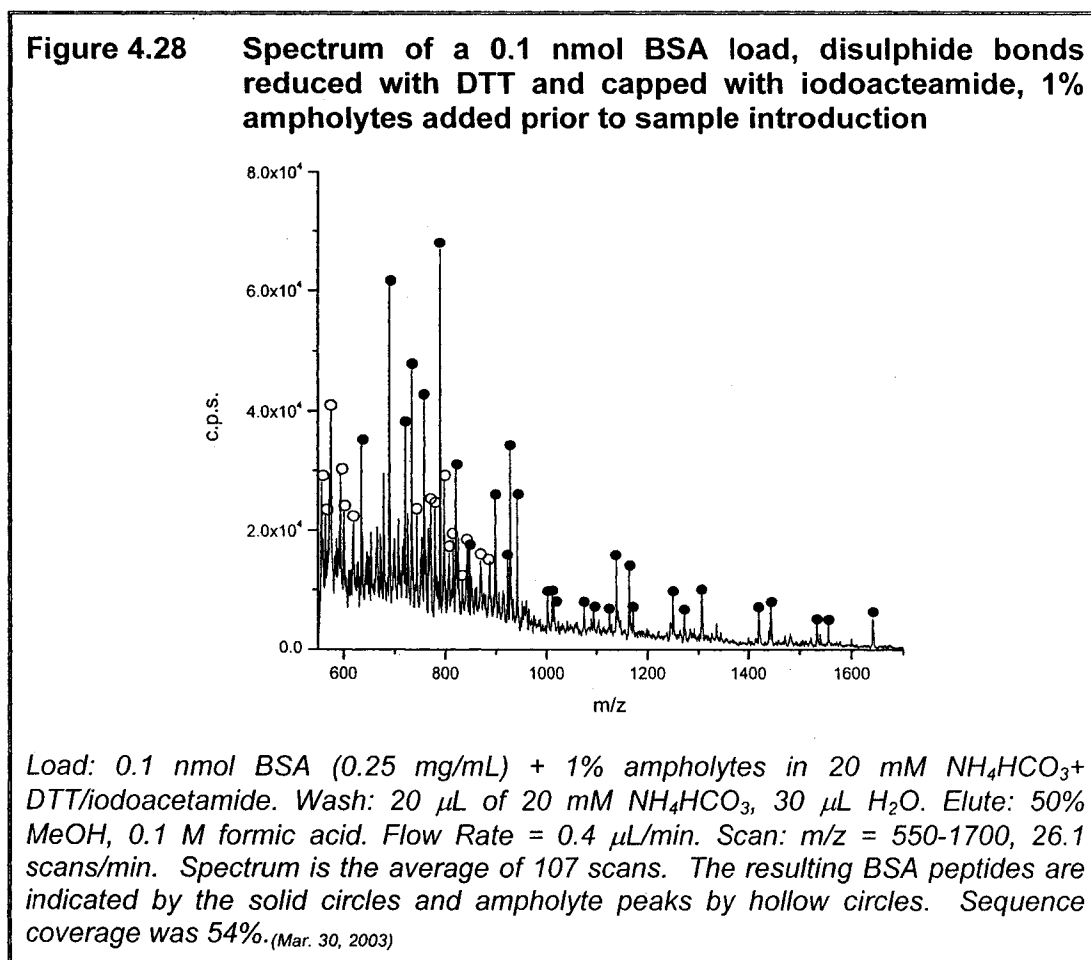
XICs for five BSA peptides. XIC
m/z value is shown above each
trace. A spectrum of all the BSA
peptides is shown in Figure 4.25
and experimental details are
given in the caption to that
figure.

The BSA was treated with DTT and iodoacetamide; the resulting peptide spectrum is shown in Figure 4.27.



A significant increase in the number of peptides was seen. Table 4.5, in the Appendix to this chapter, lists the identified peptides for the reduced BSA. Addition of the reduction and capping steps led to a sequence coverage of 78% in the m/z range scanned, compared to 24% seen without treatment. The spectrum in Figure 4.27 is the result of a higher load than was used in Figure 4.25, however spectra collected done using much higher untreated BSA loads (1.5 nmol), only resulted in a sequence coverage of 25%, justifying the need for the reduction and capping steps. Finally, ampholytes were added to the reduced/capped sample and the resulting spectrum is shown in Figure 4.28. As mentioned before, great care was taken not to assign any potential ampholyte peaks as peptides peak, resulting in the number of identified peptides being an underestimate. Since the ampholytes are seen to interfere in the lower m/z ranges, it is wise to scan higher m/z ranges, when possible, to avoid this problem. Higher molecular weight (MW) proteins are particularly amenable to

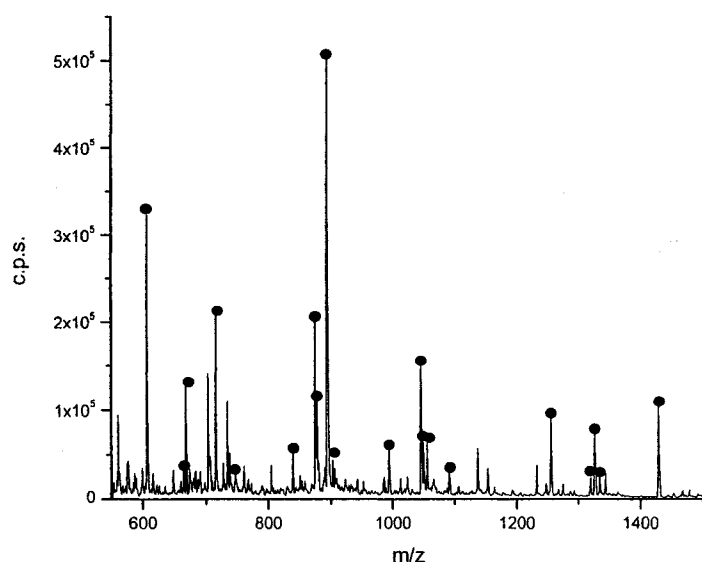
this as they exhibit a larger number of higher MW peptides, purely due to their larger size.



4.3.8.2 LYSOZYME

Finally, lysozyme was digested on-chip. After treatment with DTT and iodoacetamide, off-chip. This proved challenging as the addition of these reagents caused the protein to precipitate. Low protein concentration had to be used to avoid precipitation, which then led to excessive loading times (several hours) in order to concentrate enough sample to be detected. The resulting spectrum and XICs are shown in Figure 4.29. Table 4.6 in the Appendix lists the identified lysozyme peptides.

Figure 4.29 Spectrum and XICs of a 1 nmol lysozyme load, disulphide bonds reduced with DTT and capped with iodoacetamide



Load: Approximately 1 nmol lysozyme (0.2 mg/mL) in 20 mM NH₄HCO₃ + DTT/iodoacetamide @ 1 μL/min.

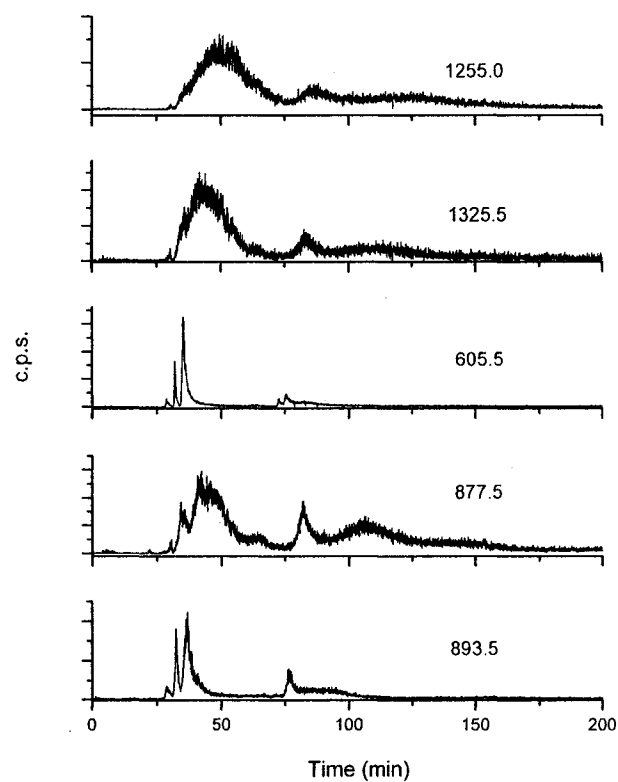
Wash: 30 μL of 20 mM NH₄HCO₃, 30 μL H₂O @ 1 μL/min.

Elute: 50% MeOH, 0.1 M formic acid @ 0.4 μL/min.

Scan: m/z = 550-1500, 31.5 scans/min.

Spectrum (top) is the average of 107 scans. The resulting lysozyme peptides are indicated by solid circles. Sequence coverage was 95%. XIC m/z value is indicated above each trace.

(Mar. 14, 2003)



The ability of this platform to handle a variety of incoming samples has been demonstrated through the analysis of these three proteins.

4.4 ELECTRICAL FRACTIONATION

Only a few attempts at electrical fractionation were made with the entire sealed system before it was decided that this part of the procedure would be best evaluated independently. Using the entire sealed system there was no way to examine the fractionation process as it was occurring near the inlet. The only detection point afforded was the outlet which led to the MS. Hence, if any problems arose it would be impossible to pinpoint where they were occurring. This being said, the fractionation process was successfully executed and the results follow.

4.4.1 METHODS

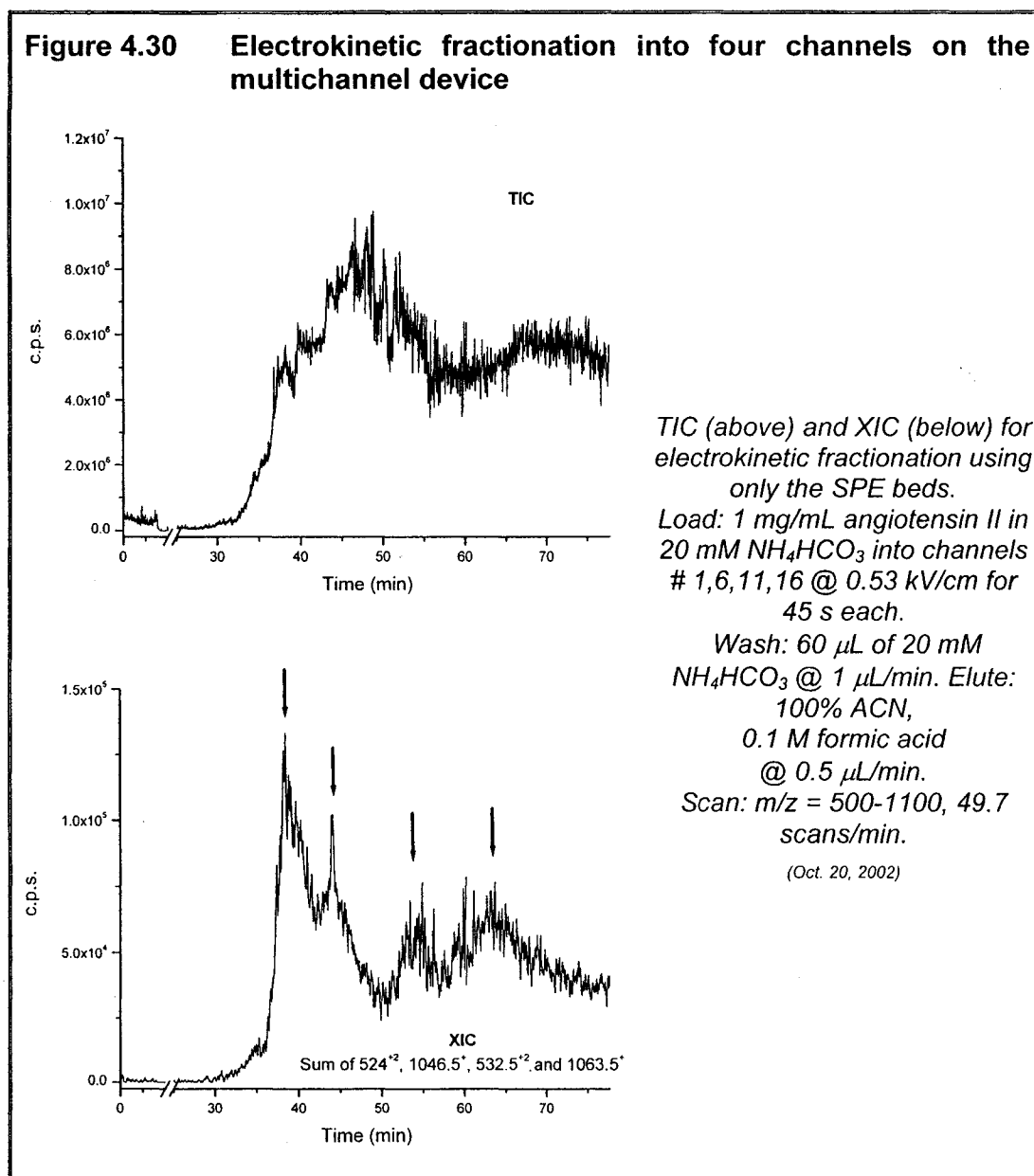
All reagents and methods are as described in Section 4.3.1. Electrical fractionation was achieved using the following procedure: the inlet capillary (25 cm) was conditioned with 0.1 M NaOH at 30 p.s.i. for 10 min, rinsed with water (10 min at 30 p.s.i.) and then loaded with sample (10 min, 30 p.s.i.). The capillary was transferred from the pressure source to the platform. One end of the capillary was placed in a reservoir containing buffer and the other was attached to the chip via the Nanoport™. The high voltage electrode was placed in the buffer reservoir and the grounding electrodes were already in place in the chip holder. Care was taken to ensure that the buffer level in the reservoir was even with the chip to avoid possible siphoning effects, see Figure 3.23 in the Chapter 3. The electrical system was initiated and the high voltage was simultaneously activated. The timer and relay boxes sequentially stepped through each timer. In this case, only the last four relays were used as flow was only directed into channels 1, 6, 11 and 16 (see Chapter 3, Figure 3.1, for channel number assignment). The high voltage was set to 15 kV resulting in an

electric field of 0.53 kV/cm. The voltage was applied to each channel for 45 s. After fractionation, the end of the capillary was removed from the vial and attached to the syringe pump allowing for the washing and elution steps. In this case, only the SPE beds were packed. For this experiment ESI interface LJ-1 was used.

4.4.2 RESULTS AND DISCUSSION

The electrical fractionation was performed using angiotensin II as the sample. The resulting TIC and XIC are shown in Figure 4.30. Spectra extracted from the TIC revealed four peaks related to angiotensin II: 524^{+2} and 1046.5^{+} , the singly and doubled charged states, and 532.5^{+2} and 1063.5^{+} , the singly and doubly charged states for oxidized angiotensin II. The XICs for these m/z values were extracted and summed resulting in the total XIC shown in the lower plot of Figure 4.30. In the resulting XIC plot, there are four peaks, indicated by arrows, which appear to correlate to the injection made into four of the twenty channels. The entire volume of the capillary was 491 nL and based on a calculate EOF flow rate of 206 nL/min (calculated by Equation 5.4 with an electric field of 0.53 kV/cm and cross-section $1963 \mu\text{m}^2$), 618 nL should be delivered to the chip. Hence, it should be expected that the last peak contains less sample than the previous three. There are several points of interest to be made when considering this plot. First, the later peaks are extremely broad and are obviously experiencing a great deal of band broadening. The calculated time delay between each of the peaks should be 2 min, considering there are five channels between each injection. Even the first two peaks, which would have experienced the least amount of band broadening, are not well resolved. The width of the peaks indicates that there could be unexpected wash-out volumes within the chip, perhaps in the packed beds or in the reservoir housing the electrode. Although some band broadening is induced by the long flow paths following the SPE beds in the higher numbered channels, Figure 3.7 in Chapter 3 proved that resolution between channels should be achievable, provided that the bands eluted from the

SPE beds are narrow, which may not be the case. The calculation leading to this plot did not account for the volume in the ESI interface and other possible dead volumes. These issues will be explored in Chapter 5.



A simple solution to reduce the longitudinal diffusion experienced by the longer channels is to place the delay line between the digestion beds and the SPE beds. This would reduce the band broadening experienced by the peaks once eluted from the SPE bed and would make the longitudinal diffusion experienced

by each channel equal. This initial attempt at electrokinetic fractionation led to valuable insights regarding the overall performance of the assembled platform and helped to determine the course of action to be taken when testing individual components.

4.5 REFERENCES

- (1) Rodriguez-Diaz, R.; Wehr, T.; Zhu, M.; Levi, V. "Chapter 4: Capillary Isoelectric Focusing" In *Handbook of Capillary Electrophoresis*; CRC Press, Inc., 1997, pp 101-138.
- (2) Mazzeo, J. R.; Krull, I. S. *Anal. Chem.* **1991**, *63*, 2852-2857. "CIEF of proteins in uncoated fused-silica capillaries using polymeric additives"
- (3) Mazzeo, J. R.; Krull, I. S. *J. Chromatogr.* **1992**, *606*, 291-296. "Improvements in the method development for performing IEF in uncoated capillaries"
- (4) Hofmann, O.; Che, D.; Cruickshank, K. A.; Muller, U. R. *Anal. Chem.* **1999**, *71*, 678-686. "Adaptation of CIEF to microchannels on a glass chip"
- (5) Tang, Q.; Harrata, A. K.; Lee, C. S. *Anal. Chem.* **1997**, *69*, 3177-3182. "Two-dimensional analysis of recombinant E-coli proteins using CIEF ESI MS"
- (6) Tang, Q.; Harrata, A. K.; Lee, C. S. *Anal. Chem.* **1995**, *67*, 3515-3519. "CIEF ESI MS for protein analysis"
- (7) Hille, J. M.; Freed, A. L.; Watzig, H. *Electrophoresis* **2001**, *22*, 4035-4052. "Possibilities to improve automation, speed and precision of proteome analysis: A comparison of two-dimensional electrophoresis and alternatives"
- (8) Kirby, D. P.; Thorne, J. M.; Gotzinger, W. K.; Karger, B. L. *Anal. Chem.* **1996**, *68*, 4451-4457. "A CE/ESI-MS interface for stable, low-flow operation"
- (9) Wang, C.; Oleschuk, R.; Ouchen, F.; Li, J. J.; Thibault, P.; Harrison, D. J. *Rapid Commun. Mass Spectrom.* **2000**, *14*, 1377-1383. "Integration of immobilized trypsin bead beds for protein digestion within a microfluidic chip incorporating CE separations and an electrospray MS interface"
- (10) King, R.; Bonfiglio, R.; Fernandez-Metzler, C.; Miller-Stein, C.; Olah, T. *J. Am. Soc. Mass Spectrom.* **2000**, *11*, 942-950. "Mechanistic investigation of ionization suppression in ESI"
- (11) Annesley, T. M. *Clin. Chem.* **2003**, *49*, 1041-1044. "Ion suppression in MS"
- (12) Yang, L. Y.; Lee, C. S.; Hofstadler, S. A.; Smith, R. D. *Anal. Chem.* **1998**, *70*, 4945-4950. "Characterization of microdialysis acidification for CIEF micro-ESI MS"
- (13) Lamoree, M. H.; Tjaden, U. R.; vanderGreef, J. *J. Chromatogr. A* **1997**, *777*, 31-39. "Use of microdialysis for the on-line coupling of CIEF with ESI-MS"
- (14) Chartogne, A.; Tjaden, U. R.; Van der Greef, J. *Rapid Commun. Mass Spectrom.* **2000**, *14*, 1269-1274. "A free-flow electrophoresis chip device for interfacing CIEF on-line with ESI-MS"

4.6 APPENDIX

Cytochrome c charge states and m/z values are listed in Table 4.1. The m/z values were generated by taking the MW of the protein, 12355 g/mol, dividing by the charge state and adding 1 to represent m/z values for $[M+nH]^{+n}$.

Table 4.1 Cytochrome c charge states

Charge	m/z
+ 7	1766.0
+ 8	1545.5
+ 9	1374.0
+ 10	1236.5
+ 11	1124.5
+ 12	1031.0
+ 13	951.5
+ 14	883.5
+ 15	825.0
+ 16	773.5
+ 17	728.0
+ 18	687.5

Cytochrome c peptides were identified by database searching using the SwissProt accession number for cytochrome c, P00004. Two databases were used, Peptide Mass by ExPASy (<http://us.expasy.org/>), and MS-Digest by Protein Prospector (<http://prospector.ucsf.edu/>). The databases were searched using: trypsin digest, 3 missed cleavages (MC), peptide N-terminus = hydrogen, peptide C-terminus = free acid, modifications considered = oxidation of methionine (Met-ox) and protein N-terminus acetylated, cysteine unmodified. Peptides m/z values are listed for $[M+nH]^{+n}$, based on monoisotopic masses. The peptides listed in Table 4.2 were identified.

Table 4.2 Cytochrome c peptides

m/z	Missed Cleavages (MC)	Position	Modifications
562.5	1	100-104	
565.5 ⁺³	3	74-88 or 73-87	
585.0 ⁺²	0	28-38	
589.5	0	1-5	acetylated
604.5	0	56-60	
634.5	0	9-13	
649.0 ⁺²	1	28-39	
676.0 ⁺²	1	89-99	
678.5	0	74-79	
737.0 ⁺³	2	56-73	
740.0 ⁺²	2	88-99 or 89-100	
755.0 ⁺²	2	92-104	
762.5	1	8-13	
767.0 ⁺³	2	61-79	1 Met-ox
779.5	0	80-86	
795.5	0	80-86	1 Met-ox
800.0 ⁺²	1	39-53	
804.5 ⁺²	3	88-100	
806.5	1	73-79	
817.5 ⁺²	1	9-22	
848.0 ⁺²	3	74-88 or 73-87	
857.5 ⁺²	1	40-55	
907.5	1	80-87	
947.5	2	6-13	
964.5	0	92-99	
1041.5 ⁺²	1	56-72	
1092.5	1	92-100	
1105.5 ⁺²	2	56-73	
1113.0 ⁺²	2	56-73	1 Met-ox
1168.5	0	28-38	

Trypsin autodigestion peaks were identified by database searching using the Swiss-Prot accession number for bovine trypsinogen [precursor], P00760, and then removing the first 20 residues which contain the signal information and the propeptide. The remaining sequence was then pasted into the database search. It should be noted that the positions below referred to the protein without its precursor and for the full protein #P00760, 20 would need to be added to the positions below. The database was searched using: trypsin digest, 3 MC, peptide N-terminus = hydrogen, peptide C-terminus = free acid, modifications considered = oxidation of M and protein N-terminus acetylated, cysteine unmodified. Peptides m/z values are listed for $[M+nH]^{+n}$, based on monoisotopic masses, unless otherwise stated. The peptides listed in Table 4.3 were identified.

Table 4.3 Trypsin autodigestion peaks

m/z	MC	Position	Modifications
758.5 ⁺³	0	70-89	
763.5 ⁺³	0	70-89	1 Met-ox
766.0 ⁺³	0	70-89	+ Na
771.0 ⁺³	0	70-89	+ K
835.5 ⁺⁴	1	92-125	
1113.5 ⁺³	1	92-125	
1137.0 ⁺²	0	70-89	

BSA peptides were identified by database searching using the Swiss-Prot accession number for bovine serum albumin [precursor], P02769 (obtained from chicken egg white), and then removing the first 24 residues which contain the signal information and the propeptide. The remaining sequence was then pasted into the database search. The MW of the protein was 66433 g/mol which was confirmed by MS data. The database was searched using: trypsin digest, 2 MC, peptide N-terminus = hydrogen, peptide C-terminus = free acid, modifications considered = oxidation of M and protein N-terminus acetylated, cysteine

unmodified. Peptides m/z values are listed for $[M+nH]^{+n}$, based on monoisotopic masses. The peptides listed in Table 4.4 were identified.

Table 4.4 BSA peptides (disulphides not reduced)

m/z	MC	Position	Modifications
634.5 ⁺³	1	397-412	
649.5	0	181-185	
665.5	0	181-185	1 Met-ox
689.5	0	212-217	
720.5 ⁺²	1	336-347	
733.5 ⁺²	1	432-444	
789.5	0	233-239	
821.0 ⁺²	1	413-427	
847.5	1	218-224	
876.5 ⁺²	2	218-232	
922.5	0	225-232	
927.5	0	137-143	
1062.0 ⁺²	1	545-563	1 Met-ox
1163.5	0	42-51	
1250.5	1	11-20	
1415.5	0	545-556	1 Met-ox
1458.5	2	209-221	

A second database search was done using reduced and carbamidomethylated cysteines. All other parameters were the same. The peptides in Table 4.5 were identified.

Table 4.5 BSA peptides (disulphides reduced and capped)

m/z	MC	Position	Modifications
572.0	1	195-198	
625.5 ⁺²	1	11-20	
634.5 ⁺³	1	99-114	
653.5 ⁺²	0	378-388	
665.5	1	132-136	
689.5	0	212-217	
707.0 ⁺³	1	82-98	
710.5 ⁺²	0	65-76	

720.5 ⁺²	1	336-347	
733.5 ⁺²	1	472-483	
740.5 ⁺²	0	397-409	
758.5	0	174-180	
767.5 ⁺²	1	274-285	
778.5 ⁺²	0	363-375	
784.5 ⁺²	0	323-335	
789.5	0	233-239	
821.0 ⁺²	1	413-427	
848.0	1	218-224	
863.5 ⁺²	0	445-458	
871.0 ⁺²	0	445-458	1 Met-ox
874.5 ⁺²	0	160-173	
898.5	0	459-465	
922.5	0	225-232	
927.5	0	137-143	
941.5 ⁺²	0	484-499	
951.5 ⁺²	1	99-114	
954.5 ⁺²	0	505-520	
964.5 ⁺²	1	557-573	
1002.5 ⁺²	0	574-583	
1010.5 ⁺²	1	115-131	
1014.5	0	525-533	
1055.5 ⁺²	2	466-483	
1074.5 ⁺²	2	115-132	
1094.5 ⁺³	2	351-377	
1104.0 ⁺³	2	545-573	
1124.5 ⁺²	1	243-261	
1138.5	0	475-483	
1143.0	1	524-533	
1163.5	0	42-51	
1171.5 ⁺³	2	286-316	
1247.0 ⁺²	0	21-41	
1249.5	1	11-20	
1271.5 ⁺²	2	94-114	
1284.0	0	337-347	
1305.5	0	378-388	
1400.0	0	545-556	
1420.0	0	65-76	
1444.0	0	262-273	

1480.0	0	397-409	
1532.5	1	274-285	
1555.0	0	363-375	
1568.0	0	323-335	
1577.0	0	115-127	
1640.0	1	413-427	

Lysozyme peptides were identified by database searching using the Swiss-Prot accession number for chicken lysozyme C [precursor], P00698 (obtained from chicken egg white), and then removing the first 18 residues, which contain the precursor information. The remaining sequence was then pasted into the database search. The MW of the protein was 14303 g/mol which was confirmed by MS data. The database was searched using: trypsin digest, 3 MC, peptide N-terminus = hydrogen, peptide C-terminus = free acid, modifications considered = oxidation of M and protein N-terminus acetylated, cysteine modified by carbamidomethylation. Peptides m/z values are listed for $[M+nH]^{+n}$, based on monoisotopic masses. The peptides listed in Table 4.6 were identified.

Table 4.6 Lysozyme peptides (disulphides reduced and capped)

m/z	MC	Position	Modifications
605.5	1	1-5	
663.5 ⁺²	0	22-33	
667.5 ⁺²	1	115-125	
715.0 ⁺²	0	34-45	
746.5 ⁺²	1	62-73	
838.5 ⁺²	0	98-112	
874.5	0	15-21	
877.5 ⁺²	0	46-61	
893.5	0	6-13	
902.5 ⁺²	1	97-112	
993.5	0	62-68	
1045.5	0	117-125	
1049.5	1	6-14	
1055.5 ⁺³	1	34-61	
1090.5 ⁺²	1	15-33	
1255.0 ⁺²	0	74-96	

1318.5 ⁺²	1	74-97	
1325.5	0	22-33	
1333.5	1	115-125	
1428.5	0	34-45	

5.1 INTRODUCTION

In order to fully characterize the platform, it was necessary to focus on specific regions of the device to explore possible sources of band-broadening and/or mixing chamber effects. By examining each of these components individually, an understanding of the potential problems associated with each was gained, and solutions were proposed which would lead to improved system performance. Several areas were explored.

- The injector region was examined using laser-induced fluorescence (LIF) in order to observe the fractionation process. Volume analysis of this region was explored in relation to sample loading limitations.
- A single channel device was used to explore the elution behaviour of cytochrome c peptides and the effects of flow rate on digestion and elution.
- Theoretical analysis of band broadening within the multichannel system was explored in relation to peak resolution.
- Band broadening issues within the electrospray interface were explored both experimentally and theoretically.
- Flow resistances within the multichannel system were explored in an attempt to explain the elution behaviour seen in previous results.

Throughout this chapter, solutions are proposed which overcome the identified problems. A summary of future work will be presented in Chapter 6.

5.2 ELECTRICAL FRACTIONATION

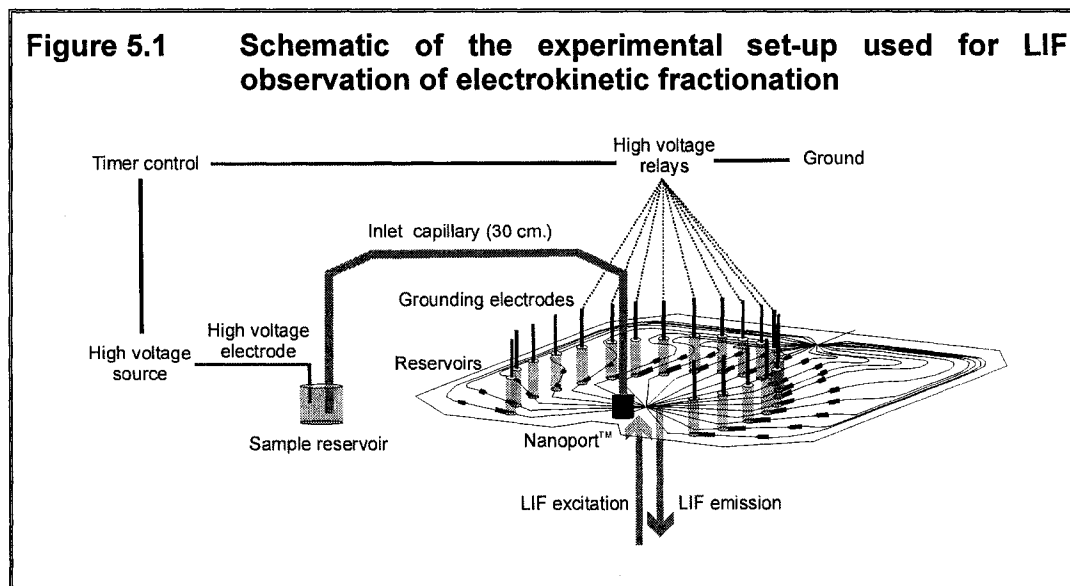
In order to evaluate the fractionation process alone, without interference from the rest of the system, fluorescence detection was used. The access reservoirs on the chip were not sealed and flow was driven from the inlet to the first available exit, the access holes located at the head of the trypsin beds. This

served to isolate the fractionation region from the rest of the chip and allowed for direct observation of the electrokinetically driven flow.

5.2.1 EXPERIMENTAL

The chip presented in Chapter 3 was used without the clamp holder to seal the channels. Reservoirs were placed above the access holes at the head of the trypsin beds, to both hold solution and to position the electrode assembly. The chip assembly was placed above an inverted confocal epiluminescent microscope, which allowed for fluorescence detection. The optical system described in Chapter 2 was used with some modifications. The excitation light from the argon ion laser was dispersed by passing the laser beam through a stretched piece of Parafilm ("M", American National Can™), allowing for a larger excitation region. A 5x microscope objective (NeoDPlan 5, Olympus) was used in order to increase the field of view used for detection. Fluorescence signal was collected by a CCD camera (TK-1280U, JVC) fitted with a 0.5x lens (D50BHC, Diagnostic Instruments) and an orange glass absorption filter (OG515, Omega Optical), to filter out the majority of the incident laser light. An inlet capillary (50 μm i.d., 360 μm o.d., 30 cm length) was coupled to the device through a Nanoport™. The capillary and chip were conditioned with 0.1 M NaOH for 20 min, water for 5 min and ammonium bicarbonate for 5 min. A schematic of the set-up is shown in Figure 5.1. The entire system was first filled with 20 mM ammonium bicarbonate. The end of the inlet capillary was placed in a reservoir containing 10 μM solution of fluorescein in 20 mM ammonium bicarbonate. Great care was taken to ensure that the levels of solution in all of the reservoirs were at the same height. The high voltage was applied to the inlet reservoir and simultaneously the first grounding relay was activated. The timers and relays stepped through each channel sequentially and when finished, the last relay was closed and the high voltage shut down simultaneously. A variety of different time and voltage parameters were used, but in the data presented the parameters

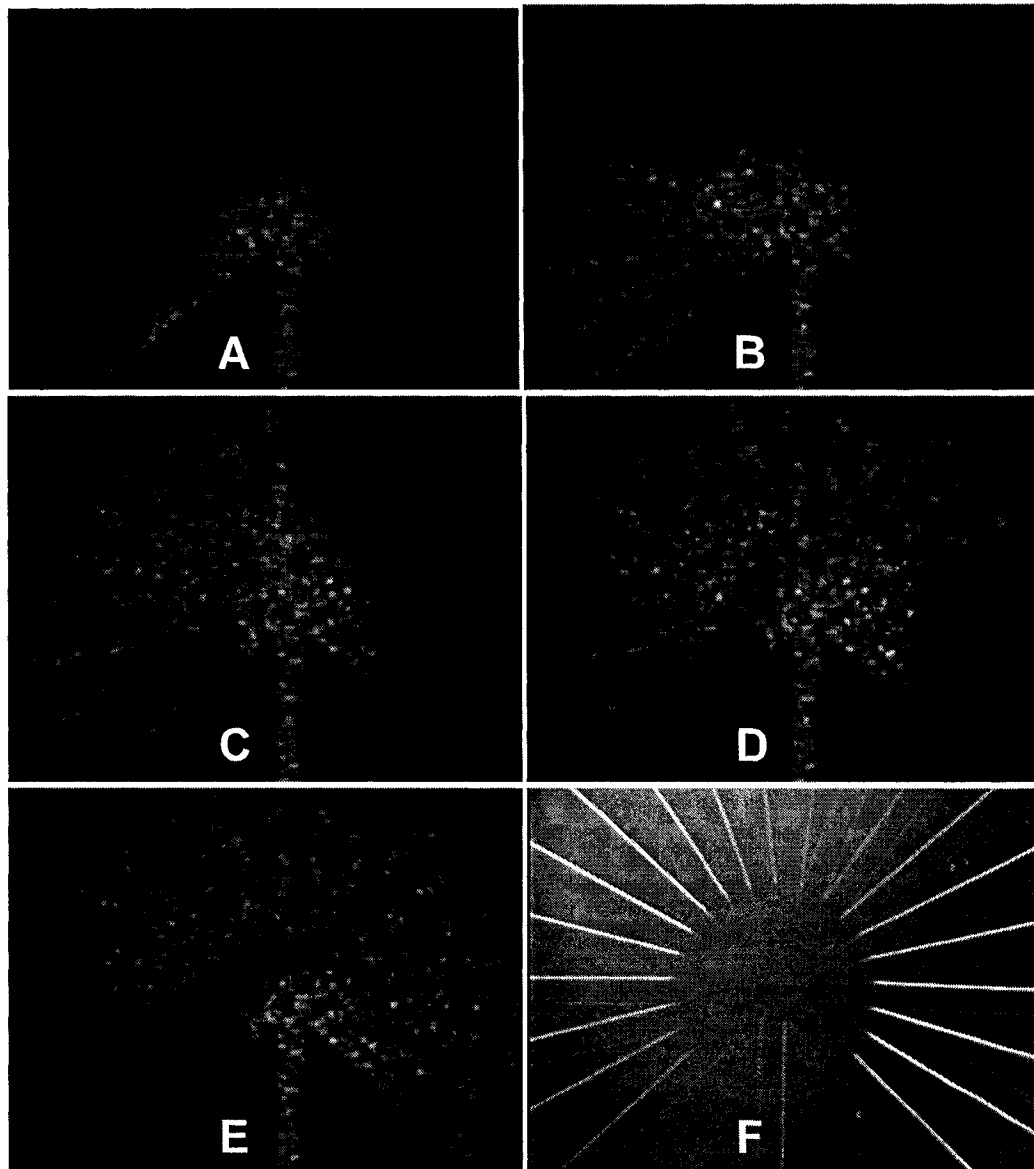
were: voltage = 13.5 kV, 1st timer = 31.5 s, all other timers = 9 s. The first timer was set longer than the rest to allow the fluorescein time to fill the inlet capillary.



5.2.2 RESULTS AND DISCUSSION

A variety of sample introduction configurations were explored. Sample was electrokinetically injected into all channels, even or odd channels only, in both the clockwise and counter clockwise directions. In all cases, the voltage used was 13.5 kV, resulting in an electric field strength of 0.41 kV/cm; comparable to the electric field that was used for CIEF separations in Section 4.2. Figure 5.2 presents a series of extracted frames from a video illustrating clockwise electrokinetic fractionation into all twenty channels. Overall, the fractionation process proceeded smoothly. In frames C and D a small amount of sample leakage is seen entering the channels in the lower right-hand corner. Throughout the course of this study it was noted that the system, as arranged in Figure 5.1, was extremely sensitive to siphoning effects and subtle differences in the buffer levels of each reservoir were enough to induce flow. By merely changing solutions in the buffer reservoirs, sample leakage could be induced or reduced.

Figure 5.2 Frames extracted from a video illustrating electrokinetic fractionation and a photo of the injector region in full light



Frames A-E were extracted from a video demonstrating electrokinetic fractionation with 10 μ M fluorescein. Frame F is a photo of the inlet "star" region in full light.

A quick calculation was done in order to assess the magnitude of the siphoning effect. Two adjacent channels were considered. The pressure drop across the flow path was calculated and related to a height-induced pressure difference. The pressure drop across a rectangular channel is defined as:¹

$$\Delta P = \Phi \left(\frac{4\eta L}{(wd)^2 F} \right) \quad (5.1)$$

where Φ is the volumetric flow rate, η is viscosity, L is the channel length, w is channel width, d is channel depth and F is a form factor defined by the ratio of d/w . As this equation is specific for rectangular channels, a channel width was defined by using the isotropic "D" shaped cross sectional area (as defined by Equation 3.1), fixing d at 22.5 μm (the experimental channel depth) and calculating the width of a rectangular channel of the same area. The area of the isotropically etched channels was 2145 μm^2 which corresponds to a rectangular channel of width 95.34 μm . The geometric form factor, F , was found to be 0.066965 as calculated by Equation 5.2¹ using the rectangular channel dimensions above.

$$F = \frac{w}{3d} - \frac{64w^2}{\pi^5 d^2} \sum_{n=0}^{\infty} \frac{\tanh\left[\frac{(2n+1)\pi d}{2w}\right]}{(2n+1)^5} \quad (5.2)$$

It should be noted that in the work presented by Attiya *et. al.*¹ there is an error in defining w and d . These should be defined as full widths and depths, not half widths and depths. The pressure exerted by a column of liquid is defined by Equation 5.3.²

$$\Delta P = \rho gh \quad (5.3)$$

Where ρ is the density of the solution, g is the acceleration due to gravity (9.80665 m/s^2) and h is the height of the column. Equations 5.1 and 5.3 were made equivalent and the volumetric flow rate due to a height difference of 1 mm

was calculated. The details of this calculation are shown below and a schematic illustrating the result in Figure 5.3. The following values were used: $w = 95.34 \mu\text{m}$, $d = 22.5 \mu\text{m}$, $L = 5 \text{ cm}$, $h = 1 \text{ mm}$, $g = 9.8 \text{ m/s}^2$, $\eta = 0.891 \times 10^{-3} \text{ kg/m}\cdot\text{s}$, $\rho = 0.997 \text{ g/mL}$.³

$$\Phi \left(\frac{4\eta L}{(wd)^2 F} \right) = \rho gh$$

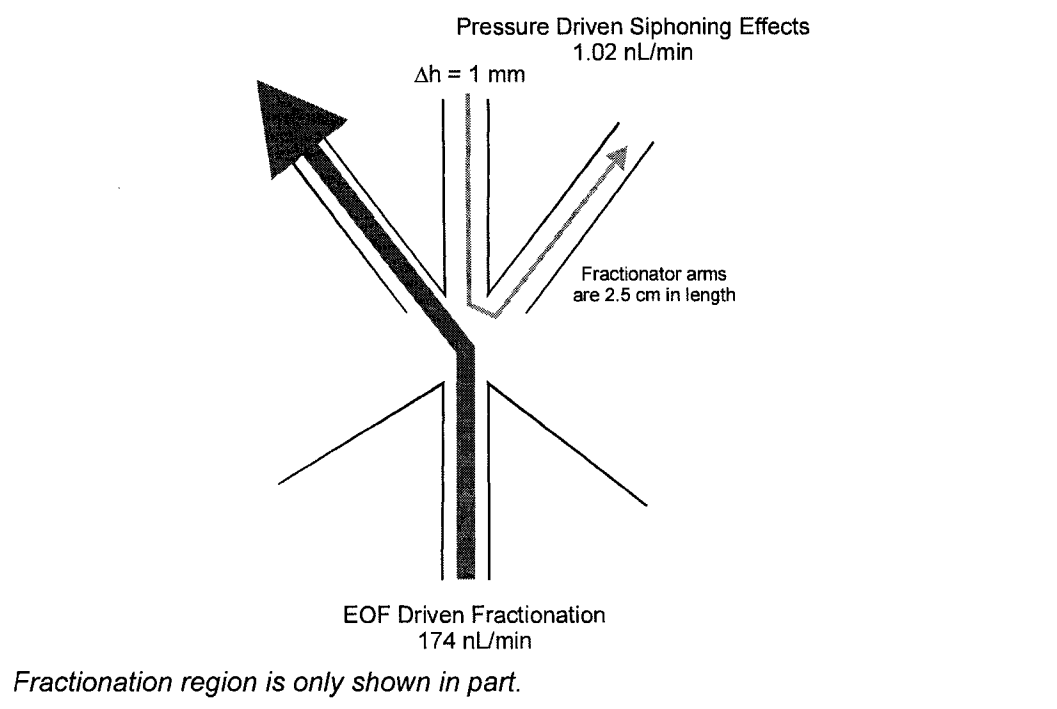
$$\Phi = \frac{\rho gh (wd)^2 F}{4\eta L} = 1.02 \text{ nL/min}$$

Hence, a height difference of 1 mm between reservoirs will result in a flow rate of 1.02 nL/min. This can be compared to the expected EOF driving the fractionation process. Equation 5.4 was used to calculate the EOF at an electric field strength of 0.41 kV/cm.

$$\Phi_{\text{EOF}} = \mu_{\text{EOF}} EA = \left(0.33 \frac{\text{cm}^2}{\text{kV}\cdot\text{s}} \right) \left(0.41 \frac{\text{kV}}{\text{cm}} \right) (2.145 \times 10^{-5} \text{ cm}^2) = 174 \text{ nL/min} \quad (5.4)$$

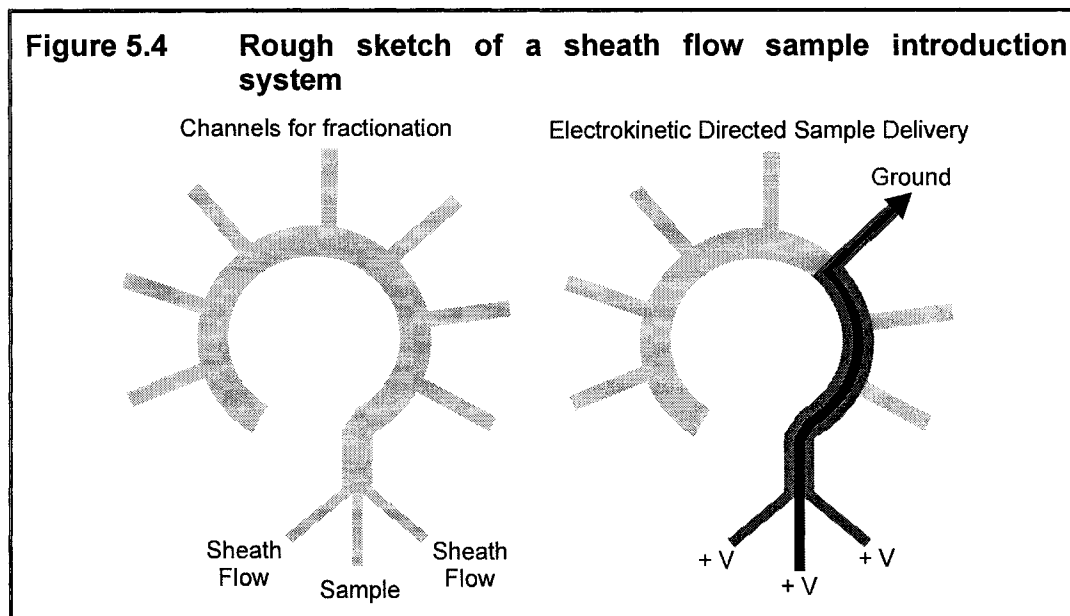
Where Φ_{EOF} is the EOF volumetric flow rate, μ_{EOF} is the electroosmotic mobility ($0.33 \text{ cm}^2/\text{kV}\cdot\text{s}$)⁴, E is the experimental electric field and A is the channel cross-sectional area. The pressure driven flow due to siphoning effects is small in comparison to the EOF but may be enough to contribute to the leakage effects seen in frames C and D of Figure 5.2. A schematic of these calculated effects is shown in Figure 5.3. These siphoning effects should not be an issue in the final application of this device as the access holes will be sealed by septa and hence forced to be at the same level. In the future, it is intended that a hole be drilled out of the bottom of the Plexiglass holder to allow for fluorescence detection of the fractionation step using the sealed system.

Figure 5.3 Schematic illustrating siphoning effects during electrokinetic fractionation



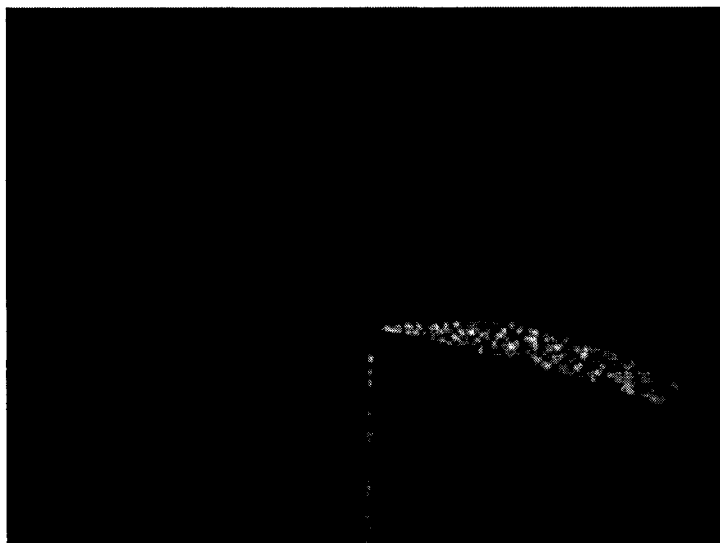
Looking at frames A and B of Figure 5.2, some outward sample movement is seen within the introductory circle, before the different channels diverge. This circular area is defined by the etched widths of the channel. All channels originate from the same point, however there is some overlap near the origin as the channels are not infinitely narrow, this can be seen in frame F. For an etch depth of $22.5 \mu\text{m}$, the volume of the frustum (cone with top cut off) formed was 6.74 nL. This volume has the potential to act like a mixing chamber and could lead to sample cross contamination when individual samples are directed to each channel. Using the current channel dimensions, the maximum sample load that can be introduced into each channel is 53.6 nL. This is the volume contained between the beginning of the star junction and the electrode at the end of the arm. Using this maximum load, the volume of the mixing chamber is relatively small. However, in order to avoid potential mixing problems, it may be necessary

to design a new method by which to introduce sample. A circular pathway with the fractionation arms extending from the edge of the circle may serve to eliminate this problem. The introduction of a sheath flow may also be necessary to avoid cross-contamination as well as to address solvent compatibility issues mentioned in Section 4.3.3. A rough draft of such a design is shown in Figure 5.4, and will be the subject of future research.



The same “star” junction is seen at the end of the variable region as the 20 channels are recombined to a single outlet. It was not expected that this region would lead to mixing as all channels should have a positive pressure driving towards the outlet. These parallel flows, once recombined, will remain striated and hence should not cause any mixing effects. This was confirmed by applying a single vacuum source to the outlet and observing the signal from a fluorescent sample in one of the channels. The result is shown in Figure 5.5 and clearly indicates that the incoming sample stream remains tightly focused and does not experience any mixing in this region.

Figure 5.5 Photo illustrating the effect of negative pressure on the single outlet with one of the twenty channels containing fluorescein



5.3 SINGLE CHANNEL WORK

In order to isolate the behaviour of sample in the bed region, one of the single channel devices, presented in Figure 3.5, was used. Device A was used for these experiments as the dimensions of the channels and beds matched those used on the multichannel system. This device was used experimentally in the same manner as the multichannel system.

5.3.1 EXPERIMENTAL

A Nanoport™ was connected to the reservoir at the head of the trypsin bed and flow was driven with a syringe pump. A septum was held in place over the access hole at the head of the SPE bed using a small clamp. Unless otherwise stated, ESI interface SS-1 was used for this work, see Section 3.6 for a description of this interface. All buffers were the same as used for the multichannel system. Cytochrome c was used exclusively as the sample for

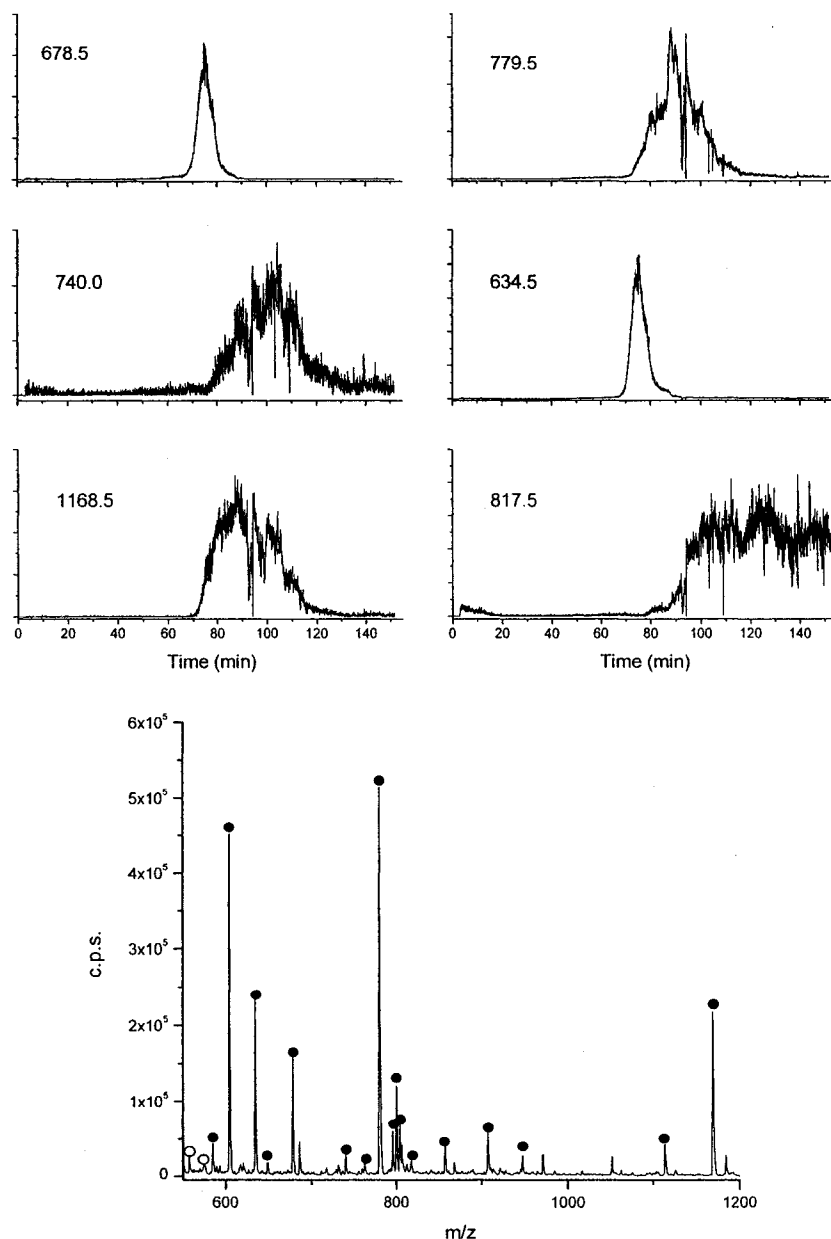
these experiments. Sample loading, bed washing and elution details are given in the figure captions.

5.3.2 COMPARISON TO THE MULTICHANNEL SYSTEM

The first experiment undertaken was to mimic the conditions used on the multichannel device. The majority of work done with the multichannel device utilized a flow rate of 0.4 $\mu\text{L}/\text{min}$, at the inlet. Sample was introduced to the single channel device using a flow rate of 0.02 $\mu\text{L}/\text{min}$, which was one twentieth of the flow used at the inlet of the multichannel device. It was hoped that this would allow the multichannel conditions to be reproduced on the single channel device, allowing for observation of a single digestion/SPE system, thereby reducing the complexity of the resulting elution profiles. After loading, the beds were washed with 2 μL of NH_4HCO_3 at the same flow rate, to ensure that the entire sample had been transferred to the SPE beds. The beds were washed with water (5-10 μL at 1 $\mu\text{L}/\text{min}$) to avoid any precipitation issues, and finally the elution buffer was introduced at a flow rate of 0.04 $\mu\text{L}/\text{min}$. This flow rate was as low as could be achieved while maintaining the electrospray signal. There were difficulties in stabilizing the electrospray signal at this low flow. Several runs were done in order to compare the results to those seen on the multichannel device. The resulting XICs and cytochrome c peptide spectrum are shown in Figure 5.6.

Looking at the resulting peptide elution traces, one can see that the peaks are extremely broad. Considering that this same process is occurring on the multichannel chip in twenty separate channels each offset in time from the other by approximately 24 s and then recombining at the outlet, there is little chance to resolve one channel from another. A more thorough analysis of the possible sources of band broadening is given in Section 5.4.

Figure 5.6 Peptide XICs and spectrum from a 0.16 nmol load of cytochrome c analyzed with single channel device A



Load: 0.16 nmol cytochrome c (2 mg/mL) in 20 mM NH_4HCO_3 + 1% ampholytes @ 0.02 $\mu\text{L}/\text{min}$; Wash: 2 μL of 20 mM NH_4HCO_3 @ 0.02 $\mu\text{L}/\text{min}$, 10 μL H_2O @ 1 $\mu\text{L}/\text{min}$; Elute: 50% MeOH, 0.1 M Formic Acid @ 0.04 $\mu\text{L}/\text{min}$. Scan: $m/z = 550-1200$, 33.3 scans/min. XIC m/z value is shown above each trace. Spectrum is the average of 99 scans centered at 82 min from the TIC (not shown). Resulting cytochrome c peptides are indicated by solid circles and ampholyte peaks by hollow circles. Sequence coverage was 91.3%. (May 21, 2003)

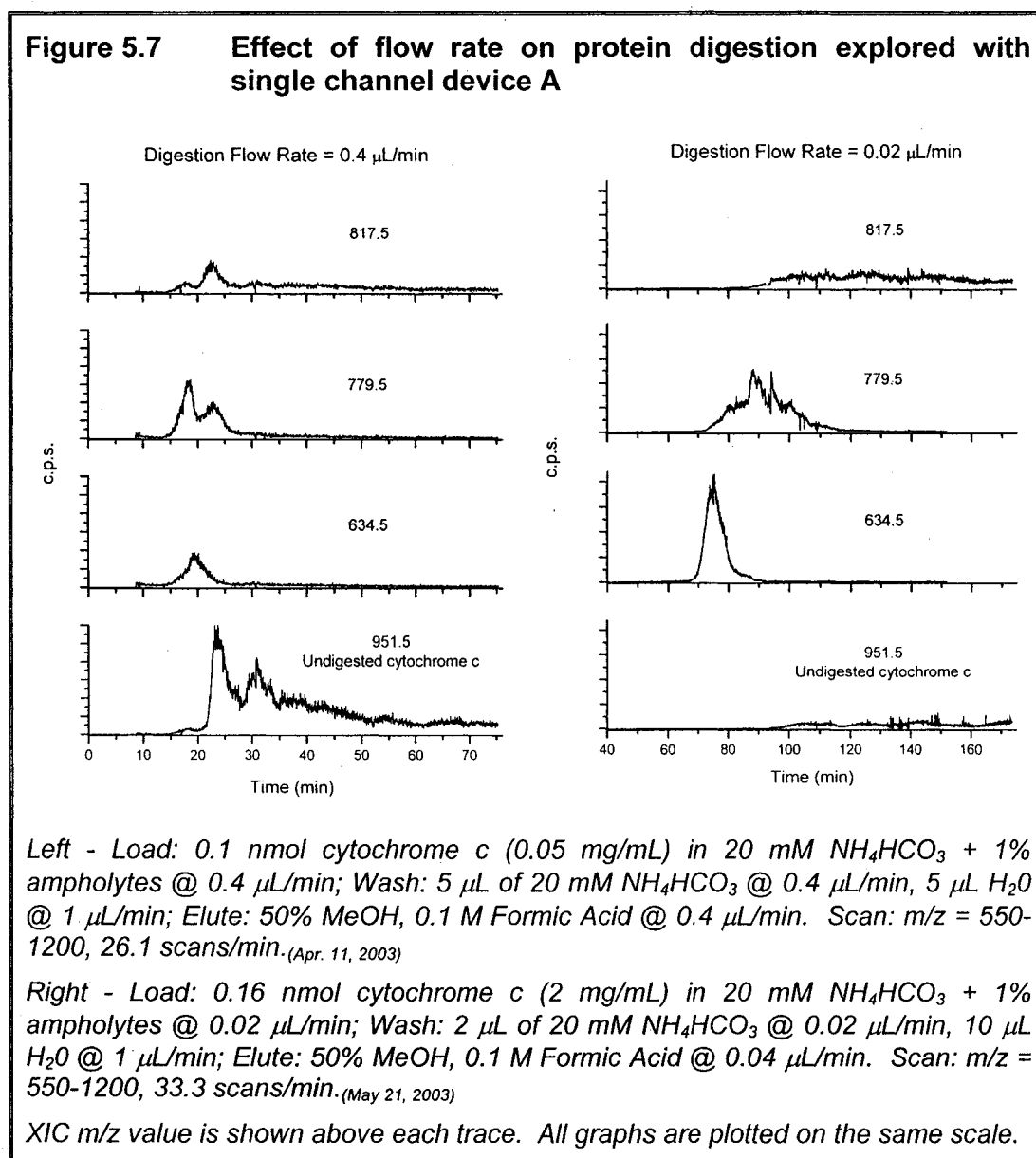
In this experiment, the peptides, with exception of 817.5, elute as one peak and not as several. This does not answer the question of what leads to the 4 or 5 separate peaks that were seen in the multichannel data, but does prove that it is not due to individual peptide elution behaviour.

5.3.3 EFFECT OF FLOW RATE ON DIGESTION

The effect of flow rate on digestion was observed during trials with the single channel device. Peptide spectra for loading flow rates of 0.4 and 0.02 $\mu\text{L}/\text{min}$ were collected. Figure 5.7 presents XICs of three peptides, 634.5, 779.5 and 817.5, the fastest, the most abundant, and the slowest eluting peptides, respectively. The XIC for $m/z = 951.5$, is also shown, representing the strongest of the undigested cytochrome c peaks.

At the higher flow rate, there is a significant amount of undigested cytochrome c. Digestion extent is dependent on protein contact time and hence is affected not only by flow rate but by bed volume, bead size and sample concentration. It should be noted that the results for the higher loading flow rate in Figure 5.7 also used a more dilute sample solution. This will also slow the digestion rate, as is discussed in the next section. Hence, the loss of digestion efficiency seen in Figure 5.7 is the result of both effects, and not entirely due to flow rate differences. If the trypsin beds on this system were larger, a faster flow rate could be used, as was shown by Wang *et al.*⁵, while still allowing for adequate contact time. High flow is desirable for several reasons: first, the reduction in sample processing time and second, the decreased dispersion of sample bands. The inlet flow rate for the multichannel device was limited due to the stability of the ESI signal using the ESI tips that were available. Flow rates up to 1 $\mu\text{L}/\text{min}$ were used successfully but it was found that the ESI signal was more easily stabilized at 0.4 $\mu\text{L}/\text{min}$. Thus, if the trypsin beds are enlarged allowing for a higher flow rate, the ESI interface will need to be adapted to be compatible with higher flow rates. Furthermore, the clamp used to seal the

multichannel device was seen to leak above inlet flow rates of 2 $\mu\text{L}/\text{min}$. Thus, if higher flow rates are desired, a better sealing system will also be necessary.



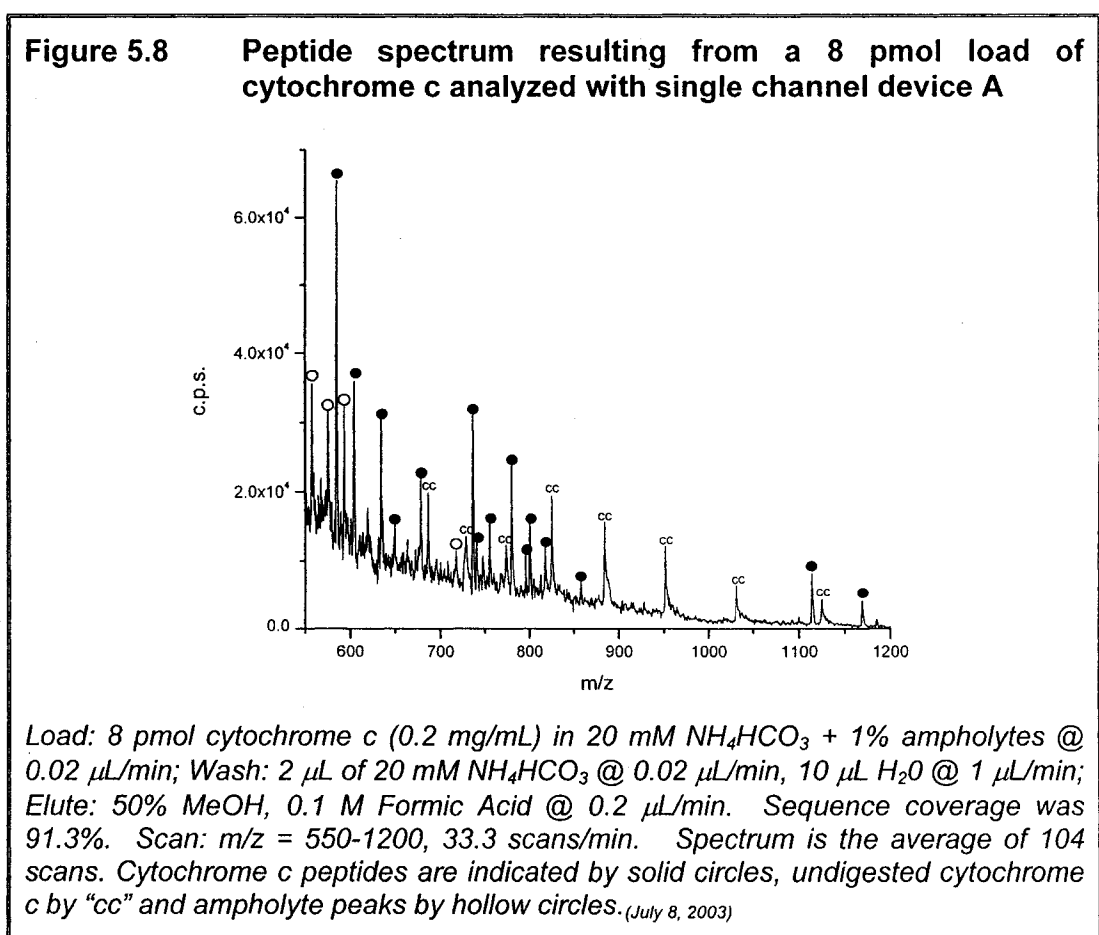
A second point of interest is noted by looking at the higher flow rate traces on the left side of Figure 5.7, both peptide 779.5 and cytochrome c (951.5) elute in two broad peaks. These multiple peak elution profiles are indicative of non-uniformities in the bed packing and become observable at higher flow rates. At

lower flow rates these types of elution profiles were not seen. Using a flow rate of 0.02 $\mu\text{L}/\text{min}$ on the single channel device, which is comparable to 0.4 $\mu\text{L}/\text{min}$ applied at the inlet of the multichannel device, multi-peak elution profiles were never seen. It was only at twenty times this value, 0.4 $\mu\text{L}/\text{min}$ on the single channel device, that these problems arose. This would correspond to a multichannel inlet flow rate of 8 $\mu\text{L}/\text{min}$, which was not used. Non-uniformities in the bed packing were expected based on the packing procedure and the bed design, as discussed in Section 3.3.2.2. Future work will explore the use of alternative bed designs, such as those demonstrated by Bergkvist *et al.*⁶. Improvements in bed packing will allow for the use of higher flow rates without concern for the creation multi-peak elution profiles, as were seen in Figure 5.7. All suggestions for future work and re-design issues are summarized in Chapter 6.

5.3.4 LOWER SAMPLE AMOUNTS

Smaller quantities of proteins were analyzed in order to evaluate the sensitivity of the system. The spectrum in Figure 5.8 is the result of a 8 pmol injection of cytochrome c. There is a significant amount of undigested cytochrome c remaining in the sample. This result can be compared to that seen in Figure 5.6, where no undigested cytochrome c was detected, under the same experimental conditions. The lower sample concentration, 0.2 mg/mL (16 μM) as compared to 2 mg/mL (160 μM), requires a longer contact time for full digestion. This is due to reduced enzyme kinetics, in the presence of limited substrate.⁷ The extent of digestion can be increased by extending the contact time, the introduction of organic solvents⁸ or by increasing enzyme or substrate⁷ concentration, thereby increasing digestion rate. The trypsin used for this work was purchased as an immobilized gel and as such, concentration was fixed. Introduction of organic solvents is also not feasible in this system as the resulting peptides would not be captured by the SPE beds. Use of slower flow rate would

extend contact time, but would also increase analysis time as well as sample dispersion. By increasing the bed length, contact time would be increased, without the need to decrease the flow rate. This would allow for more complete digestion of lower concentration samples, allowing lower quantities to be accurately identified. It should be noted that when the system is used in its entirety, digestion of low sample concentration is not a major concern, as the incoming protein samples will be first concentrated by the CIEF process. Sample concentrations factors of up to 700 times have been demonstrated for CIEF.⁹

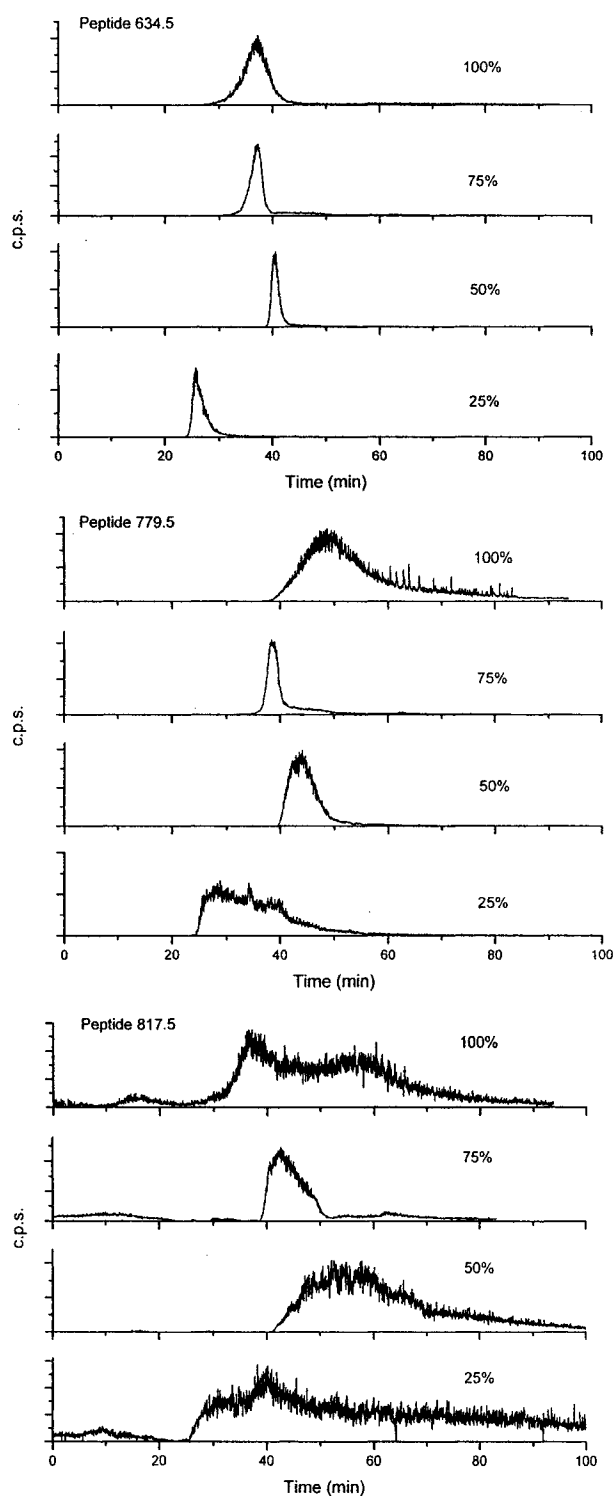


5.3.5 EFFECT OF ELUENT

In order for the delay line concept to be functional, a flash elution of the peptides from the SPE beds was necessary. It was assumed that this would be facilitated through the use of a strong eluent. However, initial trials with the multichannel device (Section 4.3.5) proved that this was not the case. In order to further explore this issue, a series of experiments were done using various MeOH concentrations, the results of which are shown in Figure 5.9. These results were obtained with the single channel device. When considering these traces, it should be noted that the starting time point for each trace was not accurately determined, hence the retention times can not be compared between MeOH concentrations. This data is presented to emphasize differences in peak shapes and widths for various peptides and eluents. All plots use the same x-scale. In all cases, elution profiles for 100% MeOH were broader than for 75% MeOH. Of the 12 peptides studied, 5 of the elution profiles were optimized at 50% MeOH and 7 at 75% MeOH. While one composition between 50-75% MeOH may be adopted to optimize elution, it is clear that the peaks are broad enough and have different enough elution profiles, that a flash elution would still be difficult. A longer delay line or a slower flow rate would allow for more time between eluting channels, but both would significantly increase the amount of dispersion experienced by the eluting peptides and thus would be counter-productive.

Use of a smaller SPE bed, with lower sample capacity has the potential to yield more rapid elution. Current bed design has the capacity to concentrate 1.8 μg of protein digest, as presented in Section 3.3.2.2. As shown in Figure 5.8, 8 pmol of cytochrome c can be easily detected (signal would be further improved by optimization of the digestion conditions).

Figure 5.9 Effect of MeOH concentration on peptide elution profiles explored with single channel device A



Load: 0.16 nmol cytochrome c
 (2 mg/mL)
 in 20 mM NH_4HCO_3
 + 1% ampholytes
 @ 0.02 $\mu\text{L}/\text{min}$.
 Wash: 2 μL of 20 mM NH_4HCO_3
 @ 0.02 $\mu\text{L}/\text{min}$,
 10 μL H_2O @ 1 $\mu\text{L}/\text{min}$;
 Elute:
 (Defined in plot)% MeOH,
 0.1 M Formic Acid
 @ 0.2 $\mu\text{L}/\text{min}$.
 Scan: $m/z = 550-1200$,
 33.3 scans/min.
 XIC m/z value is shown above
 each trace.

(June 2 and 3, 2003)

If it is assumed that 10 pmol of protein digest can be detected per bed, then each bed should be able to concentrate this amount. Using BSA, as it has the largest MW of the proteins studied, this results in a digest mass of 0.67 μg . Thus, a 50-60% reduction in bed volume should be possible allowing the beds to be driven closer to saturation. Near saturation chromatography effects are less likely to be seen and a single broad elution peak may result.

5.4 BAND BROADENING CONSIDERATIONS

The total amount of band broadening experienced by a sample plug as it travels through a system is defined as the sum of all sources of band broadening the plug experiences. A short discussion of dispersion within an open channel was introduced in Section 3.3.6, in which the term variance was introduced. Each band broadening term will have an associated variance term and the total variance experienced by the plug will be the sum of these terms. Equation 5.5 defines total sample variance.

$$\sigma_t^2(\text{Total}) = \sigma_{t,1}^2 + \sigma_{t,2}^2 + \dots + \sigma_{t,n}^2 \quad (5.5)$$

where $\sigma_{t,1}^2$, $\sigma_{t,2}^2$ and $\sigma_{t,n}^2$ are variances for independent band broadening processes. All variances described in this thesis have been expressed in units of time, indicated by the subscript "t". In order to identify all sources of band broadening one must consider the path of the sample plug. The plug will travel from the SPE bed, down a straight channel, into the electrospray (ESI) interface and finally through the ESI tip. The total variance for this system is defined by Equation 5.6.

$$\sigma_t^2(\text{Total}) = \sigma_t^2(\text{SPE bed}) + \sigma_t^2(\text{Straight Channel}) + \sigma_t^2(\text{ESI Interface}) + \sigma_t^2(\text{ESI tip}) \quad (5.6)$$

Let us first assume that the sample elutes from the SPE bed as an infinitely narrow plug, allowing $\sigma_t^2(\text{SPE bed})$ to be ignored. The variance induced

by the straight channel was addressed in Section 3.3.6 and resulted in Equation 5.7.

$$\sigma_i^2(\text{Straight Channel}) = \frac{2A^3LD}{F^3} \left[1 + \frac{5.8}{210} \left(\frac{Fd}{AD} \right)^2 \right] \quad (5.7)$$

Where A is the channel area, L is channel length, D is the molecular diffusion coefficient, F the volumetric flow rate and d is the channel depth. This equation is specific to an isotropically etched channel of depth 22.5 μm and mask width 60 μm . The majority of work presented in this chapter utilizes ESI interface SS-1. This consisted of a piece of stainless steel (SS) tubing coupled on one end to the chip and at the other to an electrospray tip. The SS tubing used in SS-1, had a large cross-sectional area of 24,053 μm^2 and as the flow exits from the chip channel ($A = 2145 \mu\text{m}^2$) it will expand into this larger volume. It is difficult to predict the amount of dispersion this will generate, but it is generally thought that this process results in disrupted flow profiles and will induce asymmetry into the resulting peak resulting in peak tailing.¹⁰ There is no equation to define this. It is possible to calculate the dispersion that would occur in this region if the flow was to behave in a non-disrupted manner. The same equations apply to this process as were used to define the dispersion in the chip channel. Equation 5.8 defines dispersivity for a pressure driven sample traveling in a non-sorptive tube, where r is the tube radius.

$$\sigma_i^2(\text{Tube}) = \frac{2A^3LD}{F^3} \left[1 + \frac{1}{48} \left(\frac{F}{\pi rD} \right)^2 \right] \quad (5.8)$$

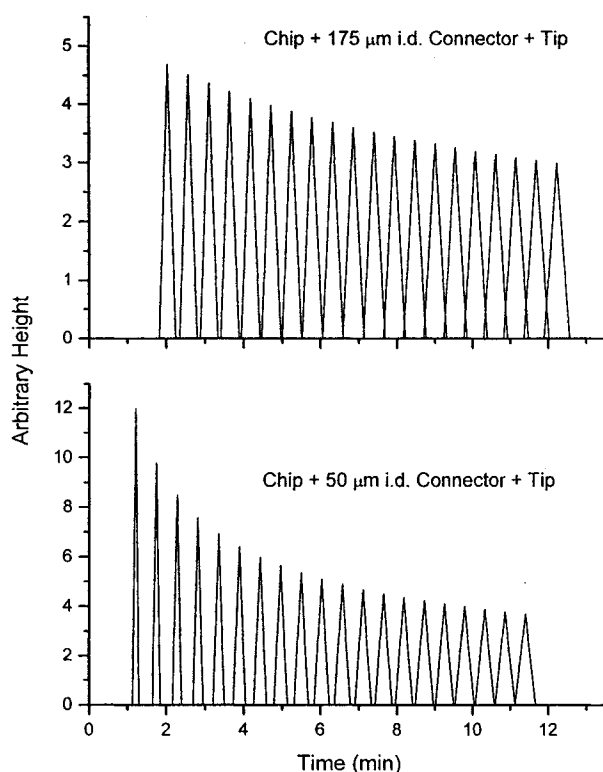
As the sample exits the SS tubing, entering the electrospray tip, it will once again undergo some disrupted behaviour due to the constricted cross section of the tip (1963 μm^2). Once, again it is difficult to predict what effect this will have on peak shape. The dispersion can again be calculated using Equation 5.8. The last potential source for band broadening occurs at the electrospray tip. If electrospray conditions are not optimized, then the flow exiting the tip will expand

into the open atmosphere before being drawn into the Taylor cone. Occasionally, multiple Taylor cones are seen as well¹¹, which will cause band dispersion. There is no way to determine the effect this will have on peak shape. The total band broadening experienced by the sample will be the sum of all these processes.

5.4.1 THEORETICAL BAND BROADENING IN THE MULTICHANNEL CHIP

Using the same approach presented in Section 3.3.6, a theoretical elution profile was generated for the entire multichannel device. Individual variances were calculated for four regions of interest. The first was the straight channel following the SPE bed. Equation 5.7 was used to calculate variance for each of the twenty channels using a flow rate of one twentieth of the input flow. Inlet flow rate was 0.4 $\mu\text{L}/\text{min}$ in order to reflect that generally used for work with the multichannel device. Channel lengths were variable, ranging from 0.85 cm for the shortest flow path to 10.35 cm for the longest channel. Channel cross-section was 2145 μm^2 , based on channel depth of 22.5 μm and a mask width of 60 μm . A diffusion coefficient of $5 \times 10^{-6} \text{ cm}^2/\text{s}$ was used. The second region was the short channel leading from the outlet star to the SS tubing. This region had a length of 0.45 cm. Equation 5.7 was used to calculate variance using the full inlet flow rate. Dispersion in the SS tubing was calculated using Equation 5.8 with a length of 1.5 cm and a radius of 87.5 μm . The area for the tubing was 24,053 μm^2 . Lastly, dispersion in the electrospray tip was calculated using Equation 5.8 with a length of 4.15 cm, radius of 25 μm and area of 1963 μm^2 . These four variances were summed and used to calculate peak width as was described in Section 3.3.6. Elution times were calculated as before, by using the total volume of the flow path and dividing by the volumetric flow rate. The resulting plot is shown in the top graph of Figure 5.10 and indicates that under these conditions, full peak resolution between channels is not theoretically possible.

Figure 5.10 Theoretical elution profiles from the multichannel device using two different ESI interfaces



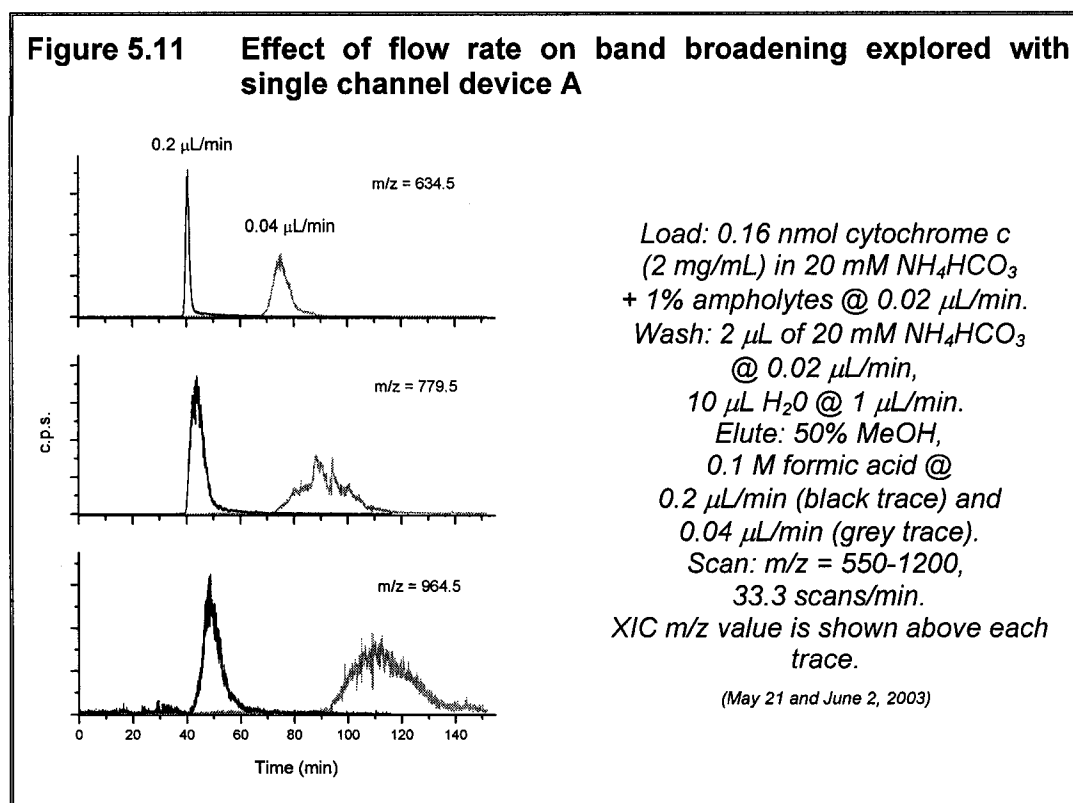
Elution profiles generated for the multichannel device using calculations defined in the text. The top plot is the result of full device simulation using an ESI interface SS tubing of 175 μm i.d. and the lower plot is the result of using an ESI interface SS tubing of 50 μm i.d.

This theoretical simulation does not account for disrupted flow effects that would occur due to the mismatched cross-section of the ESI interface. This effect would most likely serve to increase peak width and thereby further increase peak overlap. Furthermore, these calculations assume that elution from the SPE bed results in a sample plug of essentially zero width. This is not experimentally possible and hence the calculated variance would need to be added to the peak width resulting from SPE elution. In order to visualize the effects of the cross-sectional mismatch at the ESI interface a second theoretical plot was generated using a SS tubing of 50 μm i.d. as opposed to the 175 μm i.d. used in the first calculation. The result is shown in the lower plot of Figure 5.10. Simply by using a smaller i.d. connector, peak resolution is drastically increased. These results clearly indicate that some amount of ESI interface re-design is necessary in order

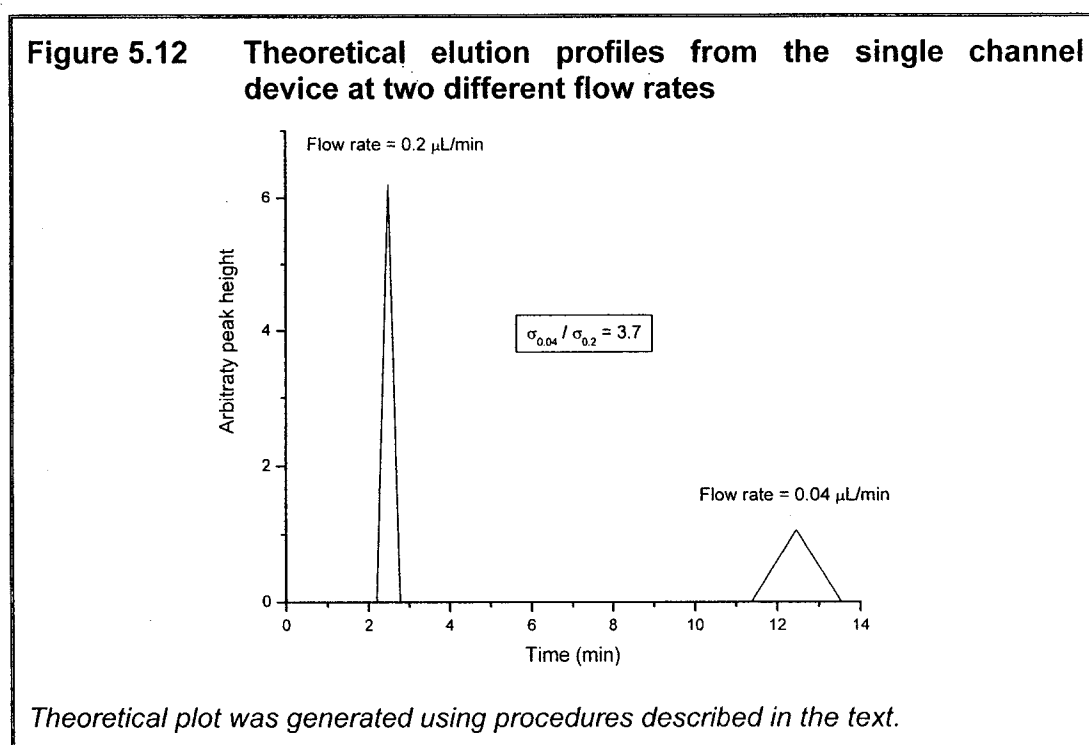
to increase peak resolution. Suggestions for such re-design are presented in part throughout this chapter and more thoroughly in Chapter 6.

5.4.2 EFFECT OF FLOW RATE ON BAND BROADENING

The effect of flow rate on peak width was experimentally explored using the single channel device A. This device consisted of a single straight channel with two beds at the introduction. The channel following the SPE bed had a length of 2.65 cm. This channel was coupled to ESI interface SS-1, comprised of a SS tube (length = 1.5 cm, 175 μm i.d.) coupled to an electrospray tip (length = 4.15 cm, 50 μm i.d., 15 μm tip). Elution of cytochrome c peptides was performed at two different flow rates, 0.04 and 0.2 $\mu\text{L}/\text{min}$. Experimental conditions are described in Section 5.3.1 and in the caption to Figure 5.11, which illustrates the results of the two flow rates. XICs for three peptides are illustrated.



Results indicate that a slower elution flow rate results in broadening of the resulting peaks, which was expected as a result of Equation 5.7. Experimental peak widths were measured and σ_t values extracted. Of the 8 peptides studied, the ratio of $\sigma_t(0.04 \mu\text{L}/\text{min})/\sigma_t(0.2 \mu\text{L}/\text{min})$ ranged from 3.59 to 5.58 with an average value of 4.36. Theoretical peaks were generated using the method described in Sections 3.3.6 and 5.4.1. Equation 5.7 was used to calculate σ_t for the straight channel and Equation 5.8 was used for the SS tubing and the electrospray tip. Channel dimensions are defined at the beginning of this section. The resulting theoretical plot is shown in Figure 5.12.



The theoretical $\sigma_t(0.04 \mu\text{L}/\text{min})/\sigma_t(0.2 \mu\text{L}/\text{min})$ ratio was 3.7. It should be noted that absolute elution times can not be compared between the theoretical and experimental plots. Theoretical time points were generated starting from the point of elution from the SPE bed, whereas, experimental time points were initiated when the elution buffer was introduced to the head of the trypsin bed. The experimental σ_t value for peptide 634.5 at a flow rate of $0.2 \mu\text{L}/\text{min}$ was 2.8 min whereas the theoretical value for a sample with $D = 5 \times 10^{-6} \text{ cm}^2/\text{s}$ was 0.15

min. The discrepancy between these two values is due to the dispersion induced by the SPE bed (which was not included in the theoretical calculation) and the disrupted flow behaviour generated at the ESI interface and other potential dead volumes. Furthermore, in all theoretical calculations a diffusion coefficient of $5 \times 10^{-6} \text{ cm}^2/\text{s}$ was used, which will not be representative of all peptides. Keeping these points in mind, it can be said that the theoretical and experimental σ_t ratio values correlate well. The discrepancy between the two values indicates that some flow-independent systemic source (such as disrupted flow in dead volumes) is contributing to the absolute band broadening.

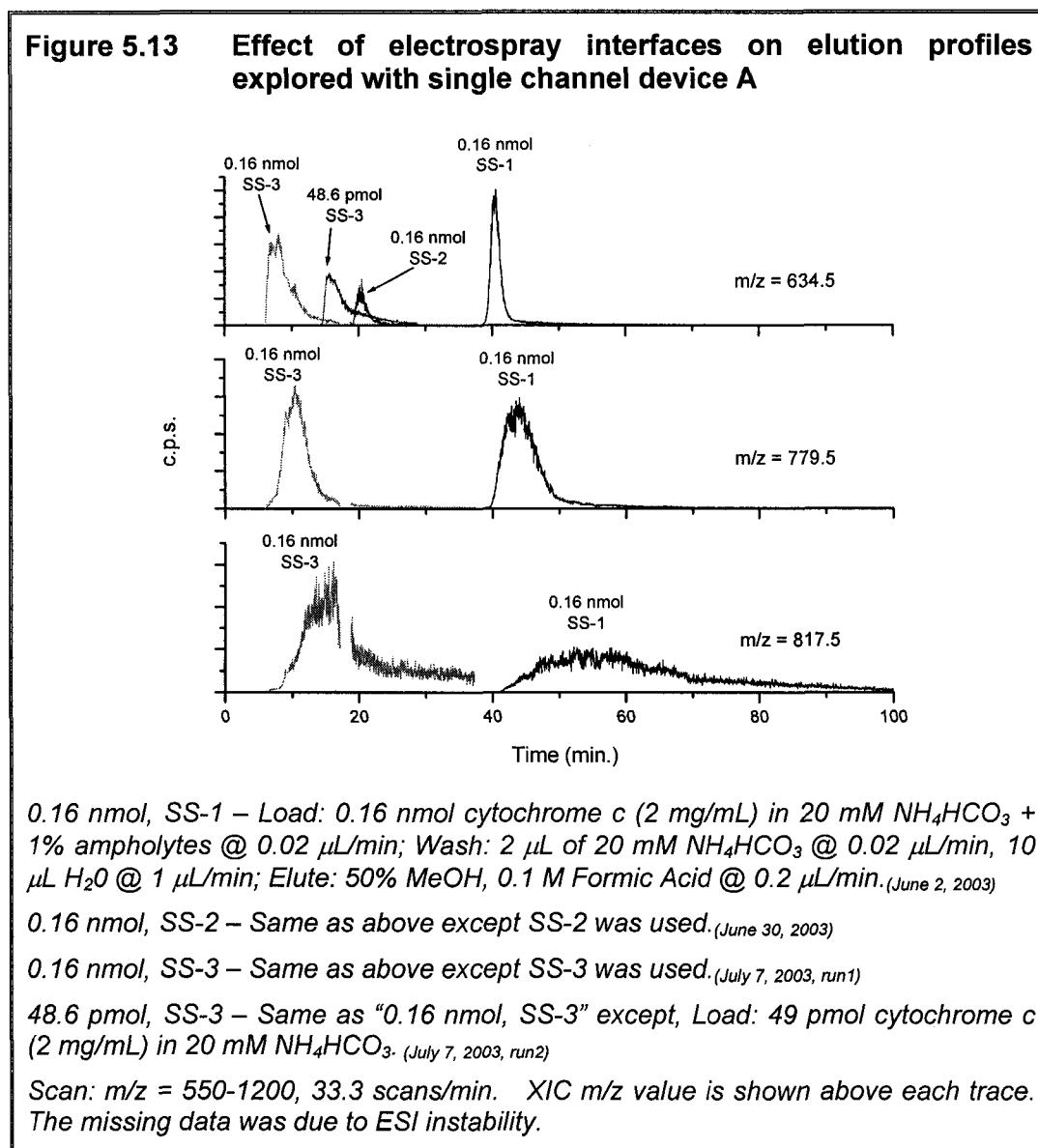
5.4.3 EFFECT OF THE ESI INTERFACE ON BAND BROADENING

In designing an ESI interface, two factors were important; the ability to apply a voltage to the sample solution reproducibly for long periods of time, and minimizing dead volumes that may be created by the coupling. Previous work done in this lab coupled an ESI tip directly to the microchip through a flat bottomed hole.¹² This interface had a minimal dead volume at the connection and the cross-sectional areas of the chip channel and the tip i.d. matched well. This interface worked well provided that the conductivity of the electrospray tip could be maintained. Fabricated ESI tips with electroplated gold coatings were seen to be very stable whereas commercial tips utilizing a sputtered metallic coating exhibited poor metal layer stability, as was discussed in Section 3.6. Four electrospray interfaces were used throughout the course of this work. All are presented in Chapter 3. ESI interface LJ-1 consisted of a capillary coupled on one end to the device and on the other to an electrospray tip. Electrical contact was provided through a controlled leak from an external solution. ESI interface SS-1 consisted of coupling a piece of SS tubing to the chip on one end and to an electrospray tip at the other. The SS tubing had a length of 1.5 cm and 175 μm i.d.. Electrical contact was made directly to the solution through the SS tubing. ESI interface SS-2, used the same design but had a SS tubing of length 0.75 cm and 50 μm i.d. Finally, ESI interface SS-3 used the same smaller i.d. SS

tubing but spray was achieved directly from the SS tubing without the use of an electrospray tip.

ESI interface LJ-1 satisfied both aforementioned criteria in that, no dead volumes were expected from the design, although no specific analysis of dead volumes was performed. However, reproducing the design proved to be overly challenging. ESI interface SS-1 was stable and easy to reproduce, however, there was a large mismatch in cross-sectional areas going from the microchip channel to the stainless steel tubing and back to the electrospray tip. The internal diameters of the chip and the ESI tip matched well, 2145 and 1963 μm^2 , respectively. However, the cross section of the SS tubing was 24,053 μm^2 , which, with a length of 1.5 cm, lead to a volume of 361 nL. This volume is extremely large considering that the entire volume of the empty SPE bed (no packing material) was only 150 nL. Ideally, the sample would elute from the SPE bed in an even smaller volume, creating an even more drastic comparison. The theoretical effect of the cross-section mismatch on dispersivity in a non-disrupted flow system has been illustrated in Figure 5.10 for the multichannel device. In order to be able to test the impact that the large SS tubing volume had on band broadening, ESI interface SS-2 was used for comparison. In this case, the i.d. of the SS tubing and the electrospray tip match exactly (1963 μm^2) and were similar to the chip channel cross-sectional area (2145 μm^2). The small o.d. of the SS tubing, 125 μm , lead to great difficulties in coupling this tubing to the electrospray tip, which had a 360 μm o.d.. The coupling was accomplished once successfully, the results of which are shown in Figure 5.13. It was then discovered that electrospray was possible directly from the SS tubing without the need for an electrospray tip (SS-3). This result has been published recently by Shui *et al.*¹¹ Results from electrospray interfaces SS1-3 are shown in Figure 5.13 for three cytochrome c peptides. The peak height for interface SS-2 was significantly reduced when compared to the trace utilizing ESI SS-1, due to the choice of instrumental settings. The results obtained were unexpected. It was assumed

that the use of a smaller i.d. SS tubing would significantly reduce peak width. This was not seen.



The peak width of peptide 634.5 (from 0.16 nmol, SS-1) was 2.6 min at the baseline. This corresponds to a volume of 520 nL at the experimental flow rate of 0.2 $\mu\text{L}/\text{min}$. This can be compared to the volume contained within the SS tubing, 361 nL, and the volume within the empty SPE bed, 150 nL. From these

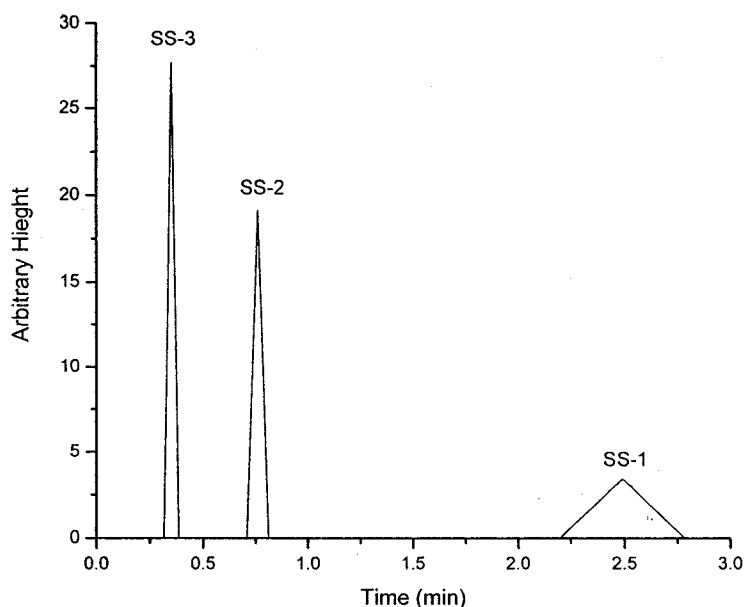
values, no definite conclusion can be made as to how much mixing is occurring in the interface, suffice to say that based on the volume values, a great deal of dispersion is expected to occur outside of the SPE beds. Even if the sample eluted from the SPE bed with a volume equal to the bed volume, this would still only account for 150 nL out of a total peak volume of 520 nL. It is possible that the reservoir allowing for bead introduction, at the head of the SPE bed, may contribute to the overall broadening effect. However, the extensive washing steps should transfer any sample initially contained in this volume to the SPE bed. Most likely, it is the large volume of the ESI interface (SS-1), which would account for most of the broadening effects. Peak detection before and after the interface would need to be used in order to assess the band broadening effects of the large i.d. SS tubing. This is not possible with the current experimental set-up but will be the subject of further research.

Theoretical peaks were generated for the three ESI interfaces and are shown in Figure 5.14. Elution times were calculated using only the volume contained in the ESI interface. Theoretical results were as expected, with the smaller i.d. interfaces (SS-2 and SS-3) demonstrating far less band broadening. Yet, experimental results for SS-3 show significant tailing, for some peptides at least. It is suspected that poor optimization of the ESI conditions for the SS emitter led to a poorly formed Taylor cone or possibly multiple Taylor cones.¹¹ Further optimization of electrospray conditions for SS emitters (such as voltage, flow rate, SS emitter size and shape) should lead to stable electrospray conditions and will avoid the need for a secondary tapered silica emitter, as was used in SS-1 and SS-2.

No conclusion can be drawn from the experimental data presented in this section as to the effects of the larger i.d. SS tubing. However, results presented in Figures 5.10 and 5.14 indicate that the system should have benefited from a smaller i.d. connection. The disagreement of experimental results with dispersion theory calculations, suggests that there are still unrecognized problems within the interface. As mentioned in the previous paragraph, these

problems may be related to the formation of the Taylor cone. Optimization of the smaller SS connection is on-going and promises to result in a reliable ESI interface, with negligible dispersive properties.

Figure 5.14 Theoretical elution profiles for three ESI interfaces



Theoretical plots were generated as described in Sections 3.3.6 and 5.4.1. ESI interfaces SS1-3 are described at the beginning of this section. A flow rate of $0.2 \mu\text{L}/\text{min}$ was used for calculations.

SS-1 – Chip channel length: 2.65 cm; SS tube: length = 1.5 cm, $175 \mu\text{m}$ i.d.; ESI tip: length = 4.15 cm, $50 \mu\text{m}$ i.d.

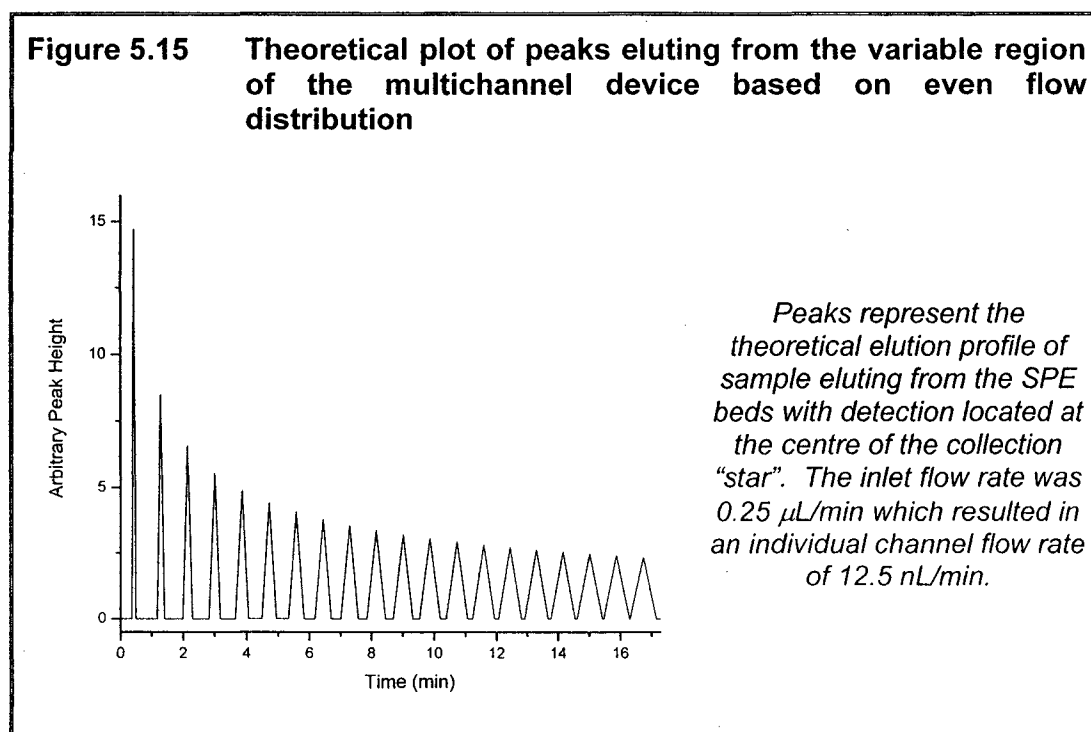
SS-2 - Chip channel length: 2.6 cm; SS tube: length = 0.75 cm, $50 \mu\text{m}$ i.d.; ESI tip: length = 4.15 cm, $50 \mu\text{m}$ i.d.

SS-3 - Chip channel length: 2.6 cm; SS tube: length = 1.5 cm, $175 \mu\text{m}$ i.d.

5.5 RESISTANCE TO FLOW WITHIN THE MULTICHANNEL SYSTEM

As stated in Section 3.3.6, when designing the delay line it was originally assumed that the back pressures exhibited by the beds would dominate flow resistance and thereby the effects of the variable channel lengths in the delay

line would be negligible. By this argument, all channels would appear to have equal flow resistances from the point of view of the single inlet which results in the inlet flow being evenly distributed. Assuming an even flow rate in all channels resulted in the theoretical plot shown in Figure 5.15 (also shown in Figure 3.7). The method used for the generation of this plot was presented in Section 3.3.6.



This plot illustrates that a constant time delay between adjacent channels was expected. Peak width was seen to increase in the later eluting peaks as the longer channel length resulted in a greater amount of dispersion. An experiment was done early in the platform testing in order to assess this. A solution of potassium permanganate was pumped through the sealed system and was visually observed through the bottom of the Plexiglass holder. In this initial experiment the dye was seen to travel from the inlet to the trypsin beds with relative ease. From this result it was concluded that the initial assumption regarding bed flow resistances was true. However, the inconsistent elution profiles that were seen in Chapter 4 lead to further exploration of this issue.

In order to test the theoretical basis of the aforementioned assumption, a series of calculations were performed. Channel resistances were calculated using Equations 5.1 and 5.2 as presented in Section 5.2.2. Equation 5.1 defines the pressure drop across a rectangular channel. This equation is comparable to the voltage drop across a resistor, where the pressure drop is equivalent to voltage drop, volumetric flow rate is equivalent to current and the remainder of the equation represents the resistance. Channel resistances were calculated using Equation 5.9

$$R = \left(\frac{4\eta L}{(wd)^2 F} \right) \quad (5.9)$$

Where R is the channel resistance, η is viscosity, L is the channel length, F is a geometric form factor calculated previously (0.066965), and w is the channel width as defined for a rectangular channel of the same area as the isotopic channel with depth: $d = 22.5 \mu\text{m}$ and mask width = $60 \mu\text{m}$. The channels in the variable region range in length from 0.25 cm to 9.75 cm. Channel depth was $22.5 \mu\text{m}$ and width was $95.34 \mu\text{m}$. Only relative values were needed, so values of R/η were calculated, resulting in relative resistances of $3.25 \times 10^{10} \text{ cm}^{-3}$ and $126 \times 10^{10} \text{ cm}^{-3}$ for the shortest and longest channels, respectively. The difference between the two channels is quite large and hence one would expect to see noticeable back pressure effects.

Calculation of the resistance generated by the beds was more complicated and most likely less accurate. The pressure drop across a packed bed can be expressed in a slightly different form than that shown in Equation 5.1. This form is known as Darcy's Law.¹⁰

$$\Delta P = \Phi \left[\frac{\eta L \varepsilon_T}{AB^o} \right] \quad (5.10)$$

From this resistance can be defined by Equation 5.11.

$$R = \left[\frac{\eta L \varepsilon_T}{AB^0} \right] \quad (5.11)$$

Where Φ is the volumetric flow rate, L the channel length, η is viscosity, A is the cross-sectional area, ε_T is the total porosity and B^0 is the specific permeability coefficient. The total porosity is defined as the sum of the interparticle porosity (ε_{inter} : fraction of total column volume contained between beads) and the intraparticle porosity (ε_{intra} : fraction of total column volume contained within the pores). For a uniformly packed column $\varepsilon_{inter} = 0.4$ and ε_{intra} is 0 for non-porous materials and 0.4 for most porous materials.¹⁰ The specific permeability is defined by the Kozeny-Carmen equation.¹⁰

$$B^0 = \frac{d_p^2}{180} \frac{\varepsilon_{inter}^3}{(1 - \varepsilon_{inter})^2} \approx \frac{d_p^2}{1000} \quad (5.12)$$

Where d_p is the diameter of the packing particles. This equation applies to irregular shaped particles, however, spherical particles have been seen to be more permeable and so the equation reduces to:

$$B^0 \approx \frac{d_p^2}{500} \quad (5.13)$$

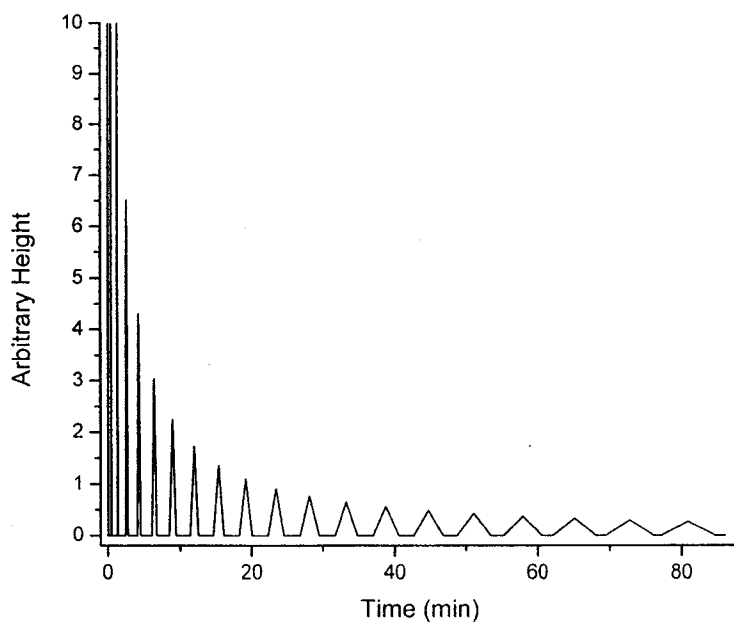
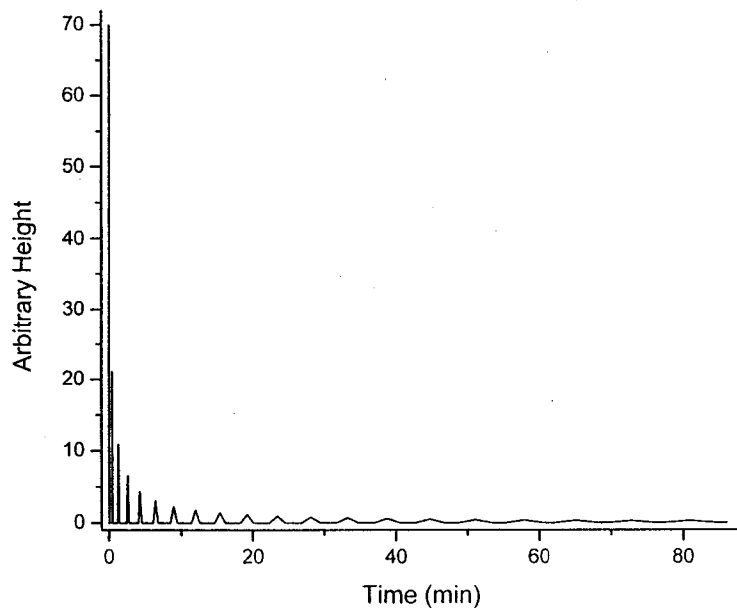
Using Equations 5.11 and 5.13, values of R/η were calculated for the two beds. The trypsin bed had a length of 0.4 cm and a cross-sectional area of 70,619 μm^2 . Trypsin was supplied as an immobilized gel and as such it was assumed to be porous ($\varepsilon_{inter} = 0.4$, $\varepsilon_{intra} = 0.4$). The particles were spherical with $d_p = 40\text{-}60 \mu\text{m}$. This resulted in R/η values of 0.62-1.42 $\times 10^{10} \text{ cm}^{-3}$. The SPE bed had a length of 0.2 cm, a cross-sectional area of 70,619 μm^2 and was packed with porous ($\varepsilon_{inter} = 0.4$, $\varepsilon_{intra} = 0.4$), spherical particles with $d_p = 60 \mu\text{m}$. This resulted in a R/η value of 0.31 $\times 10^{10} \text{ cm}^{-3}$. Even the sum of these two resistances, 0.93 – 1.73 $\times 10^{10} \text{ cm}^{-3}$, is minor when compared to the resistance generated by the smaller cross-sectional channels in the variable region. Bed packing for this bed design

has been seen to be inconsistent and as such, the above values, which are for uniform packing, can not be accurate. However, errors of this sort would most likely serve to further lower the resistance of the beds. The result of this calculation is that individual channel resistance will now be dominated by the length of the channels in the variable region. Hence, when a single pressure source is introduced at the inlet the flow will be distributed on the basis of channel resistance. Thus, the channel with the lowest resistance to flow, the shortest, will receive a larger fraction of the inlet flow. Flow distribution can be calculated using Ohm's law calculations as illustrated in Equation 5.14.

$$\begin{aligned}
 \Phi_i &= \Phi_T \left(1 - \frac{R_i}{R_{T-i}} \right) \\
 R_T &= \left(\sum_{n=1}^{n=20} \frac{1}{R_n} \right)^{-1} \\
 R_{T-i} &= \left[\left(\sum_{n=1}^{n=20} \frac{1}{R_n} \right) - \frac{1}{R_i} \right]^{-1} \\
 R_n &= \frac{4\eta L_n}{(wd)^2 F}
 \end{aligned} \tag{5.14}$$

Where Φ_i is the volumetric flow rate in channel i , Φ_T the total volumetric flow rate at the inlet, R_T the sum of all channel resistances ($n=1-20$) added inversely, R_{T-i} the sum of all channel resistances except for channel i and all other parameters have been defined previously. This allowed for an individual channel flow rate to be calculated for each channel. Using these variable flow rates a second theoretical plot was generated using the same method as was used to generate the plot in Figure 5.15. The result is shown in Figure 5.16.

Figure 5.16 Theoretical plot of peaks eluting from the variable region of the multichannel device based on a resistance biased flow distribution

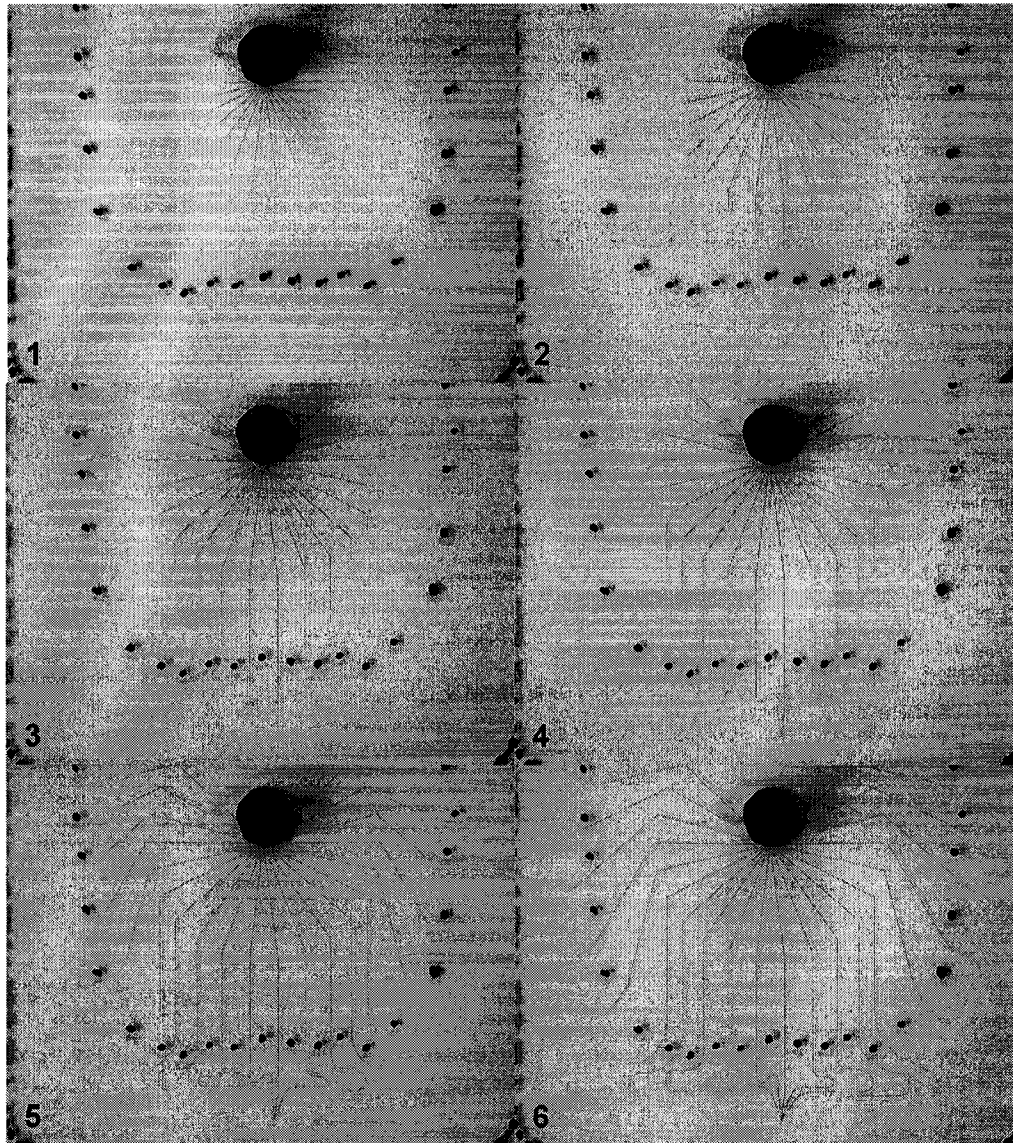


Peaks represent the theoretical elution profile of sample eluting from the SPE beds with detection at the center of the outlet "star". Plots were generated by the same method as used for Figure 5.15. The upper plot shows the full y-scale and the lower plot an expanded y-scale. Inlet flow rate, Φ_T , was $0.25 \mu\text{L}/\text{min}$.

This plot illustrates the drastic effect that the variable flow rate will have on performance. The time for full elution is increased which results in the later eluting peaks experiencing a great amount of dispersion. However, it should be noted that the concept of the delay line is still functional allowing individual channel contributions to remain resolved.

In order to test the actual platform, two visual experiments were performed. In the first, dye was pressure driven through a device which consisted of a single inlet and outlet with no beds. This served to isolate the behaviour of the delay line region. Results of this experiment are shown in Figure 5.17. The photos were taken at a one minute interval.

Figure 5.17 Photos of dye pressure driven through a multichannel device with no beds



Photos taken 1 min apart of dye driven through a multichannel device without beds. Dye was introduced at the single inlet and was pressure driven to the single outlet. Flow rate was 0.4 $\mu\text{L}/\text{min}$.

The distance that the dye traveled in between photos was measured visually for each channel. Two values were generated by taking the difference between the first and second photos and the difference between the second and third photos. The resulting distances were divided by the distance the inlet flow was expected

to travel during one minute in a channel of the same cross-sectional area (volumetric flow rate divided by cross sectional area) and expressed as a percentage of the incoming flow. This calculation is illustrated below.

$$\begin{aligned} \text{Channel Flow Rate} &= \frac{(\text{distance dye travels in 1 min interval in channel of interest})}{(\text{distance dye travels in 1 min interval in inlet channel before the frustum})} \\ &= \frac{x \text{ cm}}{(0.4 \mu\text{L} / \text{min})(1 \text{ min}) \left(\frac{1}{2.145 \times 10^{-5} \text{ cm}^2} \right)} \\ &= \frac{x \text{ cm}}{18.6 \text{ cm}} \quad (\text{expressed as a fraction of the incoming flow}) \end{aligned}$$

The two sets of data were averaged and the results are presented in Table 5.1. Flow in the shortest channel was the fastest resulting in the greatest distance travelled within the interval yielding a linear flow rate of 1.2 cm/min corresponding to 6.4% of the inlet flow rate. The theoretically predicted results were also presented in Table 5.1. Theoretical variable flow distribution elution profiles were previously presented in Figure 5.16 for an inlet flow rate of 0.25 $\mu\text{L}/\text{min}$. A change in inlet flow rate will alter elution times and dispersion but not the flow distribution which is dependent only on channel resistance and hence, channel length. At an inlet flow rate of 0.4 $\mu\text{L}/\text{min}$, the theoretically predicted flow rate within the shortest channel was 7.5 cm/min, which accounts for 40% of the incoming flow.

Table 5.1 Experimental and theoretical inlet flow distribution within the multichannel device

Channel #	Experimental flow distribution (%)	Theoretical flow distribution (%)
1 (shortest)	6.4	40
2	5.6	13
3	5.6	8.1
4	4.9	5.8
5	4.6	4.5
6	3.9	3.7
7	3.6	3.1
8	3.9	2.7

9	3.2	2.4
10	3.4	2.1
11	3.1	1.9
12	3.1	1.8
13	3.0	1.6
14	3.0	1.5
15	2.8	1.4
16	2.6	1.3
17	2.9	1.2
18	2.4	1.15
19	2.3	1.1
20 (longest)	1.8	1.0
Totals	72	100

The results of this experiment predict that there is some channel length dependent flow distribution seen within the device although the effects are not nearly as great as predicted through calculation. The largest discrepancy is seen in the first channel flow distribution. Theoretically, it was expected that a much larger fraction of the inlet flow be directed to the first channel. The reason for this difference between experimental results and theoretical predictions is unclear. However, this visual experimental has clearly shown that the delay line concept is functional. The difference in total flow distribution seen in the last row of the table can be attributed to discrepancies in the calibration of the syringe pump, leading to an inaccurate inlet flow rate.

The second visual experiment was done using a full multichannel device with beds packed and sealed in the Plexiglass holder. Dye was again pressure driven through the system from the single inlet and observed through the bottom of the holder. Experimental procedure developed for the multichannel device, presented in Chapter 4, used loading and wash volumes of 20 – 30 μL . This was the volume contained within the entire device without packing material in the beds, including the additional volumes added by the empty reservoirs. The details of this calculation are shown in Figure 5.18. All parameters have been defined in the previous two chapters.

Figure 5.18 Volume contained within the entire multichannel device

$$\begin{aligned}
 \text{Total channel length} &= \text{Introduction channel length} \\
 &+ 20 \times (\text{Fractionation radius length}) \\
 &+ 20 \times (\text{Bed region length}) \\
 &+ \text{Sum of variable channel lengths} \\
 &+ 20 \times (\text{Collection "star" length}) \\
 &+ \text{Exit channel length} \\
 &= 0.75 + 20(2) + 20(2) + \sum_{n=0}^{n=19} (0.25 + n0.5) + 20(0.5) + 0.45 \text{ cm} \\
 &= 191.2 \text{ cm} \\
 \text{Total channel volume} &= \text{Cross-sectional area} \times \text{length} = (2145 \mu\text{m}^2)(191.2 \text{ cm}) \\
 &= 4.12 \mu\text{L} \\
 \text{Total Reservoir Volume} &= 40\pi r^2(\text{depth}) = 40\pi(0.0343 \text{ cm})^2(0.098 \text{ cm}) \\
 &= 14.48 \mu\text{L} \\
 \text{Total Bed Volume} &= 20 \times \text{Cross-sectional area} \times \text{length} = (70,619 \mu\text{m}^2)(0.6 \text{ cm}) \\
 &= 8.47 \mu\text{L} \\
 \text{Total volume contained by the empty device} &= 27.1 \mu\text{L}
 \end{aligned}$$

The above volume calculation is for the device without packing material and is hence an overestimate of the volume contained within the actual experimental device. However, this value was the basis for using the relatively large wash volumes.

This second visual experiment was done keeping these volumes in mind. Photos resulting from the extended flush of potassium permanganate through the device are shown in Figure 5.19, as well as the volume injected at each time point. Once again the dye was seen to travel with relative ease to the trypsin beds. Sample was seen in all but three trypsin beds after the injection of 4.9 μL (B). The device that was used for this experiment had been used extensively, and it was assumed that these three channels had become clogged. After the injection of 10.8 μL dye (C), 17 of the trypsin beds were filled with dye as well as 4 of the SPE beds.

Figure 5.19 Observation of pressure driven flow throughout the sealed multichannel device, including beds

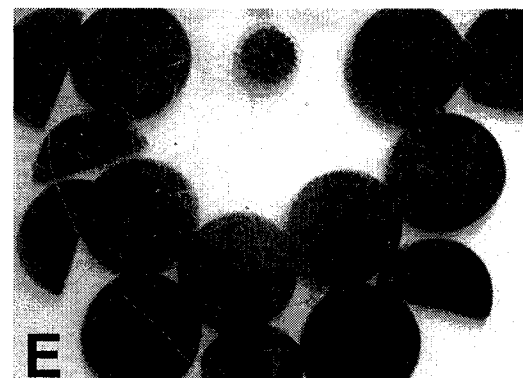
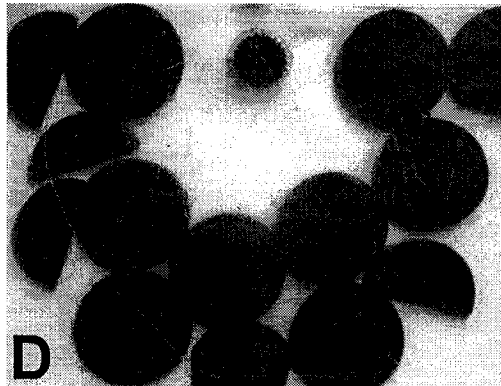
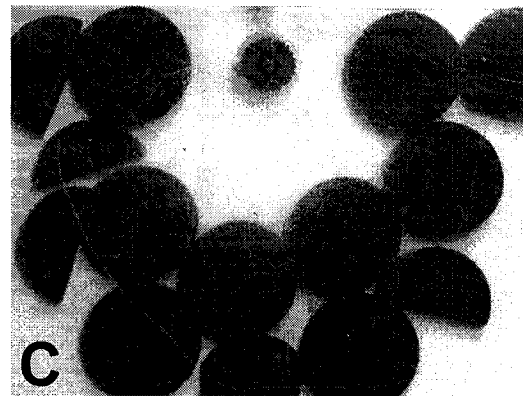
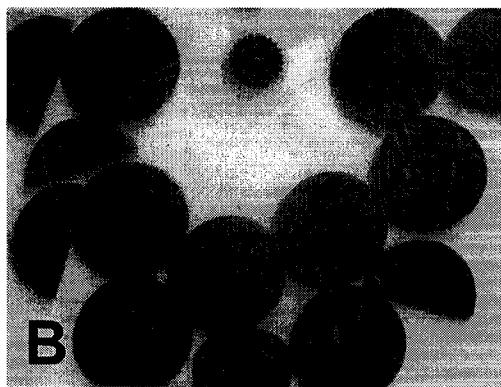
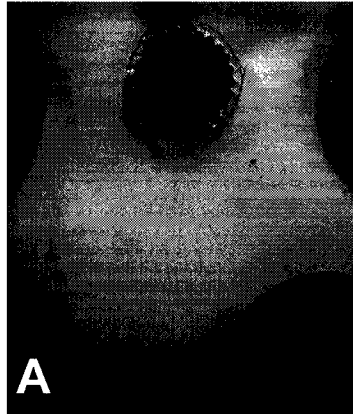
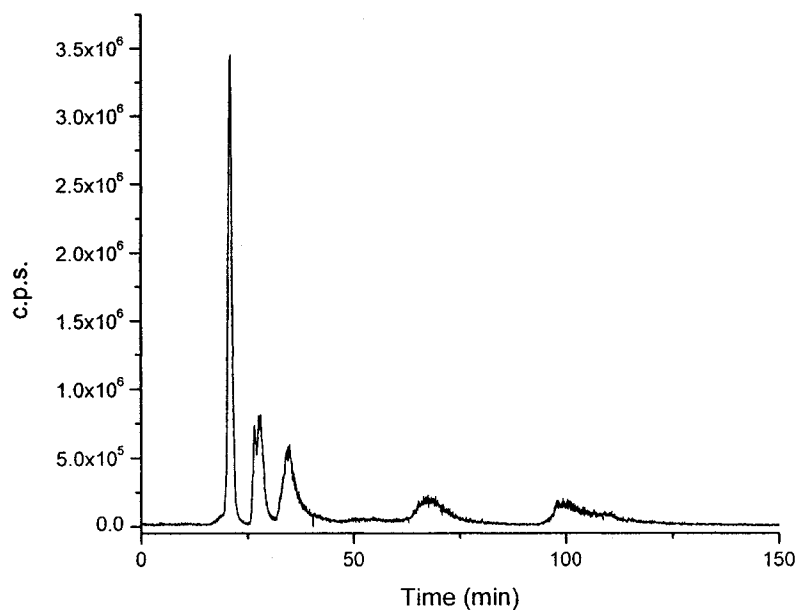


Photo A was taken after the injection of 1.4 μL of potassium permanganate. Photos B, C, D and E were taken after the injection of 4.9 μL , 10.8 μL , 24.7 μL and 147.2 μL of dye, respectively. Photos of the sealed system were taken through the bottom of the Plexiglass holder.

Of note is the position of the four SPE beds that contained dye. Dye was seen in SPE beds in channels 1, 12, 18 and 19, where numbers refer to overall channel lengths as originally defined in Figure 3.1. If back pressure due to variable channel length was a dominant force, then dye would travel to the SPE beds in the shortest channels first, 1-4. This was not seen. After the injection of 24.7 μL (D), dye was seen in 13 of the SPE beds. Finally, after extended flushing at 147.2 μL (E), dye was seen in all of the trypsin beds and 15 of the SPE beds. However, even after this extended loading time, dye was only seen in 5 of the channels following the SPE beds. Once again, dye was seen in random channels (#s: 1, 3, 12, 18, 19), that is, not in the 5 shortest channels (lowest back pressure). This would infer that in a typical multichannel experiment, as was demonstrated in Chapter 4, sample contribution would only be seen from approximately 5 channels. Considering that in many of the elution profiles seen in Chapter 4, only 3-6 broad peaks were seen, it seems logical to assume that each peak represents contribution from one channel and that the channels which contribute to the overall signal were randomly selected, with respects to length. The result in Figure 5.19 correlates well with the elution profile for a cytochrome c peptide generated with the same device as is shown in Figure 5.20, which supports this conclusion.

Figure 5.20 XIC_{634.5}, peptide elution profile collected with the same multichannel device as was used for the study in Figure 5.19



XIC for cytochrome c peptide $m/z = 634.5$ collected with the same device as was used for the study presented in Figure 5.19. Load: 1 nmol cytochrome c (0.5 mg/mL) in 20 mM NH_4HCO_3 + 1% ampholytes @ 0.4 $\mu\text{L}/\text{min}$. Wash: 20 μL of 20 mM NH_4HCO_3 @ 0.4 $\mu\text{L}/\text{min}$, 30 μL H_2O @ 1 $\mu\text{L}/\text{min}$. Elute: 50% MeOH, 0.1 M formic acid @ 0.4 $\mu\text{L}/\text{min}$. Scan: $m/z = 550-1200$, 26.1 scans/min. (Mar. 27, 2003)

Back pressure sources would appear not to be the source of the selective passage seen in Figure 5.19, as these would affect the trypsin beds in the same selective manner. It would appear that some dynamic process is occurring during sample loading that alters the resistance of the SPE beds or the flow path between the trypsin and SPE beds. Two possible explanations have been proposed. First, during bed packing it was seen that the porosity of the SPE beds would alter with increased flow time. The beds would occasionally become so tightly packed so as to stop flow. The second possibility involves the sealing of the septa. It is possible that during loading a pressure is exerted on the septa such that they deform, creating a negative pressure on the system. This seems

likely as the channels that were seen to allow passage of dye were located on the outer most edge of the device, closer to the screws that were used to seal the clamp. The septa closer to the edges of the holder may be more tightly sealed and hence are less likely to experience deformation. Those septa located in the center of the holder may be less tightly sealed and hence are able to deform. It is necessary to apply a uniform pressure across the device in order to seal all septa evenly. This appears not to be possible with the current holder design. Solutions to this problem are the focus of ongoing research.

This theoretical study has shown that the comparison between open small cross-section channels and large cross-section packed beds, should be considered for its implications on flow resistances. This point should be considered in the design of delay line systems. Furthermore, a more uniform sealing system will be necessary in order to avoid any problems related to septa deformation.

5.6 REFERENCES

- (1) Attiya, S.; Jemere, A. B.; Tang, T.; Fitzpatrick, G.; Seiler, K.; Chiem, N.; Harrison, D. J. *Electrophoresis* **2001**, *22*, 318-327. "Design of an interface to allow microfluidic electrophoresis chips to drink from the fire hose of the external environment"
- (2) Serway, R. A. *Physics for Scientists and Engineers*, Third Edition; Saunders College Publishing: Chicago, 1992.
- (3) Atkins, P. *Physical Chemistry*, Fifth Edition; W.H. Freeman and Company: New York, 1994.
- (4) Qui, X. C. *Ph.D.*, "Understanding fluid mechanics and its application to integrating calibration with on-chip immunological reactions" University of Alberta, Edmonton, Alberta, Canada, **1999**.
- (5) Wang, C.; Oleschuk, R.; Ouchen, F.; Li, J. J.; Thibault, P.; Harrison, D. J. *Rapid Commun. Mass Spectrom.* **2000**, *14*, 1377-1383. "Integration of immobilized trypsin bead beds for protein digestion within a microfluidic chip incorporating CE separations and an electrospray MS interface"
- (6) Bergkvist, J.; Ekström, S.; Wallman, L.; Löfgren, M.; Marko-Varga, G.; Nilsson, J.; Laurell, T. *Proteomics* **2002**, *2*, 422-429. "Improved chip design for integrated solid-phase microextraction in on-line proteomic sample preparation"
- (7) Craft, D.; Doucette, A.; Li, L. *J. of Prot. Res.* **2002**, *1*, 537-547. "Microcolumn capture and digestion of proteins combined with MS for protein identification"
- (8) Slys, G. W.; Schriemer, D. C. *Rapid Commun. Mass Spectrom.* **2003**, *17*, 1044-1050. "On-column digestion of proteins in aqueous-organic solvents"
- (9) Shen, Y. F.; Berger, S. J.; Anderson, G. A.; Smith, R. D. *Anal. Chem.* **2000**, *72*, 2154-2159. "High-efficiency CIEF of peptides"
- (10) Cantwell, F. F. *Lecture Notes, Chem 421: Analytical Separations*; University of Alberta, Department of Chemistry: Edmonton, Alberta, Canada, **1998**.
- (11) Shui, W.; Yu, Y.; Xu, X.; Huang, Z.; Xu, G.; Yang, P. *Rapid Commun. Mass Spectrom.* **2003**, *17*, 1541-1547. "Micro-electrospray with stainless steel emitters"
- (12) Bings, N. H.; Wang, C.; Skinner, C. D.; Colyer, C. L.; Thibault, P.; Harrison, D. J. *Anal. Chem.* **1999**, *71*, 3292-3296. "Microfluidic devices connected to fused-silica capillaries with minimal dead volume"

**CHAPTER 6: CONCLUSIONS AND FUTURE WORK
INVOLVING THE MULTICHANNEL
DEVICE**

6.1	SAMPLE INTRODUCTION.....	209
6.1.1	FRACTIONATION "STAR"	209
6.1.2	SAMPLE LOAD	210
6.2	BED REGION	210
6.2.1	DIGESTION BEDS	210
6.2.2	SPE BEDS.....	211
6.2.3	BED DESIGN	212
6.3	VARIABLE REGION	213
6.3.1	DELAY LINE.....	213
6.3.2	VALVES	214
6.4	COLLECTION REGION.....	214
6.5	SYSTEM FLOW RATE	215
6.6	APPLICATION TO PROTEOMICS	215
6.7	ALTERNATIVE APPLICATIONS	220
6.8	REFERENCES	221

As a first prototype, this initial design was useful in determining the components that were successful and those that needed re-design. The individual components of the device are explored in the following sections in terms of specific conclusions and suggestions for future work. Furthermore, a discussion of microfluidic strategies for use in proteomics, as well as alternative uses for the multi-channel device, is presented.

6.1 SAMPLE INTRODUCTION

6.1.1 FRACTIONATION "STAR"

The electrical fractionation process (as discussed in Section 5.2) functioned as expected, however, due to the initial design of the injector region, some diffusion effects were seen. It was suspected that cross-contamination issues may arise when individual samples are directed to specific channels due to the relatively large volume of the frustum formed by the intersecting channels. Through the use of a circular introduction path with fractionation arms branching away from it, this problem should be minimized. Furthermore, the introduction of a sheath flow at the inlet should also serve to reduce cross-contamination between incoming samples. A schematic of this concept has been presented in Figure 5.4. The addition of a sheath flow at the inlet also eliminates buffer compatibility issues that may arise when actual CIEF samples are introduced. The eluent from a CIEF column will contain proteins with a range of different local pHs. As proven in Section 4.3.3, trypsin will not function at acidic pH values. In order to eliminate this problem, solvent exchange must be performed or a different peptidase must be used. Introduction of a sheath flow should serve to normalize pH values, thereby reducing this problem. Furthermore, the use of the digestion buffer (20 mM ammonium bicarbonate at a pH of 8.6) as catholyte for CIEF proved problematic, as described in Section 4.2.2, Figure 4.7. Using a sheath flow, the digestion buffer could be introduced at the end of the fractionation process allowing a different catholyte to be used for focusing. The main concern with this concept is that enough CIEF catholyte be present in the

channel before the introduction of the sheath flow, so as to allow for adequate focusing. This may not be trivial and a two-step CIEF technique may need to be adopted.

6.1.2 SAMPLE LOAD

Using the current design with an etch depth of 22.5 μm , the maximum volume that can be electrokinetically injected into a single fractionation arm was 53.6 nL. This leads to a total load volume of 1.07 μL , which corresponds to a 54.5 cm long, 50 μm i.d. capillary or a 13.6 cm long, 100 μm i.d. capillary. This volume is acceptable for non-preparative CIEF, however, for preparative CIEF a greater volume will be needed. This could be achieved through increasing either the length or cross-sectional area of the loading arms. Expansion of the cross-sectional area as opposed to increasing channel length would allow the same voltage to be applied, as the electric field will remain constant. Since a SPE step will be incorporated in the device at some point after this step, diffusion and band broadening within the arms is not a concern.

6.2 BED REGION

6.2.1 DIGESTION BEDS

The digestion beds described in the text were 4 mm long and contained a volume of 0.298 μL . If it is assumed that this entire volume contains beads, then the protein digestion capability of the bed is 1.2 – 3 μg protein (as stated by the manufacturer, Pierce). Although this mass is more than sufficient to meet the needs of any incoming CIEF focused protein samples, it is based on a stop flow digestion executed in a vial, as opposed to a continuous flow system. Digestion was fully achieved with these beds using a flow rate of 0.02 $\mu\text{L}/\text{min}$ and was seen to be incomplete at a flow rate of 0.4 $\mu\text{L}/\text{min}$, as shown in Section 5.3.3. These flow rates are relatively slow and will reduce the overall throughput of the device. The extent of digestion is based on protein-trypsin contact time and sample

concentration. Variables which affect the contact time include: flow rate, bed volume and bead size. By this logic, a larger bed volume should allow digestion to go to completion, even at a flow rate of 0.4 $\mu\text{L}/\text{min}$. Digestion of a 16 μM solution of cytochrome c was incomplete even at a flow rate of 0.02 $\mu\text{L}/\text{min}$ (Section 5.3.4). This is due to reduced enzymatic kinetics in the presence of limited substrate and is a common problem. As mentioned previously, there are several solutions to this problem: increased enzyme concentration, increased substrate concentration through preconcentration¹, increased contact time or the addition of organic content to the digestion buffer². Simply by increasing the trypsin bed volume, one of these criteria is satisfied. Furthermore, the CIEF step prior to digestion will also serve to concentrate the samples making this less of an issue. Previous work by Wang *et al.*³, which was the basis for work done in this report, illustrates the improvement in sample digestion afforded through the use of a larger bed (2.5 μL). It can be concluded that use of larger trypsin beds will increase sample throughput by allowing for higher system flow rates. A simple study with a single channel, single bed system using various bed volumes, sample concentrations and flow rates would serve to determine an optimum bed volume.

6.2.2 SPE BEDS

In order for the delay line to be functional a flash elution of the peptides from the SPE beds was necessary. This was not feasible with the current system, as seen in Section 5.3.5. Despite the use of a high organic content eluent, many of the resulting peaks were still extremely broad. Furthermore, peptide behaviour was variable, with some eluting well, and others eluting as large, broad peaks. Use of a smaller SPE bed may drive the bed further to saturation and result in more plug-like elution behaviour. However, this will also limit loading capacity. The elution behaviour of the peptides is most likely too variable to expect a flash elution. The simplest solution is to allow enough time between fractions so that even the slowest eluting peptides will remain resolved.

6.2.3 BED DESIGN

The current bed design suffers from two major faults. The first is the actual bed packing procedure. The current arrangement makes it difficult to fully pack the bed without leaving some void volume in the reservoir. The packed region appears to be well packed however the reservoir used for bead introduction usually remains empty, and hence may act like a void volume or a mixing chamber. The second, more severe problem is the distribution of flow as sample enters the bed. As shown in Figure 3.3, sample enters the bed from a relatively small cross-sectional area at the bottom of the structure and is most likely not evenly distributed. Modelling of similar designs has shown there to be areas of dead volume in such beds.⁴ As shown in Section 5.3.3, instabilities in the column will lead to disrupted elution profiles, especially at higher flow rates. A new bed design, such as that presented by Bergkvist *et al.*⁴ may serve to improve the bed packing, allowing for higher flow rates to be used, thereby increasing sample throughput. Alternatively, the use of monolithic columns would also allow for a more uniform bed. These columns have been polymerized in situ in microfluidic devices for use as SPE beds⁵ and as trypsin immobilized digestion beds^{6,7}. Furthermore, this technique was recently used for immobilization of a protein digestion bed followed by a peptide concentration bed within an electrospray tip.⁸ This was the same approach taken in this thesis, using a more conventional bed structure. Columns of this type will also allow for a denser arrangement of adjacent channels. The original radius for the fractionation “star” was limited by the spacing required for the reservoirs that were drilled in the cover plate. Using a monolithic column, columns can be polymerized in-situ without the need for an access reservoir. There is still the question of the electrical contacts that need to be made if electrokinetic fractionation is to be performed. Integration of the electrodes onto the device would avoid this issue. However, the possibility of gas evolution would need to be addressed.

6.3 VARIABLE REGION

6.3.1 DELAY LINE

The delay line concept is functional in principle, as was shown in Sections 3.3.6 and 5.5. However, Figure 3.7 illustrates one of the drawbacks of the delay line in that the peaks eluted from the SPE bed will experience increasing dispersion depending on the distance they travel. Hence, those bands eluting from the longest channels in the variable region will be extremely broad. A simple solution to this is to place the SPE beds after the delay line, thereby delaying the contact of organic solvent to the bed. The bands eluting from the SPE beds would now all experience the same amount of dispersion when travelling to the MS. The only concern with this approach is that the leading edge of the organic solvent will experience dispersion and become diluted. This will affect elution of the peptides from the SPE beds possibly leading to peak fronting.

A second concern with the delay line is the amount of back pressure exhibited by the variable length channels. This was discussed in Section 5.5 and was determined to be an unresolved problem. In the current design, the resistance of the variable channels outweighs the resistance of the bed region and will dominate flow behaviour. Hence, flow will not be evenly distributed. In order to ensure even flow distribution a structure with a high resistance to flow would need to be incorporated at the head of the variable region. Such a structure would dominate flow resistance and the variable length channels beyond would be negligible in their contribution to flow resistance. Hence, at the single inlet, all channels would appear to have the same resistance. It should be noted that despite uneven flow distribution the delay line is still functional as was shown in Figure 5.16 and 5.17. The time for elution increases but the resulting peaks remain resolved.

6.3.2 VALVES

An alternative to the use of the delay line is to incorporate individually addressable valves into each of the channels so that flow may be selectively directed into only one of the twenty channels. This would avoid the need for the delay line, so that band broadening related to the variable channel lengths would be eliminated. This may be the more promising solution. Such a system would also avoid the need for a flash elution from the SPE bed, which has been shown to be non-trivial. Incorporation of valves into microfluidic devices has previously been seen as a challenge, but recent improvements in this area has led to the simple fabrication of valves. Publications involving the fabrication of valves on-chip are now too numerous and varied to be overviewed.^{12,13} Suffice to say that valves in a variety of materials, with rapid responses to various stimuli (pH, voltage, temperature, pressure) have been demonstrated.

6.4 COLLECTION REGION

The current design suffers from sample dilution at the outlet "star". In its present use, twenty flow streams recombine at this point, with only one of the incoming flows containing sample. Figure 5.5 illustrated that the sample flow will remain focused, however, the sample will only represent one component of twenty that are simultaneously introduced to the MS. Meaning that, sample from one channel will only account for one twentieth of the ESI flow rate. As the signal of a component in an ESI mass spectrum is concentration dependent, a gain in sample detection would be afforded if the sample represented the entire ESI flow rate. With the current design, utilizing a single outlet, this could be achieved through the use of a valving system that would allow flow from a single channel at a time, to reach the outlet. This should also serve to enhance the sensitivity of the system.

6.5 SYSTEM FLOW RATE

As mentioned previously, the use of a higher system flow rate will increase sample throughput by reducing analysis time. However, if the flow rate is increased several aspects of this initial prototype will need to be improved. The Nanoport™ that was used for sample introduction has been used at flow rates up to 200 $\mu\text{L}/\text{min}$ with the unsealed system without fail. Hence, it seems unlikely that it will fail even with the higher back pressure exhibited by the sealed system. The Plexiglass clamp that was used to seal the system leaked above inlet flow rates of 2 $\mu\text{L}/\text{min}$. Thus, a new clamp would need to be designed in order to seal the system at higher flow rates. Furthermore, a more evenly sealed clamp may avoid the issues related to septa deformation as discussed in Section 5.5. As mentioned before, by increasing the trypsin beds length protein digestion should be afforded at much higher flow rates. Improvement of bed design and packing procedure should allow higher flow rates to be used without fear of elution instabilities as was mentioned previously. The current sheathless ESI interface uses a tapered silica emitter, with a tip diameter of 15 μm . This tip could be used to generate signal at flow rates up to 1 $\mu\text{L}/\text{min}$, provided that the electrospray signal was first established at a lower flow rate. This approach was not always successful and the spray was much more stable at lower flow rates (100-400 nL/min). If higher system flow rates were to be used, a new interface would need to be designed that would allow for sample ionization at these higher flow rates. This should not be difficult as electrospray was originally designed for much higher flow rates than what are used in nano- or micro-electrospray techniques which have been used in most chip-MS couplings.

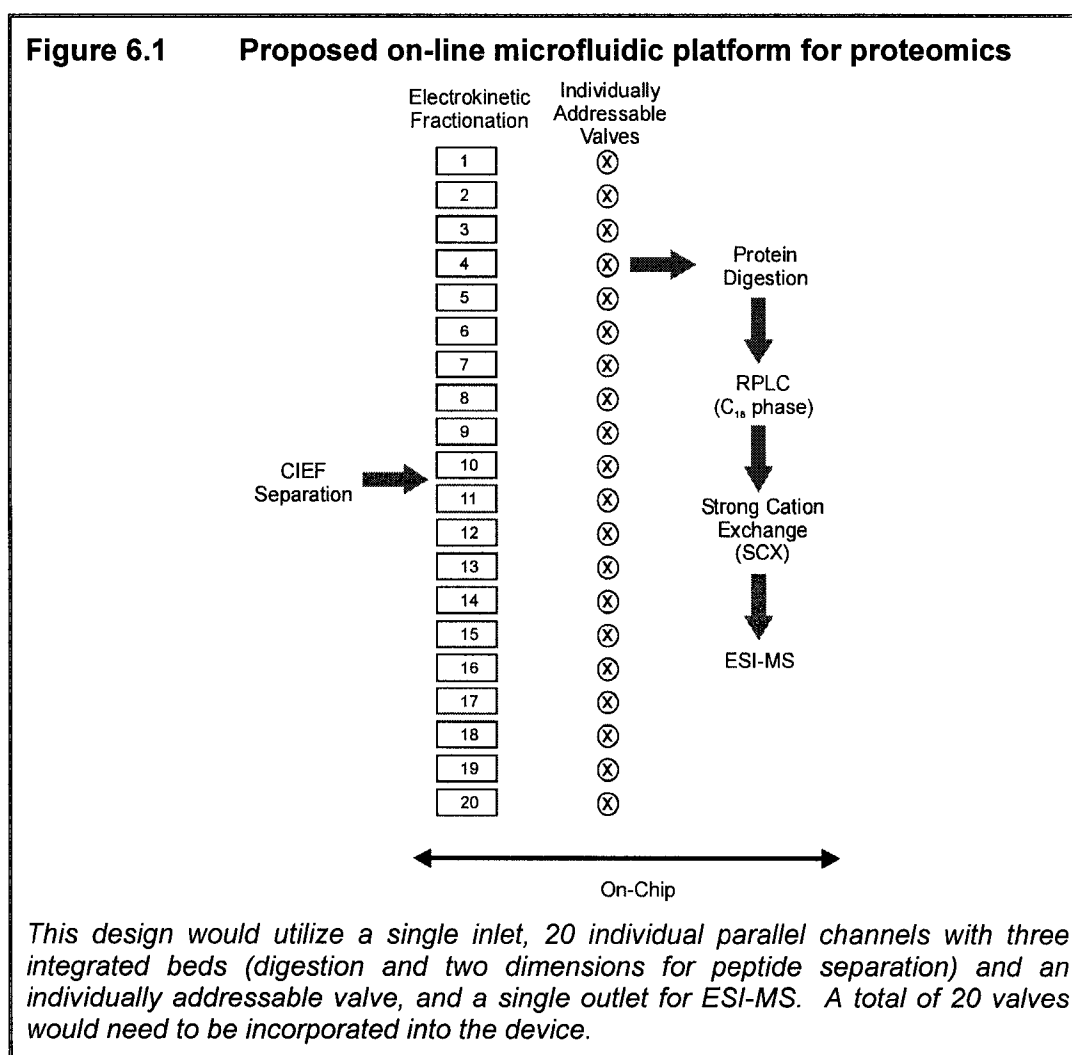
6.6 APPLICATION TO PROTEOMICS

Application of this device for use in analyzing real proteomic samples will require the use of another separation technique. Each of the twenty fractions would contain a mixture of proteins initially separated by CIEF. Digestion of

these proteins on-chip will lead to an even greater number of peptides. To identify all of the proteins in the original fraction, a means by which to separate the generated peptides is necessary in order to simplify the MS spectra. This could be achieved through the integration of another separation bed onto the device. Introducing another separation dimension on-chip will require additional fluidic contacts. A more reasonable approach may be to manipulate each fraction individually as opposed to simultaneously, as was intended for this initial prototype. Two approaches may be taken. There is the on-line approach, in which two separation dimensions are used simultaneously to separate peptide mixtures. Each fraction from the CIEF column would be adsorbed to the first bed (after digestion), and then, through gradient or step elution, be transferred and separated by the second bed. This approach has been successfully used off-chip for both 2 and 3 dimension separations.^{9,10} Using this technique, only a single buffer gradient system is needed at the head of the separations beds. As an example, the following strategy could be envisioned. One step-CIEF is coupled to electrokinetic fractionation, followed by pressure driven mobilization, driving the proteins through the trypsin beds and onto the C₁₈ phase. This is the same initial step that was used in the prototype presented in this thesis. The integration of individually addressable valves could allow for elution of each of the fraction independently. A series of step-gradients, similar to those presented by Yates^{9,10}, are applied to each fraction, allowing for peptide separation utilizing both separation dimensions simultaneously. A schematic of such an approach is illustrated in Figure 6.1. The RPLC and strong cation exchange (SCX) beds are merely examples of separation techniques that could be employed. The order in which they occur could also be switched. If the SCX phase was to be used first, the peptides would have to be acidified before introduction to the bed. In choosing techniques to be used in such an online configuration, buffer compatibility issues between separation dimensions become significant. A simple SPE C₁₈ bed after protein digestion may serve to simplify sample handling by allowing the peptides to be trapped before transfer to other separation techniques. Thus, such a system might employ the following path: CIEF,

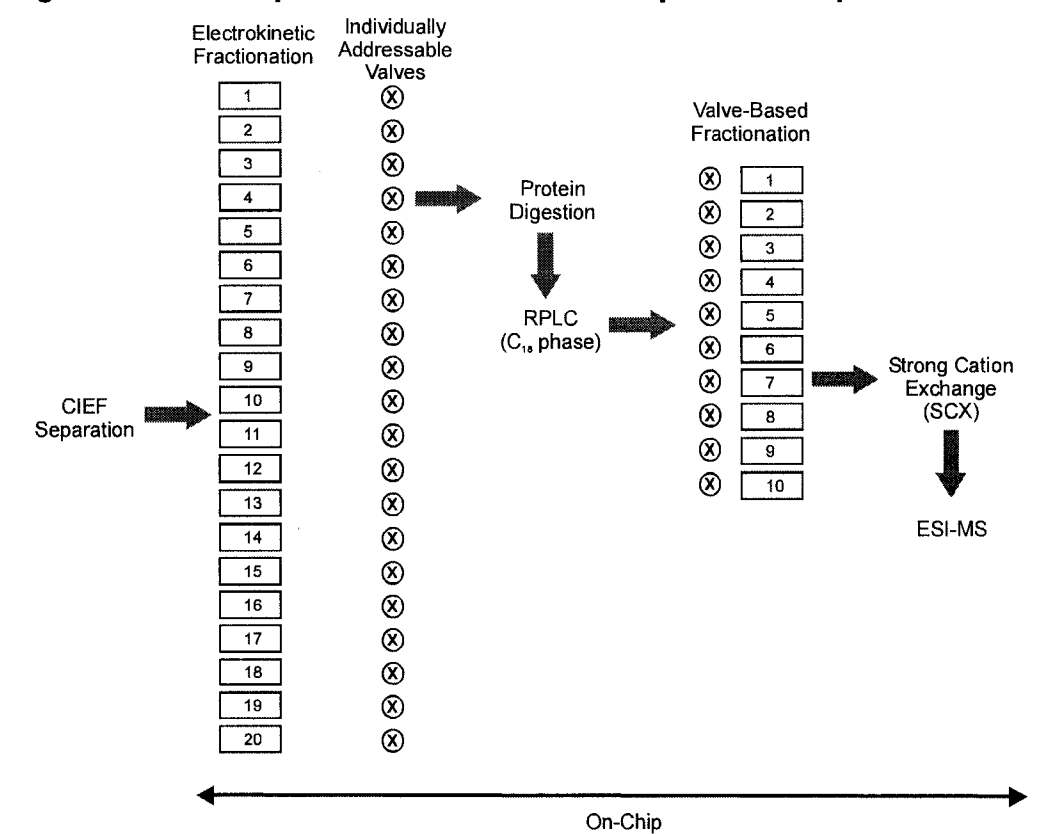
electrical fractionation, digestion, SPE trapping, SCX, C₁₈ and MS/MS analysis, as has been demonstrated off-chip⁹.

The elution gradient could be applied at the single inlet of such a device, provided that the elution buffers will not deactivate the trypsin beds. Otherwise, a fluidic contact at the head of each C₁₈ bed would be necessary. One of the limitations of on-line multi-dimensional separations is that the time allowed for collection of the resulting MS/MS spectra is limited by the separation technique. Hence, separation time actually limits the number of spectra that can be collected, leading to a loss in protein identification abilities. The application of this technique will depend on the complexity of the sample to be analysed.



The offline method, avoids the aforementioned problem, as the MS/MS analysis is performed for each fraction individually. This technique has been used with success off-chip and gives the analyst more control over the separation and data analysis processes.¹¹ In this method, peptides are separated in one dimension, collected in separate fractions and then individually separated by the second separation technique. On-chip, this would require a second fractionation step after the first dimension of peptide separation. This would greatly increase the number of valves needed. A strategy employing this design could include the same initial electrokinetic fractionation step. Peptides could then be eluted from the C₁₈ bed and fractionated again through the use of valves this time. Using a 10 part fractionation technique, the eluent from the C₁₈ bed would be fractionated to the second separation dimension on the basis of increasing organic content, for example. Hence, the first channel would be at 10%, the second at 20% and so on. Elution from the second dimension is achieved through the use of the same addressable valves, to elute each fraction separately to the MS. This requires a fluidic contact at head of the second fractionation step, 20 in total. The complexity of this design is greatly increased, but an improvement in separation should lead to the identification of more proteins. A schematic of such a system is shown in Figure 6.2. This strategy employs 200 valves and at least 20 individual fluidic contacts. This may seem daunting, but systems with similar complexity have recently been demonstrated^{12,13}, and thus it is not out of the realm of possibility. Furthermore, the complexity of proteomic analysis requires such systems and hence the field of microfluidics must advance in order to remain competitive.

Figure 6.2 Proposed off-line microfluidic platform for proteomics



This design would utilize a single inlet which fractionates into 20 individual parallel channels with two integrated beds (digestion and one dimension of separation) and an individually addressable valve. Each of these channels then splits into 10 parallel channels each with an addressable valve and a bed (second dimension of separation). Finally, these channels should lead to a single outlet for ESI-MS. A total of 200 valves would need to be incorporated into the device.

6.7 ALTERNATIVE APPLICATIONS

In designing the multichannel device its intended purpose was that each of the twenty parallel channels would ultimately contain a different sample. Each channel would contain identical processing beds, and the delay line after the beds would serve to separate the different samples as they eluted. This device could also be used with a single sample at the inlet and variable chemistries contained within the beds. One could envision this could be used as a high throughput technique for drug candidate screening or affinity selection. An idea similar to that presented by Murer *et al.*¹⁴ could be used. In this work, a library of 36 L-amino acid anilides were immobilized on macroporous beads. Mixtures of the beads were then used as column packing material in order to select the best chiral stationary phase. By using mixed packings of smaller subsets of the total library, in conjunction with a deconvolution method, fewer columns are screened. Provided that the delay line is functional, this device should be able to function in this single sample mode as well.

6.8 REFERENCES

- (1) Craft, D.; Doucette, A.; Li, L. *J. of Prot. Res.* **2002**, *1*, 537-547. "Microcolumn capture and digestion of proteins combined with MS for protein identification"
- (2) Slys, G. W.; Schriemer, D. C. *Rapid Commun. Mass Spectrom.* **2003**, *17*, 1044-1050. "On-column digestion of proteins in aqueous-organic solvents"
- (3) Wang, C.; Oleschuk, R.; Ouchen, F.; Li, J. J.; Thibault, P.; Harrison, D. J. *Rapid Commun. Mass Spectrom.* **2000**, *14*, 1377-1383. "Integration of immobilized trypsin bead beds for protein digestion within a microfluidic chip incorporating CE separations and an ESI-MS interface"
- (4) Bergkvist, J.; Ekström, S.; Wallman, L.; Löfgren, M.; Marko-Varga, G.; Nilsson, J.; Laurell, T. *Proteomics* **2002**, *2*, 422-429. "Improved chip design for integrated solid-phase microextraction in on-line proteomic sample preparation"
- (5) Yu, C.; Davey, M. H.; Svec, F.; Frechet, J. M. J. *Anal. Chem.* **2001**, *73*, 5088-5096. "Monolithic porous polymer for on-chip SPE and preconcentration prepared by photoinitiated in situ polymerization within a microfluidic device"
- (6) Peterson, D. S.; Rohr, T.; Svec, F.; Frechet, J. M. J. *Anal. Chem.* **2002**, *74*, 4081-4088. "Enzymatic microreactor-on-a-chip: Protein mapping using trypsin immobilized on porous polymer monoliths molded in channels of microfluidic devices"
- (7) Peterson, D. S.; Rohr, T.; Svec, F.; Frechet, J. M. J. *J. Prot. Res.* **2002**, *1*, 563-568. "High-throughput peptide mass mapping using a microdevice containing trypsin immobilized on a porous polymer monolith coupled to MALDI TOF and ESI TOF mass spectrometers"
- (8) Peterson, D. S.; Rohr, T.; Svec, F.; Frechet, J. M. J. *Anal. Chem.* **2003**, *75*, 5328-5335. "Dual-function microanalytical device by in situ photolithographic grafting of porous polymer monolith: Integrating SPE and enzymatic digestion for peptide mass mapping"
- (9) McDonald, W. H.; Ohi, R.; Miyamoto, D. T.; Mitchison, T. J.; Yates, J. R. *Int. J. Mass Spectrom. Ion Processes* **2002**, *219*, 245-251. "Comparison of three directly coupled HPLC MS/MS strategies for identification of proteins from complex mixtures"
- (10) Wolters, D. A.; Washburn, M. P.; Yates, J. R. *Anal. Chem.* **2001**, *73*, 5683-5690. "An automated multidimensional protein identification technology for shotgun proteomics"
- (11) Wagner, Y.; Sickmann, A.; Meyer, H. E.; Daum, G. *J. Am. Soc. Mass Spectrom.* **2003**, *14*, 1003-1011. "Multidimensional nano-HPLC for analysis of protein complexes"
- (12) Thorsen, T.; Maerkl, S. J.; Quake, S. R. *Science (Washington, D. C., 1883-)* **2002**, *298*, 580-584. "Microfluidic large-scale integration"
- (13) Liu, J.; Hansen, C.; Quake, S. R. *Anal. Chem.* **2003**, *75*, 4718-4723. "Solving the "World-to-Chip" interface problem with a microfluidic matrix"

- (14) Murer, P.; Lewandowski, K.; Svec, F.; Fréchet, J. M. J. *Anal. Chem.* **1999**, *71*, 1278-1284. "On-bead combinatorial approach to the design of chiral stationary phases for HPLC"

APPENDIX

SUPPLIERS OF REAGENTS AND EQUIPMENT

AB-M, Inc.

San Jose, CA, USA
www.abmfg.com

Adtek

Montreal, QC, Canada
www.adtekphotomask.com

Applied Biosystems

Foster City, CA, USA
www.appliedbiosystems.com

Arch Chemicals, Inc.

Norwalk, CT, USA
www.archchem.com

Aremco Products, Inc.

Valley Cottage, NY, USA
www.aremco.com

BDH Inc.

Toronto, Ontario, Canada
www.bdh.com

Beckman Coulter

Mississauga, Ontario, Canada
www.beckmancoulter.com

bioMérieux

Marcy l'Étoile, France
www.biomerieux-vitek.com

Bio-Rad

Hercules, CA, USA
www.bio-rad.com

Caledon Laboratories Ltd

Georgetown, Ontario, Canada
www.caledonlabs.com

Carl Zeiss Jena

Jena, Germany
www.zeiss.de

Chromatographic Specialties Inc.

Brockville, Ontario, Canada
www.chromspec.com

Diagnostic Instruments Inc.

Sterling Heights, MI, USA
www.diaginc.com

Fisher Scientific

Hanover Park, IL, USA
www.fisherscientific.com

GE Silicones

www.gesilicones.com

Hamamatsu

Tokyo, Japan
www.hamamatsu.com

Hamilton Company

Reno, NV, USA
www.hamiltoncorp.com

Harvard Apparatus

Saint-Laurent, Quebec, Canada
www.harvardapparatus.com

JDS Uniphase

San Jose, CA, USA
www.jdsu.com

JVC Company of America

Wayne, NJ, USA
pro.jvc.com

Kilovac Corporation

Santa Barbara, CA, USA
www.kilovac.com

Kyocera Tycom

Mississauga, ON, Canada
www.kyoceratycom.com

Lunzer, Inc.

Saddle Brook, NJ, USA
www.lunzer.com

MDS Sciex

Concord, Ontario, Canada
www.sciex.com

Melles Griot

Ottawa, Ontario, Canada
www.mellesgriot.com

Micalyne Inc.

Edmonton, Alberta, Canada
www.micalyne.com

Millipore Canada
Mississauga, Ontario, Canada
www.millipore.com

National Instruments
Austin, TX, USA
www.ni.com

National Research Council Canada
Ottawa, Ontario, Canada
www.nrc-cnrc.gc.ca

New Objective, Inc.
Woburn, MA, USA
www.newobjective.com

Newport
Irvine, CA, USA
www.newport.com

OCG Microelectronic Materials Inc
West Paterson, NJ, USA
201-977-6002

Olympus
Melville, NY, USA
www.olympusamerica.com

Omega Optical
Battleboro, VT, USA
www.omegafilters.com

Pierce Chemical Company
Rockford, IL, USA
1-800-8-PIERCE

Polymicro Technologies, L.L.C.
Phoenix, AZ, USA
www.polymicro.com

Rose Scientific Ltd.
Edmonton, Alberta, Canada
www.rosesci.com

Servo Products Company
Pasadena, CA, USA
www.servoproductsco.com

Shiple Company, L.L.C.
Marlborough, MA, USA
www.shiple.com

Sigma-Aldrich
Milwaukee, WI, USA
www.sigmaaldrich.com

Solitec Wafer Processing, Inc.
Milpitas, CA, USA
www.solitec-wp.com

Spellman®
Hauppauge, NY, USA
www.spellmanhv.com

Upchurch Scientific
Oak Harbour, WA, USA
www.upchurch.com

Waters
Milford, MA, USA
www.waters.com